2016

Damage Analysis of Steel Concentrically Braced Frame Systems under Seismic Conditions

Ebrahim Tahmasebi
Lehigh University

Damage Analysis of Steel Concentrically Braced Frame Systems under Seismic Conditions

by

Ebrahim Tahmasebi

Presented to the Graduate and Research Committee

of Lehigh University

in Candidacy for the Degree of

Doctor of Philosophy

in

Structural Engineering

Lehigh University

Bethlehem, PA

January 2016

Approved and recommended for acceptance as a dissertation in partial fulfillment of the requirements for the degree of Doctor of Philosophy.

Date

Dr. Richard Sause
Dissertation Co-Advisor

Dr. James M. Ricles
Dissertation Co-Advisor

Accepted Date

Committee Members:

Dr. John L. Wilson
Committee Chairperson

Dr. Paolo Bocchini
Committee Member

Dr. Maria Garlock
External Member

Dedicated to my beautiful wife Forough for her endless love and constant support

with appreciation for patiently enduring these years of doctoral study

and always standing by my side.

Acknowledgements

The research presented in this dissertation was conducted at the Engineering Research Center for Advanced Technology for Large Structural System (ATLSS), Department of Civil and Engineering, Lehigh University, Bethlehem, Pennsylvania. The financial support from the Civil and Environmental Engineering Department of Lehigh University is greatly appreciated.

I would like to express my deepest gratitude to my research advisors, Dr. Richard Sause and Dr. James M. Ricles for their excellent guidance, advice, and patience. I would also like to thank Dr. John L. Wilson, the chair of my research committee, for his advice and support. The time, input, and contributions of my other research committee members, Dr. Paolo Bocchini and Dr. Maria Garlock, are greatly appreciated.

I would like to thank my friends and colleagues at Lehigh University and specifically my fellow graduate students and scholars at ATLSS Engineering Research Center. The input and help from Brent Chancellor, Akbar Mahvashmohammadi, Choung-Yeol Seo, Mohamed Soliman, Aman Karamlou, Attila László Joó, and Chinmoy Kolay is greatly appreciated. I greatly appreciate the support and patience of ATLSS personnel, specifically Peter Bryan and Tommy Marullo.

I also would like to thank the Lehigh University high performance computing team for their help and patience. The high performance computing facilities at Lehigh University greatly expedited the analyses conducted in this research.

Finally, and most importantly, I would like to thank my wife Forough. Her support, encouragement, patience, and endless love were undeniably the bedrock upon which the past seven years of my life have been built. I am also thankful to my loving parents, Mr. Abbasali Tahmasebi and Mrs. Tahereh Bostanian, for their constant support and their faith in me during my doctoral studies. I would have not been able to complete this dissertation without the support from my wife and my parents.

Table of Contents

List of Tables

List of Figures

Notation

Abbreviations

AE	Assessment event, page 120
BRB	Buckling restrained braces, page 18
CDF	Cumulative distribution function, page 84
CP	Collapse prevention performance objective, page 53
DBE	Design basis earthquake, page 52
DS	Damage state, page 120
DSTA	Damage scenario tree analysis, page 119
EDP	Engineering demand parameter, page 76
ELF	Equivalent lateral force, page 49
ETA	Event tree analysis, page 119
FOSM	First-order second-moment, page 31
GM	Ground motion record, page 122
IDA	Incremental dynamic analysis, page 76
IE	Initiating event, page 119
IM	Hazard intensity measure, page 76

IO	Immediate occupancy performance objective, page 53
LHS	Latin Hypercube sampling, page 170
MCE	Maximum considered earthquake, page 53
PE	Pivotal events, page 120
PFDC-MRF	Moment resisting frame with post-tensioned friction damped connection, page 13
PFDC	Post-tensioned friction damped connection, page 13
PGV	Peak ground acceleration, page 77
PT	Post tensioning, page 11
RA	Repair action, page 120
RSA	Response spectrum analysis, page 52
RTR	Record-to-record variability in structural response, page 90
SCBF	special concentrically braced frame, page 42
SC-CBF	Self-centering concentrically braced frame, page 16
SCED	Self-centering energy dissipative (steel brace), page 18
SLFRS	Seismic lateral force resisting system, page 42
VDCSR	Viscously damped controlled seismic rocking, page 19

Greek Symbols

β_{DR}	Logarithmic standard deviation for collapse capacity uncertainty due to DR variability, page 99

β_{MDL} Logarithmic standard deviation for collapse capacity uncertainty due to MDL variability, page 99

β_{RTR} Logarithmic standard deviation for collapse capacity uncertainty due to RTR variability, page 99

β_{TD} Logarithmic standard deviation for collapse capacity uncertainty due to TD variability, page 99

β_{TOT} Logarithmic standard deviation for total collapse capacity uncertainty, see equation (4.9), page 99

Δ_{Oi} Normalized initial out-of-straightness of braces, page 168

Δ_{Or} Normalized residual out-of-plane deformation at the mid-length of the braces, page 146

$\Delta_{Or_{x,BM}}$ Δ_{Or} values for GM_x and base model, page 184

$\Delta_{Or_{x,i}}$ Δ_{Or} values for GM_x and sample model MDL_i, page 184

$\tilde{\Delta}_{Or_{x,i}}$ Median of $\Delta_{Or_{x,i}}$ values, page 184

δ_u Ultimate roof displacement in a pushover analysis, page 72

$\delta_{y,eff}$ Effective yield roof displacement, see equation (4.6), page 96

$\varepsilon_{PT,m}$ Maximum strain in PT bars (for SC-CBF system), page 278

θ_m Maximum story drift ratio, page 77

$\theta_{m,C}$ θ_m limit value separating non-collapse from collapse DS, page 124

$\theta_{m_{x,BM}}$ θ_m value for GM_x sample model MDL_i, page 177

$\theta_{m_{x,i}}$ θ_m value for GM_x sample model MDL_i, page 177

$\tilde{\theta}_{m_{x,i}}$ Median of $\theta_{m_{x,i}}$ values, page 177

θ_r Maximum (over all stories) residual story drift ratio, page 107

$\theta_{r,D}$ θ_r limit value separating non-demolition from demolition DS, page 124

$\theta_{r_{x,BM}}$ θ_r value for GM_x and the base model, page 181

$\theta_{r_{x,i}}$ θ_r value for GM_x and sample model MDL_i, page 181

$\tilde{\theta}_{r_{x,i}}$ Median of $\theta_{r_{x,i}}$ values, page 181

λ_{DR} Random variable representing the uncertainty in collapse capacity due to DR variability, page 99

λ_{MDL} Random variable representing the uncertainty in collapse capacity due to MDL variability, page 99

λ_{RTR} Random variable representing the uncertainty in collapse capacity due to RTR variability, page 99

λ_{TD} Random variable representing the uncertainty in collapse capacity due to TD variability, page 99

λ_{TOT} Random variable representing the total uncertainty in collapse capacity, see equation (4.8), page 99

μ_T Period based ductility, see equation (4.5), page 96

$\boldsymbol{\rho}_{\Delta_{Oi}}$ Correlation matrix between SCBF brace initial out-of-straightness, see equation (6.20), page 170

$\boldsymbol{\rho}_{\Delta_{Oi},LL}$ Correlation matrix between SCBF brace initial out-of-straightness and live load at different building floors, see equation (6.22), page 170

$\boldsymbol{\rho}_{LL}$ Correlation matrix between live load at different building floors, see equation (6.21), page 170

$\boldsymbol{\rho}_{TOT}$ Total correlation matrix (between SCBF brace initial out-of-straightness and live load at different building floors), see equation (6.19), page 169

$\sigma_{\ln S_{a,C}}$ Logarithmic standard deviation of $S_{a,C}$ values (assuming lognormal distribution for $S_{a,C}$ values), see equation (4.2), page 89

Ω Overstrength factor, page 69

Roman Symbols

ACMR Adjusted collapse margin ratio, see equation (4.4), page 96

$ACMR_{10\%}$ *ACMR* corresponding to 10% probability of collapse, page 100

$ACMR_{20\%}$ *ACMR* corresponding to 20% probability of collapse, page 100

BR Brace replacement repair action, page 146

BS Brace straightening repair action, page 146

C Collapse damage state, page 120

CMR Collapse margin ratio, see equation (4.3), page 95

C_S Seismic response coefficient, see equation (3.2), page 49

C_{vx} Vertical distribution factor, see equation (3.6), page 50

D Demolition and reconstruction, page 121

DR Variability in design requirements, page 98

$DS_{c,q,n}$ n^{th} Damage state for q^{th} component, page 147

DS_s	System level damage state, page 120
DS_{ss}	Subsystem level damage state, page 121
EDP_c	EDP corresponding to the component level damage assessment, page 122
EDP_{cpcty}	EDP capacity, see equation (2.1), page 28
$EDP_{c,q}$	EDP used for the q^{th} component damage assessment, page 123
$EDP_{c,q,DS,n}$	EDP limit value separating the $(n-1)^{th}$ DS and n^{th} DS for the q^{th} component, page 123
EDP_{dmnd}	EDP demand, see equation (2.1), page 28
$EDP_{DS,i}$	EDP limit values separating the $(i-1)^{th}$ DS and i^{th} DS, page 123
EDP_s	EDP corresponding to the system level damage assessment, page 122
$EDP_{s,C}$	EDP limit value separating collapse from non-collapse DS, page 123
$EDP_{s,DS,ns}$	EDP limit value separating the $(ns-1)^{th}$ and ns^{th} system level damage state, page 123
EDP_{ss}	EDP corresponding to the subsystem level damage assessment, page 122
$EDP_{ss,p}$	EDP used for the p^{th} subsystem damage assessment, page 123
$EDP_{ss,p,D}$	EDP limit value separating demolition from non-demolition DS, page 123
$EDP_{ss,p,DS,nss}$	EDP limit value separating the $(nss-1)^{th}$ DS and nss^{th} DS for the p^{th} subsystem, page 123
$F_{EDP_{DS,i}}$	i^{th} EDP limit value fragility function, see equation (5.1), page 124
$F_{\Delta_{Or,DS,n}}$	Brace n^{th} DS fragility function, page 146

$F_{\theta_{m,C}}$	Collapse fragility function, page 124
$\bar{F}_{\theta_{m,C,l,i}}$	Complementary collapse fragility function for the MDL_i and GM_l, see equation (6.10), page 162
$F_{\theta_{m,C,l,i}}$	Collapse fragility function for the MDL_i and GM_l, see equation (6.8), page 161
$F_{\theta_{r,D}}$	Demolition fragility function, page 124
$F_{\theta_{r,D,MDL}}$	Demolition fragility function including the system parameter variability and modeling uncertainty, page 191
$F_{IM_{C,l}}$	IM-based collapse fragility function for GM_l, page 152
$\bar{F}_{IM_{C,l}}$	IM-based complementary collapse fragility function for GM_l, page 153
$\bar{F}_{IM_{C,l,i}}$	Complementary collapse fragility function for GM_l and MDL_i, see equation (6.16), page 165
$F_{IM_{C,l,i}}$	Collapse fragility function for GM_l and MDL_i, see equation (6.14), page 164
F_x	Lateral seismic force at story x, see equation (3.6), page 50
GM_l	Ground motion record number l from a ground motion record set containing L ground motion records, page 122
I_e	Seismic importance factor, page 46
IM	Hazard intensity measure value, page 151
IM_C	IM value at collapse, page 151
$IM_{C,l,i}$	IM_C for GM_l and MDL_i, page 164
MD	Variability in modeling, page 98

MDL_i	Numerical model developed using the i^{th} set of samples for random system and modeling parameters, page 158
NC	Non-collapse damage state, page 120
ND	Non-demolition, page 121
NR	No repair, page 146
OM_D	Decompression overturning moment, page 53
PT_{DS}	PT bar damage state (for SC-CBF system), page 278
RTR	Variability in ground motion record, page 98
$S_{a,C}$	$S_a(T,5\%)$ at building collapse, page 84
$\tilde{S}_{a,C}$	Estimated median of $S_{a,C}$ values (assuming lognormal distribution for $S_{a,C}$ values), see equation (4.1), page 89
$S_a(T,5\%)$	5% damped spectral acceleration at fundamental period of the building, page 76
$\hat{S}_{CT}$	Median (counting) collapse capacity of a SLFRS, page 90
S_e	Median of initial slopes of IDA curves for a ground motion record set and a building, page 84
S_{MT}	$S_a(T,5\%)$ for maximum considered earthquake, page 95
SSF	Spectral shape factor, page 96
T	Approximate fundamental period of archetype building, see equation (3.1), page 47
TD	Variability in test data, page 98

V	Seismic design base shear, see equation (3.2), page 49
V_D	Base shear at column decompression for SC-CBF system, page 72
V_{max}	Maximum base shear capacity in pushover analysis, page 69
V_Y	Base shear at PT bar yielding for SC-CBF system, page 72
W	Effective seismic weight, see equation (3.2), page 49

Abstract

The overall objective of this research is to understand the potential for earthquake-induced damage of the steel self-centering concentrically braced frame (SC-CBF) system and compare this damage potential with the damage potential for the conventional special concentrically braced frame (SCBF) system. The SC-CBF system is a new seismic lateral force resisting system (SLFRS) that was developed and studied at ATLSS Engineering Research Center at Lehigh University. Extensive analytical simulations and experimental hybrid simulations were conducted on a 60% scale 4-story SC-CBF system using the Network for Earthquake Engineering Simulation (NEES) facility located at the ATLSS center. While the SC-CBF system was damage free under the ground motions at the DBE hazard level and self-centered under the ground motions at the MCE hazard level, the potential for damage of the SC-CBF system at hazard intensities beyond MCE had not been studied. The scope of this research includes: (i) collapse performance evaluation of the SC-CBF and conventional SCBF in accordance with FEMA P695; (ii) development of a probabilistic seismic damage analysis framework considering damage states other than building collapse; (iii) including system parameter variability and modeling uncertainty in the probabilistic damage analysis framework; and (iv) developing and comparing damage scenario fragilities for the innovative SC-CBF and conventional SCBF systems.

Collapse performance evaluations for the innovative SC-CBF system and the conventional SCBF system were conducted in accordance with FEMA P695. It was observed that the margin against collapse for the SC-CBF system is greater than the margin against collapse for the SCBF system. Residual drift for the SC-CBF system is observed at relatively

large hazard intensity levels compared to the SCBF system.

A probabilistic seismic damage analysis framework was developed for buildings using the event tree diagram concept. Damage states other than the collapse of the building were considered in developing the probabilistic seismic damage analysis framework. In the framework, damage assessments are performed at the system level, subsystem level, and component level. Damage scenarios are defined using the three levels of damage assessments.

System parameter variability and modeling uncertainty were included in the probabilistic seismic damage analysis framework using results from Monte Carlo simulation. An approximate method for including the system parameter variability and modeling uncertainty in the damage scenario probabilities was developed and presented.

Fragilities were developed for different damage scenarios for the SCBF and SC-CBF systems using the probabilistic seismic damage analysis framework. Damage scenario fragilities were compared for the SCBF and SC-CBF archetype buildings. It was observed that the SC-CBF system has a smaller probability of collapse than the SCBF system, and has smaller probability of structural damage (when collapse has not occurred) than the SCBF system.

Chapter 1

Introduction

1.1 Overview

Current building codes allow seismic lateral force resisting systems to undergo nonlinear response and damage under the design basis earthquake (DBE) by specifying response modification factors which are used in calculating earthquake design forces. Past earthquakes indicate that damage to structural systems is a main source of social and economic losses [42]. Seismic design of structural systems with the objective of withstanding the DBE without serious damage can reduce social and economic losses.

Two typical, conventional seismic lateral force resisting systems are the special moment resisting frame (SMRF) system and the steel special concentrically braced frame (SCBF) system. The SMRF system provides good ductility capacity with a higher cost of construction compared to the SCBF system (e.g., more larger members and expensive detailing). The SCBF system is an efficient and economical seismic lateral force resisting system due to the diagonal braces, which does not provide as much deformation capacity as the SMRF system, before damage initiates, due to buckling of the braces. The steel self-centering concentrically braced frame (SC-CBF) system is a new seismic lateral force resisting system that takes advantage of the efficiency of the SCBF system, but also provides excellent ductility capacity, without excessive permanent drift and damage, due to the self-centering, rocking behavior of the SC-CBF [66].

The SC-CBF system consists of structural members similar to those of the SCBF system: columns, beams, and braces. In addition to these structural members, the SC-CBF system has post tensioning (PT) bars that run over along the height of the structure, which are anchored at the roof level and at the foundation. The main feature of the SC-CBF system is the decompression and uplift of the columns from the foundation, which enables the SC-CBF to rock on its foundation. The tension force in the PT bars and the gravity loads are restoring force components during rocking that cause the columns to return to the foundation so that the SC-CBF self-centers [75].

An experimental study of a 60% scale 4-story SC-CBF system was conducted at Lehigh University. The 4-story SC-CBF, designed using the first generation design procedure for SC-CBF systems developed by Roke [66], was subjected to a large number of strong ground motion records, at the design basis earthquake (DBE) and maximum considered earthquake (MCE) level using hybrid simulation. Excellent self-centering behavior and no damage to the structural members were observed. A second generation SC-CBF system design procedure was developed by Chancellor [11].

The performance of the SC-CBF system at the DBE and MCE level has been studied [66, 11]. The effect of rocking on the collapse performance of the SC-CBF systems has not been studied yet. This research is the first to study the collapse performance of the SC-CBF system and compare it with the collapse performance of the conventional SCBF system. Evaluation of the collapse performance is conducted in accordance with the FEMA P695 methodology [23]. The margin against collapse of the SC-CBF system is established and compared to that of the conventional SCBF system.

This research also addresses seismic damage states other than the collapse damage state. A probabilistic damage analysis framework is developed and applied to the SCBF and SC-CBF systems. The damage analysis framework is comprehensive and assesses damage at

the system level, subsystem level, and component level. Damage scenarios are defined within the developed damage analysis framework and different approaches for evaluating the damage scenarios are studied. Damage scenario fragility curves are developed for the SCBF and SC-CBF systems and are compared.

The effects of system parameter variability and modeling uncertainty are considered in an extended version of the probabilistic damage analysis. An example to demonstrate the effect of system parameter variability and modeling uncertainty is developed for the SCBF system. An approximate method of including the system parameter variability and modeling uncertainty is presented and discussed.

1.2 Research Objectives

The overall objective of this research program is to understand the potential for earthquake-induced damage of the new SC-CBF system under earthquake ground motions at various levels of intensity, and compare this potential for damage to the earthquake-induced damage potential of the conventional SCBF system. The specific objectives necessary to achieve the overall objective are as follows:

1. To conduct a collapse performance evaluation of the SC-CBF system and the SCBF system in accordance with FEMA P695 document methodology [23], and compare the results
2. To develop a framework for conducting probabilistic seismic damage analysis of buildings
3. To include damage states other than building collapse in the probabilistic damage analysis, using this framework

4. To include the effect of system parameter variability and modeling uncertainty in the probabilistic seismic damage analysis framework

5. To compare the probabilities of different damage scenarios for the SC-CBF system and the SCBF system

1.3 Research Scope

To achieve the research objectives, several tasks were undertaken as follows:

1. **Archetype building development and design**

   Four buildings with different numbers of stories are considered in this research. The two seismic lateral force resisting systems, SCBF and SC-CBF, are used for each building, so a total of eight archetype buildings are developed. The SCBF archetype buildings are designed in accordance with ASCE 7-10 [4]. The SC-CBF archetype buildings are designed using the design procedure proposed by Roke [66] and modified by Chancellor [11].

2. **Numerical model development**

   Two dimensional nonlinear numerical models appropriate for each archetype building are developed using the OpenSEES computational framework [53]. Stiffness deterioration, strength deterioration, and fracture of the main structural members are included in the numerical models.

3. **Nonlinear static pushover analyses and dynamic response history analyses**

   Nonlinear static pushover analyses are conducted for the archetype buildings. Important lateral strength and deformation parameters are calculated from the static pushover analyses results for each archetype building. Nonlinear dynamic response

history analyses are conducted in the form of incremental dynamic analyses for each archetype building.

4. **Collapse performance evaluation**

   The collapse capacity of each archetype buildings is estimated from the incremental dynamic analysis results. The collapse margin ratio and adjusted collapse margin ratio are determined for each archetype building in accordance with the FEMA P695 document methodology [23]. Collapse fragility curves are developed for each archetype building using the incremental dynamic analysis results.

5. **Probabilistic seismic damage analysis framework**

   A probabilistic seismic damage analysis framework is developed for buildings using the event tree diagram concept. Damage states other than the collapse of the building are considered in developing the probabilistic seismic damage analysis framework. In the framework, damage assessments are performed at the system level, subsystem level, and component level. Damage scenarios are defined using the three levels of damage assessments. Mathematical formulas are developed for evaluating the damage scenario probabilities.

6. **Extension for system parameter variability and modeling uncertainty**

   Mathematical formulas are developed for including system parameter variability and modeling uncertainty in the probabilistic seismic damage analysis framework using results from Monte Carlo simulation. These mathematical formulas are demonstrated using a 9-story SCBF archetype building as an example. An approximate method for including the system parameter variability and modeling uncertainty in the damage scenario probabilities is developed and presented.

7. **Damage scenario probability comparison for SC-CBF and SCBF systems**

   Fragilities are developed for different damage scenarios for the SCBF and SC-CBF

archetype buildings using the probabilistic seismic damage analysis framework. Damage scenario fragilities are compared for the SCBF and SC-CBF archetype buildings.

1.4 Outline of Dissertation

This dissertation consists of eight chapters as follows:

Chapter 1 gives an overview of the research, including research objectives and scope, and outlines the organization of the dissertation.

Chapter 2 reviews background information related to this research. Previous research on self-centering and rocking systems are summarized. Current methods for collapse assessment of seismic lateral force resisting systems are summarized. Current damage analysis methods are summarized.

Chapter 3 describes the design of the archetype buildings and the nonlinear analysis modeling and typical results for the archetype buildings. The plan and numbers of stories of the archetype buildings are presented. The design processes for the SCBF and SC-CBF archetype buildings, including important design parameters and the final design of main structural members are summarized. The numerical modeling of the archetype buildings in OpenSEES is discussed. The process for the nonlinear static pushover analyses and the dynamic response history analyses is explained and results of the analyses are presented.

Chapter 4 presents collapse performance evaluations of the SCBF and SC-CBF archetype buildings. Collapse fragility curves are presented for the archetype buildings. The collapse margin ratio and adjusted collapse margin ratio are estimated and compared against the acceptable values for the archetype buildings. The effect of varying the collapse criteria is studied. Residual story drift ratios for the archetype buildings from the nonlinear dynamic response history analyses are presented and compared for the SCBF and SC-CBF

systems.

Chapter 5 presents a framework for a probabilistic seismic damage analysis of buildings. Damage assessments are conducted at the system level, subsystem level, and component level. Damage scenarios are developed by organizing the results of the damage assessments into a damage scenario tree. Mathematical expressions are developed for evaluating the damage scenario probabilities. An engineering demand parameter-based method and a hazard intensity measure-based method for quantifying the probability of the collapse damage state are presented and applied. The framework and mathematical expressions are applied to a 9-story archetype building.

Chapter 6 considers the effect of variability of the building system parameters and the uncertainty regarding numerical modeling decisions and parameters in a seismic damage analysis. The system parameter variability and modeling uncertainty is included in the seismic damage analysis framework developed in Chapter 5, in addition to the variability in structural response due to the variation of ground motion records. Mathematical expressions are developed for including the system parameter variability and modeling uncertainty in the seismic damage analysis framework using the results of a Monte Carlo simulation. A 9-story archetype building is used to demonstrate the application of these mathematical expressions in Chapter 6. An approximate method for including the system parameter variability and modeling uncertainty is presented.

Chapter 7 presents and compares the damage scenario fragilities for the SCBF and the SC-CBF archetype buildings. The damage scenario fragilities are developed using the seismic damage analysis framework presented in Chapter 5.

Chapter 8 summarizes the findings from this research and presents conclusions and recommendations for future research.

Chapter 2

Background

2.1 Introduction

This chapter summarizes some of the previous research conducted on the topics relevant to the present research. The first section reviews different self-centering and rocking structural systems. In the second section, the related collapse assessment methodologies are summarized. In the third section, some of the previous studies that addressed uncertainty in structural system parameters, in addition to ground motion randomness, are summarized. Finally, related methodologies for damage assessment of structures are reviewed.

2.2 Self-Centering and Rocking Structural Systems

Among the earliest studies on rocking structures, shaking table tests by Clough and Huckleridge [14] demonstrated promising results. Allowing column uplift was shown to significantly reduce both the seismic forces and ductility demand, when compared to the fixed base response, for a 3-story steel frame. A summary of some of the previous studies on self-centering and rocking seismic lateral force resisting systems is presented in this section.

2.2.1 Unbonded Post-Tensioned Precast Concrete Walls

An unbonded post-tensioned precast concrete wall consists of precast wall panels and post tensioning (PT) bars or tendons (unbonded to the concrete) which are anchored at the roof and the foundation. The bottom wall panel is not attached to the foundation to allow rocking of the wall. Unbonded post-tensioned precast walls resist lateral forces and gravity loads. The lateral force resistance is provided by the PT bars. Spiral reinforcing steel is used in the wall panel near the base of the wall to provide additional confinement to the concrete in that region. Figure 2.1 shows a schematic of the unbonded post-tensioned precast wall configuration and the cross section of the wall panel adjacent to the foundation [43].

The primary limit states of the unbonded post-tensioned precast concrete wall system are: (i) decompression at the base and gap initiation between the lower wall panel and the foundation; (ii) a softening state that identifies the beginning of a significant reduction in the lateral stiffness of the wall due to increased gap opening and nonlinear behavior of the concrete; (iii) a yielding state that identifies the first instance of yielding in the PT bars; and (iv) a failure state that identifies the flexural failure of the wall as a result of crushing of the spiral confined concrete. The schematic base shear versus roof drift relationship of the unbonded post-tensioned precast concrete wall system along with four limit states of the system is shown in Figure 2.2.

2.2.2 Self-Centering Steel Moment Resisting Frames

Self-centering steel moment resisting frames (SC-MRF) have been the subject of previous studies as an improvement over conventional steel moment resisting frames (MRFs) by introducing an alternative moment connection [61, 62, 12, 63, 25, 91, 26, 40, 46, 37, 41, 90]. Unlike a conventional steel MRF, the beam is not rigidly connected to the columns by welds in a SC-MRF; instead the beam is post-tensioned to the columns using post tensioning

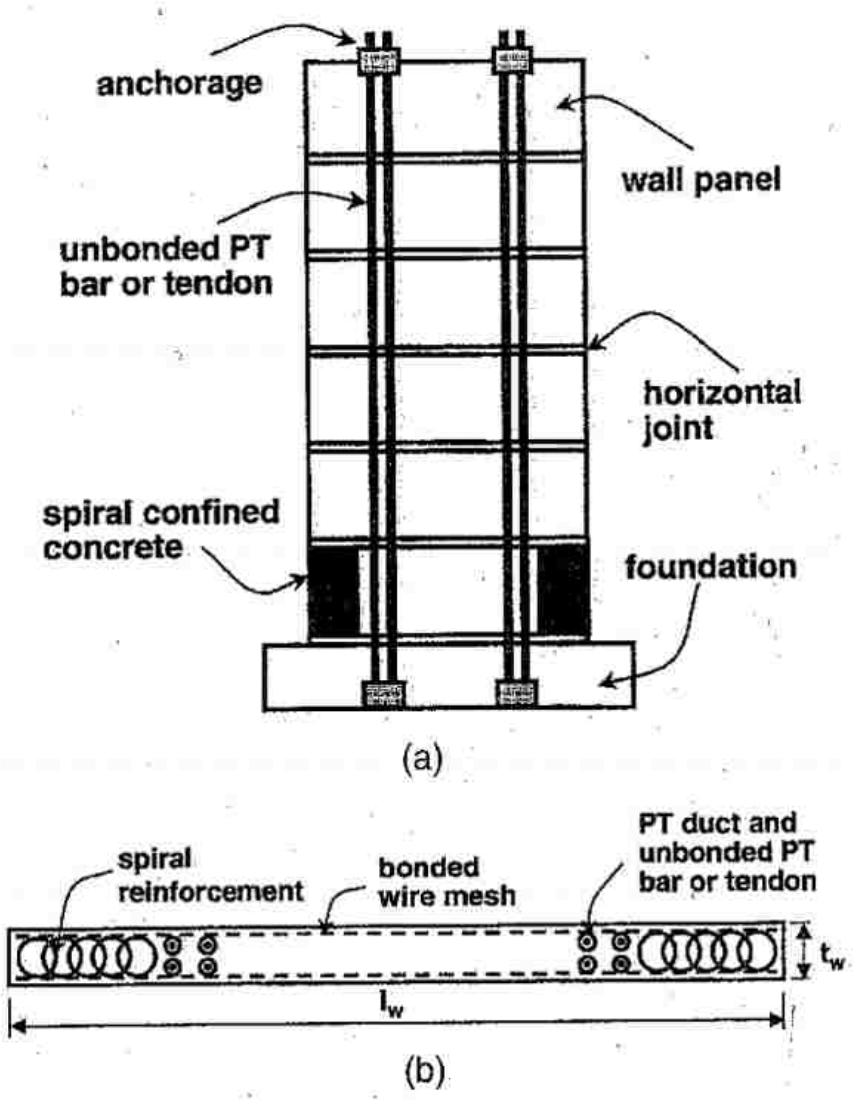

Figure 2.1: Unbonded post-tensioned precast wall: (a) elevation; and (b) cross section near base (enlarged), from [43]

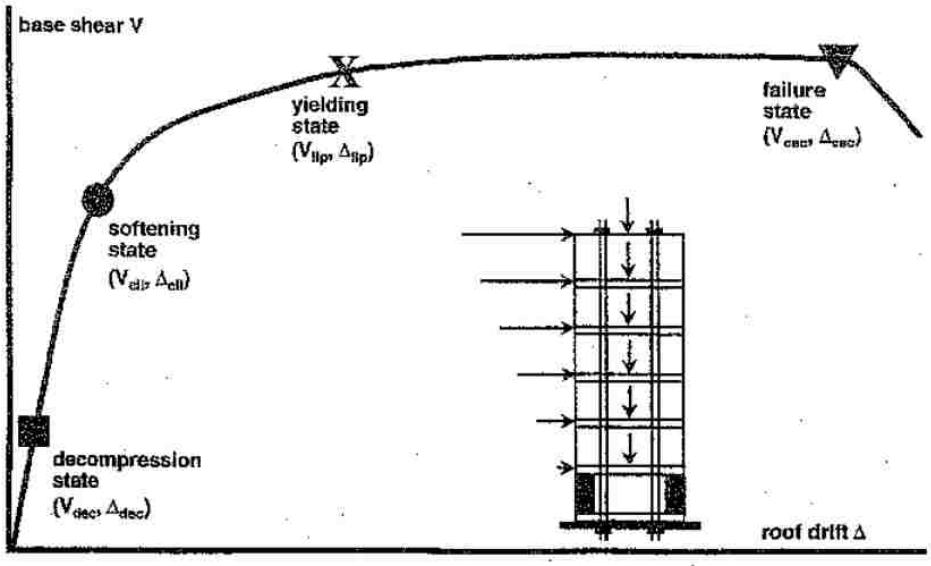

Figure 2.2: Schematic base shear versus roof drift with limit states for unbonded post-tensioned precast concrete wall, from [43]

(PT) steel strands. A conventional steel MRF and an SC-MRF beam-to-column connection are shown in Figure 2.3 (a) and (b), respectively [61]. The flexural behavior of a SC-MRF beam-to-column connection is characterized by gap opening and closing at the beam-column interface under cyclic loading. The schematic moment-rotation relationship for a SC-MRF beam-to-column connection is shown in Figure 2.4. The rotation in Figure 2.4 is the relative rotation that occurs between the beam and the column when the gap opening occurs. The restoring force after the gap opening at the beam-column interface is provided by the PT strands. In the SC-MRF system studied by [61], the damage to the connections is concentrated in the angles at the top and bottom of the beam, and occurs in the form of plastic hinges. As a result of gap opening, the beam and column stay damage free and the connection is self-centering without residual deformation [61].

A modified SC-MRF connection with friction devices at the top and bottom of the beam, called a post-tensioned friction damped connection (PFDC) was studied by Rojas et al. [63]. The MRF with PFDC is denoted by PFDC-MRF [63]. In this system the angles at the top and bottom of the beam [61] are replaced by an assembly of friction plates and brass

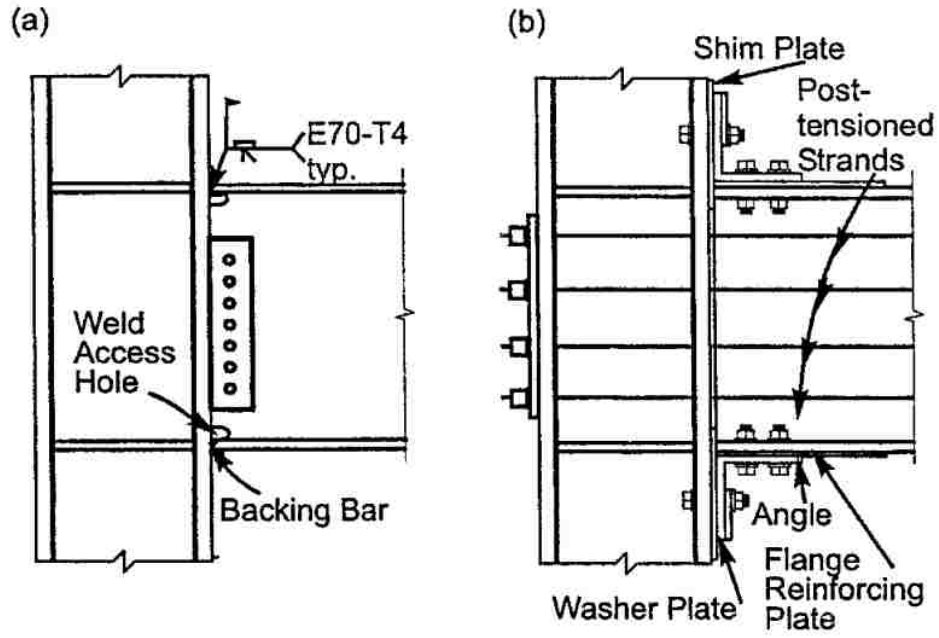

Figure 2.3: Moment connections: (a) conventional steel MRF (pre-Northridge welded); and (b) SC-MRF post-tensioned connection, from [61]

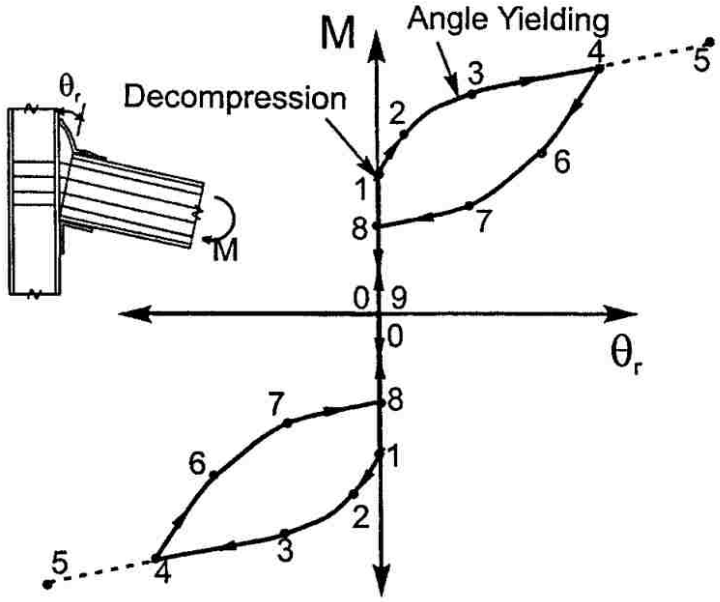

Figure 2.4: Moment-rotation behavior of posttensioned connection, from [61]

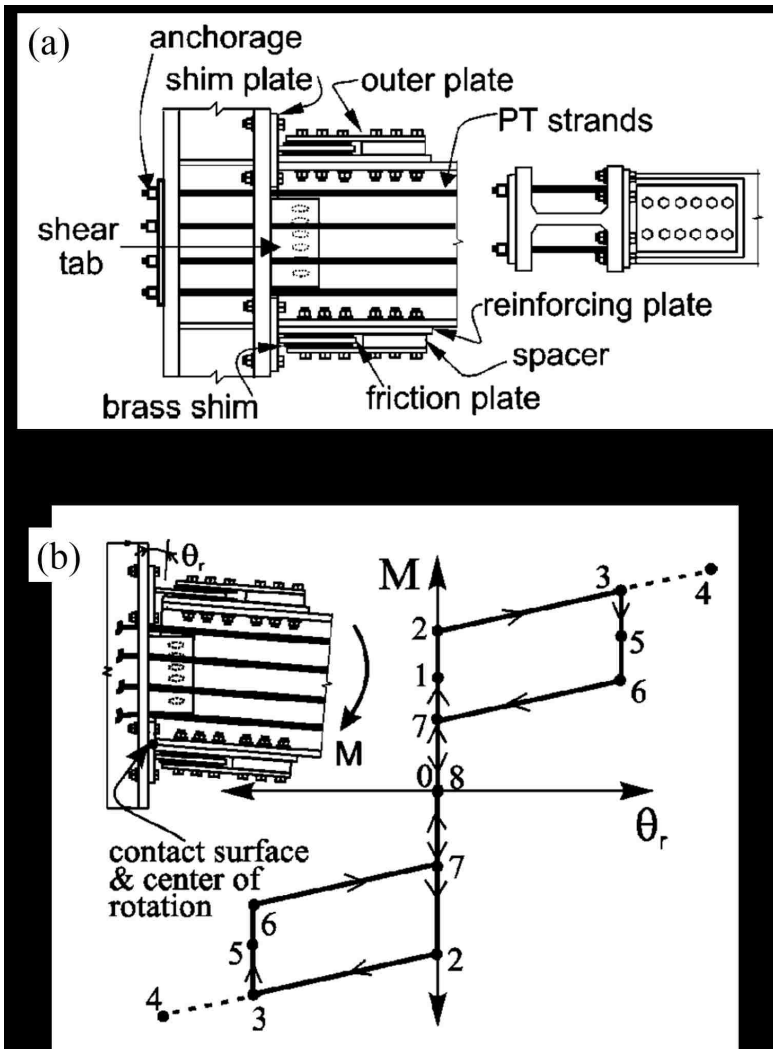

Figure 2.5: Post-tensioned friction damped connection (PFDC) in a moment resisting frame: (a) connection details; and (b) idealized moment-relative rotation behavior, from [63]

shims. The beam shear force is transmitted through a shear tab at the web of the beam. The details of the beam column connection of the PFDC-MRF system and the idealized schematic moment-relative rotation relationship for the beam column connection of the PFDC-MRF system are shown in Figure 2.5. The self-centering capability of the PFDC-MRF systems is compared with lack of self-centering in a fully restrained conventional steel MRF system in Figure 2.6 [63].

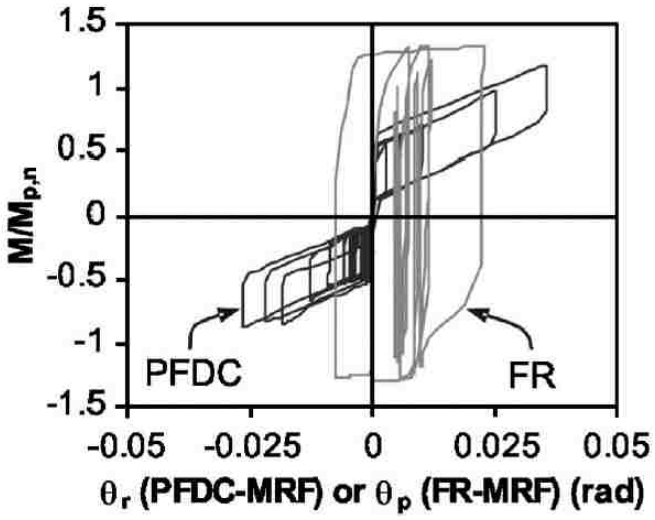

Figure 2.6: Behavior of post-tensioned friction damped (PFDC) connection and fully restrained-moment (FR) resisting frames under the Miyagi maximum considered earthquake ground motion, from [63]

2.2.3 Steel self-centering concentrically braced frames

The innovative steel self-centering concentrically braced frame (SC-CBF) system was developed at Lehigh University as a new seismic lateral force resisting system. The SC-CBF consists of a concentrically braced frame, PT bars, friction bearings, and gravity column. The SC-CBF columns are detailed to allow uplift of each column from the foundation. The PT bars which are anchored at the roof level (in most configurations) and at the foundation provide the restoring force during rocking. The friction bearings transfer the lateral inertial forces from the floor system and gravity framing at each floor level to the system. The friction bearings are also a source of energy dissipation during the rocking. A schematic of one of the configurations of the SC-CBF system is shown in Figure 2.7.

The limit states considered in the performance-based seismic design of the SC-CBF system are: (i) decompression and uplift of column under tension from overturning moment; (ii) yielding of the PT bars; (iii) significant yielding of the structural members; and

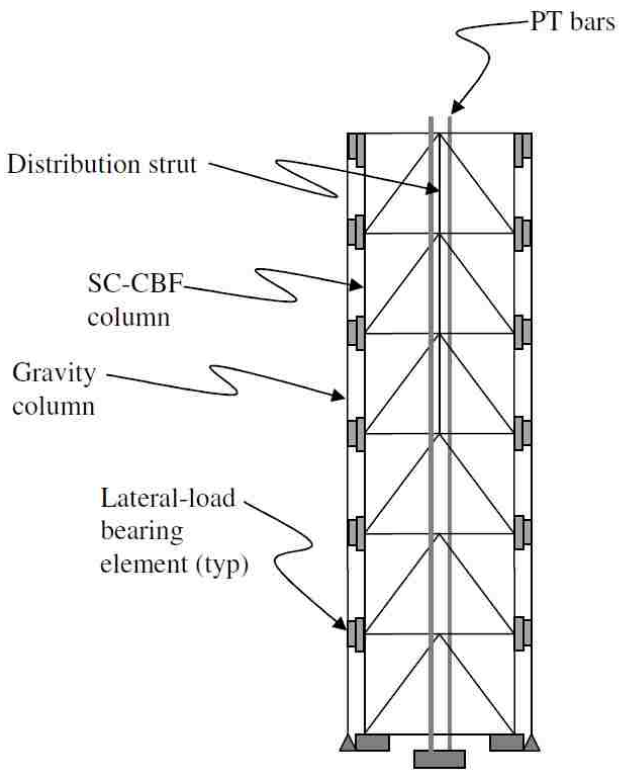

Figure 2.7: Schematic of one configuration of SC-CBF system, from [66]

(iv) failure of the structural members. The performance objectives for the seismic design of a SC-CBF system are immediate occupancy (IO) under the design basis earthquake (DBE) and collapse prevention (CP) under the maximum considered earthquake (MCE). Since decompression and uplift of the SC-CBF column does not cause any damage to the structural members, column decompression is allowed to occur at the DBE hazard level without violating the IO performance objective. Yielding of the PT bars, however, causes loss of the pre-stressing force in the PT bars. The loss of pre-stressing force in the PT bars is considered to be a form of structural damage that does not compromise the safety of the SC-CBF system, however, it must be repaired after an earthquake. Therefore, yielding of the PT bar is a limit state that satisfies the CP performance level but not the IO performance level [73]. The performance-based design objectives of the SC-CBF system are shown on a schematic pushover curve showing the limit states of the SC-CBF system [73]. More discussion on other configurations and behavior of the SC-CBF system can be found in [65, 66, 74, 73].

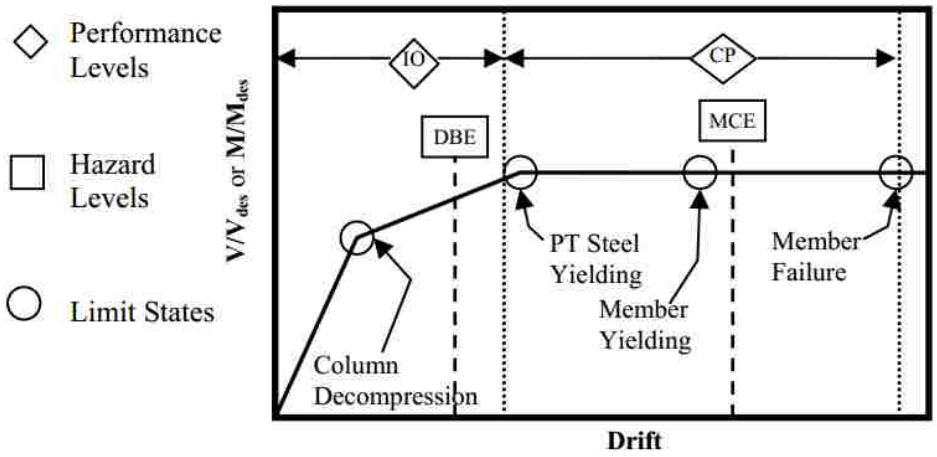

Figure 2.8: Summary of performance-based design objectives of SC-CBF system shown on an idealized pushover curve, from [73]

An experimental study of a 4-story 60% scale SC-CBF system was performed at Lehigh University. A photograph of the 60% scaled frame can be seen in Figure 2.9. Thirty one ground motion records, scaled to DBE and MCE hazard levels, were applied to the test structure using the hybrid simulation technique. Good performance and self-centering behavior was observed. In addition to the experiments, thorough numerical simulations were performed using the OpenSEES computational framework [53]. Figure 2.10 shows an example of good agreement between the experimental results and the numerical simulations as well as the excellent self-centering response of the SC-CBF system. Figure 2.11 shows a photograph of the SC-CBF system without the gravity columns being removed from the laboratory test set-up after the experiments.

2.2.4 Other self-centering seismic lateral force resisting systems

Self-centering energy dissipative (SCED) steel braces were studied by Tremblay et al. [80]. The axial force-deformation hysteresis of conventional braces, buckling restrained braces (BRBs), and SCED braces are shown in Figure 2.12(a), (b), and (c), respectively. Tremblay et al. [80] used BRB and SCED brace systems as two choices for lateral force resisting

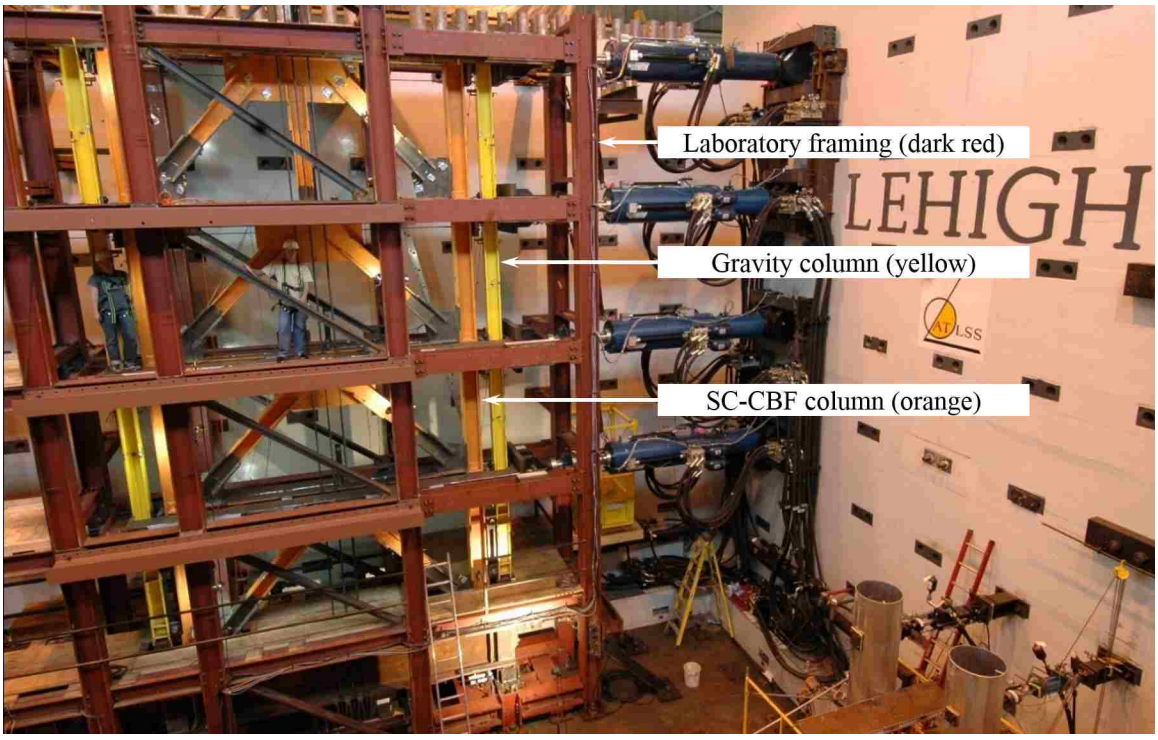

Figure 2.9: 60% scaled 4-story SC-CBF frame in test set-up, from [66]

systems of 8-story and 12-story buildings. The story-shear drift response history of the first story for the 8-story and 12-story buildings are shown in Figure 2.13. While the magnitude of the story shear is similar for the BRB and SCED brace systems, the BRB system shows considerable residual drift while the SCED brace system self-centers.

A rocking concentrically braced frame with viscous dampers at the column bases, called viscously damped controlled seismic rocking (VDCSR), was studied by Tremblay et al. [79]. A schematic of a two story VDCSR and details of the base of the column are shown in Figure 2.14. The viscous dampers are used to control the lateral displacement of the frame during the uplift of the column (i.e., rocking). Shake table tests of a 2-story 50% scale VDCSR system were performed. It was found that the rocking response of the VDCSR is dominated by rigid body rotation. The laboratory test setup is shown in Figure 2.15 [79].

A rocking self-centering concentrically braced frame system similar to the SC-CBF,

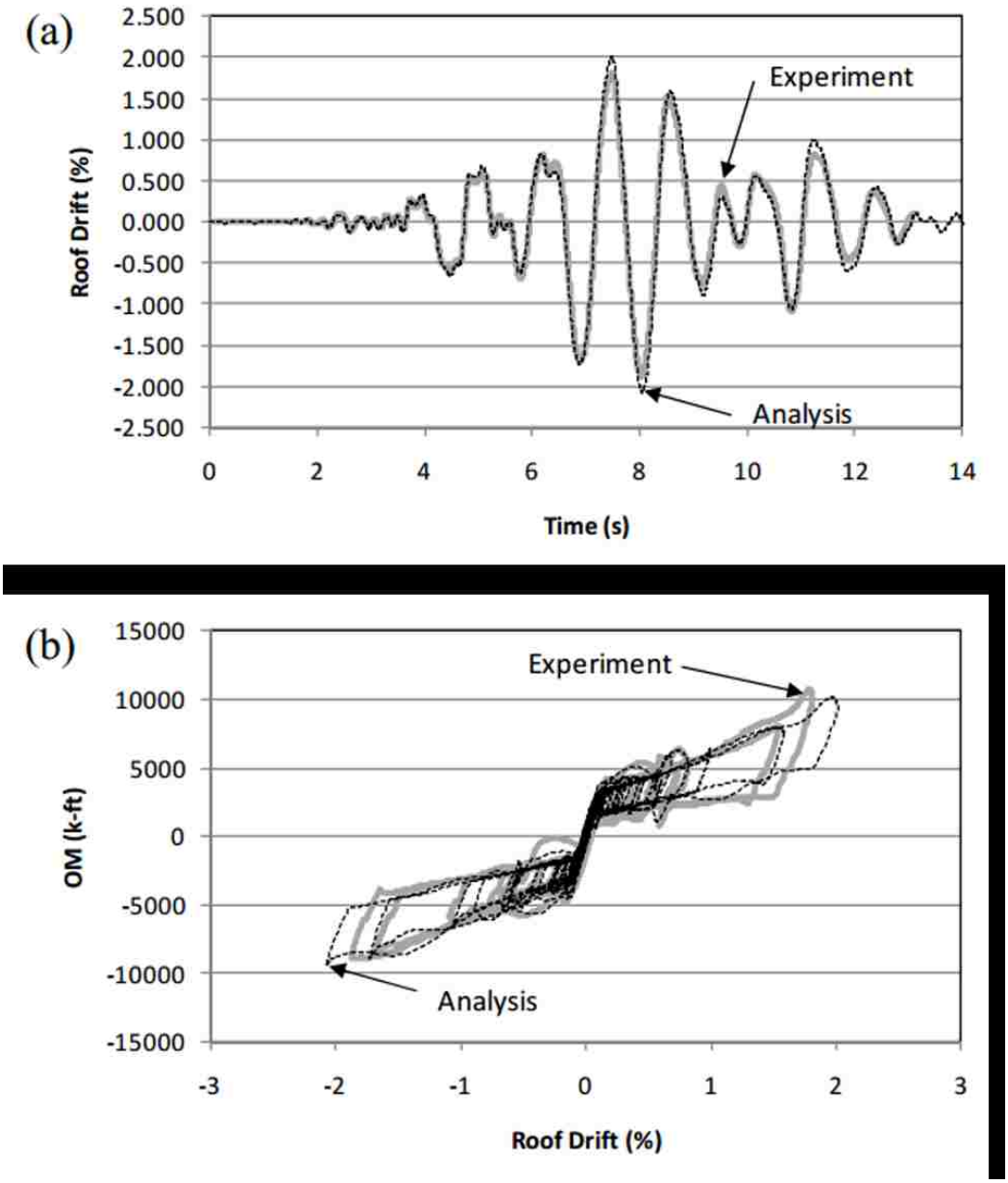

Figure 2.10: Response history under 1989 Loma Prieta earthquake, Capitola ground motion record, (a) roof drift and (b) overturning moment versus roof drift, from [73]

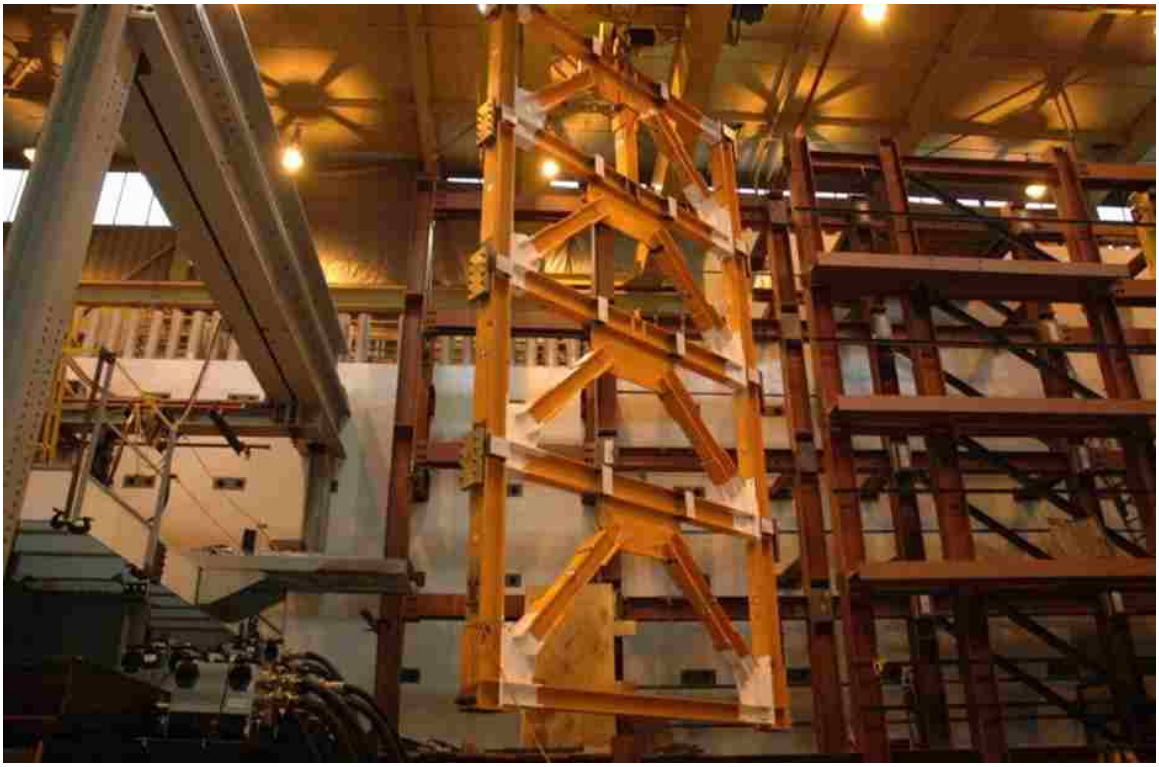

Figure 2.11: 60% scaled 4-story SC-CBF frame being removed from test setup after the experiments, from [66]

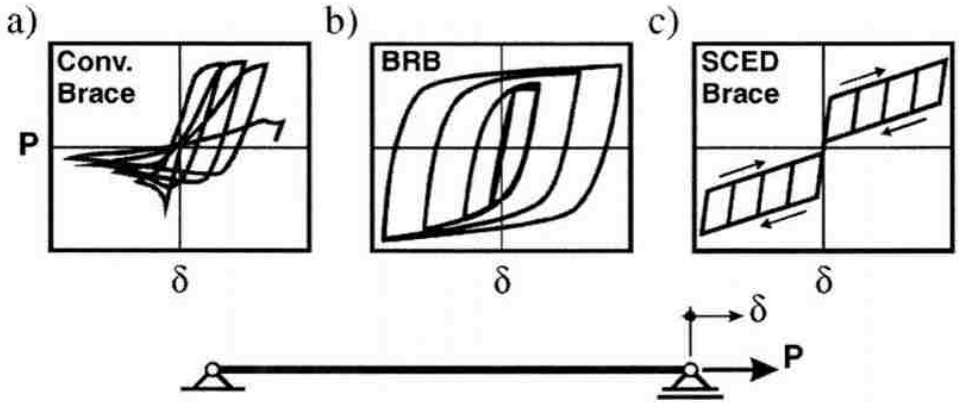

Figure 2.12: Brace hysteresis response: (a) conventional brace; (b) buckling restrained brace; and (c) SCED brace, from [80]

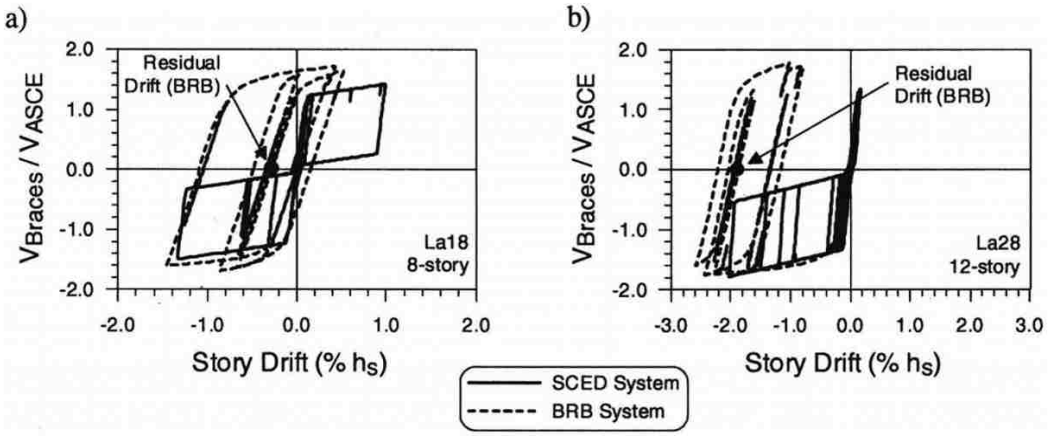

Figure 2.13: First-story lateral load-lateral deformation response: (a) 8-story frames under record LA18 (10% in 50 years); and (b) 12-story frames under record LA28 (2% in 50 years), from [80]

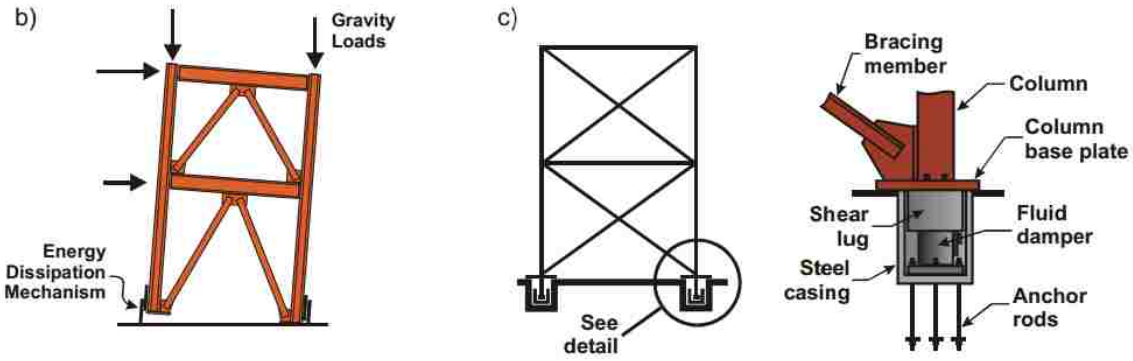

Figure 2.14: Schematic of VDCSR system; (a) frame layout and rocking behavior; (b) braced frame with viscous dampers at the column base; and (c) viscous damper details, from [79]

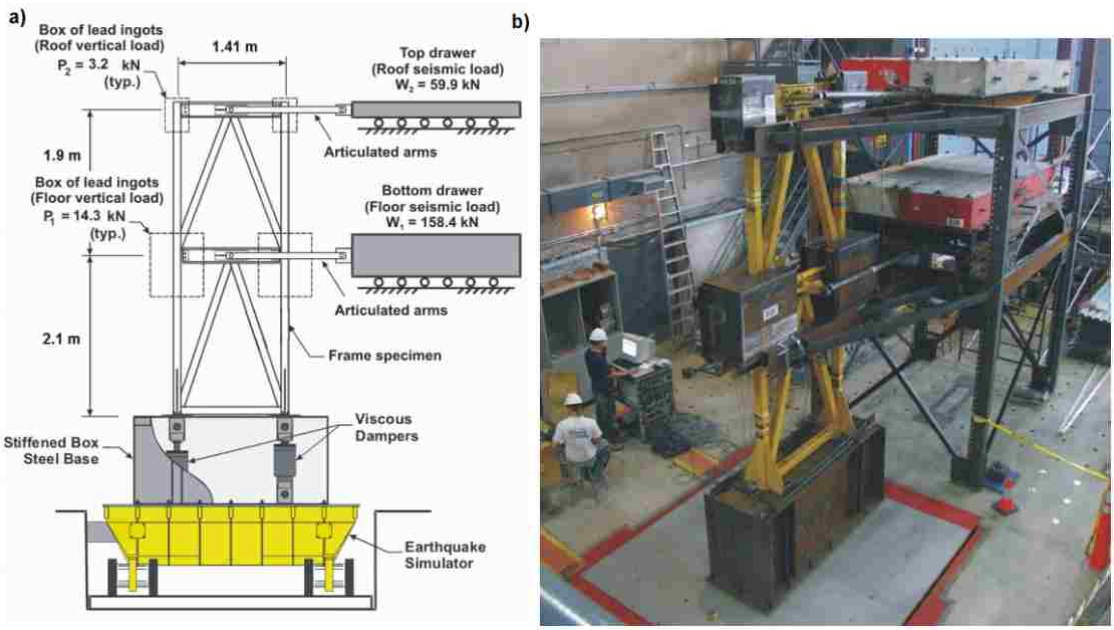

Figure 2.15: Shake table test setup: (a) schematic of the test model; and (b) Entire test setup with seismic mass system, from [79]

called the controlled rocking system, was studied by Eatherton et al. [19, 18] and Ma et al. [49]. The column in this system is allowed to uplift from the foundation and as a result the system rocks. PT bars, anchored at the top and the foundation, provide the restoring force after the rocking occurs. A schematic of one configuration of the controlled rocking system is shown in Figure 2.16. In this configuration, two braced frames are side-by-side with steel shear fuses connecting them as a source of energy dissipation. Quasi-static and hybrid simulation tests were performed on a 3-story 50% scale controlled rocking system. A photograph of the test specimen is shown in Figure 2.17. Numerical simulations were performed to predict the controlled rocking system response under quasi-static loading. Comparison of the numerical simulations and test results can be seen in Figure 2.18.

Wiebe et al. [88, 89] studied the effect of more than one force-limiting mechanism on the seismic demand forces in braced frames. A second rocking joint, in addition to the base rocking joint, was introduced at mid-height of the frame to better control the mid-height overturning moment. A schematic of the finite element model of an 8-story braced frame

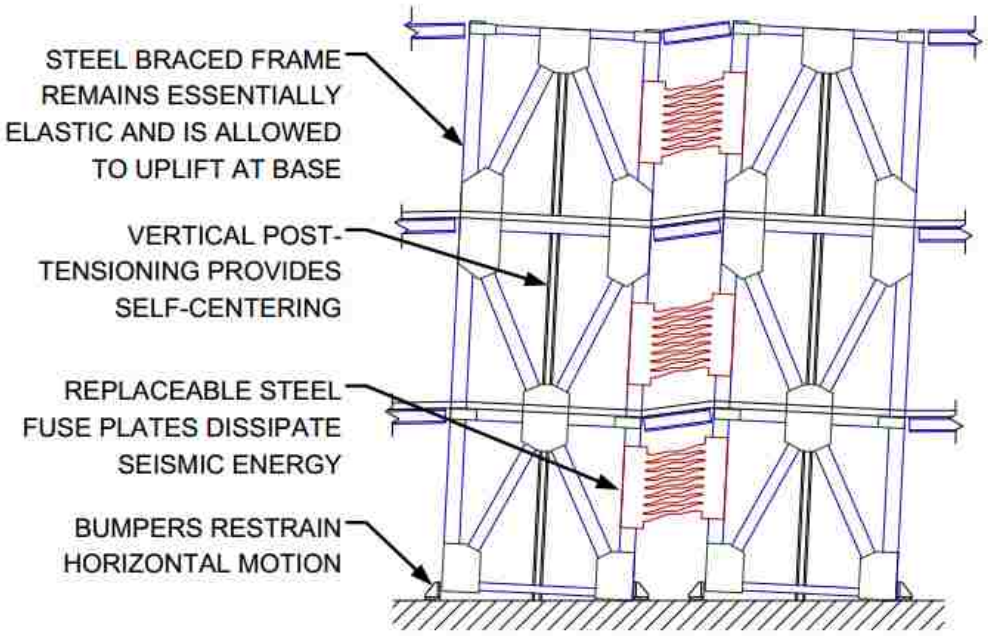

Figure 2.16: Schematic configuration of the controlled rocking system, from [19]

with a second rocking joint at the 4th floor is shown in Figure 2.19. In addition to the second rocking joint along the height of the structure, an SCED brace was also used at the first story to act as a shear fuse at the first story. The combination of having a second rocking joint at the mid-height of the frame and the SCED brace at the first story creates four distinct cases for which the peak story shear and the peak overturning moment at each story are shown in Figure 2.20. It can be seen that the base shear of the case with only the base rocking joint and no shear mechanism (1M0V) is reduced considerably when the SCED braces are used at the base (1M1V). The story overturning moment for the 1M0V case is also reduced considerably when the second rocking joint is introduced at the mid-height of the frame (2M0V) [88].

2.3 Collapse Performance Evaluation of Buildings

Collapse of a building can be established when the building loses its gravity force carrying capability in the presence of the lateral seismic forces. Two major contributing factors to

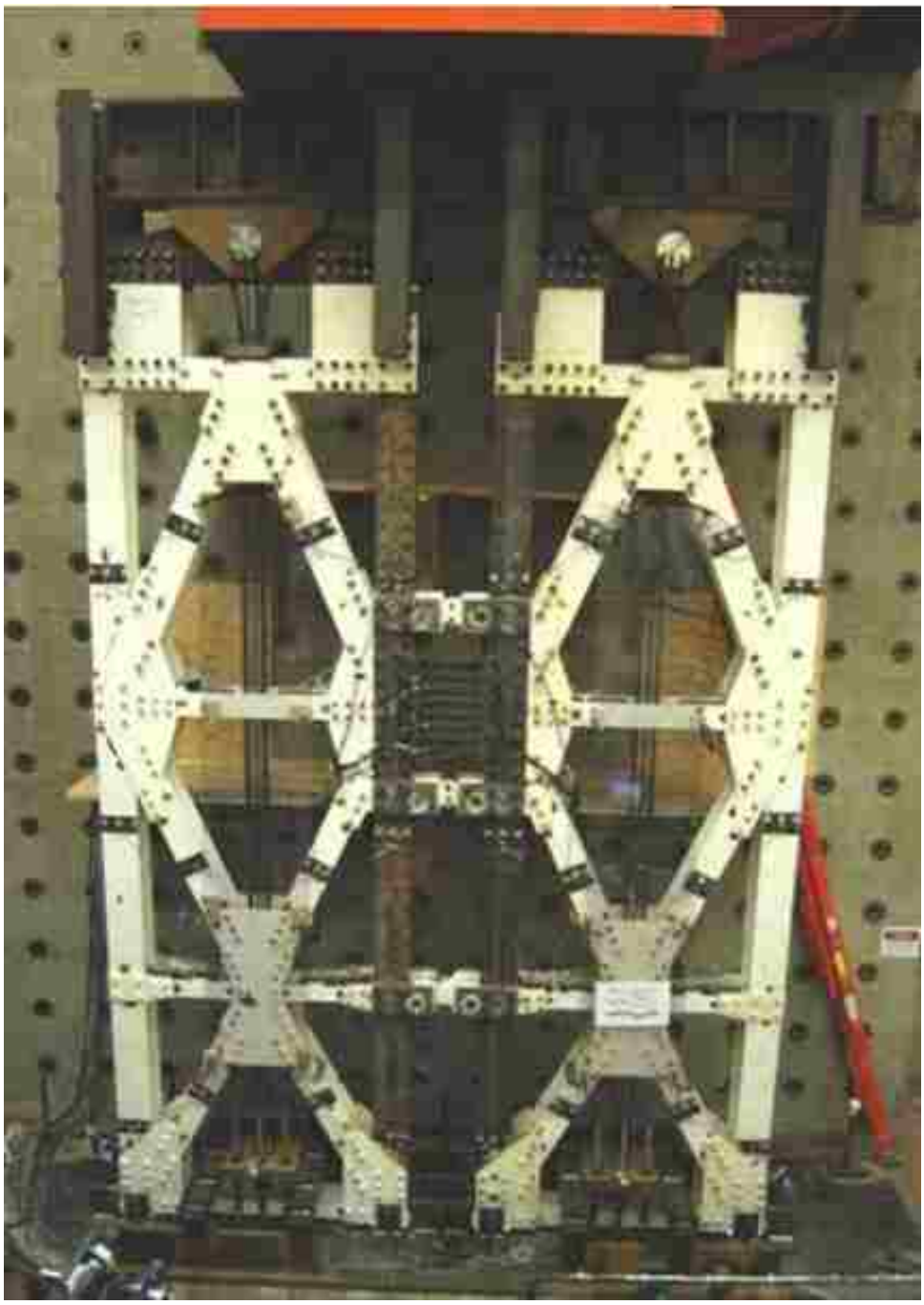

Figure 2.17: Photograph of controlled rocking system test specimen, from [19]

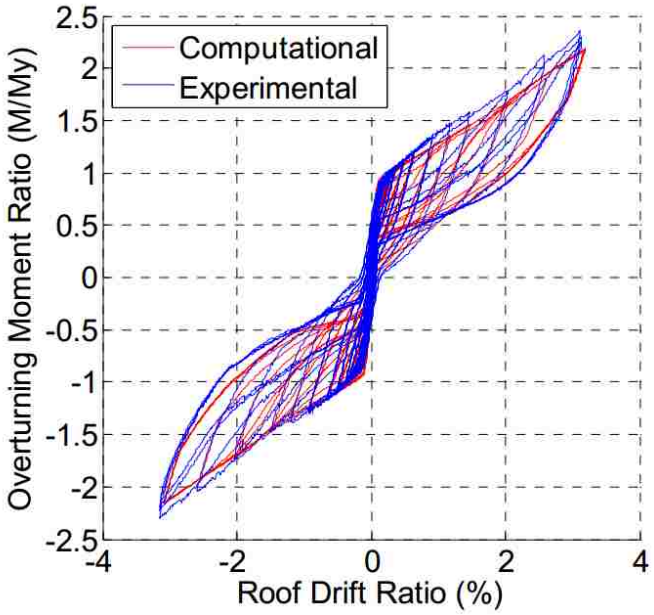

Figure 2.18: Comparison of overturning moment versus roof drift between experimental results and numerical simulation prediction for controlled rocking system, from [19]

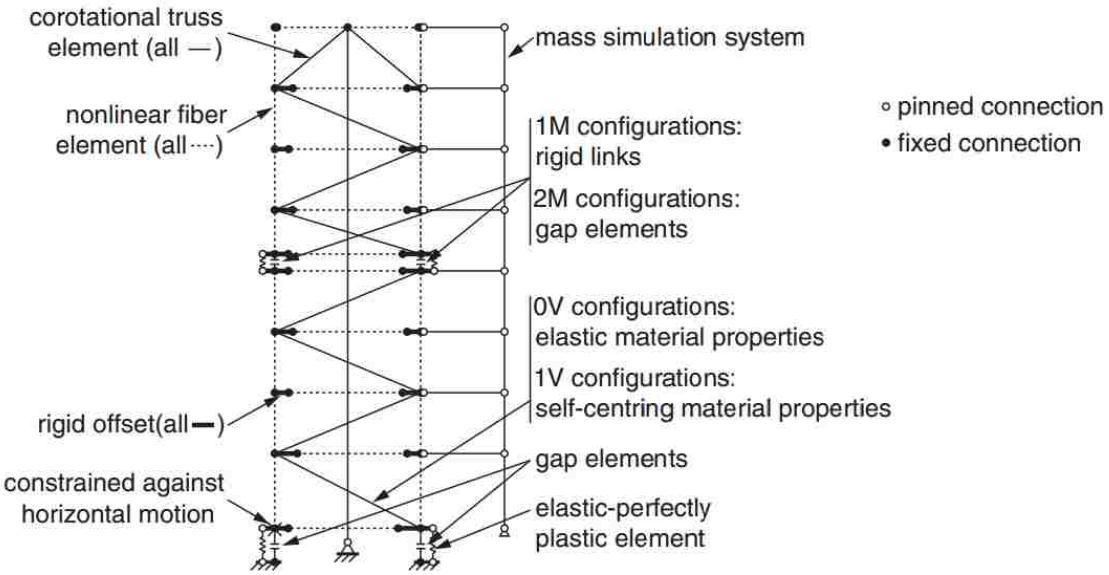

Figure 2.19: Overview of numerical model with second rocking joint at 4th floor level, from [88]

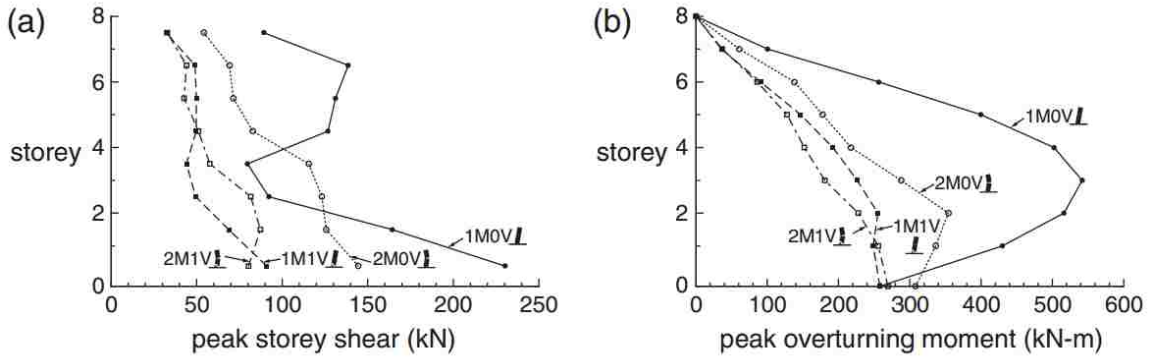

Figure 2.20: Predicted envelopes for all configurations (combination of second rocking joint and SCDE brace) during a record at the 2% in 50-years hazard level: (a) story shear; and (b) overturning moment [88]

collapse of a buildings are stiffness and strength deterioration of key structural components during cyclic loading and second order effects of the gravity forces known as the P-Δ effect. Various studies have been conducted to predict the collapse of structural systems; studies focusing on simplified single-degree-of-freedom systems to studies considering sophisticated multi-degree-of-freedom systems capable of simulating failure of key structural components [1, 78, 72, 36]. In addition to strength and stiffness deterioration, member fracture has been modeled in several collapse studies [78, 82].

Due to the complexity of global collapse of a structural system and random nature of earthquake ground motions, probabilistic approaches have been introduced that incorporate different sources of uncertainties in the process of collapse prediction [17, 28, 35, 93, 94, 23, 22]. In performance-based earthquake engineering, a performance objective in the context of collapse safety can be quantified as a tolerable probability of collapse at a given seismic hazard level [94]. As a result, collapse fragility curves are developed for seismic lateral force resisting systems to relate probability of collapse to the seismic hazard level.

FEMA [22] uses an engineering demand parameter (EDP) approach for estimating probability of collapse at a given hazard intensity measure (IM).In this EDP-based ap-

proach, collapse is reached when the EDP demand (EDP_{dmnd}) exceeds the EDP capacity (EDP_{cpcty}). The probability of collapse at a given IM value can be expanded using the law of total probability as follows [94]:

$$\begin{aligned} P(C|IM) &= P(EDP_{dmnd} \geq EDP_{cpcty}|IM) \\ &= \sum_{all\ edp_{cpcty}} P(EDP_{dmnd} \geq EDP_{cpcty}|EDP_{cpcty} = edp_{cpcty}, IM) \\ &\quad \cdot P(EDP_{cpcty} = edp_{cpcty}) \end{aligned} \quad (2.1)$$

where $P(EDP_{dmnd} \geq EDP_{cpcty}|IM, EDP_{cpcty} = edp_{cpcty})$ is the probability of EDP_{dmnd} exceeding EDP_{cpcty} given that $EDP_{cpcty} = edp_{cpcty}$ at a given IM value and $P(EDP_{cpcty} = edp_{cpcty})$ is the probability of EDP_{cpcty} taking a value of edp_{cpcty}. The selected EDP should be a good representative of the global behavior of the building. The maximum story drift ratio (θ_m) is used by Cornell et al. [17] as the EDP for assessment of building collapse.

$P(EDP_{dmnd} \geq EDP_{cpcty}|EDP_{cpcty} = edp_{cpcty}, IM)$ and $P(EDP_{cpcty} = edp_{cpcty})$ can be estimated using the results of incremental dynamic analysis (IDA) [86]. In an IDA, values of EDP_{dmnd} at a given IM values are obtained by performing dynamic response history analyses using a set of ground motion records scaled to the given IM value. The process is repeated for increasing IM values until collapse is reached. A lognormal distribution is often used for the EDP_{dmnd} values at building collapse [17, 35]. The process of constructing the collapse fragility curve using the IDA results for an 8-story moment frame structure is shown in Figure 2.21 [94]. The data points shown at the right side of the IDA results in Figure 2.21 are the collapse fragility data points at increasing IM values, determined using Equation (2.1), shown in the form of a vertical CDF. This approach of evaluating the probability of collapse is often called the EDP-based approach because the EDP_{dmnd} value

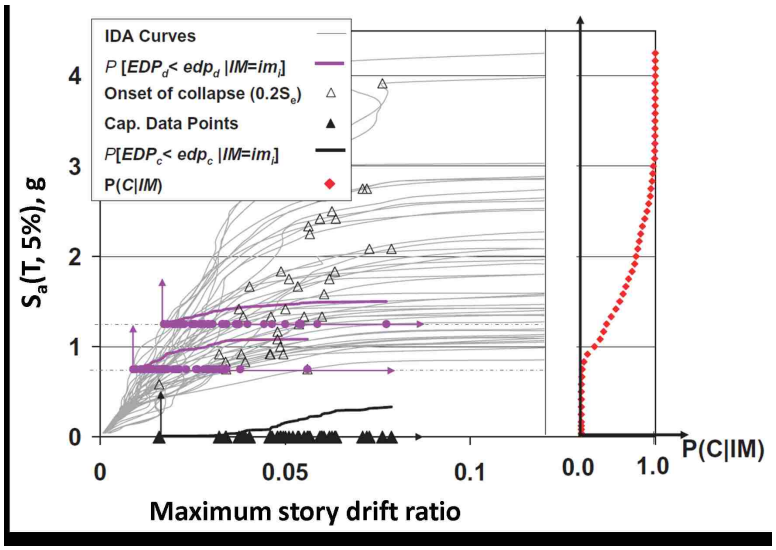

Figure 2.21: Obtaining probability of collapse for given IM ($S_a(T, 5\%)$) using EDP-based approach (with maximum story drift ratio as EDP) by utilizing incremental dynamic analysis, from [94]

is compared against the EDP_{cpcty} value, as shown by Equation (2.1).

An alternative approach introduced by Ibarra et al. [33] uses the IM value directly to estimate the probability of collapse, and therefore is called the IM-based approach for evaluating probability of collapse. In the IM-based approach, the collapse capacity of the system, defined as a random variable, is the IM value at which collapse occurs (IM_C). Similar to the EDP-based approach, the IDA results can be used to construct the fragility curve using the IM-based approach. Since the collapse capacity is directly defined to be the IM value at collapse (denoted by IM_C), the collapse fragility curve is the CDF of all the IM_C values from various ground motion records used to conduct the IDA [94]. The probability of collapse can be evaluated using the IM-based approach as follows [94]:

$$P(C|IM) = P(IM \geq IM_C) \tag{2.2}$$

The process of evaluating the probability of collapse using the IM-based approach and

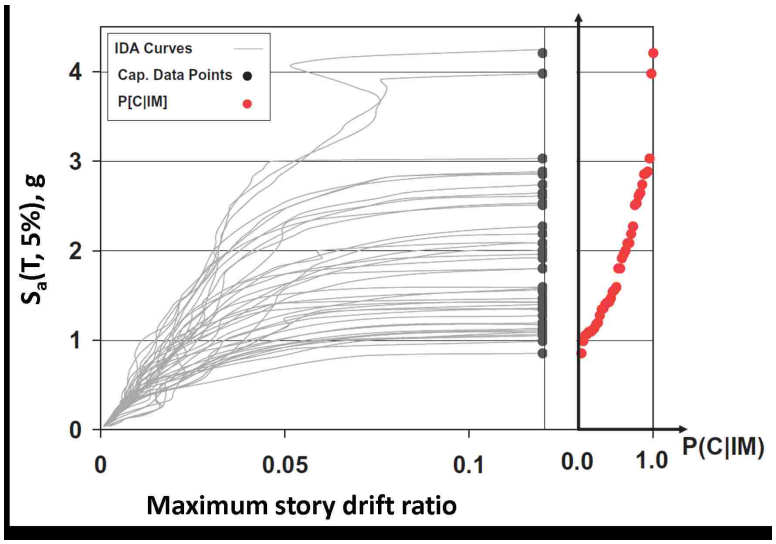

Figure 2.22: Obtaining collapse capacity data using IM-based approach by utilizing incremental dynamic analysis, from [94]

Equation (2.2) is illustrated in Figure 2.22 [94]. The collapse capacity (i.e., the IM_C value) for each ground motion record is projected to the right side of the IDA plot, shown with black circles. The counting probability of collapse at any given IM value is determined and shown in the plot at the right side of the IDA curves, as shown in Figure 2.22. It is often assumed that the IM_C values follow a lognormal distribution [35].

The collapse fragility curves constructed using the EDP-based method and the IM based method are shown in Figure 2.23. The collapse fragility curve constructed using the EDP-based approach gives greater probability of collapse compared to the collapse fragility curve constructed using the IM-based approach. The difference between the two fragility curves is from the difference in definition of collapse capacity for the two approaches [94].

2.4 System parameter variability

The uncertainty in the probability of collapse is from various sources. The uncertainty in the probability of collapse, calculated using the results of structural response history

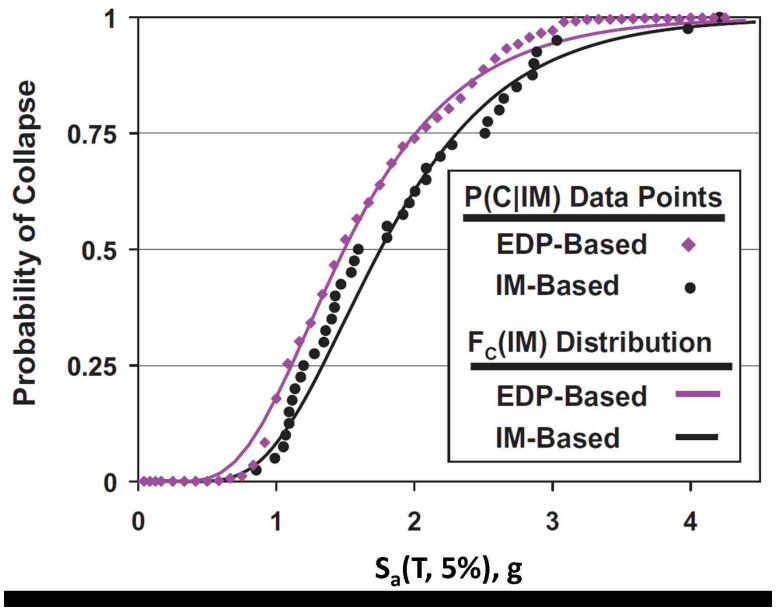

Figure 2.23: Collapse fragility curves obtained by fitting lognormal distributions to the data points obtained using the IM-based and EDP-based approaches, from [94]

analyses of numerical models of the building under different ground motion records, have three major sources: (i) the record-to-record (RTR) variability in structural response; (ii) the variability of the building system parameters; and (iii) the uncertainty regarding the numerical modeling decisions and parameters. The RTR variability in structural response is directly included by using the structural response from different ground motion records when conducting an IDA. The contribution of the variability of the building system parameters and the uncertainty regarding the numerical modeling decisions and parameters may be be included using techniques such as Monte Carlo (MC) simulation or first-order second-moment (FOSM) method. The variability of the building system parameters has been included in previous studies. Luco and Cornell [48, 47] study the effect of random connection fractures on the dynamic response of steel moment frames. Foutch et al. [24] considered the effect of hysteretic models for the moment connections.

Ibarra and Krawinkler [35, 34] have studied the effect of the variation of deterioration parameters on the collapse capacity of SDOF oscillators using FOSM method. A peak

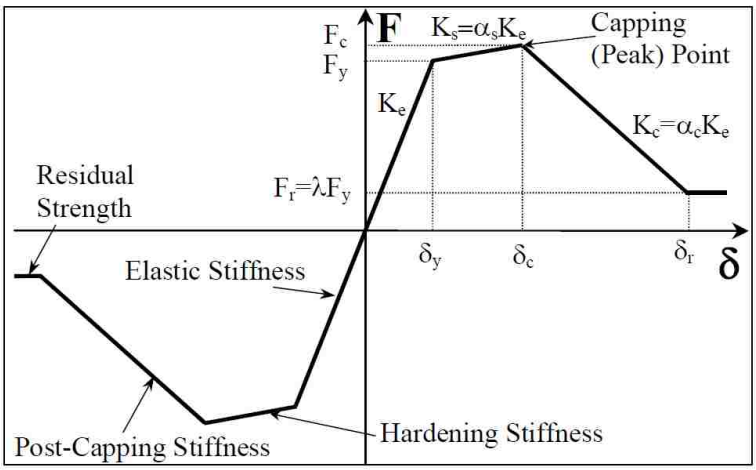

Figure 2.24: Backbone curve for hysteresis models, from [35]

oriented deterioration model developed by Ibarra et al. [36] was used for the SDOF oscillators, as shown in Figure 2.24. The amount of deterioration is defined to be a function of the hysteresis energy dissipated and a selected reference hysteretic energy dissipation capacity of the component, calibrated to experimental results [35]. The ductility capacity (δ_c/δ_y), the post-capping stiffness ratio (α_c) and the cyclic deterioration rate (γ) are defined as random system parameters.

Ibarra and Krawinkler estimate the variance of collapse the capacity (denoted by $S_{a,C}$) using FOSM method as follows [35, 9, 8]:

$$\sigma^2_{\ln S_{a,C}(TOT)} \cong \sum_{i=1}^{n}\sum_{j=1}^{n}\left(\frac{\partial g(\bar{X})}{\partial x_i}\frac{\partial g(\bar{X})}{\partial x_j}\right)_{\bar{X}=\bar{\mu}_x} \rho_{x_i,x_j}\sigma_{x_i}\sigma_{x_j} + \sigma^2_{\ln S_{a,C}(RTR)} \tag{2.3}$$

where $\bar{X}$ is the vector of the natural logarithm of the probabilistic system parameters, $\bar{\mu}_x$ is the vector of the mean values of $\bar{X}$, g is the collapse performance function in the log domain, ρ_{x_i,x_j} is the correlation coefficient between the i^{th} and j^{th} random system parameters, and σ_{x_i} is the standard deviation of the i^{th} random system parameter. The first term on the right hand side of Equation (2.3) is the contribution of the uncertainty in all random system

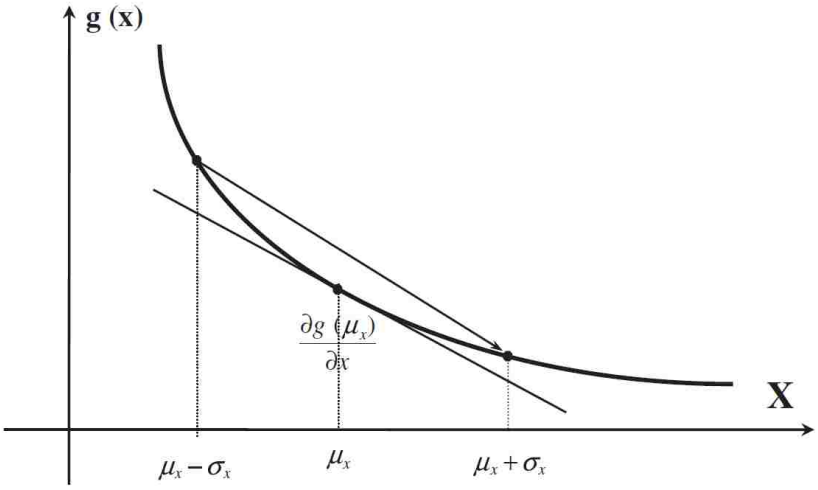

Figure 2.25: Approximating partial derivative of collapse performance function with respect to random system parameter, from [35]

parameters to the variance of the collapse capacity. The second term is the contribution of the RTR variability to the variance of the collapse capacity [35].

Since it is not practical to determine a mathematical expression for the collapse performance function of structural systems (i.e., $g(\bar{X})$), the partial derivatives of $g(\bar{X})$ in the first term of the right hand side of Equation (2.3) are being estimated numerically. The median collapse capacity is calculated for two variations of each system parameter: (i) $\mu_x - \sigma_x$; and (ii) $\mu_x + \sigma_x$. The variation of the collapse performance function $g(\bar{X})$ with respect to a system parameter is $\partial g(\bar{X})/\partial x_i$ for the i^{th} random system parameter in Equation (2.3). This numerical determination of the partial derivative is schematically shown in Figure 2.25.

Figure 2.26 shows the contribution of different terms of Equation (2.3) to the collapse capacity of SDOF oscillators with different natural periods. The RTR variability in structural response seems to be the greatest contributor and the combined correlation of the system parameters is the second largest contributor. The combined correlation of the system parameters is the sum of those terms of the double summation of Equation (2.3) when $i \neq j$ [35].

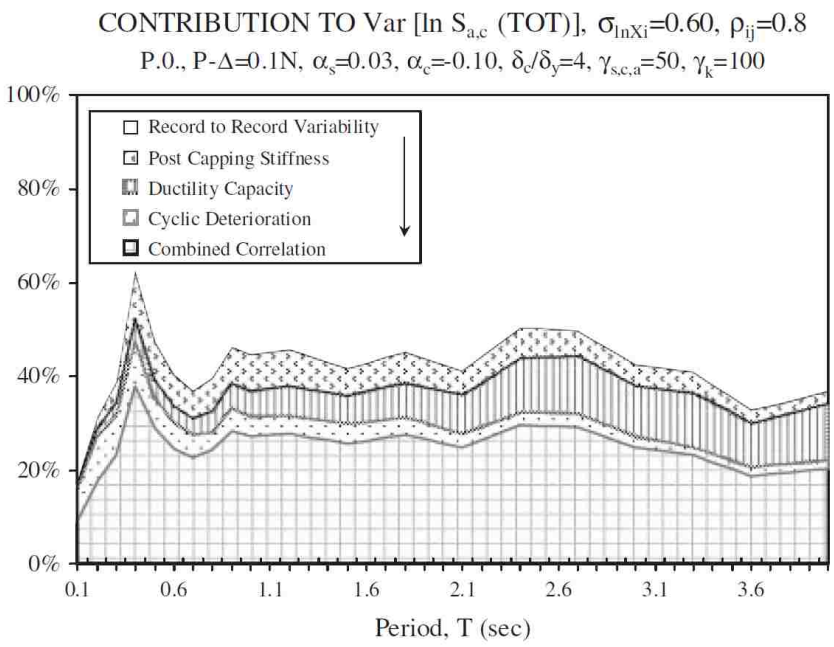

Figure 2.26: Relative contribution of different random system parameters to variance of collapse capacity, from [35]

Liel et al. [45] use a combination of the FOSM method and Monte Carlo simulation approach coupled with a response surface methodology to evaluate the collapse uncertainty of concrete MRFs. An example of the response surface developed for the collapse capacity versus the variability in beam and column strength and ductility is shown in Figure 2.27. The assumed plastic hinge backbone curve for beam and columns is similar to the one introduced by Ibarra et al. [35], shown in Figure 2.24. Several parameters of the backbone curve such as flexural strength, initial stiffness, post-yield stiffness, capping point, post capping deformation capacity, and cyclic deterioration are included as random system parameters for beams and columns. The collapse fragility curve for a 4-story reinforced concrete moment frame developed with and without considering the modeling uncertainties is shown in Figure 2.28 [45]. It can be seen that considering the effect of the system uncertainty increases the dispersion in collapse fragility curve.

Vamvatsikos and Fragiadakis [87] study the effect of variability of MRF system by

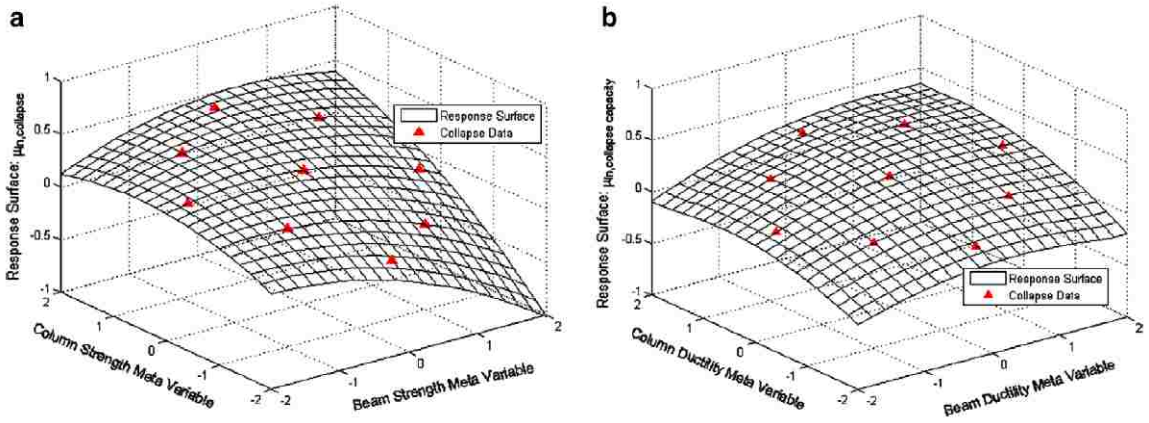

Figure 2.27: Graphical representation of the polynomial response surface for collapse capacity of 4-story ductile MRF. Each plot represents a slice of a multidimensional surface: (a) effects of column strength and beam strength are shown, while beam ductility and column ductility variables are held constant (at 0, their mean values); (b) effects of varying beam and column ductility, from [45]

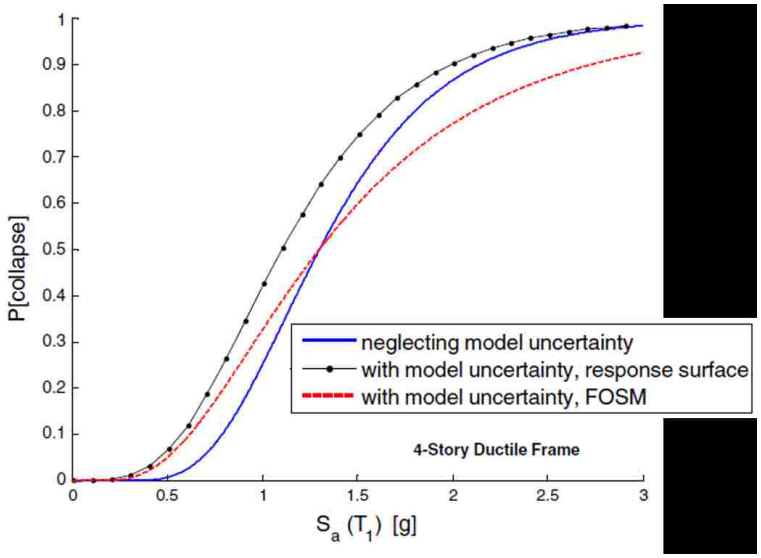

Figure 2.28: Collapse fragilities obtained for reinforced concrete MRF, from [45]

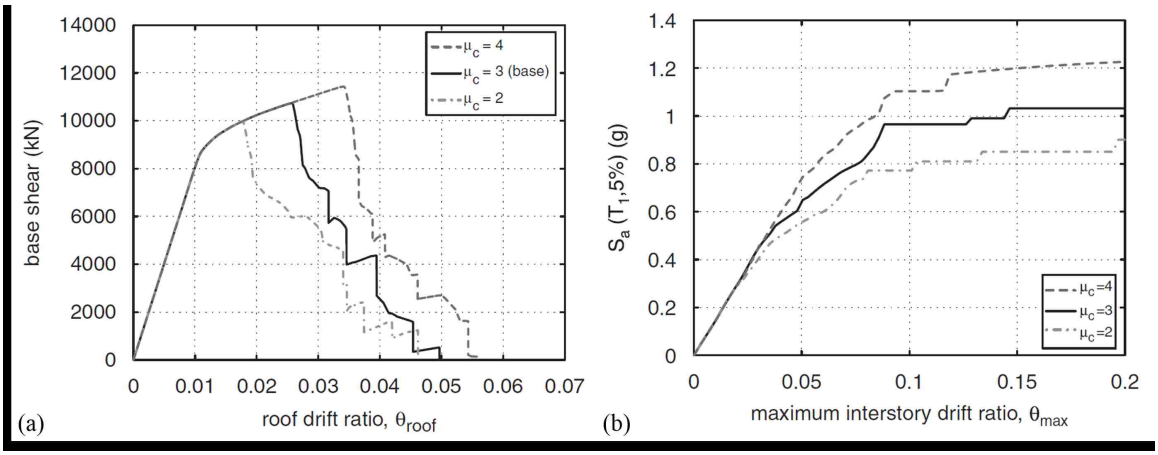

Figure 2.29: Sensitivity to variation of ductility capacity of beam hinges: (a) static pushover analysis results; and (b) median IDA curves, from [87]

varying the backbone curve random parameters for the plastic hinges in beams of the MRF. Figure 2.29 shows the sensitivity of the static pushover curve and median IDA curve to variation of the ductility capacity of the beam hinges. The effect of uncertainty in the beam hinge backbone parameters are evaluated using Monte Carlo simulation, an FOSM method, and a point estimation method. The lognormal standard deviation of $S_a(T_1, 5\%)$, determined at different maximum story drift ratio values, is shown in Figure 2.30, where LHS refers to Monte Carlo simulation results, FOSM refers to the FOSM results, and PEM refers to the point estimate results. The distribution of $S_a(T_1, 5\%)$ values at four values of maximum story drift ratio due to the variation of MRF plastic hinge ductility is shown in Figure 2.31. The variability in the beam hinge ductility is an important contributor to the overall dispersion in the performance of a steel MRF.

2.5 Damage Analysis

The four stages of performance-based earthquake engineering are hazard analysis, structural analysis, damage analysis, and loss analysis. The analysis in these stages involve distinct categories of random variables denoted as: IM, EDP, damage measure, and de-

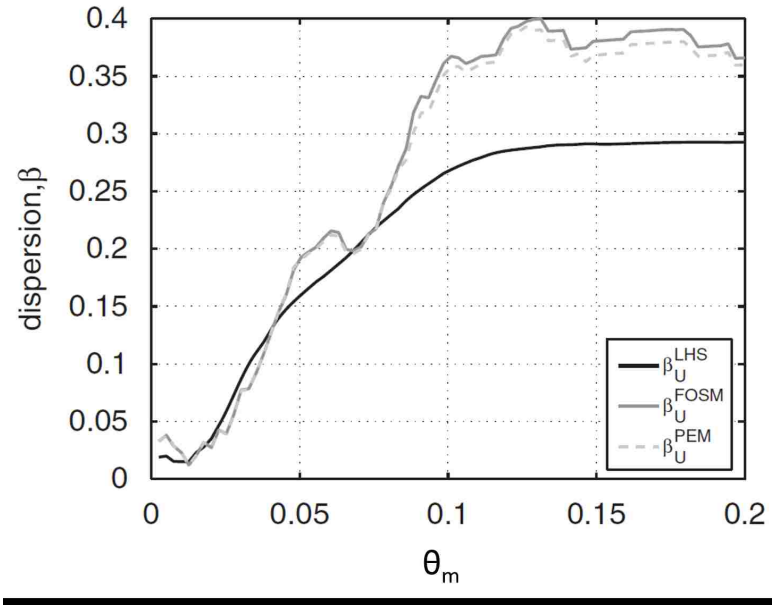

Figure 2.30: Dispersion of IM values at given maximum story drift ratio values due to uncertainty in MRF hinge ductility, from [87]

cision variable. The result from structural analysis and damage analysis are used in loss estimations of buildings [92, 55, 60].

While collapse of a structural system is a major contributor to the total expected loss, the extent of the damage in a building that survives a catastrophic seismic event without collapse can also result in significant economic loss. The required demolition of numerous reinforced concrete buildings in Mexico City after the 1985 Michoacan, Mexico earthquake [69] and numerous reinforced concrete bridge piers after 1995 Hyogo-ken Nambu earthquake [38] are examples of such losses.

The amplitude of residual deformations after a seismic event is an indicator of the extent of the induced damage and can be used in damage analysis. Increases in inelastic deformations in structural components increases the probability of residual reformations [13, 39, 50, 51, 57, 70, 71] Current seismic lateral force resisting systems that are designed to have large inelastic deformation capacity with the objective of having a low probability of collapse are more likely to sustain residual deformations [32, 31, 44].

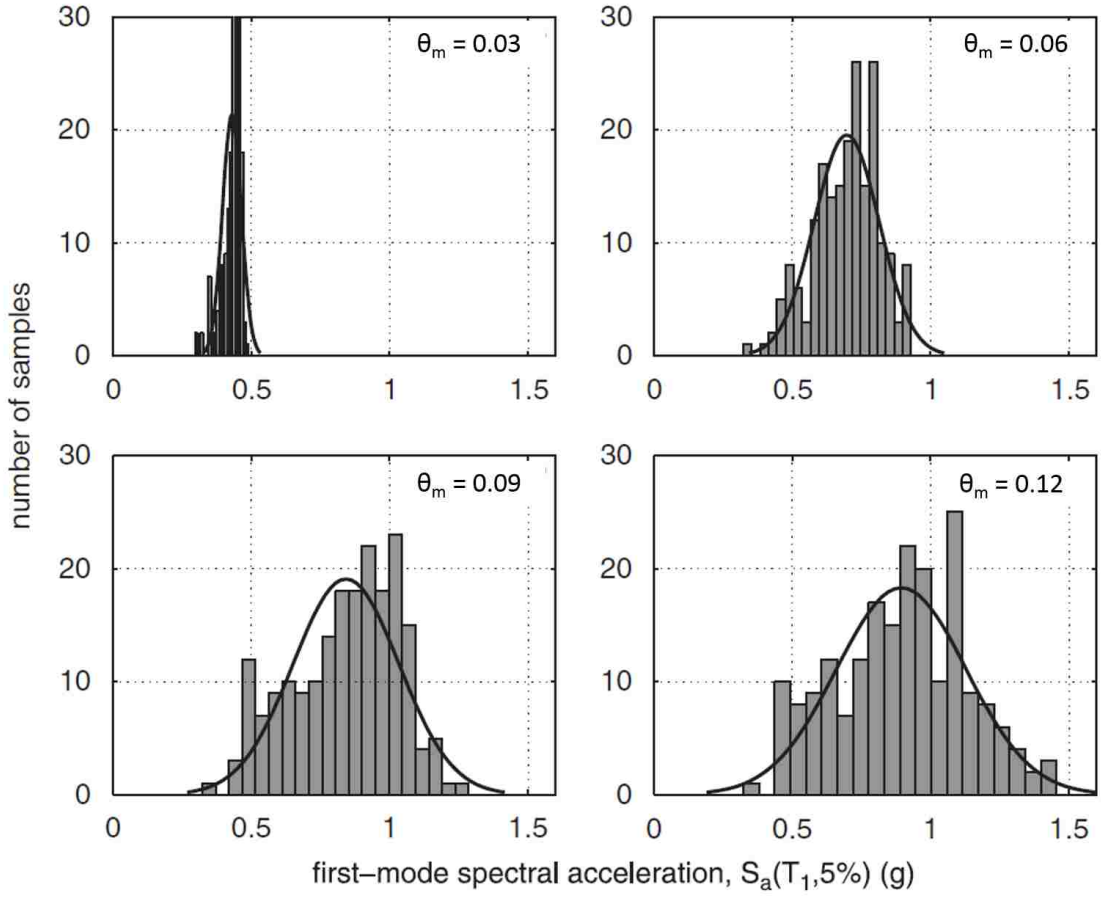

Figure 2.31: Distribution of median $S_a(T_1, 5\%)$ values due to the variability of ductility parameters of beam plastic hinge in MRFs at four given values of maximum story drift ratio (θ_m), from [87]

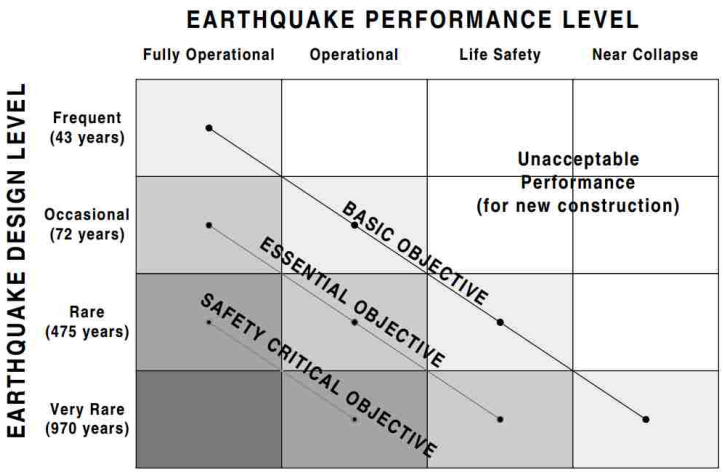

Figure 2.32: Seismic performance design objectives, from [16]

The Structural Engineers Association of California (SEAOC) Vision 2000 [16] defines the performance design objectives by combining multiple desired performance levels with multiple seismic hazard levels in a performance design objective matrix as shown in Figure 2.32. Uma et al. [81] use the joint distribution of maximum story drift and residual story drift ratios to extend the performance design objective matrix approach into a three-dimensional performance matrix, which is then used to define performance objectives at increasing hazard levels. A schematic of the three dimensional performance objective matrix is shown in Figure 2.33(a). The performance levels of interest at an arbitrary seismic intensity level are shown in Figure 2.33(b). The performance levels are defined as a function of both maximum story drift ratio and residual story drift ratio.

Ramirez and Miranda [60] improved the PEER performance-based design methodology by using residual story drift ratio and incorporating losses due to the cases of required demolition into the total economic losses. The total economic loss can be expressed as the summation of the loss associated to collapse and the loss associated to non-collapse as follows [5, 60]:

$$E(L_T|IM) = E(L_T|NC,IM) \cdot P(NC|IM) + E(L_T|C,IM) \cdot P(C|IM) \tag{2.4}$$

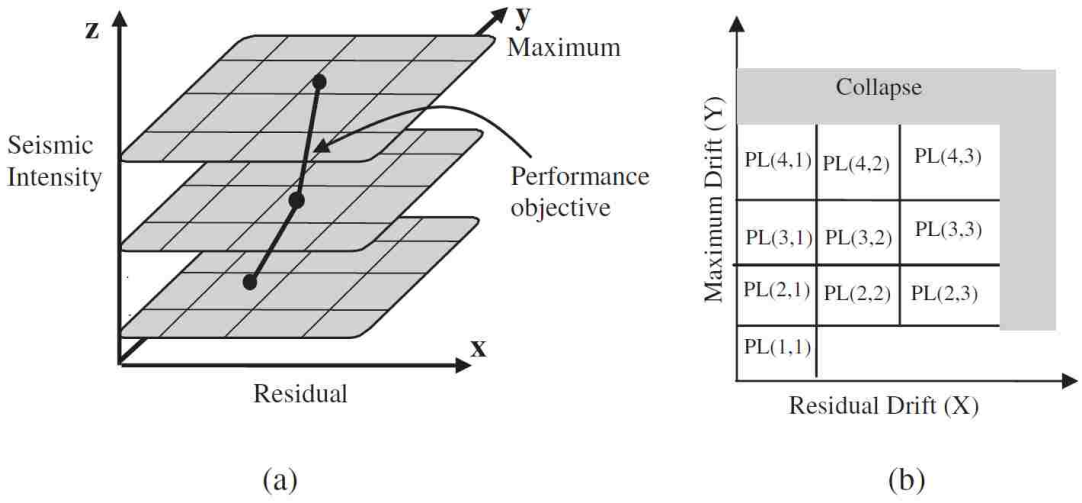

Figure 2.33: Building performance objectives considering maximum and residual drift: (a) three dimensional performance objective matrix; and (b) performance levels at an arbitrary seismic intensity, from [81]

where $E(L_T|NC,IM)$ and $E(L_T|C,IM)$ are the expected value of the economic loss associated to repair actions when the building has not collapsed (non-collapse, NC) and the expected value of economic loss associated to collapse (C), respectively, when the building is subjected to a ground motion at IM hazard level [60]. Ramirez and Miranda [60] split the loss due to non-collapse into two components of loss due to repair action, $L_{NC\cap R}$, and loss due to demolition of the building, $L_{NC\cap D}$. Using the law of total probability, Equation (2.4) can be rewritten as follows:

$$E(L_T|IM) = E(L_T|NC\cap R)\cdot P(NC\cap R|IM) + E(L_T|NC\cap D|IM) \cdot P(NC\cap D|IM) + E(L_T|C,IM)\cdot P(C|IM) \quad (2.5)$$

where $E(L_T|NC\cap R,IM)$ is the expected value of the total economic loss given that the collapse does not occur and the building is required to be repaired and it has been subjected to an earthquake at the IM hazard level. The normalized expected loss due to collapse, non-collapse and demolition, and non-collapse and repair were calculated for a 4-story ductile building and are shown in Figure 2.34 [60]. It can be seen that at the DBE hazard level, the

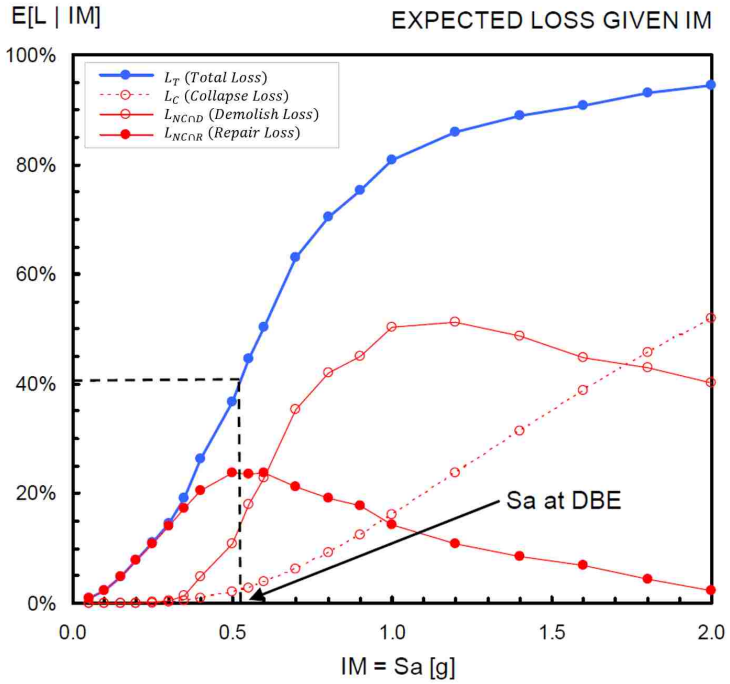

Figure 2.34: Normalized expected economic loss as a function of ground motion intensity for a 4-story ductile building, from [60]

contribution to the total economic loss of non-collapse and repair is the largest followed by the non-collapse and demolition. The contribution of building collapse in total economic loss at the DBE hazard level is small. Ignoring the contribution of required demolition will result in an underestimation of the total economic loss.

Chapter 3

Nonlinear Model Development and Analysis Methodology

3.1 Introduction

Collapse evaluation of a seismic lateral force resisting system (SLFRS) requires example buildings which use the SLFRS (known as archetype buildings) and accurate and effective numerical models of the archetype buildings and the associated SLFRS, capable of simulating important nonlinearities in key structural components. This chapter describes the archetype buildings and the SLFRS considered in this research, and outlines the numerical models and analyses (simulations) that are used in the research.

3.2 Archetype Buildings

Four buildings with 4, 6, 9, and 12 stories are considered in this research. It is assumed that these buildings are office buildings, located in the Los Angeles area. The distribution of the SLFRS in a typical floor plan of the buildings is shown in Figure 3.1. The story height is 15 ft. for the first story and 13 ft. for stories other than the first story for all buildings. Details of the dead loads and live loads are given in Table 3.1 and Table 3.2, respectively.

Two types of SLFRS, a special concentrically braced frame (SCBF) and a self-centering concentrically braced frame (SC-CBF), are considered for each building. Considering the four buildings with different numbers of stories and the two types of SLFRS, a total of eight different *archetype buildings* with a different numbers of stories and SLFRS are studied in

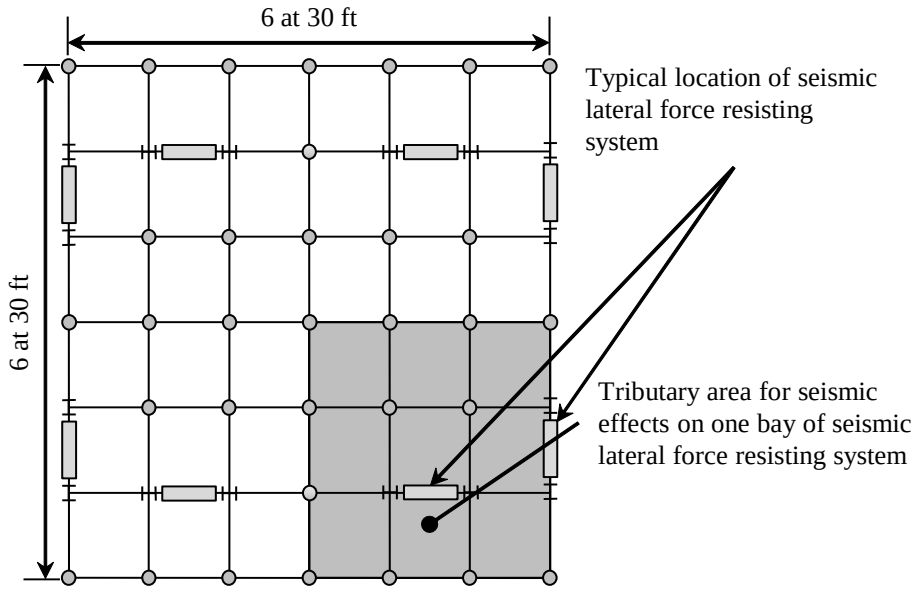

Figure 3.1: Typical floor plan and distribution of seismic lateral force resisting system

this research. The identifiers and general properties of the archetype buildings are summarized in Table 3.3. For each archetype building, a one-bay SLFRS and the seismic mass and seismic weight tributary to the one-bay SLFRS (as shown in Figure 3.1 for a typical floor plan) are modeled numerically, based on the symmetry of the building. As a result of this symmetry, the responses of the archetype SLFRS from static pushover analyses or dynamic response history analyses are assumed to represent the responses of the archetype buildings. The numerical model of the one-bay SLFRS and the seismic mass and gravity load system tributary to the one-bay SLFRS is denoted as an *archetype SLFRS*. The identifiers for the archetype SLFRS are identical to the identifiers for the archetype buildings given in Table 3.3.

The SCBF system studied in this research is the special steel concentrically braced frame SLFRS, as listed and defined in ASCE 7-10 [4]. it consists of beams, columns, and braces in a conventional (2-story X bracing) configuration. The members of the SCBF system are designed to satisfy the ASCE 7-10 [4] seismic design criteria and also the AISC seismic provisions for structural steel buildings [2].

Table 3.1: Dead load details

Item	First floor (psf)	Typ. floor (psf)	Roof (psf)
Floor/roof deck	3	3	3
floor/roof slab	43	43	0
Roofing material	0	0	10
Mech. weight	10	10	10
Ceiling material	5	5	5
Floor finish	2	2	0
Structural steel	15	15	10
Steel fireproofing	2	2	2
Building envelope	7.8	7.2	5.3
Mech. equipment on roof	0	0	25
Total	87.8	87.2	70.3

Table 3.2: Live load details

Item	First floor (psf)	Typ. floor (psf)	Roof (psf)
Office	50	50	0
Partitions	15	15	0
Roof (unreduced)	0	0	20
Total	65	65	20

Table 3.3: Archetype buildings and approximate fundamental period

Archetype identifier	No. of stories	SLFRS	Height (ft.)	T (sec.)
4SCBF	4	SCBF	54	0.56
6SCBF	6	SCBF	80	0.75
9SCBF	9	SCBF	119	1.01
12SCBF	12	SCBF	158	1.25
4SC-CBF	4	SC-CBF	54	0.56
6SC-CBF	6	SC-CBF	80	0.75
9SC-CBF	9	SC-CBF	119	1.01
12SC-CBF	12	SC-CBF	158	1.25

The SC-CBF system is an innovative SLFRS [66] consisting of beams, columns, and braces in a conventional arrangement similar to a SCBF system. In contrast with the SCBF system, the column base detail of the SC-CBF system permits the column to uplift at the foundation and rock [75]. A schematic configuration of SC-CBF system is shown in Figure 3.2. Post-tensioning (PT) bars are anchored to the SC-CBF beam at the roof level and at the foundation. The SC-CBF system can have one or more distribution strut(s) to distribute the force from the PT bars (anchored at the roof level) to the braces over several stories, as shown in Figure 3.2(a). Also, a base strut is included at the base of the SC-CBF system to transfer the base shear to the SC-CBF column base which is in contact with the foundation.

Under low levels of lateral force, the SC-CBF deforms elastically similar to a conventional SCBF. Under high levels of lateral force, the overturning moment at the base of the frame becomes large enough for the "tension" column to decompress, and uplift of the column occurs, as shown in Figure 3.2(b). To enable the column uplift and rocking of the SC-CBF, the beams of SC-CBF are not connected to the floor diaphragm at each floor level and can freely move in the vertical direction as the SC-CBF rocks. Therefore, the gravity loads on floor levels adjacent to the SC-CBF are not transfered to the SC-CBF beams, rather, they are carried by the so-called gravity columns adjacent to the SC-CBF. The only vertical load applied to the SC-CBF is the self weight of the SC-CBF structural members (i.e., beams, columns, braces, etc.) [75].

A restoring force after the SC-CBF column uplifts and rocking of the frame occurs, is provided by the PT bars and weight of the SC-CBF. The gravity columns (part of the gravity framing of the building) are connected to the SC-CBF system by friction bearings at each floor level. A schematic of a typical friction bearing setup between a gravity column and an SC-CBF column at each floor level is shown in Figure 3.3. The lateral inertial forces that develop during an earthquake at each floor level are transfered from the floor diaphragm to the gravity column and then to the SC-CBF system through the friction bearings. In

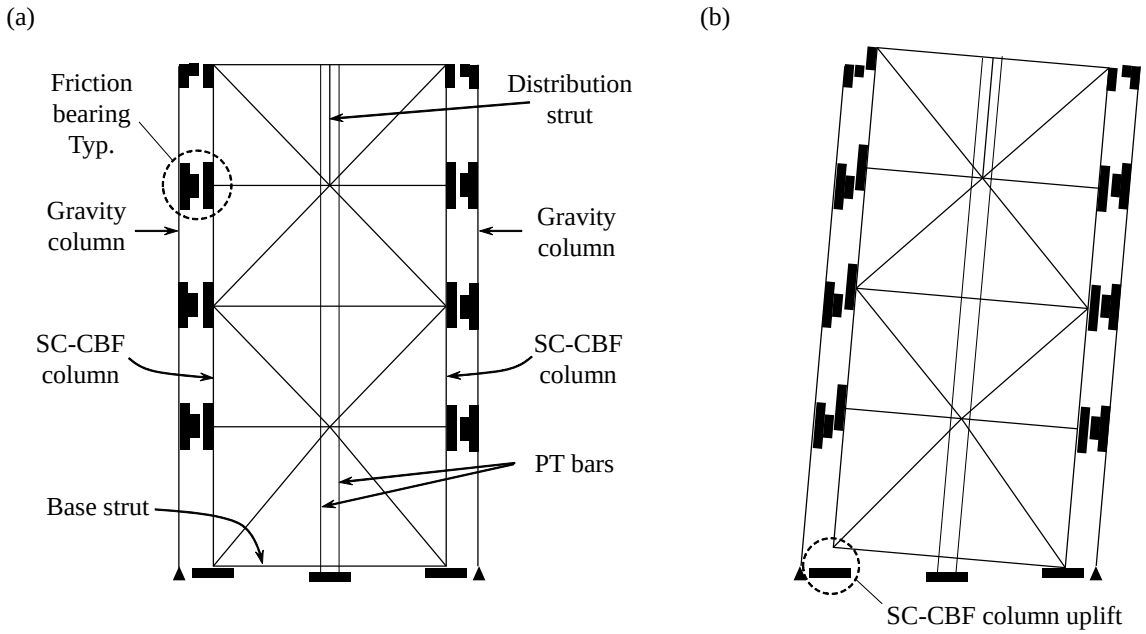

Figure 3.2: Schematic of 4-story SC-CBF system: (a) elements of SC-CBF; and (b) SC-CBF in rocking position [11]

addition to transferring the lateral inertial forces, the friction bearings are a source of energy dissipation during the rocking of the SC-CBF system.

3.3 Archetype Building Design

All archetype buildings are assumed to be in risk category II from Table 1.5-1 of ASCE 7-10 [4]. A seismic importance factor of $I_e = 1.0$ is assigned for risk category II from Table 1.5-2 of ASCE 7-10 [4] for all archetype buildings. Site class D is assumed. Mapped acceleration parameters are determined as $S_s = 1.5g$ and $S_1 = 0.6g$ from Section 11.4.1 and Figures 22-1 and 22-2 of ASCE 7-10 [4]. Site coefficients are determined as $F_a = 1.0$ and $F_v = 1.5$ for site class D from Tables 11.4-1 and 11.4-2 of ASCE 7-10 [4]. "Risk-targeted" maximum considered earthquake spectral response acceleration parameters are calculated as $S_{MS} = 1.5g$ and $S_{M1} = 0.9g$ using Equations (11.4-1) and (11.4-2) of ASCE 7-10 [4]. Design spectral acceleration parameters are determined as $S_{DS} = 1.0g$ and $S_{D1} = 0.6g$ using

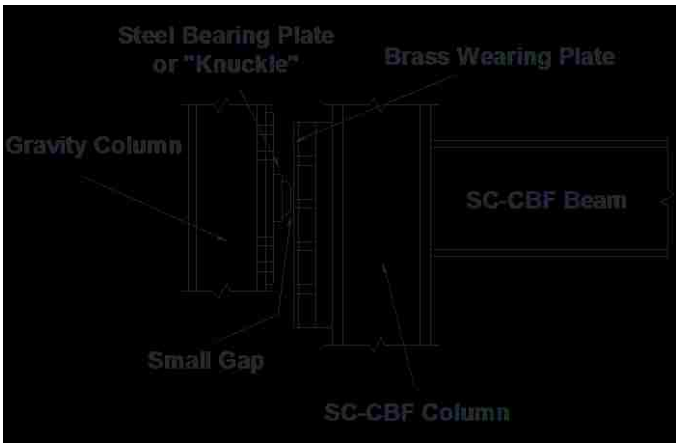

Figure 3.3: Schematic of typical friction bearing, from [11]

Equations (11.4-3) and (11.4-4) of ASCE 7-10 [4]. The long period transition, T_L, is 8 seconds from Figure 22-12 of ASCE 7-10 [4] for Los Angeles. Seismic design category D is assigned to the archetype buildings based on Tables (11.6-1) and (11.6-2) of ASCE 7-10 [4].

Members of the SCBF and SC-CBF are designed using wide flange sections for all archetype buildings. The bracing configuration is an X configuration over two stories, as shown in the three dimensional view of the SCBF for the 4SCBF archetype building in Figure 3.4. The bracing configuration is the same for the other archetype buildings.

The approximate fundamental period (T) for design of each archetype building is estimated using the following equation [23, 4]:

$$T = C_u T_a = C_u C_t h_n^x \geq 0.25 \text{ sec.} \tag{3.1}$$

where $C_u = 1.4$ from Table 12.8-1 of ASCE 7-10 [4], T_a is the approximate fundamental period, $C_t = 0.02$ and $x = 0.75$ from Table 12.8-2 of ASCE 7-10 [4] for "all other structural system" type, and h_n is the building height. The approximate fundamental periods for the design of archetype buildings are given in Table 3.3.

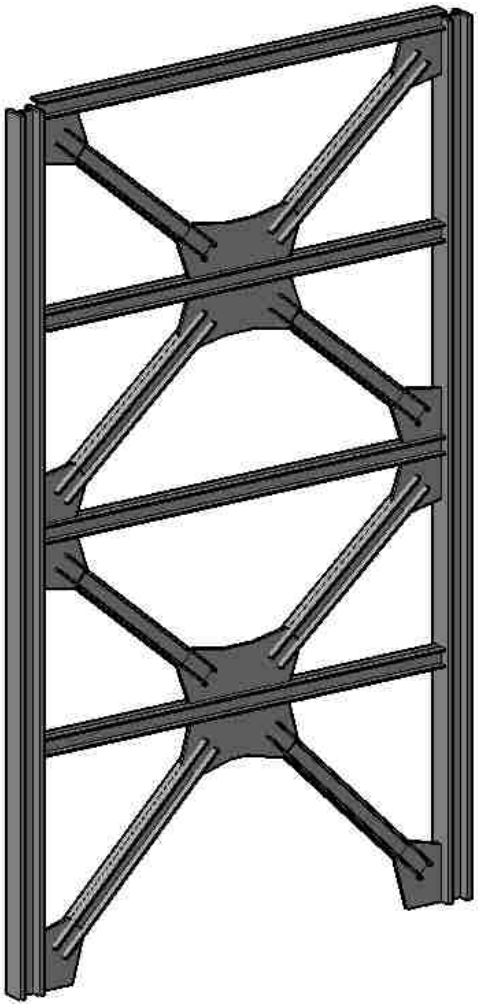

Figure 3.4: Three dimensional view of SCBF for 4SCBF archetype building

3.3.1 Design of SCBF

The SCBF systems are designed using the equivalent lateral force (ELF) method of ASCE 7-10 [4], and the AISC seismic design provisions for structural steel buildings [2]. The seismic design base shear (V) for the SCBF archetype SLFRS (i.e., for each individual SCBF in the archetype building) is calculated using Equation (12.8-1) of ASCE 7-10 [4] as follows:

$$V = C_s W \tag{3.2}$$

where C_s is the seismic response coefficient and W is the seismic weight [4]. C_s is determined using S_{DS} and S_{D1} as the smallest from the following equations:

$$C_s = \frac{S_{DS}}{\left(\frac{R}{I_e}\right)} \tag{3.3}$$

$$C_s = \frac{S_{D1}}{T\left(\frac{R}{I_e}\right)} \tag{3.4}$$

$$C_s = \frac{S_{D1} T_L}{T^2\left(\frac{R}{I_e}\right)} \tag{3.5}$$

A response modification factor of $R = 6$ is used based on Table 12.2-1 of ASCE 7-10 [4]. Table 3.4 gives the values of W, C_S, and V for the SCBF archetype SLFRS. These values of W and V are for the tributary area for a one-bay SLFRS shown in Figure 3.1.

The seismic base shear is distributed over the height of the structure using Equation

Table 3.4: Seismic weight and design base shear tributary to one SCBF

Archetype	W (kips)	C_S	V (kips)
4SCBF	3058	0.167	510
6SCBF	4714	0.167	787
9SCBF	7198	0.139	1000
12SCBF	9682	0.112	1084

Table 3.5: Vertical distribution factor, C_{vx}, for SCBF archetype buildings

Floor level x	4SCBF	6SCBF	9SCBF	12SCBF
1	0.124	0.057	0.022	0.011
2	0.231	0.107	0.044	0.022
3	0.338	0.157	0.068	0.035
4	0.306	0.208	0.092	0.048
5		0.259	0.117	0.063
6		0.213	0.142	0.077
7			0.168	0.093
8			0.194	0.108
9			0.152	0.124
10				0.141
11				0.158
12				0.120

(12.8-11) of ASCE 7-10 [4] as follows:

$$F_x = C_{vx} V \tag{3.6}$$

where C_{vx} is vertical distribution factor. C_{vx} is determined using Equation (12.8-12) of ASCE 7-10 [4] as follows:

$$C_{vx} = \frac{w_x h_x^k}{\sum_{i=1}^{n} w_i h_i^k} \tag{3.7}$$

where w_x is the portion of total effective seismic weight at floor level x, h_x is the height from the base to floor level x, and k is an exponent related to the fundamental period of the structure [4]. Values of C_{vx} at various floor levels for the SCBF archetype buildings are given in Table 3.5.

Table 3.6: Member design of 4-story SCBF and SC-CBF archetype SLFRS

Story number	SCBF			SC-CBF		
	Column	Brace	Beam	Column	Brace	Beam
1	W12×106	W12×106	W12×96	W12×252	W12×136	W12×96
2	W12×106	W12×88	W12×96	W12×252	W12×106	W12×96
3	W12×96	W12×77	W12×96	W12×96	W12×190	W12×96
4	W12×96	W12×77	W12×96	W12×96	W12×96	W12×96

Table 3.7: Member design of 6-story SCBF and SC-CBF archetype SLFRS

Story number	SCBF			SC-CBF		
	Column	Brace	Beam	Column	Brace	Beam
1	W14×311	W12×120	W12×96	W14×455	W12×252	W12×96
2	W14×311	W12×106	W12×96	W14×455	W12×210	W12×96
3	W14×159	W12×96	W12×96	W14×342	W12×106	W12×96
4	W14×159	W10×88	W12×96	W14×342	W12×136	W12×96
5	W12×96	W10×77	W12×96	W14×82	W14×311	W12×96
6	W12×96	W10×68	W12×96	W14×82	W12×106	W12×96

Structural member designs for the SCBF archetype SLFRS are given in Table 3.6 through Table 3.9. For the design of the column members, seismic load effects including the overstrength factor are considered in accordance with Section 12.4.3 of ASCE 7-10 [4]. The maximum story drift ratios are determined in accordance with Section 12.8.6 of ASCE 7-10 [4], and checked to satisfy the allowable story drift ratio from Table 12.12-1 of ASCE 7-10 [4].

3.3.2 Design of SC-CBF

The SC-CBF systems are designed using a modal response spectrum analysis (RSA) method with modifications proposed by Roke et al. [64] and improvements proposed by Chancellor [11]. The RSA requires the mode shapes and periods of vibration for the structural system, which are determined from an eigenvalue analysis. This eigenvalue analysis was performed on a linear elastic model of the SLFRS with the tributary seismic mass and grav-

Table 3.8: Member design of 9-story SCBF and SC-CBF archetype SLFRS

Story number	SCBF			SC-CBF		
	Column	Brace	Beam	Column	Brace	Beam
1	W14×500	W12×120	W12×96	W14×665	W14×311	W12×96
2	W14×500	W12×120	W12×96	W14×665	W14×311	W12×96
3	W14×311	W12×106	W12×96	W14×665	W14×193	W12×96
4	W14×311	W12×106	W12×96	W14×655	W14×159	W12×96
5	W14×211	W12×96	W12×96	W14×500	W14×145	W12×96
6	W14×211	W12×96	W12×96	W14×500	W14×159	W12×96
7	W14×132	W12×88	W12×96	W14×257	W14×257	W12×96
8	W14×132	W12×88	W12×96	W14×257	W14×257	W12×96
9	W14×132	W12×88	W12×96	W14×257	W14×257	W12×96

Table 3.9: Member design of 12-story SCBF and SC-CBF archetype SLFRS

Story number	SCBF			SC-CBF		
	Column	Brace	Beam	Column	Brace	Beam
1	W14×730	W12×136	W12×96	W14×730	W14×500	W12×96
2	W14×665	W12×136	W12×96	W14×730	W14×455	W12×96
3	W14×500	W12×120	W12×96	W14×730	W14×311	W12×96
4	W14×500	W12×120	W12×96	W14×730	W14×283	W12×96
5	W14×342	W12×106	W12×96	W14×730	W14×211	W12×96
6	W14×342	W12×106	W12×96	W14×730	W14×193	W12×96
7	W14×211	W12×96	W12×96	W14×730	W14×193	W12×96
8	W14×211	W12×96	W12×96	W14×730	W14×193	W12×96
9	W14×132	W10×88	W12×96	W14×500	W14×193	W12×96
10	W14×132	W10×88	W12×96	W14×500	W14×176	W12×279
11	W14×82	W10×77	W12×96	W14×132	W14×550	W12×96
12	W14×82	W10×77	W12×96	W14×132	W14×132	W12×136

ity load system (represented as a lean-on-column). For the SC-CBF SLFRS, the SC-CBF columns are fixed at the base in this linear model. The modal lateral forces are determined for a sufficient number of modes, with at least 90% of the total seismic mass included in the modal mass for these modes. The modal responses are combined using a modal combination method [11].

The main design objective for the SC-CBF system is to be damage free under the design basis earthquake (DBE) and an SC-CBF building is intended to remain functional so that it can be immediately occupied after the earthquake. This performance objective is different from the standard seismic design performance objective of life-safety under the DBE. The SC-CBF design procedure targets a performance objective of immediate occupancy (IO) under the DBE and a performance objective of collapse prevention (CP) under the maximum considered earthquake (MCE). Schematic relationships between SC-CBF limit states and SC-CBF design performance objectives are shown in Figure 3.5. Four limit states of column decompression (followed by rocking), PT bar yielding, member yielding, and member failure are shown in Figure 3.5. Member yielding should not occur before PT bar yielding.

The PT bar yielding limit state can have different consequences depending on the amount of yielding that occurs. Yielding of PT bars causes loss of the initial post-tensioning force in the PT bars. With limited PT bar yielding, the SC-CBF still self-centers without significant damage and the IO performance objective is still achievable. Therefore, the SC-CBF system is designed so the median DBE response occurs without PT bar yielding. For response under the DBE greater than the median response, limited PT bar yielding is expected.

The limit state of member yielding will not cause collapse and is an acceptable limit state for CP performance. Failure of the members of the CBF, however, can lead to collapse

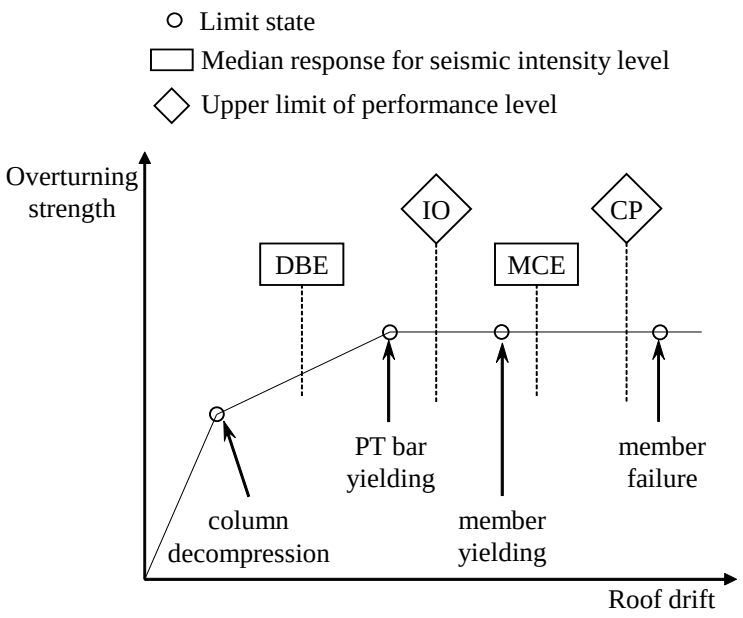

Figure 3.5: Schematic representation of SC-CBF limit states and performance objectives, from [66]

Table 3.10: Natural periods (seconds) for first four modes of SC-CBF archetype buildings

Mode number	4SC-CBF	6SC-CBF	9SC-CBF	12SC-CBF
1	0.42	0.65	1.02	1.58
2	0.16	0.20	0.28	0.35
3	0.10	0.14	0.16	0.19
4	0.09	0.10	0.13	0.14

or near collapse conditions.

In the RSA-based SC-CBF design method of Roke [66] and Chancellor [11], the response of the higher modes is amplified to account for the effect of rocking of the SC-CBF and to produce a low probability of member yielding or buckling under the DBE. The period of the first four natural vibration modes of the SC-CBF archetype buildings are given in Table 3.10. The design spectral acceleration for the first four natural modes of the SC-CBF archetype SLFRS are given in Table 3.11.

The first mode response of the SC-CBF is limited by the overturning moment capacity

Table 3.11: Design spectral acceleration (g) for first four modes of SC-CBF archetype buildings

Mode number	4SC-CBF	6SC-CBF	9SC-CBF	12SC-CBF
1	1.00	0.92	0.59	0.38
2	1.00	1.00	1.00	1.00
3	0.89	1.00	1.00	1.00
4	0.84	0.87	1.00	1.00

at column decompression, OM_D (i.e., the initiation of rocking). For the SC-CBF system with lateral load bearings, it is assumed that the lateral force profile is proportional to the first natural mode for calculating the OM_D [66, 11]. Several response modification factors are defined during the design of the SC-CBF system [11]. The response modification factor R_A for the SC-CBF is used to compare with the response modification factor R for a conventional SCBF. R_A is defined as follows:

$$R_A = \frac{OM_{elastic}}{OM_D} \tag{3.8}$$

where $OM_{elastic}$ is defined as the overturning moment caused by lateral forces (with $R = 1$) from the ELF procedure of ASCE 7-10 [4] as follows [11]:

$$OM_{elastic} = \boldsymbol{h}^T \boldsymbol{F}_{ELF} \tag{3.9}$$

where $\boldsymbol{h}^T = \{h_1 \cdots h_x \cdots h_n\}$ is the vector of floor heights from the base and $\boldsymbol{F}_{ELF}^T = \{F_1 \cdots F_x \cdots F_n\}$ is the vector of lateral forces applied at floor levels. F_x is determined using Equation (12.8-11) of ASCE 7-10 [4] with $R = 1$ (see Equation (3.6)). It can be seen from Equation (3.8) that R_A is defined and calculated by dividing the elastic response of the SC-CBF (i.e., $OM_{elastic}$) by the response at column decompression (i.e., OM_D). R_A for the SC-CBF system is similar to R for a conventional SLFRS, since it is the ratio of the elastic strength to the strength at first nonlinearity of the SC-CBF system (i.e., column decompression). The seismic design forces for the SC-CBF system, however, are not capped by R_A

Table 3.12: OM_D, $OM_{elastic}$, and R_A values for SC-CBF archetype SLFRS

Archetype	OM_D (kip-in)	$OM_{elastic}$ (kip-in)	R_A
4SC-CBF	181,000	1,329,000	7.52
6SC-CBF	266,000	2,852,000	10.7
9SC-CBF	440,000	4,252,000	9.66
12SC-CBF	783,000	6,223,000	7.95

Table 3.13: Design roof drift ratio for SC-CBF archetype SLFRS

Archetype	θ_D (%)	μ_{DBE}	$\theta_{DBE,dd}$ (%)
4SC-CBF	0.068	12.47	0.848
6SC-CBF	0.076	15.39	1.170
9SC-CBF	0.097	12.30	1.193
12SC-CBF	0.190	6.38	1.212

(in contrast to a conventional SCBF system for which the elastic seismic design forces are capped by R), rather the first mode design forces are capped by the overturning moment at the PT bar yield. The process of calculating the seismic design forces for the SC-CBF system is discussed later in this section. The OM_D, $OM_{elastic}$, and R_A values for the SC-CBF archetype SLFRS are given in Table 3.12.

The design roof drift ratio under the DBE ($\theta_{DBE,dd}$) is predicted using the roof drift ratio at column decompression (θ_D) and a ductility coefficient for the DBE-level response of a self-centering system (μ_{DBE}) as follows:

$$\theta_{DBE,dd} = \mu_{DBE}\theta_D \tag{3.10}$$

Formulas for estimating μ_{DBE} were developed for self centering systems by Seo [77, 76]. $\theta_{DBE,dd}$ is an estimate of the median peak roof drift ratio under the DBE and therefore has a 50% probability of being exceeded. Values of θ_D, μ_{DBE}, and $\theta_{DBE,dd}$ for the SC-CBF archetype SLFRS are given in Table 3.13.

The PT bars are designed so that the $\theta_{DBE,dd}$ value does not exceed the roof drift ca-

Table 3.14: PT bar design parameters for SC-CBF archetype SLFRS

Archetype	Bar type	No. of bars	A_{PT} (in^2)	PT_Y (kips)	r_{PT}
4SC-CBF	D-1.25	12	15.0	1800	0.40
6SC-CBF	D-1.375	14	22.1	2654	0.47
9SC-CBF	D-2.5	6	31.2	3744	0.60
12SC-CBF	D-1.75	18	47.2	5659	0.75

pacity at nominal yield of the PT bars ($\theta_{Y,n}$). The nominal yield force of the PT bars (PT_Y, which depends on the PT bar area and the nominal PT bar yield tress) and the initial prestressing force in the PT bars (PT_0) are two independent parameters determined in the design process to satisfy the $\theta_{DBE,dd} \leq \theta_{Y,n}$ condition [11]. When designing the PT bars, PT_Y equals the number of PT bars multiplied by the bar area (i.e., total PT bar area, denoted by A_{PT}) multiplied by the nominal yield stress for the PT bars. PT_0 is usually normalized as $r_{PT} = PT_0/PT_Y$. The design values for A_{PT}, and r_{PT} are given in Table 3.14 for the SC-CBF archetype SLFRS.

The SC-CBF member design method assumes that the first mode lateral forces are reduced from the elastic response level by the ratio of the overturning moment at PT bar yielding (OM_Y) to the overturning moment from unreduced first mode forces (OM_1) as follows:

$$\alpha_{Y,1} = \frac{OM_Y}{OM_1} \cdot g \tag{3.11}$$

where OM_1 is as follows:

$$OM_1 = \boldsymbol{h}^T \boldsymbol{F_1} = \boldsymbol{h}^T \Gamma_1 \boldsymbol{m} \phi_1 \tag{3.12}$$

where Γ_1 is the modal contribution factor for the first natural vibration mode, $\boldsymbol{m}$ is the diagonal mass matrix with seismic mass at each floor level as the diagonal elements, and ϕ_1 is the the first natural vibration mode shape. The $\alpha_{Y,1}$ parameter is used to reduce the elastic first mode design forces. The higher mode lateral forces are assumed to be unreduced by rocking of the SC-CBF and determined using the unreduced (i.e., $R = 1$)

Table 3.15: Design spectral acceleration and amplification factors for 4SC-CBF archetype SLFRS

Mode no. n	Spectral acceleration (g)		γ_n	$\gamma_1 \alpha_{Y,1}$ or $\gamma_n S_a(T_n, 5\%)$ (g)
	$S_a(T_n, 5\%)$	$\alpha_{Y,1}$		
1	use $\alpha_{Y,1}$	0.38	1.20	0.46
2	1.00		1.60	1.60
3	0.89		1.60	1.42
4	0.84		1.60	1.34

Table 3.16: Design spectral acceleration and amplification factors for first four modes of 6SC-CBF archetype SLFRS

Mode no. n	Spectral acceleration (g)		γ_n	$\gamma_1 \alpha_{Y,1}$ or $\gamma_n S_a(T_n, 5\%)$ (g)
	$S_a(T_n, 5\%)$	$\alpha_{Y,1}$		
1	use $\alpha_{Y,1}$	0.23	1.49	0.34
2	1.00		1.60	1.60
3	1.00		1.60	1.60
4	0.87		1.60	1.40

design response spectrum of ASCE 7-10 [4]. Based on the studies by Roke et al. [67] and Chancellor [11] modal load amplification factors are developed for different modes to achieve a 10% probability of the member force demand value under the DBE exceeding the member force design demand. These modal amplification factors are denoted by γ_n for the n^{th} mode. Therefore, the elastic first mode forces are multiplied by $\gamma_1 \alpha_{Y,1}$ and the elastic higher modes are multiplied by $\gamma_n S_a(T_n, 5\%)$ for design. Values of $\alpha_{Y,1}$ and γ_n for the first four modes of the SC-CBF archetype SLFRS are given in Tables 3.15 through 3.18. Using the proposed design method for the SC-CBF system, the structural members are designed to remain elastic (less than 10% probability of yielding or buckling) under the DBE level ground motion. Structural member sizes for the SC-CBF archetype SLFRS are given in Table 3.6 through Table 3.9. The member design for the distribution strut and base strut of the SC-CBF archetype buildings are given in Table 3.19.

Table 3.17: Design spectral acceleration and amplification factors for first four modes of 9SC-CBF archetype SLFRS

Mode no. n	Spectral acceleration (g)		γ_n	$\gamma_1 \alpha_{Y,1}$ or $\gamma_n S_a(T_n, 5\%)$ (g)
	$S_a(T_n, 5\%)$	$\alpha_{Y,1}$		
1	use $\alpha_{Y,1}$	0.14	1.93	0.27
2	1.00		1.60	1.60
3	1.00		1.60	1.60
4	1.00		1.60	1.40

Table 3.18: Design spectral acceleration and amplification factors for first four modes of 12SC-CBF archetype SLFRS

Mode no. n	Spectral acceleration (g)		γ_n	$\gamma_1 \alpha_{Y,1}$ or $\gamma_n S_a(T_n, 5\%)$ (g)
	$S_a(T_n, 5\%)$	$\alpha_{Y,1}$		
1	use $\alpha_{Y,1}$	0.12	2.00	0.23
2	1.00		1.60	1.60
3	1.00		1.60	1.60
4	1.00		1.60	1.40

Table 3.19: Base strut and distribution strut member sizes for SC-CBF archetype SLFRS

Archetype	Base strut	Distribution strut (top story)	Distribution strut (story below top story)
4SC-CBF	W12×120	W12×210	
6SC-CBF	W12×170	W14×283	
9SC-CBF	W14×193	W14×211	W14×211
12SC-CBF	W14×257	W14×550	

3.4 Numerical Models for Archetype Buildings

Numerical modeling and nonlinear response analyses are carried out using the OpenSEES computational framework [53]. A two dimensional finite element model of the one-bay SLRFS (i.e., SCBF or SC-CBF) is developed for each archetype SLFRS in OpenSEES. The seismic mass and gravity load, tributary to the one-bay SLFRS are included in the finite element model. The secondary effect of the gravity load, the so-called P-Δ effect, is simulated using a lean-on-column. Gravity loads are applied to the lean-on-column at each floor level to include the P-Δ effect during the static pushover analyses and the dynamic response history analyses. The lean-on-column gravity loads are determined from the following combination of dead load and live load [23]:

$$1.05DL + 0.25LL \tag{3.13}$$

where *DL* is the nominal dead load and *LL* is the nominal live load (see Table 3.1 and Table 3.2).

The seismic mass is determined from the dead load and the partition load (see Table 3.1 and Table 3.2). The dead load, live load, gravity load, and seismic mass applied at the 1st floor level, typical floor level, and roof level are given in Table 3.20 for the SCBF archetype SLFRS. The gravity loads that are directly transfered to the SCBF, as part of the gravity load carrying system, are directly applied to the SCBF archetype SLFRS at each floor level. The weight of the SCBF structural members is also included as vertical loads applied at each floor level, separately. A detail of the numerical model for the 4SCBF archetype SLFRS is shown in Figure 3.6.

The dead load, live load, gravity load, and seismic mass applied at the 1st story floor level, typical story floor level, and roof level are given in Table 3.21 for the SC-CBF

Table 3.20: Gravity load and seismic mass at various floor levels for SCBF archetype SLFRS

	Dead load (kips)	Live load (kips)	Gravity load on lean-on-column (kips)	Gravity load on SCBF (kips)	Seismic mass ($\frac{\text{kip}\cdot\text{s}^2}{\text{in}}$)
1st story	711	527	829	49	2.156
Typ. story	707	527	825	49	2.145
Roof	569	162	565	33	1.474

archetype SLFRS. As stated previously, the SC-CBF system does not carry gravity loads from the adjacent floors at different floor levels as the SC-CBF is not connected to the floor diaphragms. The connection between the SC-CBF and the gravity framing of the building is through friction bearings between SC-CBF columns and the adjacent gravity columns. The weight of the SC-CBF structural members is included in the SC-CBF archetype SLFRS as vertical loads at each floor level. A detail of the numerical model for the 4SCBF archetype SLFRS is shown in Figure 3.7. Details of the SC-CBF column base and the PT bar connection at the foundation level are shown in Figure 3.8. As it can be seen from Figure 3.8, the boundary conditions for the SC-CBF columns are modeled using materials with asymmetric behavior in compression and tension. Namely, the column bases transmit compression to the foundation but do not transmit tension, to allow for column uplift and rocking. Also shear keys at the SC-CBF column bases are modeled so that the left SC-CBF column base transmits shear force which acts to the left to the foundation, but does not transmit shear force which acts to the right to the foundation. Similarly, the right SC-CBF column base transmits shear force which acts to the right to the foundation, but does not transit shear force which acts to the left to the foundation. A tension-only element is modeled in *series* with the PT bars at the foundation level so that the combination of this tension-only element and PT bars will carry tension but will not carry compression.

Structural members (i.e., beams, columns, and braces) are modeled using multiple nonlinear beam-column elements (*forceBeamColumn* element in OpenSEES [56]) per member

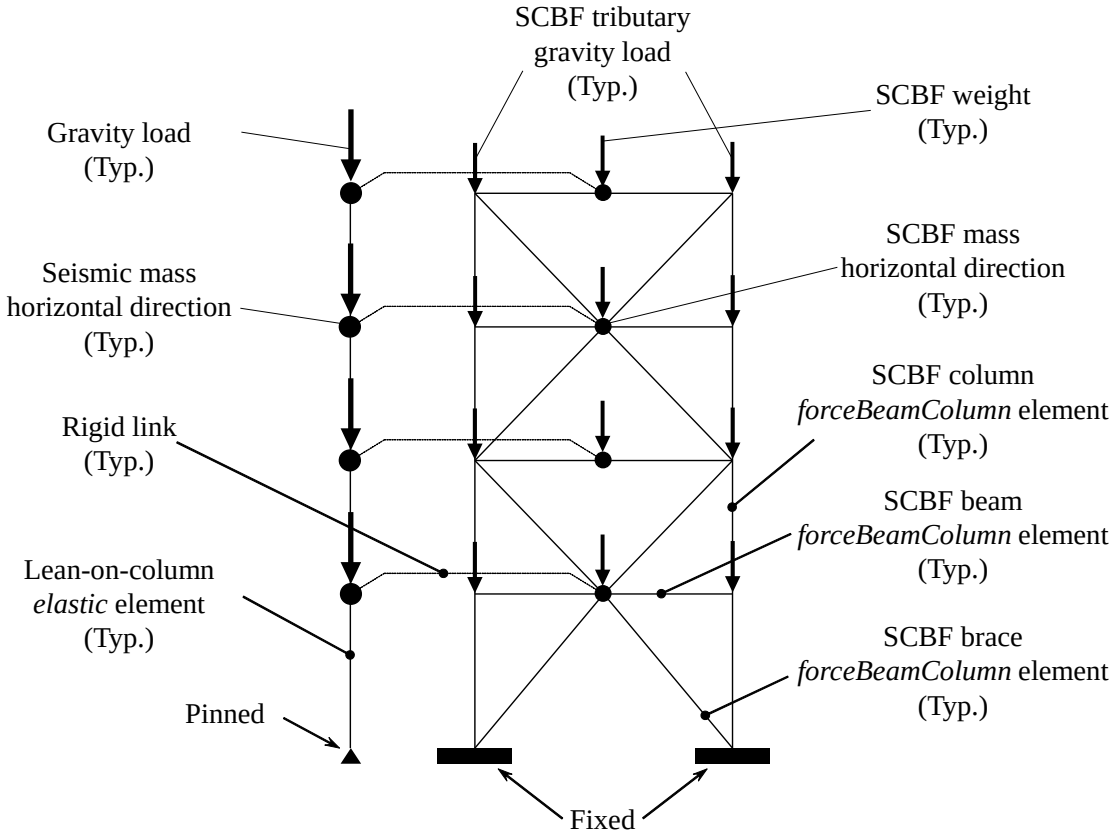

Figure 3.6: Detail of numerical model for 4SCBF archetype SLFRS

Table 3.21: Gravity load and seismic mass at various floor levels for SC-CBF archetype SLFRS

	Dead load (kips)	Live load (kips)	Gravity load on lean-on-column (kips)	Gravity load on SC-CBF (kips)	Seismic mass ($\frac{\text{kip}\cdot\text{s}^2}{\text{in}}$)
1st story	711	527	878	0	2.156
Typ. story	707	527	874	0	2.145
Roof	569	162	598	0	1.474

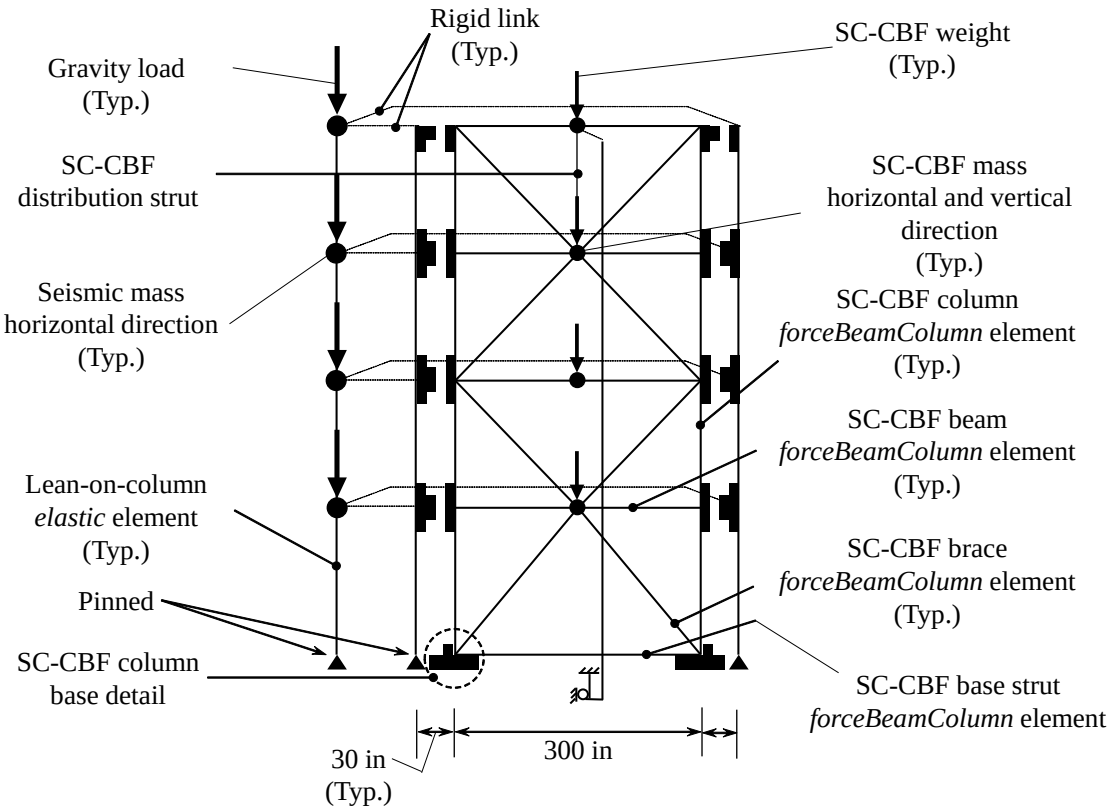

Figure 3.7: Detail of numerical model for 4SC-CBF archetype SLFRS, from [11]

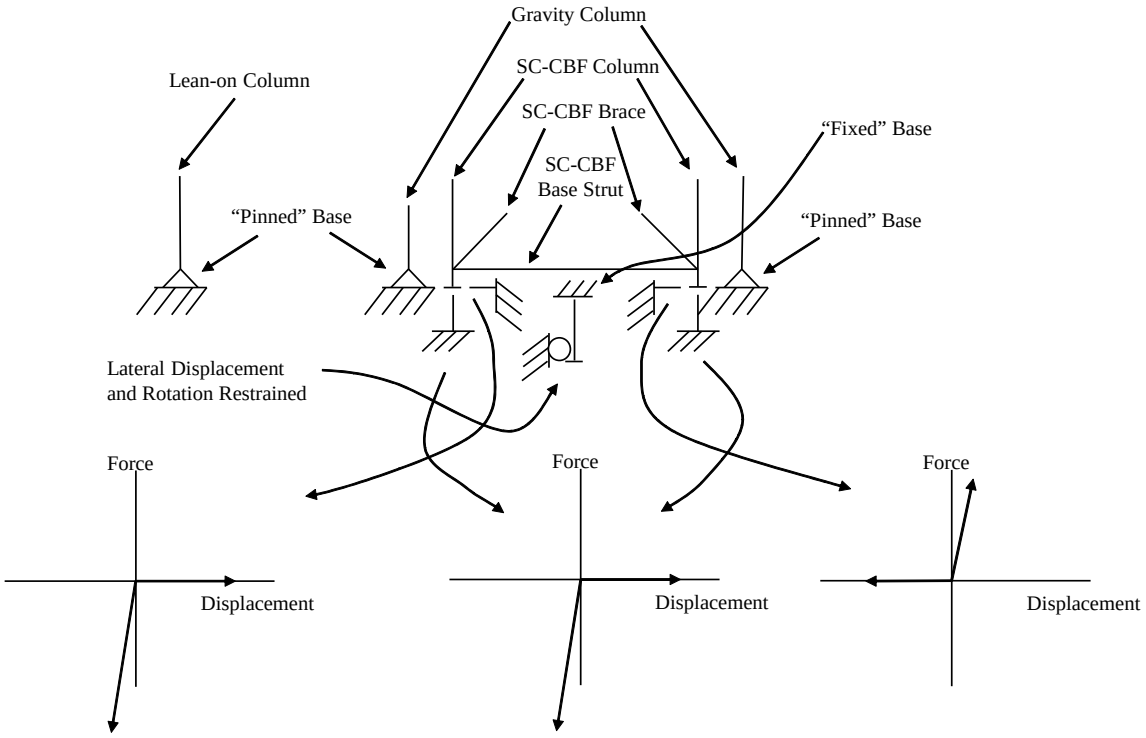

Figure 3.8: Detail of column base and PT bar connection at the base for SC-CBF archetype SLFRS, from [11]

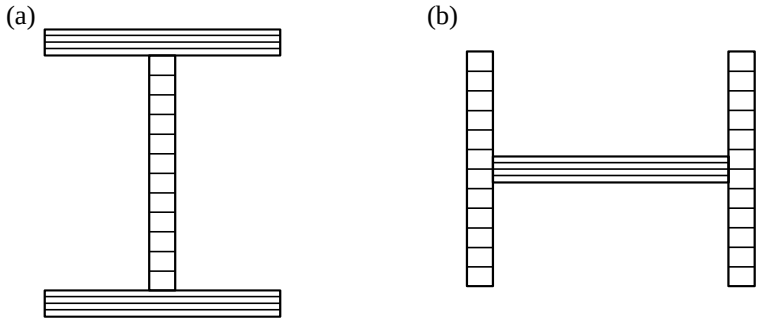

Figure 3.9: Fiber discretization of wide flange cross section for: (a) beams and columns bending about strong axis; and (b) braces bending about weak axis

for the SCBF and SC-CBF archetype SLFRS. Beams and columns are modeled with 4 beam-column elements per member. Braces are modeled with 16 beam-column elements per member. Fiber sections are used for each element to include axial force-bending moment interaction. For two dimensional analyses, bending of the beams and columns occurs about the strong axis of the members (which have a wide flange cross section). To simulate gradual yielding of the wide flange cross sections about the strong axis, 4 fibers through the flange thickness and 12 fibers over the web height are used to model the wide flange cross sections of the beams and columns, as shown in Figure 3.9(a). Bending of the braces (due to buckling) occurs about the weak axis of the members (which have wide flange cross sections). To simulate gradual yielding of the wide flange cross sections about the weak axis, 4 fibers through the web thickness and 12 fibers over the flange width are used to model the wide flange cross section of the braces, as shown in Figure 3.9(b).

Looking at Figure 3.4, it can be seen that buckling of the braces will occur about the weak axis of the brace cross section, out of the plane of the SCBF. After buckling of a brace, flexural plastic hinges form in the gusset plates at each end of the brace as shown in Figure 3.10. In a two dimensional finite element model, the out-of-plane buckling of the braces cannot be simulated. To capture the weak axis buckling of the brace members in a two dimensional simulation, the braces are rotated 90 degrees about their longitudinal axis in the model, so that the buckling about the weak axis of the brace occurs in the plane

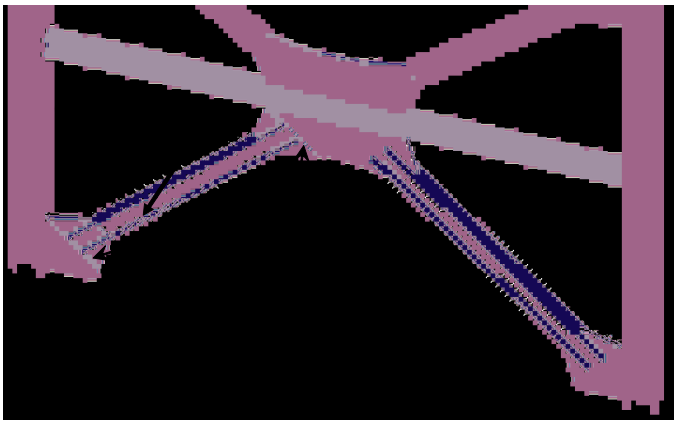

Figure 3.10: Out-of-plane buckling of brace and flexural plastic hinge in gusset plates

of the SCBF. Figure 3.11 shows the rotated braces. When a brace buckles out-of-plane in a three dimensional model, the plastic moments of the gusset plates do not have an in-plane component acting on the adjacent beams and columns. Therefore, to avoid this in-plane moment, the flexural strength of the gusset plate plastic hinge is not modeled (it is neglected) in the two dimensional model and the brace ends have pin boundary conditions.

Rigid offset regions such as gussets plate and beam-to-column connection regions are modeled with stiff elastic elements. The "rigid" offsets are shown in Figure 3.11 and 3.12 by a heavy line.

3.4.1 Models for Nonlinearity and Strength and Stiffness Deterioration

Material and geometric nonlinearity are considered in the finite element models. The Menegotto-Pinto hysteresis model is used for the structural steel material. Strength and stiffness deterioration due to buckling is used in the modeling of the braces. The braces are modeled with 16 beam column elements per member and an initial lateral imperfection of 1/1000 of the brace length at the middle of the braces to initiate brace buckling, using the approach of Uriz et al. [84]. Fracture of the brace members due to low-cycle

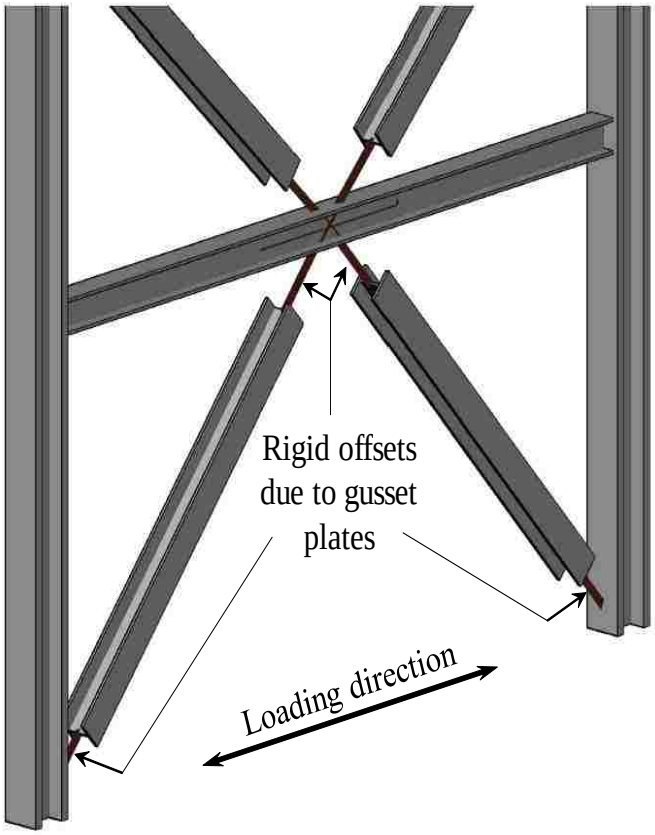

Figure 3.11: Brace orientation for two dimensional numerical modeling

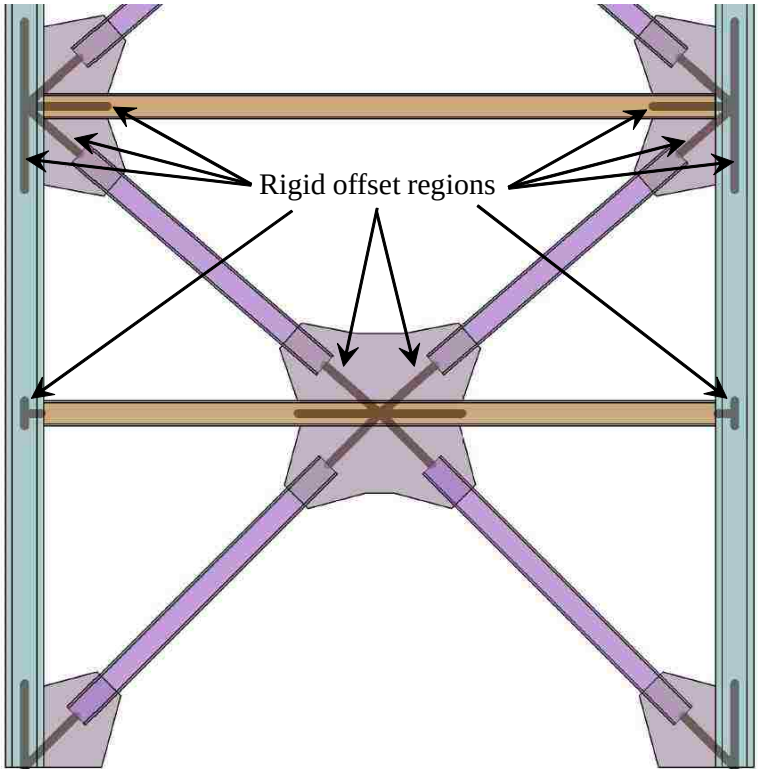

Figure 3.12: Rigid offset regions at gusset plate connections and beam-to-column connections

fatigue, induced by local buckling, is simulated using a rainflow cycle counting method as described by Uriz [83]. Such local buckling is not directly modeled. The "corotational" geometric transformation is used for the brace elements to enable simulation of large deformation and buckling of the brace members. While the columns are modeled without initial imperfection, column buckling is allowed by using 4 elements per column and the corotational transformation for the column elements. Deformation of a column member (i.e., a deviation from the initially perfectly straight transverse position of the column) during a static pushover analysis or a dynamic response history analysis is similar to the initial imperfection in a brace member. Therefore, when the combination of column transverse deformation, axial force, and bending moment reaches a critical limit (of instability), buckling occurs in a column member. Buckling is prevented for the beam members of the SCBF archetype SLFRS by using a "linear" geometric transformation for the beam elements, as the beams are laterally supported by the floor diaphragm for the SCBF archetype buildings. Buckling is allowed for the beam members of the SC-CBF archetype SLFRS by using 4 elements per beam and a corotational geometric transformation for the beam elements, similar to the column members.

3.5 Static Pushover Analysis

Nonlinear static pushover analysis is performed for all archetype SLFRS. The lateral force profiles used for static pushover analyses are proportional to the natural first mode shape of vibration (ϕ_1) multiplied by the seismic mass (tributary to the one-bay SLFRS) at each floor [23]:

$$F_x \propto m_x \phi_{1,x} \tag{3.14}$$

where F_x is the lateral force at floor level x, m_x is the seismic mass at level x, and $\phi_{1,x}$ is the ordinate of the first natural vibration mode shape at floor level x. The natural vibra-

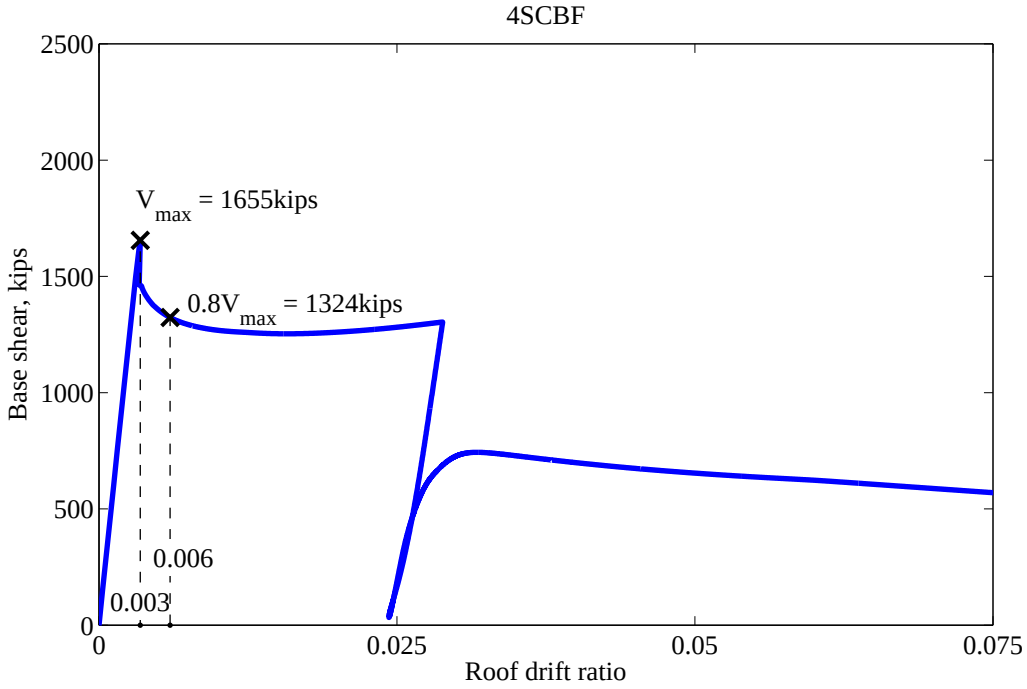

Figure 3.13: Pushover curve for 4SCBF archetype SLFRS

tion mode shapes are determined from an eigenvalue analysis for each archetype SLFRS including the P-Δ effect. As discussed later, the results of the nonlinear static pushover analysis are used to determine the overstrength factor (Ω) and period based ductility (μ_T) for the archetype buildings. The static pushover analyses are conducted for each archetype SLFRS, not for each archetype building. Therefore, the base shear strengths shown in the pushover diagrams are one fourth of the base shear strengths for the archetype buildings (see discussion in Section 3.2 and Figure 3.1). The roof drift ratios, however, are the same for archetype SLFRS and archetype buildings. The P-Δ effect is included in the static pushover analyses.

The nonlinear pushover curves for the SCBF archetype SLFRS are shown in Figures 3.13 through 3.16. Two points are marked on each pushover curve for the SCBF archetype SLFRS: (i) at the maximum base shear strength shown by V_{max}; and (ii) at the point where the base shear is reduced by 20%, after the maximum base shear, shown by $0.8V_{max}$. The

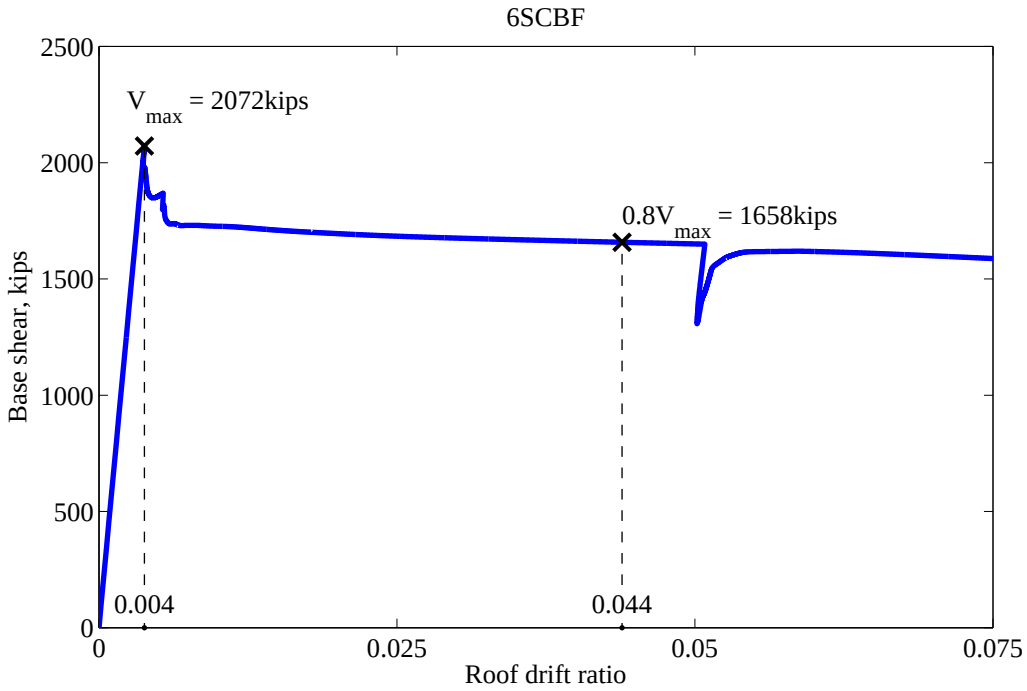

Figure 3.14: Pushover curve for 6SCBF archetype SLFRS

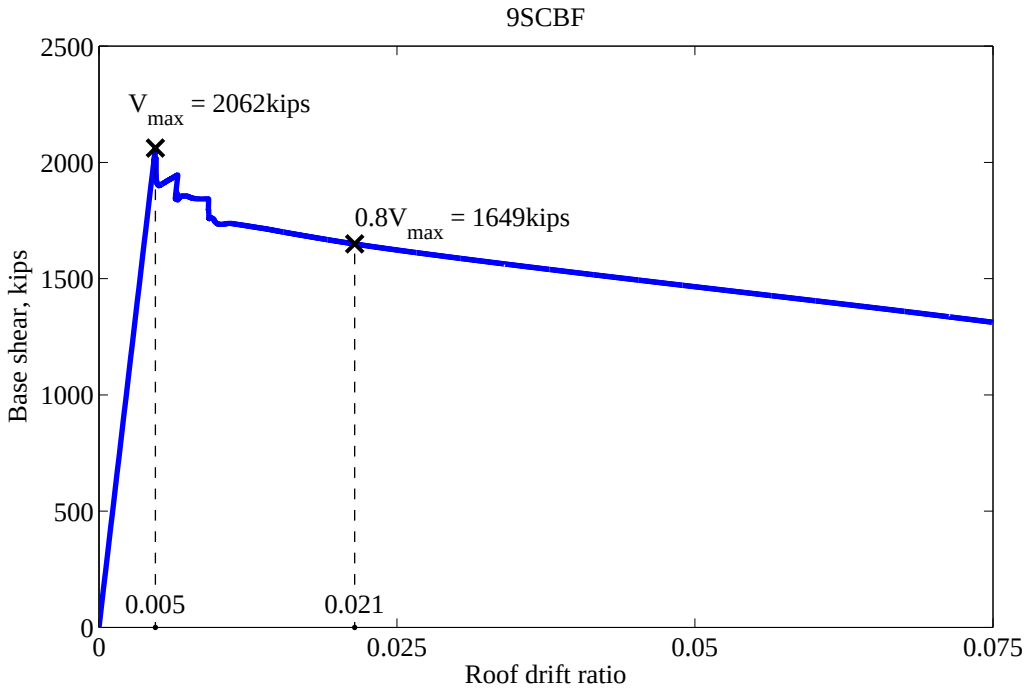

Figure 3.15: Pushover curve for 9SCBF archetype SLFRS

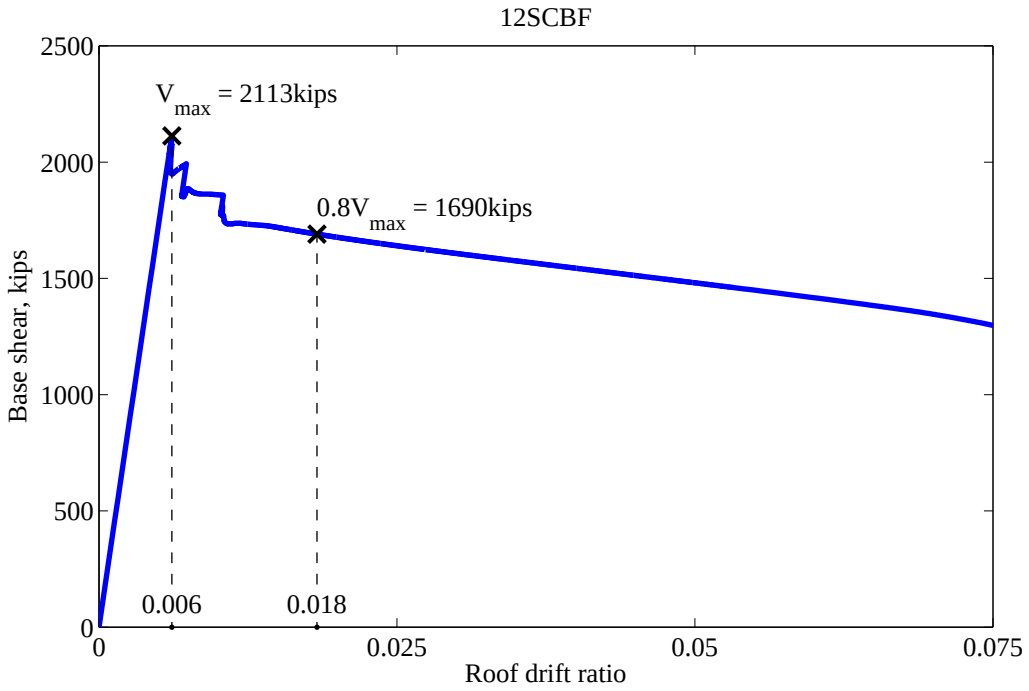

Figure 3.16: Pushover curve for 12SCBF archetype SLFRS

deformed shapes of the 4SCBF, 6SCBF, 9SCBF, and 12SCBF archetype SLFRS (without the lean-on-column) are shown in Figure 3.17. The first significant decrease (drop) in the pushover curve of the 4SCBF archetype SLFRS occurs with buckling of the second story right brace and first story left column, and the second drop occurs with buckling of the first story left brace. The first drop in the pushover curve for the 6SCBF archetype SLFRS occurs with buckling of the third story left brace, the second drop occurs with buckling of the second story right brace, and the third drop occurs with buckling of the fifth story left brace. The first drop in the pushover curve for the 9SCBF archetype SLFRS occurs with buckling of the third story left brace, the second drop occurs with buckling of the fifth story left brace, and the third drop occurs with buckling of the second story right brace. The first drop in the pushover curve for 12SCBF archetype SLFRS occurs with buckling of the fifth story left brace, the second drop occurs with buckling of the seventh story left brace, and the third drop occurs with buckling of the fourth story right brace.

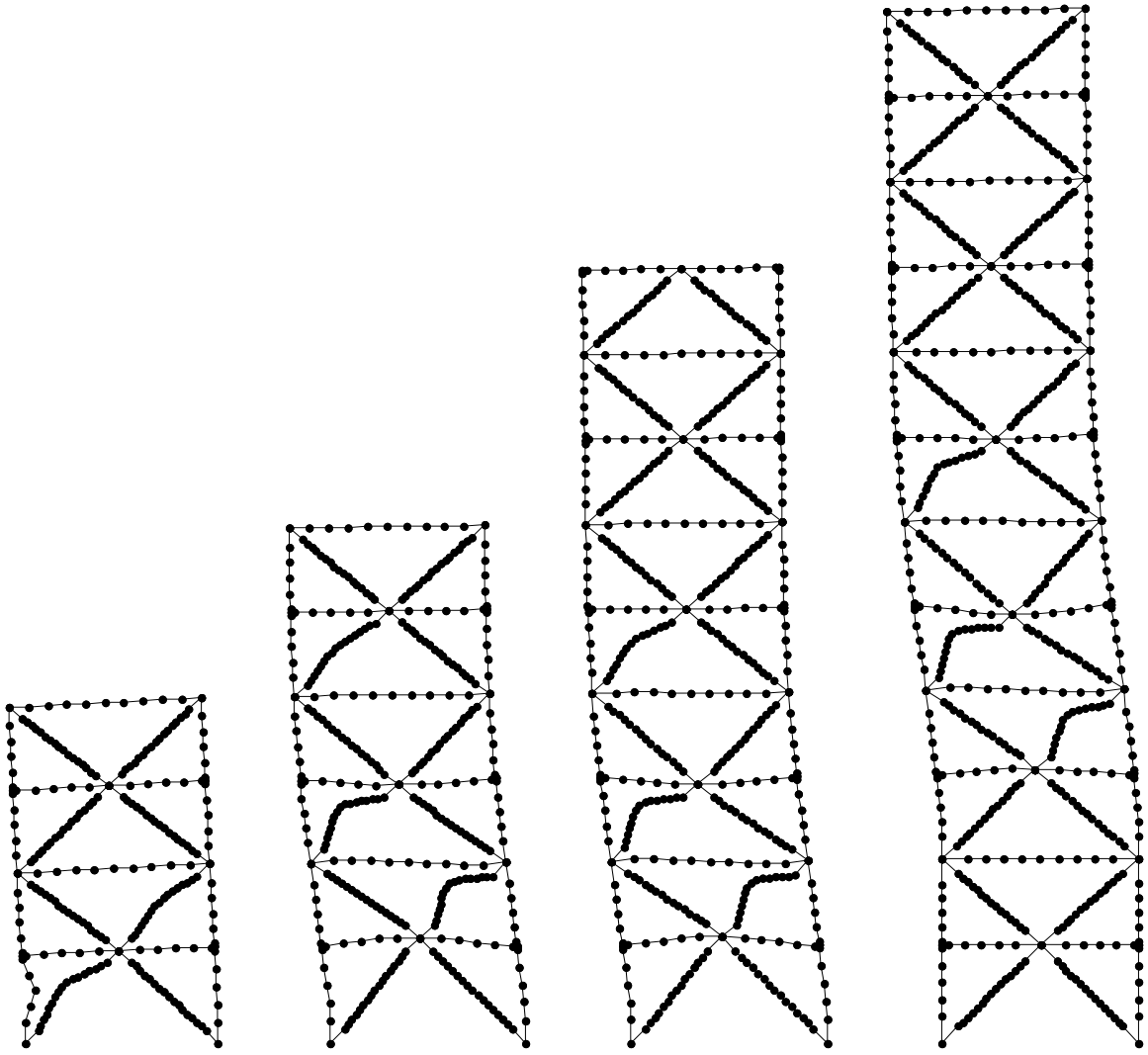

Figure 3.17: Deformed shapes of 4SCBF, 6SCBF, 9SCBF, and 12SCBF archetype SLFRS at approximately 6% roof drift ratio

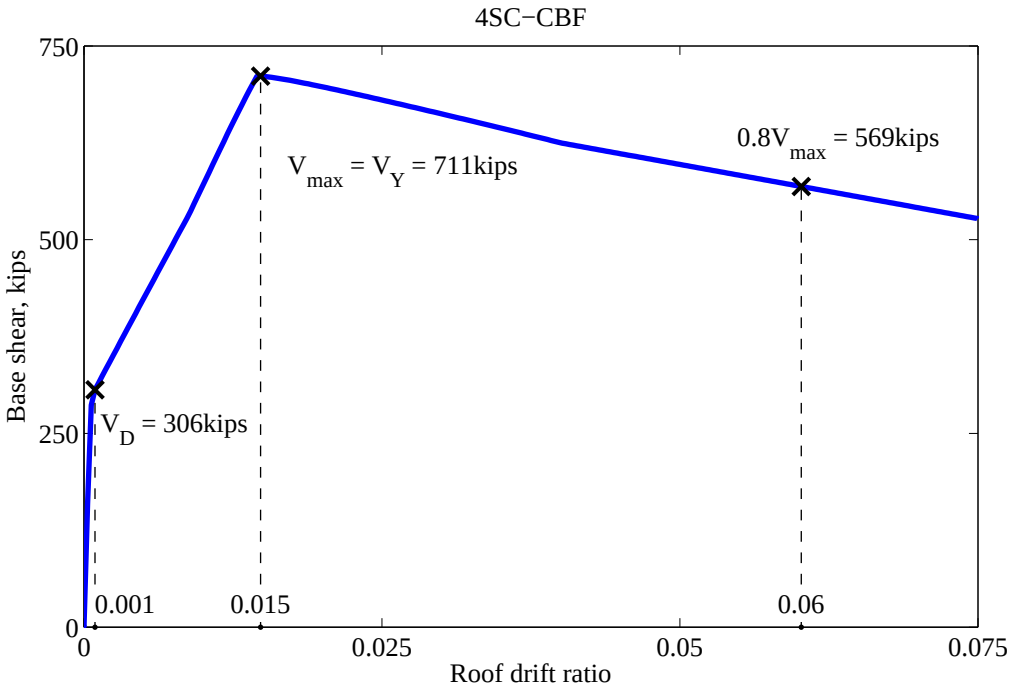

Figure 3.18: Pushover curve for 4SC-CBF archetype SLFRS

The nonlinear pushover curves for the SC-CBF archetype SLFRS are shown in Figures 3.18 through 3.21. The base shear at three points are marked on each pushover curve for each SC-CBF archetype SLFRS: (i) at the column decompression point shown by V_D; (ii) at the PT bar yielding shown by V_Y which is also the point of maximum base shear (V_{max}); and (iii) at the point where the base shear is reduced by 20%, after the maximum base shear shown by $0.8V_{max}$.

The ultimate roof displacement, δ_u, is the roof displacement associated with a 20% reduction in the maximum base shear strength of the building after V_{max} is passed, in the nonlinear pushover curve. As discussed in Chapter 4, δ_u is used in calculating μ_T. The 20% reduction in base shear points along with their corresponding roof drift ratios are shown in Figures 3.18 through 3.21.

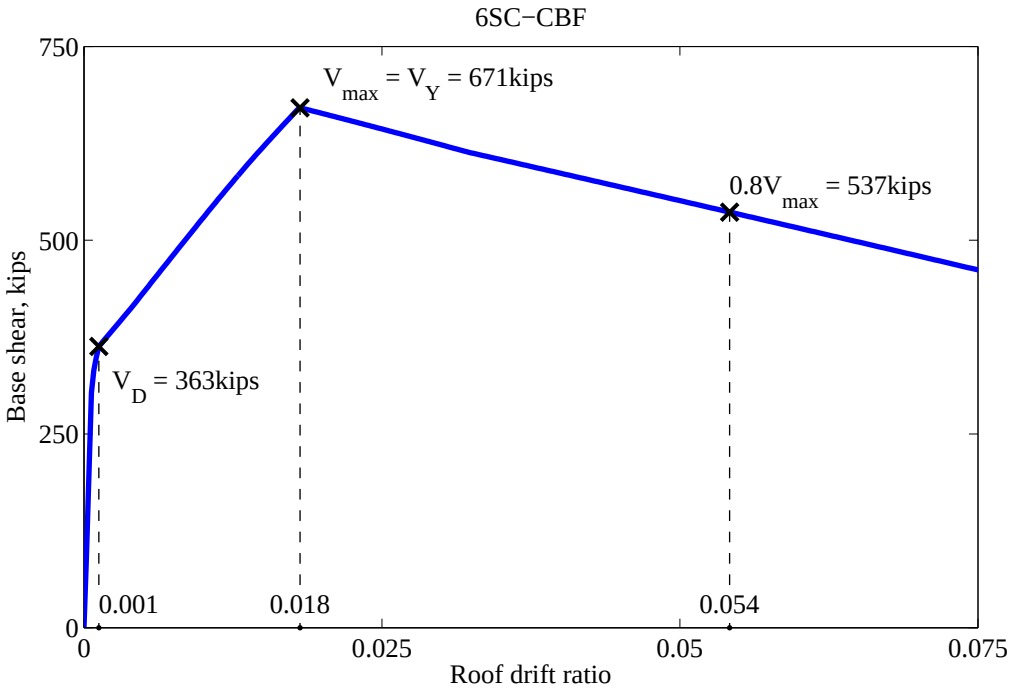

Figure 3.19: Pushover curve for 6SC-CBF archetype SLFRS

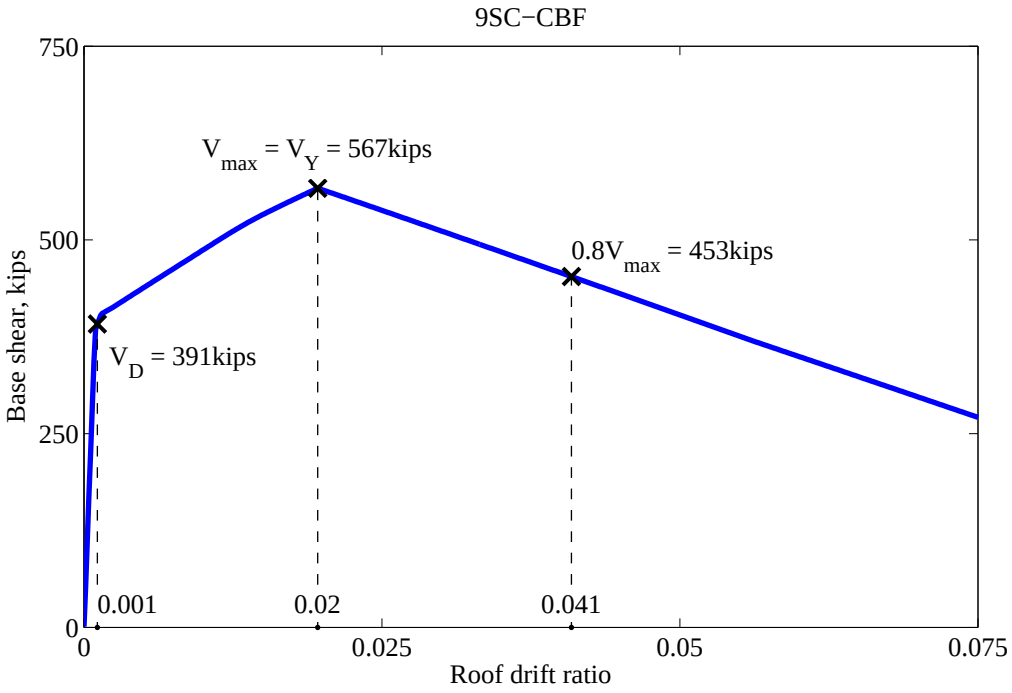

Figure 3.20: Pushover curve for 9SC-CBF archetype SLFRS

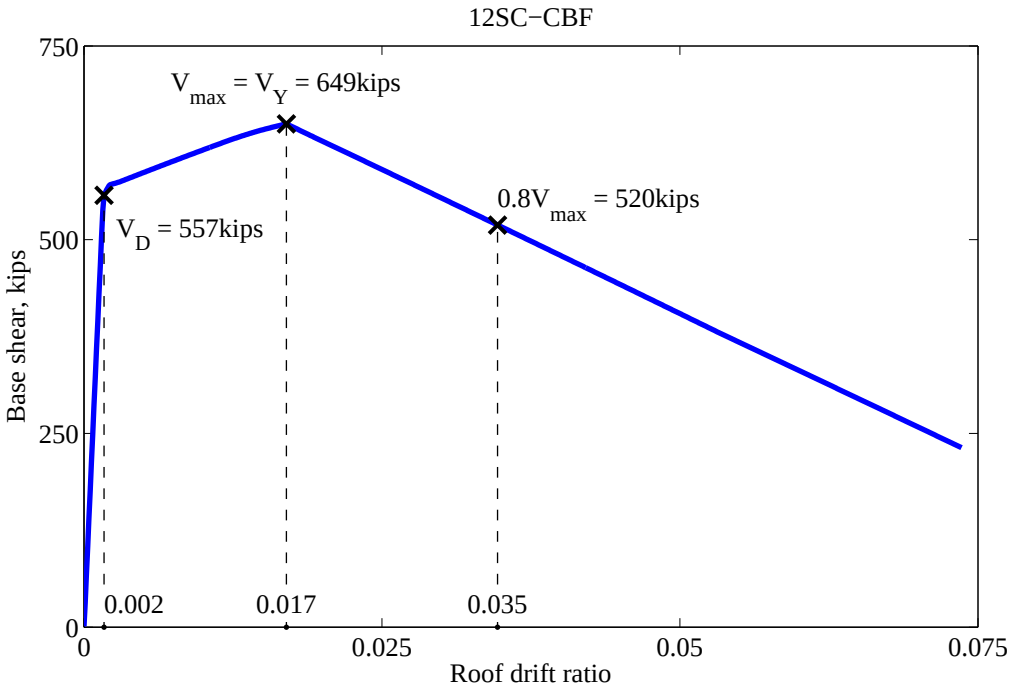

Figure 3.21: Pushover curve for 12SC-CBF archetype SLFRS

3.6 Evaluation of Overstrength Factor

The overstrength factor for a given archetype building, Ω, is defined from the nonlinear static pushover analysis, as the ratio of the maximum base shear, V_{max}, to the design base shear, V:

$$\Omega = \frac{V_{max}}{V} \tag{3.15}$$

The overstrength factors for the archetype buildings are given in Table 3.22. In calculating Ω for the SC-CBF system, the base shear at column decompression (V_D) is used as the design base shear, V, and the base shear at the PT bar yielding is used as V_{max}. It can be seen that Ω reduces as the number of stories increases. This is due to the increase of the design pre-stressing ratio r_{PT} as the height of the archetype building increases (see Table 3.14). An increase in the PT bar pre-stressing ratio increases V_D, but not $V_{max} = V_Y$.

Table 3.22: Overstrength factor for archetype buildings

Archetype building	V (kips)	V_{max} (kips)	Ω
4SCBF	510	1655	3.2
6SCBF	787	2072	2.6
9SCBF	1000	2062	2.1
12SCBF	1084	2113	1.9
4SC-CBF	306	711	2.3
6SC-CBF	363	671	1.8
9SC-CBF	391	567	1.5
12SC-CBF	557	649	1.2

3.7 Incremental Dynamic Analysis

In this research, the damage assessment of the archetype buildings is done using incremental dynamic analysis (IDA). In an IDA, an individual ground motion record is scaled to increasing intensities and nonlinear response history analyses are performed at each intensity, until the global instability of the system (i.e., system collapse) is reached. An IDA curve (constructed for a structural system subjected to a single ground motion record) is a plot of a selected hazard intensity measure (IM) versus a selected engineering demand parameter (EDP). In this reseach, the 5% damped spectral acceleration at the approximate fundamental period T (see Table 3.3) of the building, $S_a(T, 5\%)$, is used as the IM. In most IDA plots presented here, the maximum story drift ratio, θ_m, is used as the EDP. However, for damage analyses that include damage states other than building collapse, other appropriate EDP parameters are used (as discussed in Chapters 5 and 6) . Other choices of IM and EDP (such as peak ground acceleration and peak floor acceleration) have been used by others [86].

3.7.1 Ground motion records

The ground motion records used for the IDA and other nonlinear response history analyses in this research are from the Far-Field record set documented in the FEMA P695 methodology document [23]. The Far-Field record set consists of 22 pairs of horizontal ground motion records from sites located no closer than 10 km from the fault rupture. The pairs of ground motion records consists of orthogonal horizontal components. The total number of ground motion records is 44. The records are from large-magnitude events (M $\geq$ 6.5) and are mostly from either strike-slip or reverse rupture sources. Only ground motions recorded on site class C or D are used. No more than two pairs of ground motion records from an earthquake event are selected. Other criteria for record selection can be found in Appendix A of FEMA P695 [23].

3.7.2 Ground motion scaling

The scaling procedure outlined in FEMA P695 consists of two steps: (i) normalization of the ground motion records and (ii) scaling of the ground motion record set. To remove unwanted variability between records due to differences in event magnitude, distance to source, etc., the ground motion records are normalized using the geometric mean of peak ground velocity (PGV) values of the two horizontal components of each ground motion pair in the set [23]. One normalization factor is defined for the two horizontal components of each ground motion pair as the ratio of the median of the geometric means of the PGV values for all the ground motion pairs in the record set divided by the geometric mean of the PGV values for each record pair [23].

After normalization, the ground motion record set is scaled up (or down) collectively to match the IM of interest. One scaling factor is calculated to scale all the ground motion records (in the set) so that the median IM (i.e., $S_a(T,5\%)$) matches the IM of interest. In

an IDA, the scaling is repeated incrementally. For a collapse assessment based on FEMA P695 [23] the records are scaled up (and the IDAs are conducted) to the point that the archetype building reaches the collapse point under 50% of the ground motion records.

3.7.3 IDA results

The results of the IDA for the SCBF archetype SLFRS are shown in Figure 3.22 through Figure 3.25. The results of the IDA for the SC-CBF archetype SLFRS are shown in Figure 3.26 through Figure 3.29. As stated earlier, these results for the archetype SLFRS are taken as the results for the archetype building. Each data point shown in Figure 3.22 through Figure 3.29 represent a nonlinear response history analysis result for an archetype SLFRS (or archetype building), under an individual ground motion record, and at a given IM value. In Chapter 4, these IDA results are used for a collapse performance evaluation of the archetype buildings. Collapse points are determined and collapse fragility curves are constructed for each archetype building.

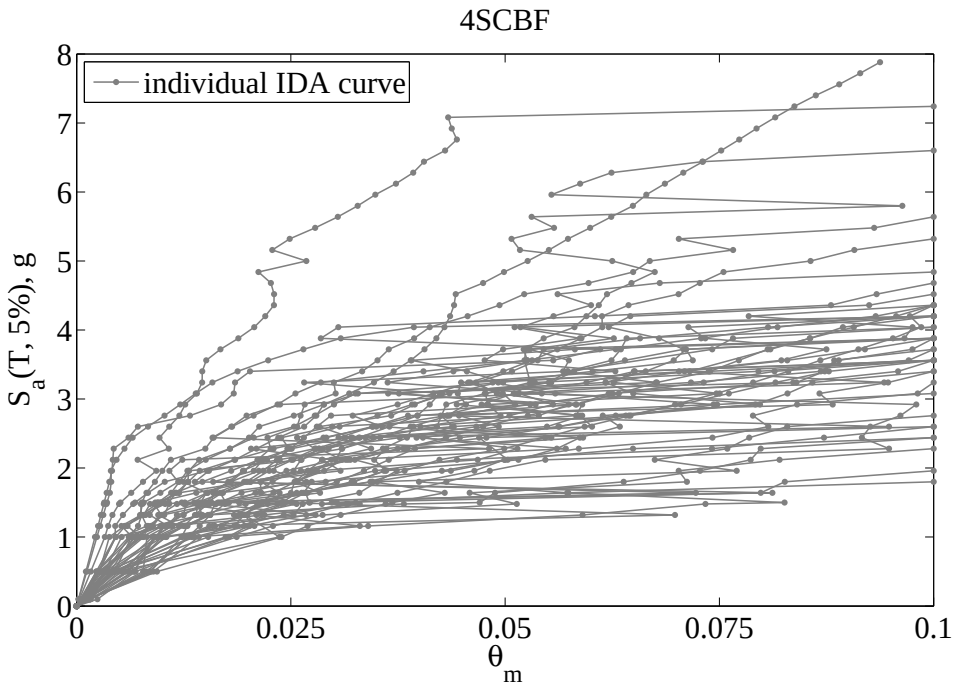

Figure 3.22: IDA results for 4SCBF archetype building

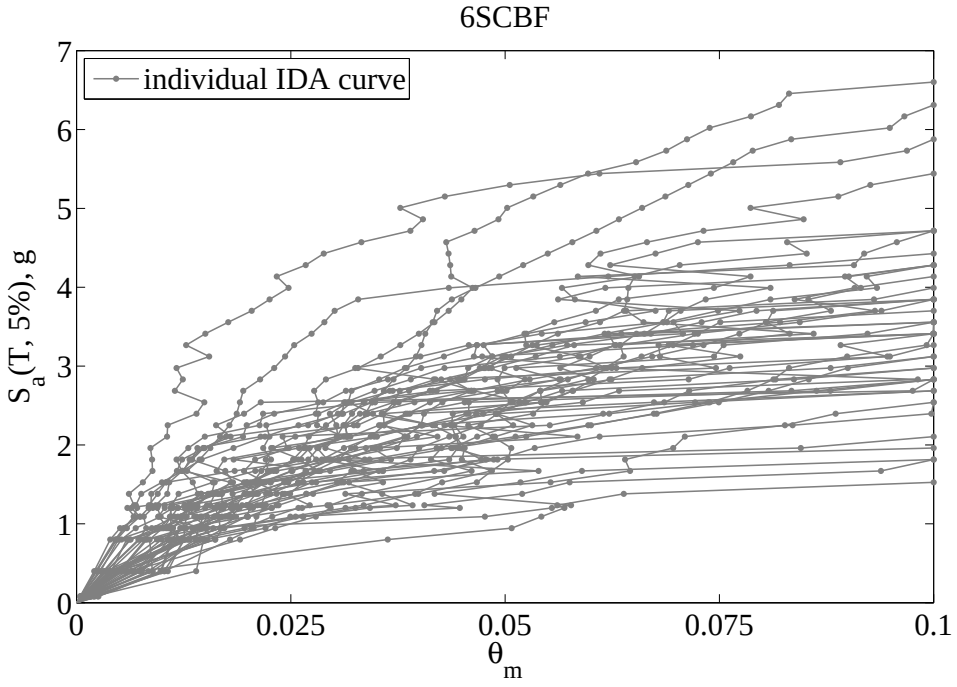

Figure 3.23: IDA results for 6SCBF archetype building

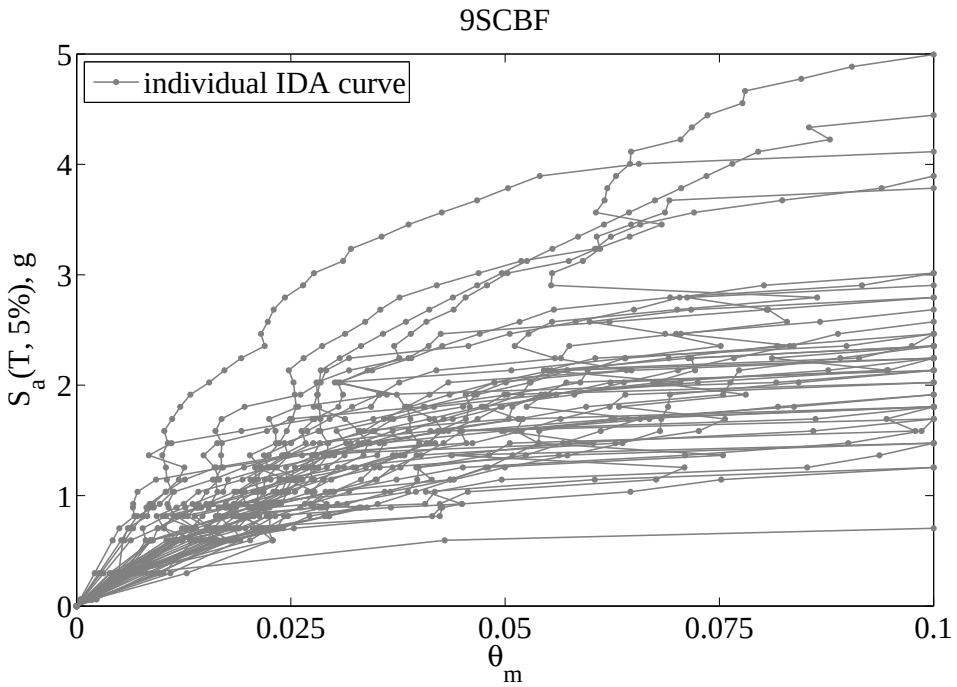

Figure 3.24: IDA results for 9SCBF archetype building

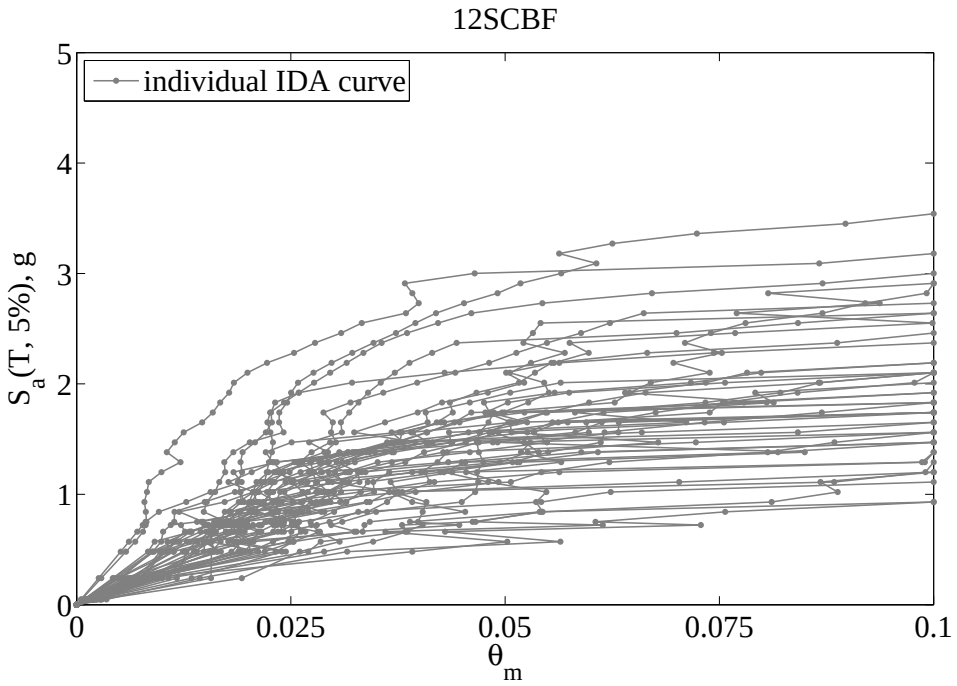

Figure 3.25: IDA results for 12SCBF archetype building

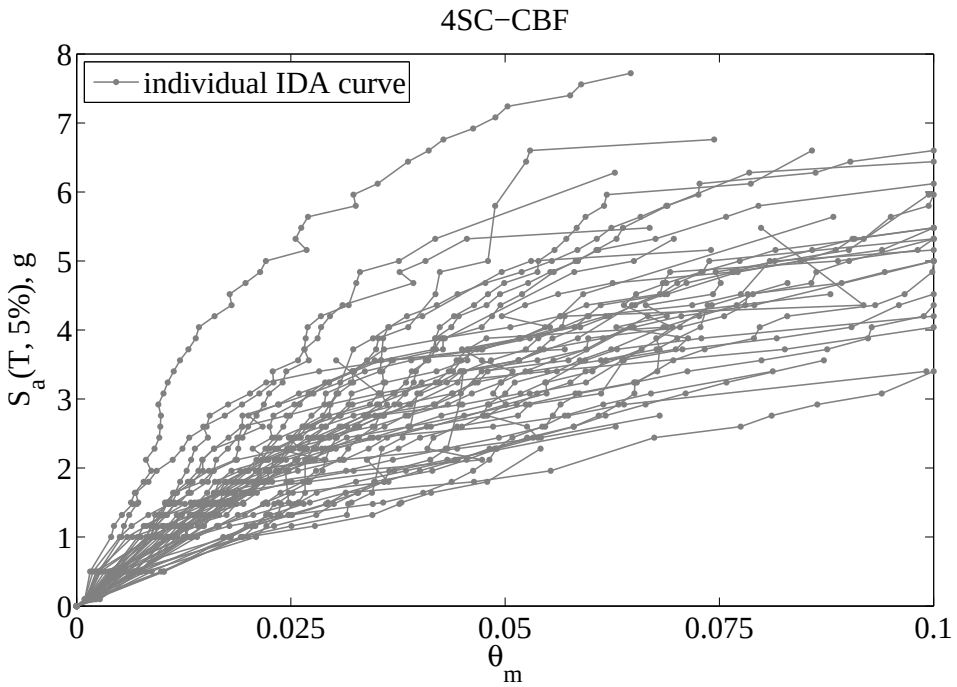

Figure 3.26: IDA results for 4SC-CBF archetype building

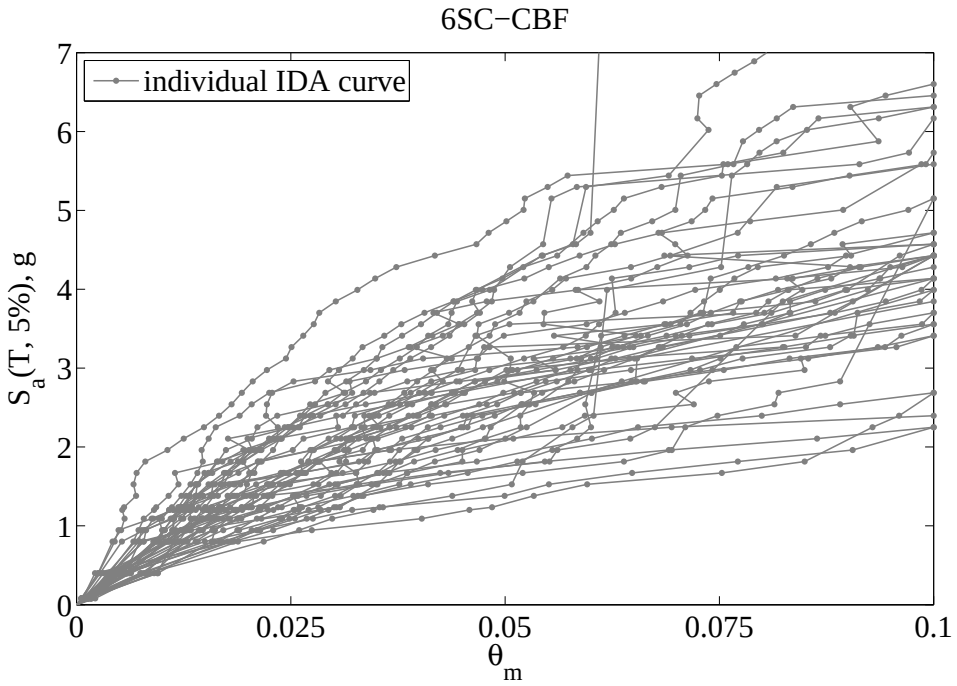

Figure 3.27: IDA results for 6SC-CBF archetype building

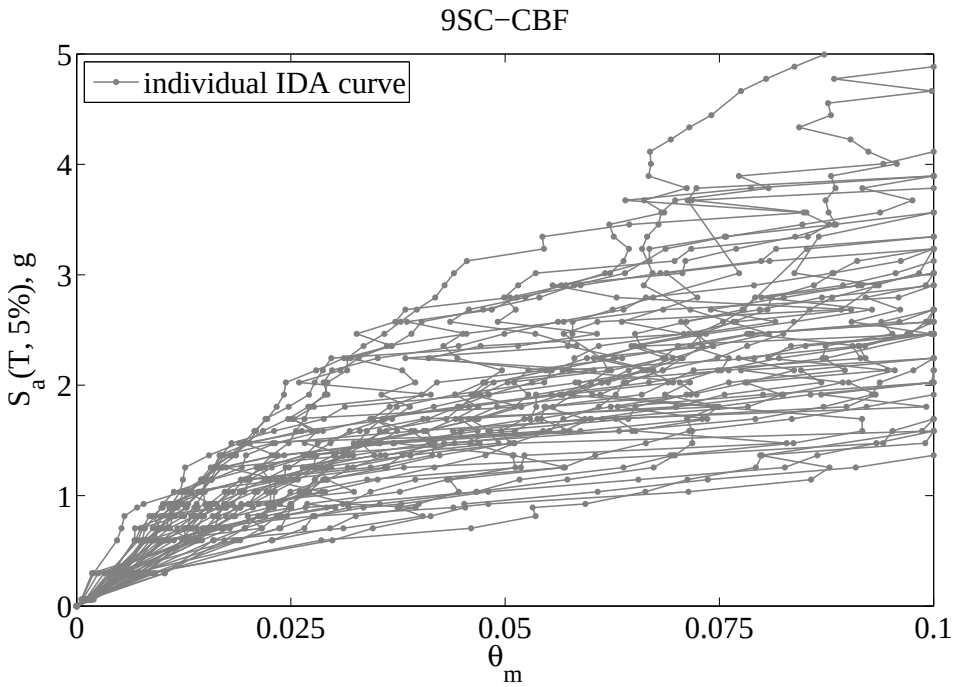

Figure 3.28: IDA results for 9SC-CBF archetype building

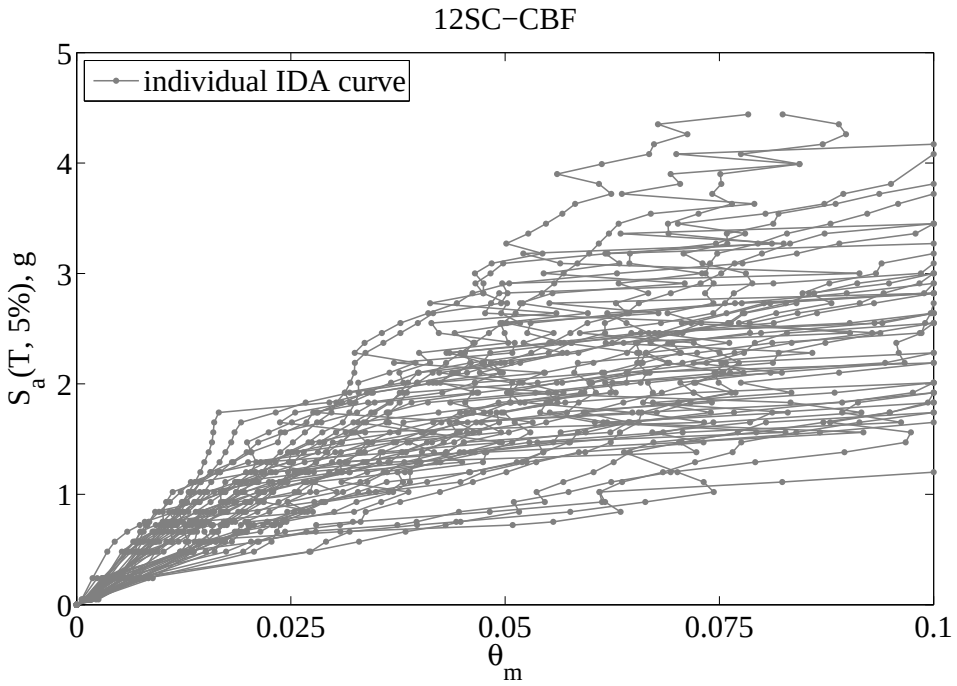

Figure 3.29: IDA results for 12SC-CBF archetype building

Chapter 4

Performance Evaluation of SCBF and SC-CBF Archetype Buildings

4.1 Introduction

The seismic performance of the SCBF and SC-CBF archetype buildings is evaluated and compared in this chapter following the guidelines of FEMA P695 [23]. Using the incremental dynamic analysis (IDA) results, the median collapse capacity is determined and collapse margin ratios (CMR) are calculated for the SCBF and SC-CBF archetype buildings in accordance with FEMA P695 document methodology [23]. The total uncertainty in the collapse capacity is estimated based on factors considered by FEMA P695 [23]. Adjusted collapse margin ratios (ACMR) are estimated by considering the effect of the spectral shape of the ground motion record set used for conducting the IDAs [23]. The estimated ACMR values for the SCBF and SC-CBF archetype buildings are compared against the acceptable ACMR values, determined using the FEMA P695 [23] guidelines. The effect of varying the collapse damage state criteria on the ACMR values is discussed. Finally, distributions of residual story drift ratio at three hazard intensity measure (IM) values are presented and compared for the SCBF and SC-CBF archetype buildings.

4.2 Collapse Fragility Curve

A collapse fragility curve is a cumulative distribution function (CDF), showing the probability of exceeding the collapse capacity at a given IM value. Collapse of a building subjected to an earthquake ground motion record, scaled to a given IM value, can be defined as global instability of the building during a nonlinear response history analysis. The collapse capacity of a building can be quantified as the IM value at which the building becomes globally unstable. This is an IM-based method for quantifying the collapse capacity. Building collapse can also be quantified using one or more appropriate engineering demand parameters (EDP) such as the maximum story drift ratio (known as an EDP-based method). The EDP-based method of quantifying collapse is discussed in later chapters. In this chapter, the IM-based method of quantifying collapse is used. The $S_a(T,5\%)$ value at which the building collapses, i.e., the IM-based collapse capacity, is denoted by $S_{a,C}$. Here, T used in $S_a(T,5\%)$ is the approximate fundamental period of the building (per FEMA P695 [23]), as defined in Chapter 3.

The point in an individual IDA curve corresponding to collapse of a building (i.e., the building collapse point) needs to be established before the collapse capacity can be evaluated. The collapse point for an individual IDA curve of $S_a(T,5\%)$ versus the maximum story drift ratio (θ_m) is defined as the point at which the slope of the curve reduces considerably and the IDA curve flattens. Flattening of the IDA curve (i.e., the collapse point) is quantified in FEMA 355F [22] as a reduction in the slope of the curve with respect to the median initial slope of the ($S_a(T,5\%)$ versus θ_m) IDA curves for the ground motion record set (denoted by S_e). FEMA 355F [22] specifies an 80% reduction in the slope of an individual IDA curve (compared to S_e) as the limit for building collapse. For the current discussion, when the slope of an individual IDA curve reaches 20% of S_e (i.e., reduces to 80% of S_e as described in FEMA 355F [22]) and does not increase to more than 20% of S_e

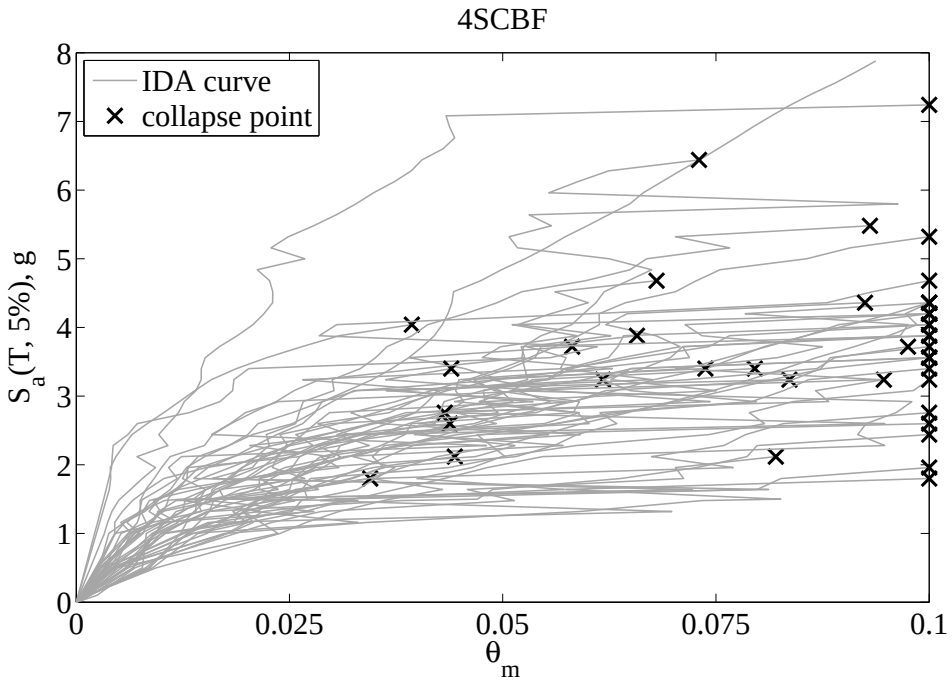

Figure 4.1: IDA results and collapse points for 4SCBF archetype building

for larger $S_a(T,5\%)$ values, the collapse point is established. Later, other slope reduction values in a range around 20% are considered as alternative collapse points. An additional collapse criterion of a limit on θ_m of 0.1 radians from FEMA P695 [23] is used along with the slope reduction criterion. That is, $\theta_m = 0.1$ is the collapse point if the slope is greater than or equal to 20% of S_e up to $\theta_m = 0.1$. Collapse points, established using these two criteria (i.e., 80% slope reduction and $\theta_m = 0.1$), from the IDA results for the archetype buildings are shown in Figure 4.1 through Figure 4.8.

The probability distribution for the collapse capacity is assumed to follow a lognormal distribution [17]. Therefore, a lognormal distribution was fit to the $S_{a,C}$ values obtained from the IDA results for each archetype building to produce a smooth collapse fragility curve. The estimated median of $S_{a,C}$ values, denoted as $\tilde{S}_{a,C}$, and the logarithmic standard deviation of the $S_{a,C}$ values, denoted as $\sigma_{\ln S_{a,C}}$, used for fitting a lognormal distribution to the $S_{a,C}$ values, are as follows:

$$\tilde{S}_{a,C} = e^{E(\ln S_{a,C})} \tag{4.1}$$

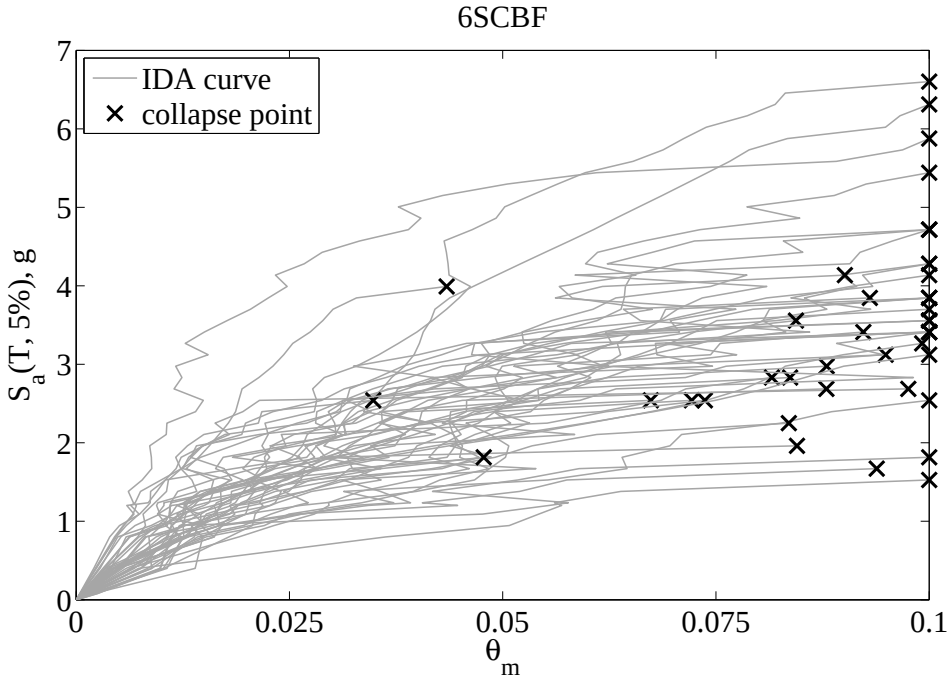

Figure 4.2: IDA results and collapse points for 6SCBF archetype building

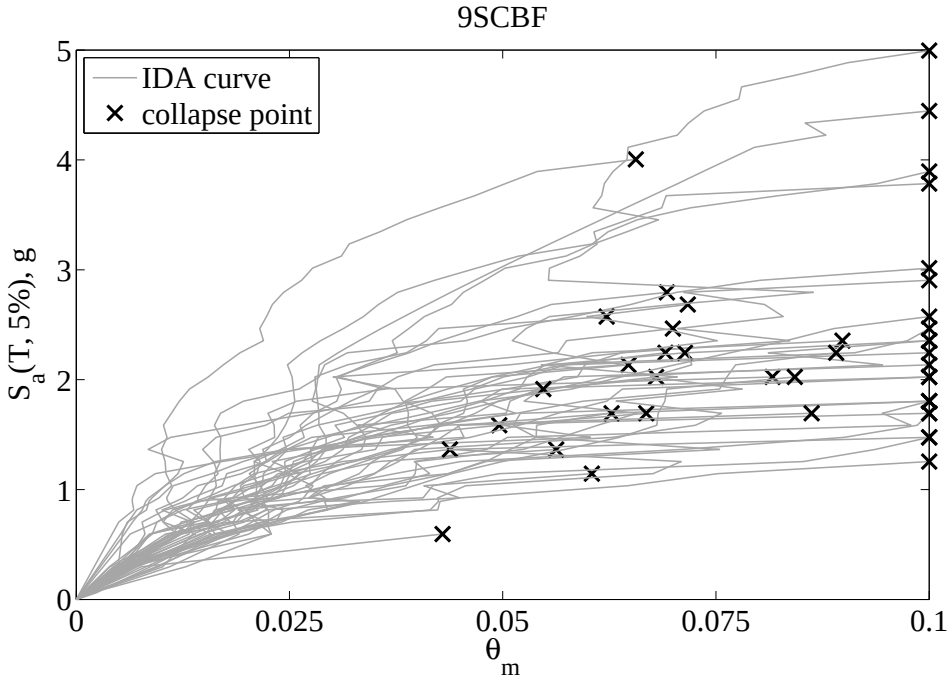

Figure 4.3: IDA results and collapse points for 9SCBF archetype building

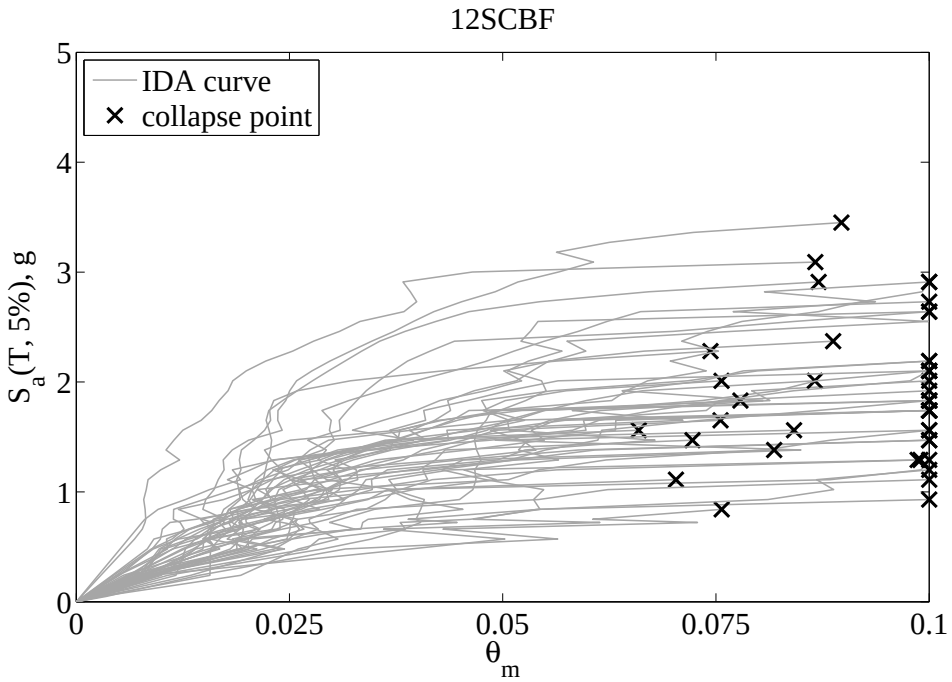

Figure 4.4: IDA results and collapse points for 12SCBF archetype building

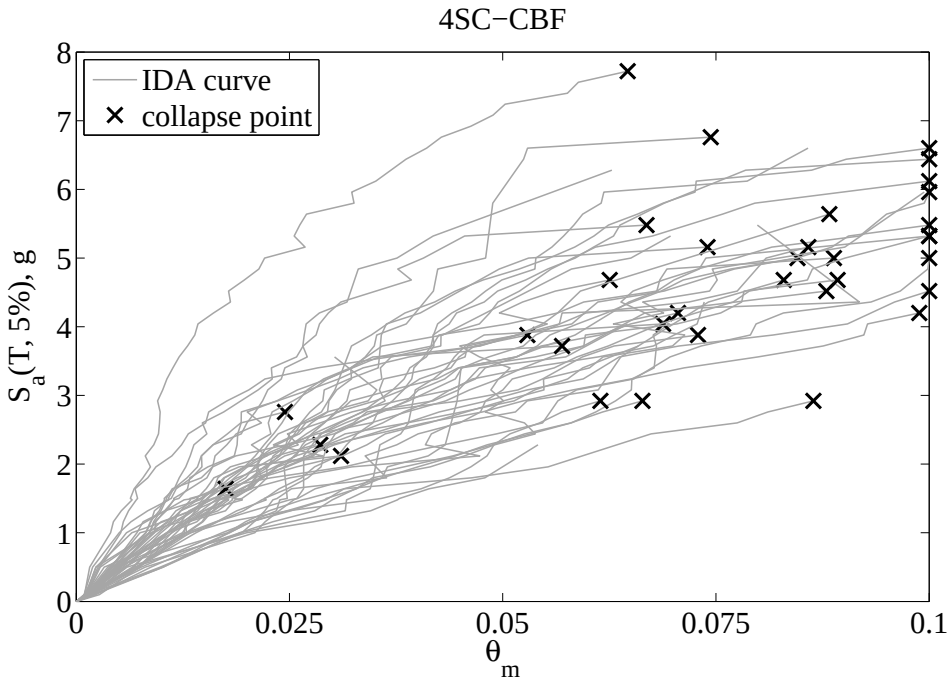

Figure 4.5: IDA results and collapse points for 4SC-CBF archetype building

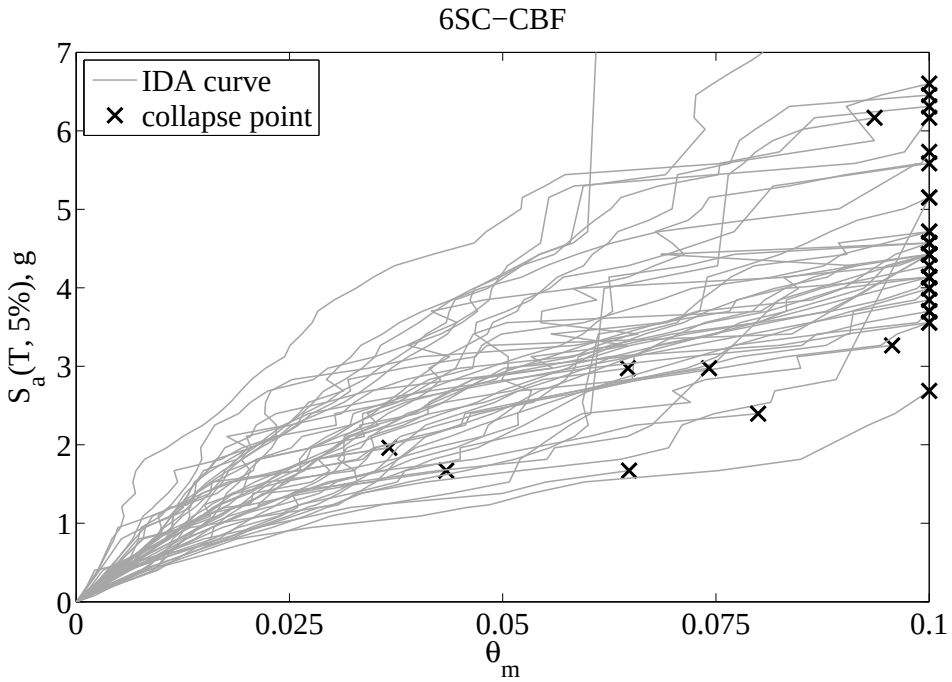

Figure 4.6: IDA results and collapse points for 6SC-CBF archetype building

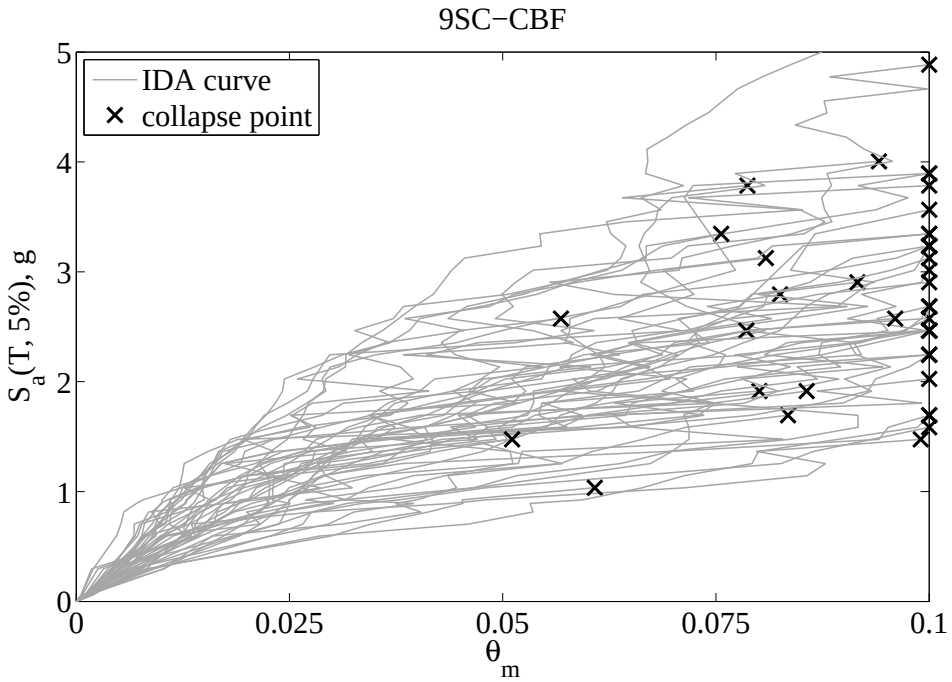

Figure 4.7: IDA results and collapse points for 9SC-CBF archetype building

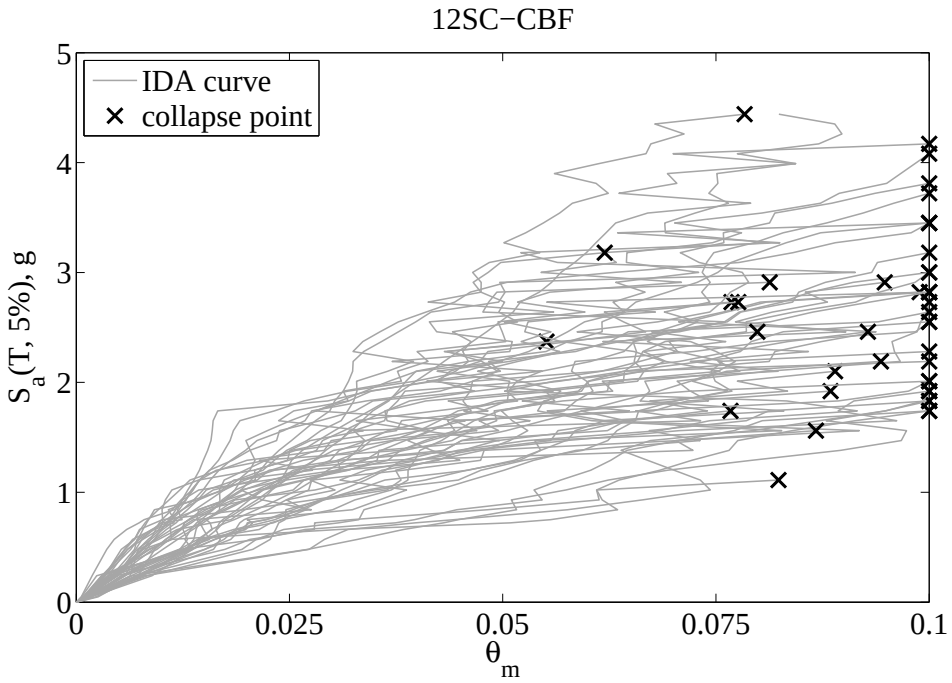

Figure 4.8: IDA results and collapse points for 12SC-CBF archetype building

$$\sigma_{\ln S_{a,C}} = \sqrt{Var(\ln S_{a,C})} \tag{4.2}$$

where $E(\ln S_{a,C})$ is the expected value of the natural logarithm of the $S_{a,C}$ values and $Var(\ln S_{a,C})$ is the variance of the natural logarithm of the $S_{a,C}$ values. The $\tilde{S}_{a,C}$ values and $\sigma_{\ln S_{a,C}}$ values for the archetype buildings are given in Table 4.1. It can be seen from Table 4.1 that the $\tilde{S}_{a,C}$ values for the SC-CBF archetype buildings are greater than the $\tilde{S}_{a,C}$ values for the SCBF archetype buildings.

A smooth collapse fragility curve for an archetype buildings is the cumulative distribution function (CDF) of the fitted lognormal distribution to the $S_{a,C}$ values for the archetype building. The smooth collapse fragility curves for the SCBF archetype buildings are shown in Figure 4.9 through Figure 4.12. The smooth collapse fragility curves for the SC-CBF archetype buildings are shown in Figure 4.13 through Figure 4.16. The collapse data points shown in Figure 4.9 through Figure 4.16 are the "counting" probability of exceeding an $S_{a,C}$

Table 4.1: Median and logarithmic standard deviation for smooth collapse fragilities

Archetype building	$\tilde{S}_{a,C}$ (g)	$\sigma_{\ln S_{a,C}}$
4SCBF	3.53	0.309
6SCBF	3.30	0.339
9SCBF	2.10	0.382
12SCBF	1.81	0.322
4SC-CBF	4.37	0.352
6SC-CBF	4.05	0.329
9SC-CBF	2.63	0.338
12SC-CBF	2.53	0.294

value (shown on the vertical axis) versus the $S_{a,C}$ values (shown on the horizontal axis). The dispersion of the fragility data shown in Figure 4.9 through Figure 4.16 represents the variability in structural response because of the variation of ground motion records, and is often called the record-to-record (RTR) variability.

4.3 Collapse Margin Ratio

The ratio between the *counting* median collapse capacity for a ground motion record set and the IM value corresponding to the maximum considered earthquake (MCE) is defined as the collapse margin ratio (*CMR*) in FEMA P695 [23].

According to FEMA P695 [23] the collapse margin ratio for an archetype building is based on the "counting" median of the collapse capacities, i.e., the counting median of the $S_{a,C}$ values. The smallest $S_{a,C}$ value at which at least half of the ground motion records cause collapse of the archetype building is considered the counting median collapse capacity and is denoted by $\hat{S}_{CT}$. Note that the $\hat{S}_{CT}$ value is different from the $\tilde{S}_{a,C}$ value as the $\hat{S}_{CT}$ value is determined by counting the $S_{a,C}$ values while $\tilde{S}_{a,C}$ is calculated using Equation (4.1). The $\hat{S}_{CT}$ values for the archetype buildings are given in Table 4.2. It can be seen from Table 4.2 that $\hat{S}_{CT}$ values for the SC-CBF archetype buildings are greater than

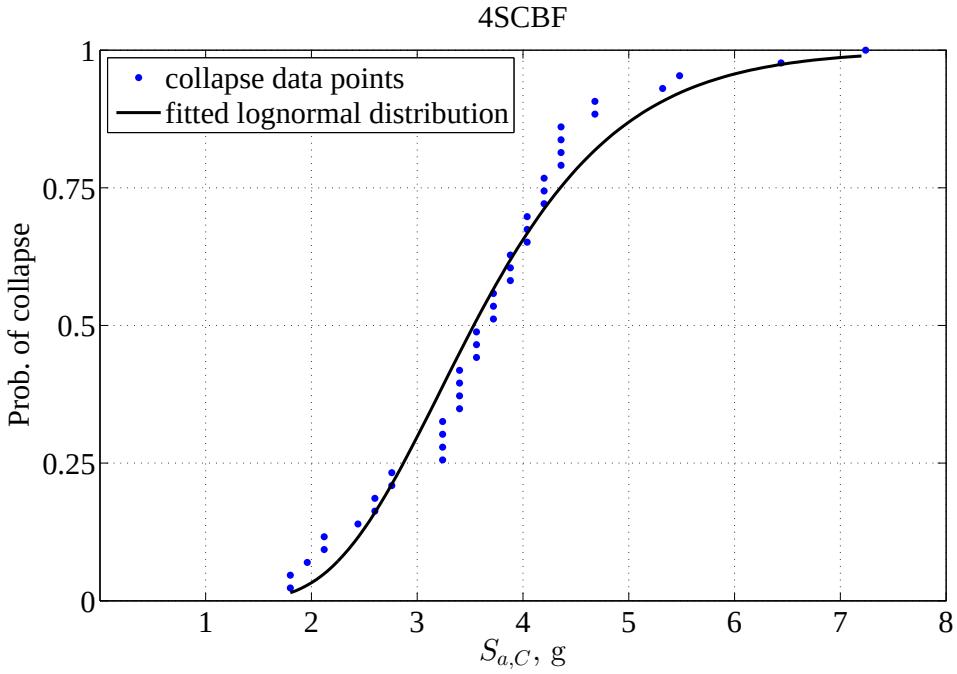

Figure 4.9: Smooth collapse fragility curve for 4SCBF archetype building

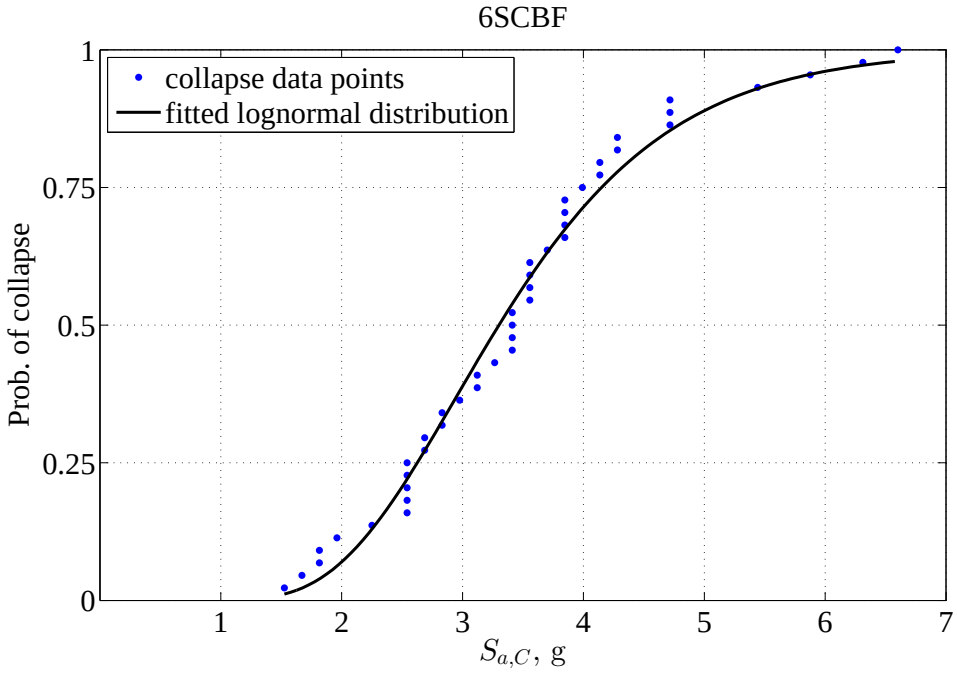

Figure 4.10: Smooth collapse fragility curve for 6SCBF archetype building

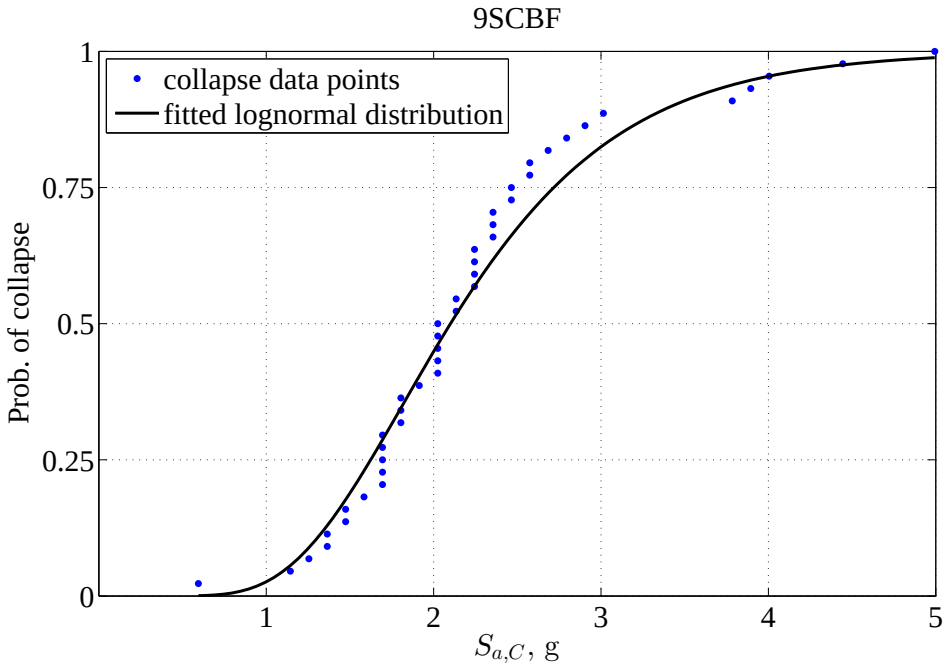

Figure 4.11: Smooth collapse fragility curve for 9SCBF archetype building

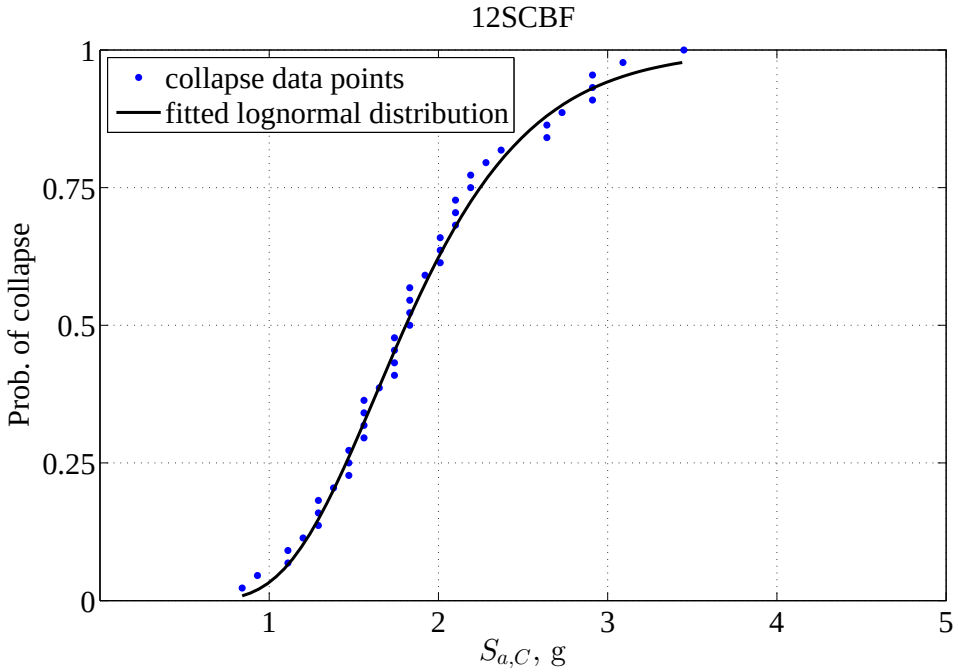

Figure 4.12: Smooth collapse fragility curve for 12SCBF archetype building

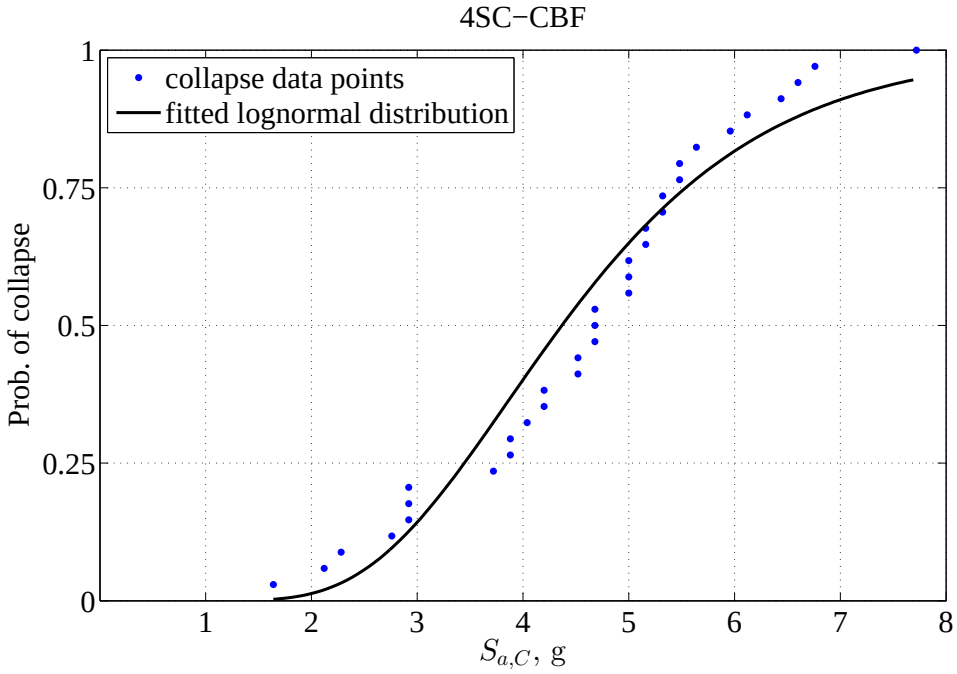

Figure 4.13: Smooth collapse fragility curve for 4SC-CBF archetype building

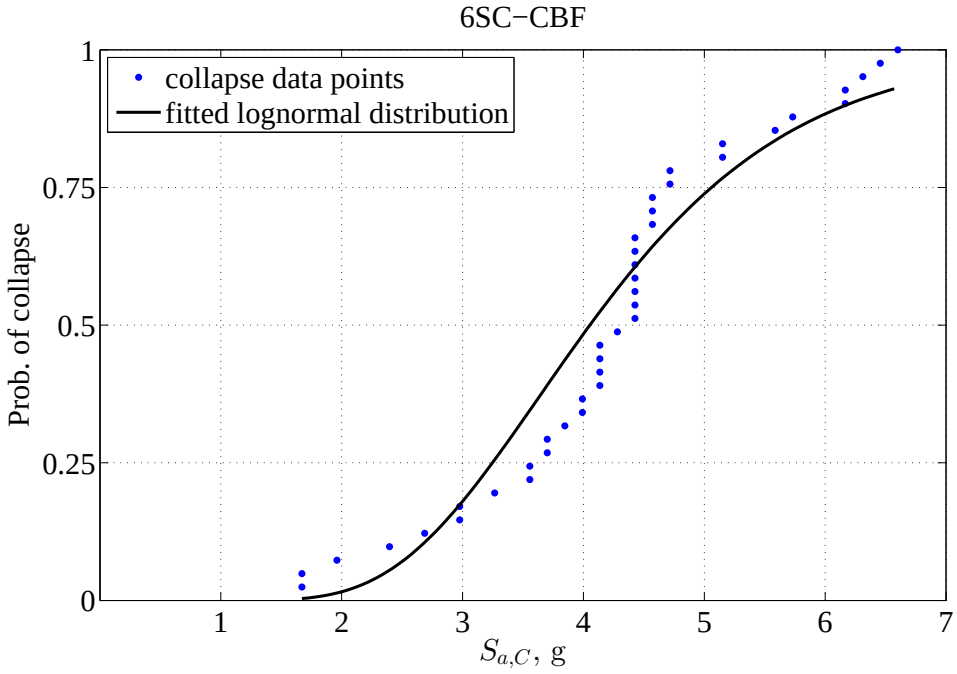

Figure 4.14: Smooth collapse fragility curve for 6SC-CBF archetype building

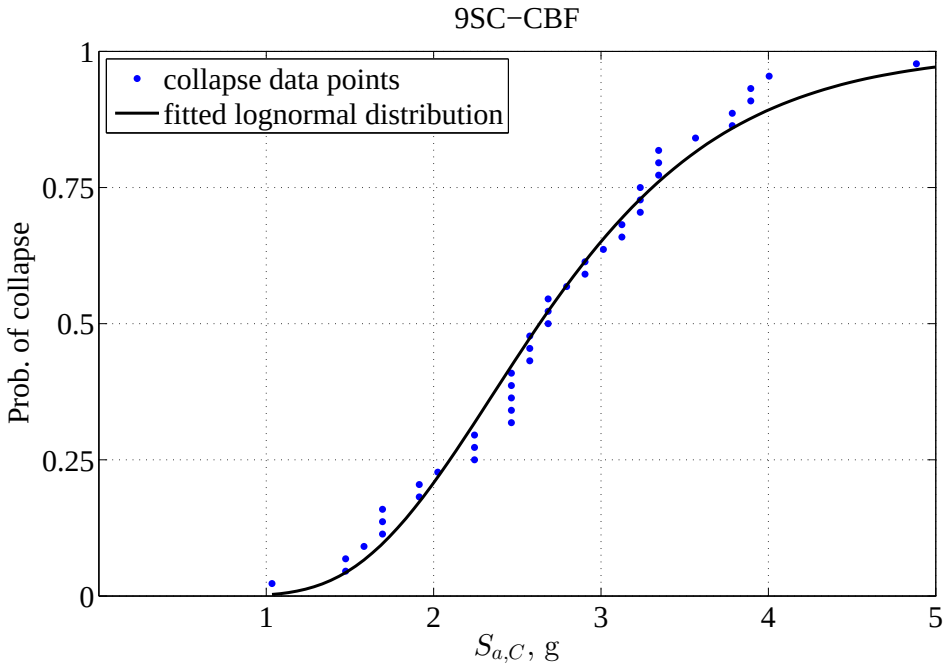

Figure 4.15: Smooth collapse fragility curve for 9SC-CBF archetype building

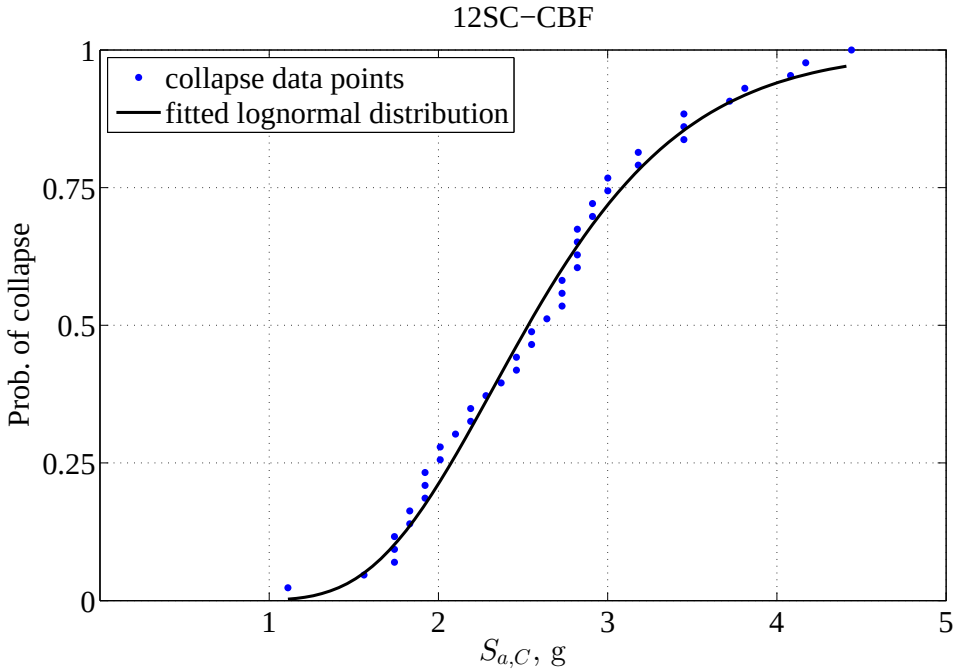

Figure 4.16: Smooth collapse fragility curve for 12SC-CBF archetype building

Table 4.2: Median collapse capacity and collapse margin ratio values for archetype buildings

Archetype building	$\hat{S}_{CT}$ (g)	S_{MT} (g)	*CMR*	*ACMR*
4SCBF	3.72	1.50	2.48	2.60
6SCBF	3.41	1.20	2.84	3.98
9SCBF	2.02	0.89	2.27	3.21
12SCBF	1.83	0.72	2.54	3.51
4SC-CBF	4.68	1.50	3.12	4.21
6SC-CBF	4.43	1.20	3.69	5.16
9SC-CBF	2.68	0.89	3.02	4.40
12SC-CBF	2.64	0.72	3.67	5.65

the $\hat{S}_{CT}$ values for the SCBF archetype buildings.

The $S_a(T, 5\%)$ value at the MCE intensity is denoted by S_{MT}. The collapse margin ratio, *CMR*, is defined as follows [23]:

$$CMR = \frac{\hat{S}_{CT}}{S_{MT}} \tag{4.3}$$

Values of $\hat{S}_{CT}$, S_{MT}, and *CMR* for the the archetype buildings are given in Table 4.2. It can be seen from Table 4.2 that the *CMR* values for the SC-CBF archetype buildings are all greater that the *CMR* values for the SCBF archetype buildings. This result shows that the rocking and self-centering features of the SC-CBF system, which are the main reasons for the damage-free characteristic of the SC-CBF system, do not reduce the margin against collapse of the system, but actually increases the margin against collapse.

4.3.1 Adjusted collapse margin ratio

The spectral shape of the ground motion record set can affect the set of IDA curves used in a collapse assessment and the resulting collapse capacity. Studies by Baker [6, 7], Goulet [27], Haselton [29], and Zareian [92] focused on the effect of spectral shape on the collapse capacity of structural systems. This previous work shows that the shape of the response

spectrum for a rare ground motion with a large IM value decreases more rapidly at periods both greater than and less than the period of interest, as compared to the spectra of less rare ground motions with smaller IM values. More details about the effect of spectral shape can be found in FEMA P695 [23]. To account for the effect of the spectral shape, the *CMR* values are modified by a spectral shape factor (*SSF*) to determine the adjusted collapse margin ratio (*ACMR*) as follows:

$$ACMR = SSF \times CMR \tag{4.4}$$

One of the parameters needed to calculate *SSF* is the period-based ductility, μ_T, which is defined as follows:

$$\mu_T = \frac{\delta_u}{\delta_{y,eff}} \tag{4.5}$$

where δ_u is the ratio of ultimate roof displacement (which is established from the pushover analysis results presented in Chapter 3) and $\delta_{y,eff}$ is the effective yield roof displacement. $\delta_{y,eff}$ represents the effective roof displacement for an elastic system loaded to the maximum base shear capacity of the system. The value of $\delta_{y,eff}$ can be found using the following equation [23]:

$$\delta_{y,eff} = C_0 \frac{V_{max}}{W} \left(\frac{g}{4\pi^2}\right) (\max(T, T_1))^2 \tag{4.6}$$

where C_0 is a modification factor to relate the displacement of an equivalent single degree-of-freedom system to the roof displacement of the building, determined from Table 3-2 of ASCE/SEI 41-6 [15], V_{max} is the maximum base shear (which is established from the pushover analysis results presented in Chapter 3), W is seismic weight of the building, T is the fundamental period of the building (calculated using Equation 3.1), and T_1 is undamped first mode period of the structural model computed using an eigenvalue analysis.

Using μ_T, the *SSF* values can be found from Appendix B of FEMA P695 [23]. The values of C_0, $\delta_{y,eff}$, μ_T, *SSF* and other related parameters for calculation of *SSF* are given

Table 4.3: Parameters for calculation of SSF

Archetype building	C_0	V_{max} (kips)	W (kips)	$max(T, T_1)$ (sec)	$\delta_{y,eff}$ (in)	δ_u (in)	μ_T	SSF
4SCBF	1.35	1655	3316	0.56	2.1	3.9	1.9	1.05
6SCBF	1.42	2072	4972	0.75	3.3	49.1	15.1	1.40
9SCBF	1.48	2062	7455	1.08	4.6	30.0	6.5	1.41
12SCBF	1.50	2113	9939	1.54	7.4	34.1	4.6	1.38
4SC-CBF	1.35	711	3316	0.56	0.9	38.9	43.8	1.35
6SC-CBF	1.42	671	4972	0.75	1.1	60.3	57.2	1.40
9SC-CBF	1.48	567	7455	1.01	1.1	58.5	52.1	1.46
12SC-CBF	1.50	649	9939	1.25	1.5	66.4	44.3	1.54

in Table 4.3.

The $\delta_{y,eff}$ values for the SC-CBF archetype buildings given in Table 4.3 are considerably smaller that the $\delta_{y,eff}$ values for the SCBF archetype buildings. Among the four variables C_0, V_{max}, W, and $max(T, T_1)$ in Equation (4.6), V_{max} varies the most between the SCBF archetype buildings and the SC-CBF archetype buildings. The C_0 and W values are identical for the SCBF and SC-CBF archetype buildings with the same number of stories. The $max(T, T_1)$ values are also identical for the SCBF and SC-CBF archetype buildings with 4 and 6 number of stories. The $max(T, T_1)$ value of 1.08 seconds for the 9SCBF archetype building is close to the $max(T, T_1)$ value of 1.01 seconds for the 9SC-CBF archetype building. The $max(T, T_1)$ value of 1.54 seconds for the 12SCBF archetype building is larger than the $max(T, T_1)$ value of 1.25 seconds for the 12SC-CBF archetype building. Therefore, the significant differences between the $\delta_{y,eff}$ values for the SCBF and SC-CBF archetype buildings (with the values being significantly smaller for the SC-CBF archetype buildings) are significantly affected by the differences between the V_{max} values for the SCBF and SC-CBF archetype buildings. δ_u is generally large for the SC-CBF archetype buildings (especially for the 4SC-CBF archetype building) and as a result of the difference in $\delta_{y,eff}$ and δ_u, μ_T is considerably large for the SC-CBF archetype buildings.

4.4 Uncertainty in Collapse Capacity

The actual collapse capacity of an archetype building depends on various uncertain parameters. A larger uncertainty in the collapse capacity requires a greater margin against collapse to ensure an acceptable probability of collapse at a given IM value. FEMA P695 [23] categorizes major sources of uncertainty related to the collapse capacity of a building into four independent types: (i) variability in structural response as the ground motion records are varied, also known as RTR variability (*RTR*); (ii) variability in design requirements (*DR*); (iii) variability in test data (TD); and (iv) variability in modeling (*MDL*). The MDL variability includes the effect of uncertain system parameters and uncertain parameters used for the numerical model used in the structural response history analyses (i.e., the IDAs).

The variability in $S_{a,C}$, shown by $\sigma_{\ln S_{a,C}}$ in Table 4.1, is an example of *RTR*. Previous research [30, 35, 92] using the FEMA P695 Far-Field ground motion record set led to a fixed value for uncertainty in the collapse capacity due to RTR variability as described in FEMA P695 [23]. This fixed value for the uncertainty in the collapse capacity for a system with $\mu_T \geq 3$ is given in the form of a logarithmic standard deviation (denoted with the symbol β) as $\beta_{RTR} = 0.4$. The $\sigma_{\ln S_{a,C}}$ values in Table 4.1 are between 0.3 and 0.4 (with the exception of the 12SC-CBF archetype building with $\sigma_{\ln S_{a,C}} = 0.297$, which is close to 0.3).

The total uncertainty in collapse capacity is calculated by combining *RTR*, *DR*,*TD*, and *MDL* uncertainties, represented by a random variable λ_{TOT}. The random variable S_{CT} is defined for each archetype building as follows [23]:

$$S_{CT} = \hat{S}_{CT}\lambda_{TOT} \tag{4.7}$$

where λ_{TOT} is assumed to be lognormally distributed with a median value of 1 and a logarithmic standard deviation of β_{TOT}. The random variable λ_{TOT} is defined as the product of

four other random variables, each representing one source of uncertainty as follows [23]:

$$\lambda_{TOT} = \lambda_{RTR}\lambda_{DR}\lambda_{TD}\lambda_{MDL} \tag{4.8}$$

where λ_{RTR}, λ_{DR}, λ_{TD}, and λ_{MDL} are assumed to be independent from each other and follow a lognormal distribution with a median value of 1 and a logarithmic standard deviation of β_{RTR}, β_{DR}, β_{TD}, and β_{MDL}, respectively [23]. Since λ_{RTR}, λ_{DR}, λ_{TD}, and λ_{MDL} are assumed to be independent from each other, the total collapse capacity uncertainty, combining the uncertainties from *RTR*, *DR*, *TD*, and *MDL* variabilities, is calculated using the square root of sum of the squares, as follows [23]:

$$\beta_{TOT} = \sqrt{\beta_{RTR}^2 + \beta_{DR}^2 + \beta_{TD}^2 + \beta_{MDL}^2} \tag{4.9}$$

According to FEMA P695 [23], the values of β_{DR}, β_{TD}, and β_{MDL} are determined using a quality rating scale of: (A) Superior, $\beta = 0.10$; (B) Good, $\beta = 0.20$; (C) Fair, $\beta = 0.35$; and (D) Poor, $\beta = 0.50$ [23]. In this research, the modeling quality is rated good ($\beta_{MDL} = 0.20$), quality of the design requirements is rated superior ($\beta_{DR} = 0.10$), and the quality of test data is rated good ($\beta_{TD} = 0.20$) for the SC-CBF archetype buildings. Similar ratings are assign for the SCBF archetype buildings. Using Equation (4.9), $\beta_{TOT} = 0.50$ for the SCBF and SC-CBF archetype buildings.

4.5 Acceptable Probability of Collapse

FEMA P695 [23] specifies an acceptable probability of collapse of 10% at the MCE hazard level for a group of related archetype buildings, called a performance group. Archetype buildings in each performance group have similarities in terms of important system param-

eters that impact the seismic behavior of the system (such as design seismic load intensity, fundamental period, building height, etc.). While the probability of collapse at the MCE hazard level (i.e., S_{MT}) for a performance group is 10%, the FEMA P695 [23] methodology accepts up to 20% probability of collapse at the MCE hazard level (S_{MT}) for an individual building archetype within the performance group. The acceptable *ACMR* corresponding to the 10% and 20% probability of collapse at the MCE hazard level are denoted by $ACMR_{10\%}$ and $ACMR_{20\%}$, respectively.

From the acceptable probability of collapse and the total system collapse capacity uncertainty, β_{TOT}, the minimum acceptable median collapse capacity can be determined. Using the minimum acceptable median collapse capacity and the IM value at the MCE (S_{MT}), the minimum acceptable *ACMR* can be found. In other words, given β_{TOT} and a 10% probability of collapse at the MCE hazard level, the minimum ACMR can be determined.

A summary of the collapse performance assessment of all the archetype buildings, including *ACMR*, $ACMR_{10\%}$, and $ACMR_{20\%}$, is given in Table 4.4. It can be seen from Table 4.4 that the *ACMR* values for all archetype buildings are larger than the $ACMR_{10\%}$ and $ACMR_{20\%}$ values. The *ACMR* value for the 4SCBF archetype building is smaller than that of the other archetype buildings because of the small *SSF* value for the 4SCBF archetype building. The smaller *SSF* value for the 4SCBF archetype building is caused by the small δ_u value from the pushover analysis of the 4SCBF archetype building.

4.6 Uncertainty in Collapse Criteria

The effect of uncertainty in the collapse criteria on the collapse capacity is studied in this section. As stated previously, two criteria for establishing the building collapse are: (i) a reduction in the slope of the IDA curve to 20% S_e; and (ii) a maximum story drift ratio $\theta_m = 0.1$. The 80% reduction in the slope, suggested in FEMA 355F [22], is a deterministic

Table 4.4: Adjusted collapse margin ratios and acceptable values for archetype buildings

Archetype building	*CMR*	*SSF*	*ACMR*	$ACMR_{10\%}$	$ACMR_{20\%}$
4SCBF	2.48	1.05	2.60	1.47	1.29
6SCBF	2.84	1.40	3.98	1.90	1.52
9SCBF	2.27	1.41	3.21	1.90	1.52
12SCBF	2.54	1.38	3.51	1.90	1.52
4SC-CBF	3.12	1.35	4.21	1.90	1.52
6SC-CBF	3.69	1.40	5.16	1.90	1.52
9SC-CBF	3.02	1.46	4.40	1.90	1.52
12SC-CBF	3.67	1.54	5.65	1.90	1.52

value. This means that for a given ground motion record, the probability of collapse varies from 0 to 1 at the IM value when the 80% slope reduction criterion is reached.

In this study of the uncertainty in the collapse criteria, the slope reduction criterion for collapse is varied from 70% to 90% (i.e., the slope reduces to a limit ranging from 30% to 10% of S_e) and the limiting value of θ_m at collapse is varied from 2% to 10%. The collapse capacity of each archetype building is established for all combinations of the slope reduction limit and the θ_m limit. The variation of the *ACMR* values, corresponding to the collapse capacities, considering the variation of the slope reduction criterion are shown in Figures 4.17 through 4.20 for the SCBF archetype buildings and in Figures 4.21 through 4.24 for the SC-CBF archetype buildings. Five curves, labeled $\theta_m = 0.02$, 0.04, 0.06, 0.08, 0.10, are shown in Figures 4.17 through 4.24. The collapse capacity (and the corresponding *ACMR*) values for data points of each line are determined using the θ_m limit value and the slope reduction limit shown on the horizontal axis. Also shown in Figures 4.17 through 4.24 are the $ACMR_{10\%}$ and $ACMR_{20\%}$ values.

The change in the *ACMR* values as the slope reduction limit varies for $\theta_m = 0.02$, 0.04, and 0.06 is small. Small changes in the *ACMR* value are observed for $\theta_m = 0.04$ and 0.06 for the 4SCBF archetype building, for $\theta_m = 0.06$ for the 6SCBF archetype building, for $\theta_m = 0.04$ and 0.06 for the 9SCBF archetype building, and for $\theta_m = 0.06$ for the 4SC-CBF

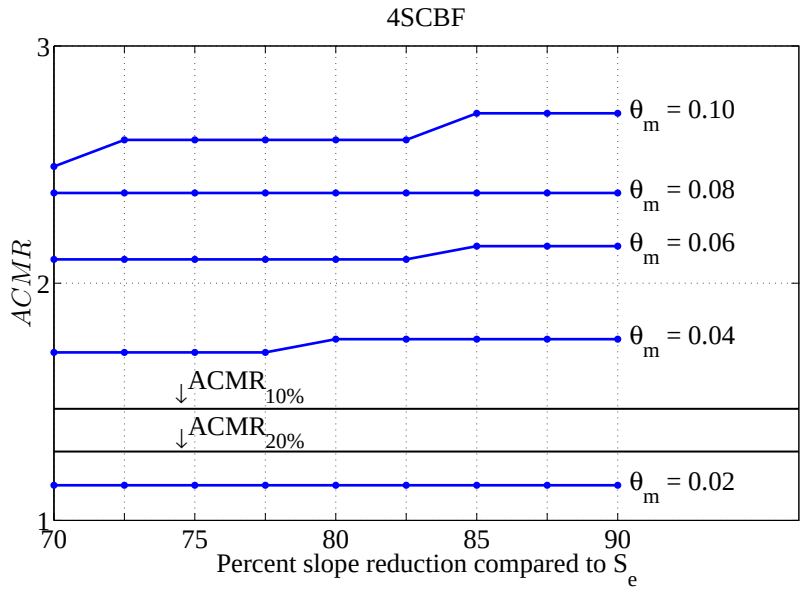

Figure 4.17: Variation of *ACMR* with variation of collapse criteria for 4SCBF archetype building

archetype building. These small changes (or no change) indicates that the limit θ_m values of 0.02, 0.04, and 0.06 control the building collapse when used in conjunction with a slope reduction limit ranging from 70% to 90%. The *ACMR* values change more significantly for cases with $\theta_m = 0.08$ and 0.10 as the slope reduction limit varies. The variation of *ACMR* with the variation of the slope reduction collapse limit for a given value of θ_m shows that the slope reduction limit controls the collapse capacity. This result is important when the slope reduction criterion is a deterministic limit (e.g., 80% reduction). In Chapter 5, the slope reduction collapse criterion is defined using a range of slope reduction limits in a probabilistic manner.

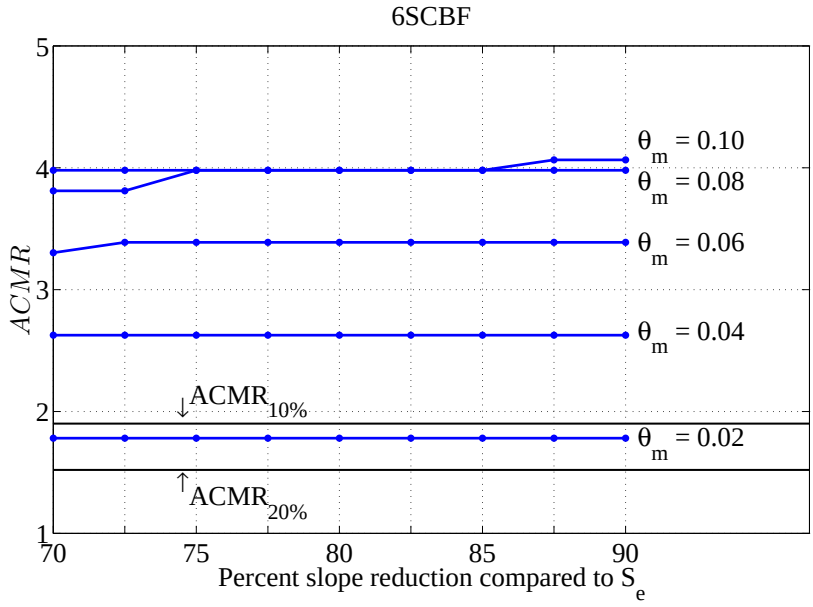

Figure 4.18: Variation of *ACMR* with variation of collapse criteria for 6SCBF archetype building

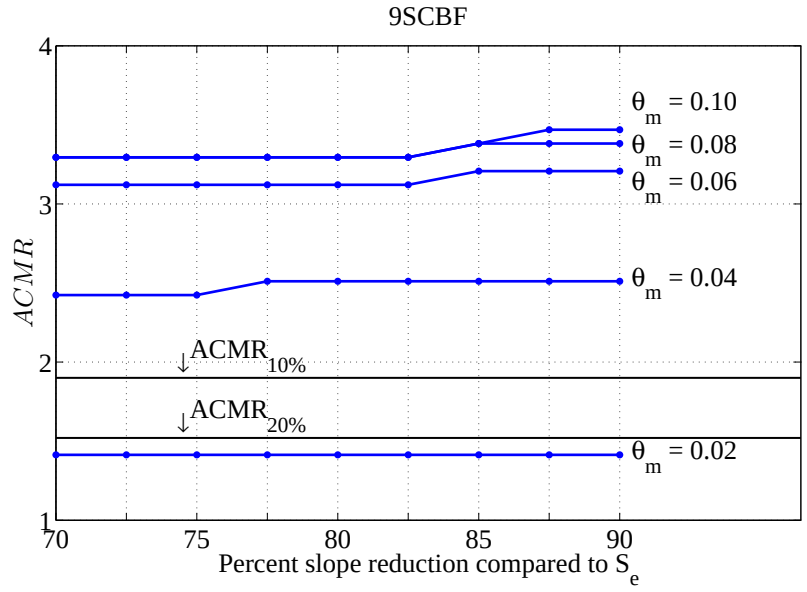

Figure 4.19: Variation of *ACMR* with variation of collapse criteria for 9SCBF archetype building

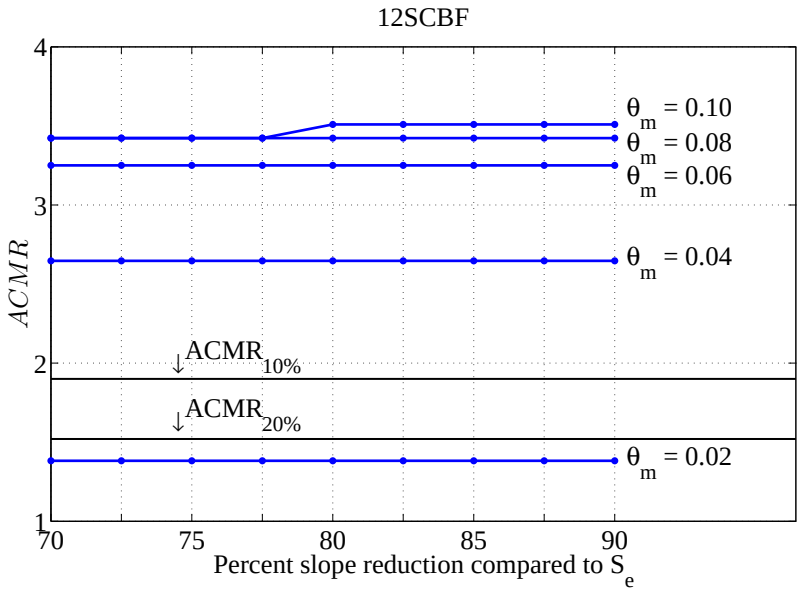

Figure 4.20: Variation of *ACMR* with variation of collapse criteria for 12SCBF archetype building

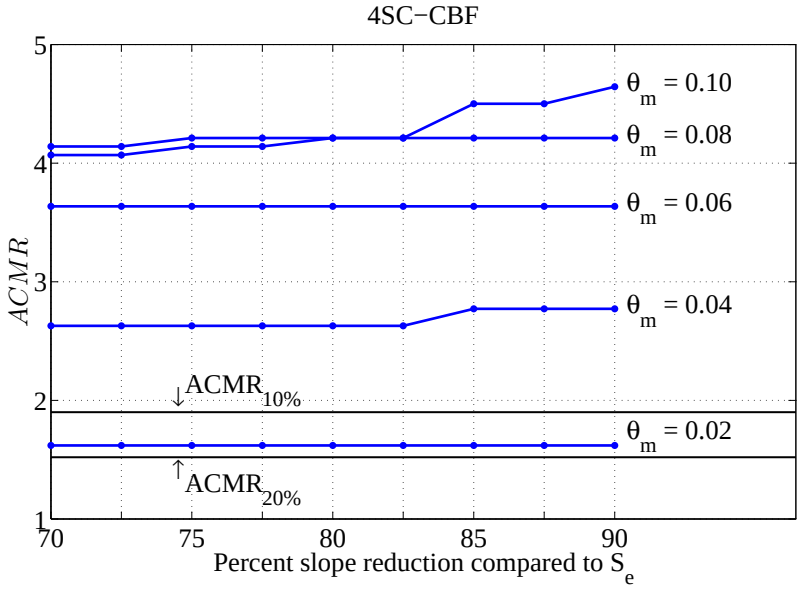

Figure 4.21: Variation of *ACMR* with variation of collapse criteria for 4SC-CBF archetype building

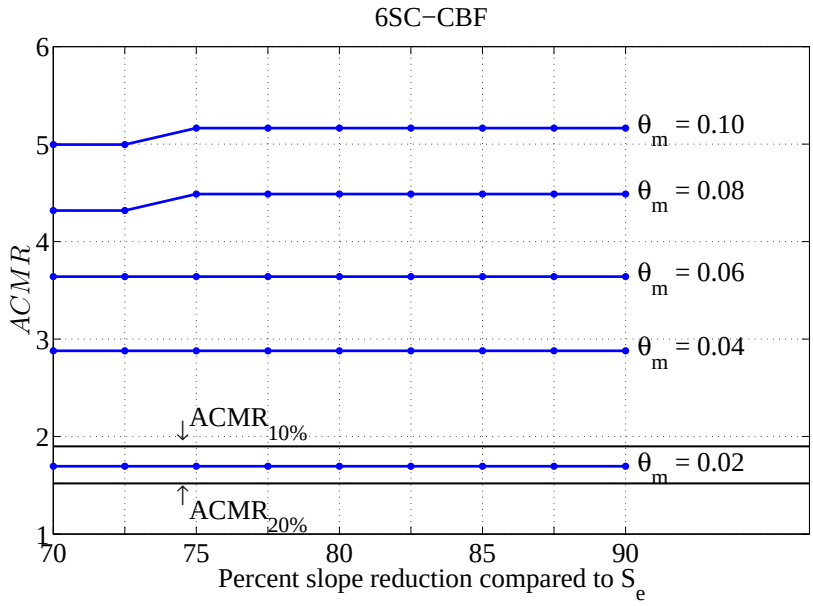

Figure 4.22: Variation of *ACMR* with variation of collapse criteria for 6SC-CBF archetype building

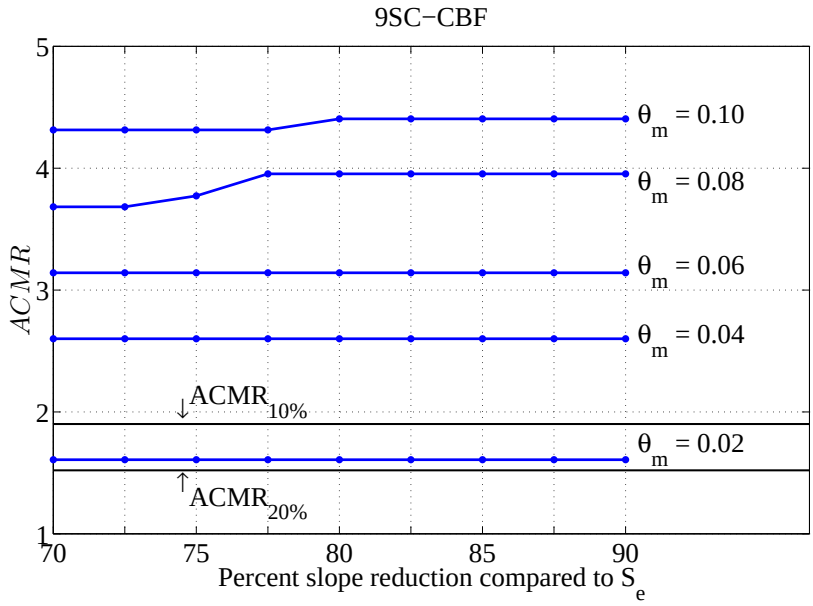

Figure 4.23: Variation of *ACMR* with variation of collapse criteria for 9SC-CBF archetype building

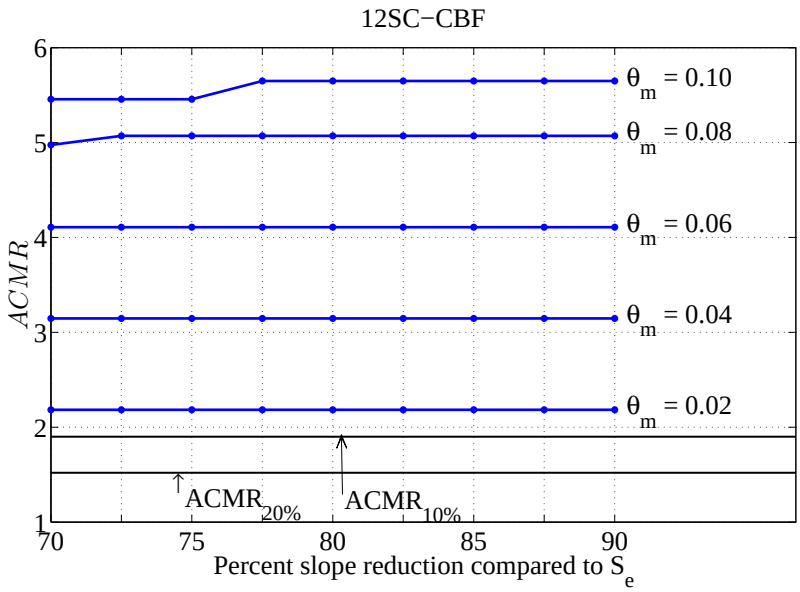

Figure 4.24: Variation of *ACMR* with variation of collapse criteria for 12SC-CBF archetype building

4.7 Residual Story Drift Ratio

Residual lateral drift after an earthquake ground motion is considered to be an important indication of earthquake-induced damage [60]. The residual story drift ratio has been shown to be an important EDP used for deciding to demolish a damaged building after an earthquake [60]. The collapse capacity study presented earlier does not consider any damage state other than collapse. It is possible for an archetype building to be heavily damaged under an earthquake ground motion record so that repair is not possible, but the collapse criteria are not reached. This heavily damaged building does not contribute to the calculated *ACMR* value presented earlier, but the cost of demolishing and reconstructing the building is not less than the cost of reconstructing a building which is collapsed. Therefore, considering the residual deformations (e.g., residual story drift ratio) is important in evaluating the loss of buildings to severe earthquake ground motions

The maximum (over all stories) residual story drift ratio, θ_r, is used as the EDP for residual drift of the archetype buildings. The θ_r values are separated into four bins: (i) $\theta_r < 0.005$; (ii) $0.005 \leq \theta_r < 0.01$; (iii) $0.01 \leq \theta_r < 0.02$; and (iv) $\theta_r \geq 0.02$. The $\theta_r < 0.005$ bin is assumed to correspond to negligible damage and $\theta_r \geq 0.02$ is assumed to correspond to heavy damage. Histograms for θ_r values are shown for the archetypes buildings in Figures 4.25 through 4.28 using the four bins described. The histograms for θ_r are shown at three IM values corresponding to the MCE (i.e., S_{MT}), 1.5 times the MCE (1.5 MCE or 1.5 S_{MT}), and 2 times the MCE (2 MCE or 2 S_{MT}).

Comparing the frequency of the θ_r values at each bin for the SCBF and SC-CBF archetype buildings, it can be seen that the number of θ_r values less than 0.005 for the SC-CBF archetype buildings are considerably larger than the number of θ_r values less than 0.005 for the SCBF archetype buildings. The SCBF archetype buildings, have more θ_r values greater than or equal to 0.005 compared to the SC-CBF archetype buildings. This

clearly indicates the damage-free characteristic of the SC-CBF system.

Looking at Figures 4.25 through 4.28, it can also be seen that the total number of θ_r values (considering all four bins) decreases as the IM value increases (e.g., from MCE to 1.5 MCE) for the SCBF and SC-CBF archetype buildings. This result is due to the occurrence of building collapse as the IM value increases.

The median of the θ_r values at each IM value is plotted for the SCBF and SC-CBF archetype buildings in Figures 4.29 through 4.32. It can be seen that for each pair of SCBF and SC-CBF archetype buildings with the same number of stories, the median θ_r value for the SC-CBF archetype buildings is smaller than the median θ_r values for the SCBF archetype buildings at a given IM value. Also, it can be seen that the median θ_r values for the SCBF archetype buildings start to increase away from zero at smaller IM values than the SC-CBF archetype buildings. This result shows that the damage (that causes residual story drift) does not occur until larger IM values are reached for the SC-CBF archetype buildings compared to the SCBF archetype buildings.

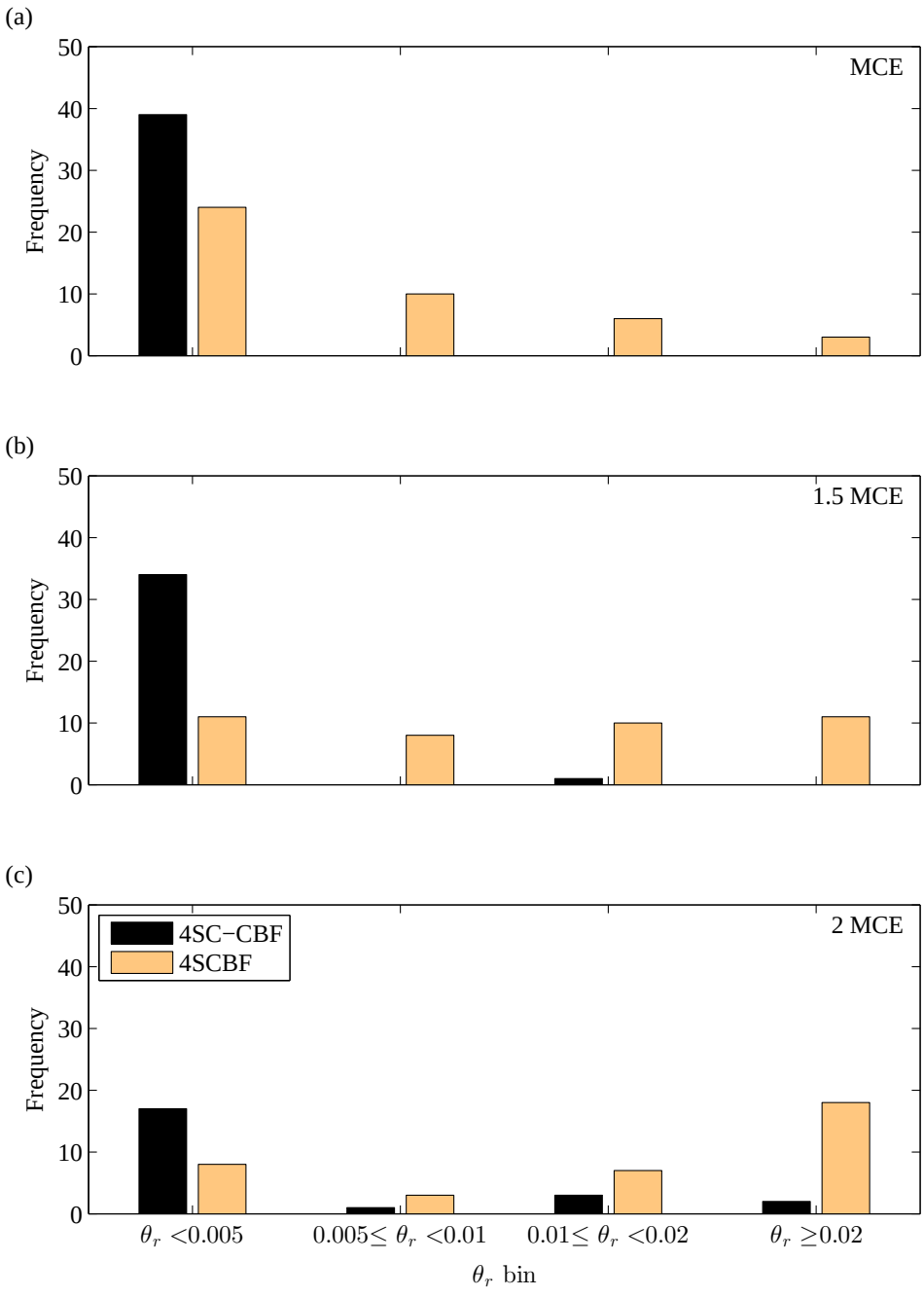

Figure 4.25: Distribution of θ_r for 4-story archetype buildings at: (a) MCE IM value; (b) 1.5 MCE IM value; and (c) 2 MCE IM value

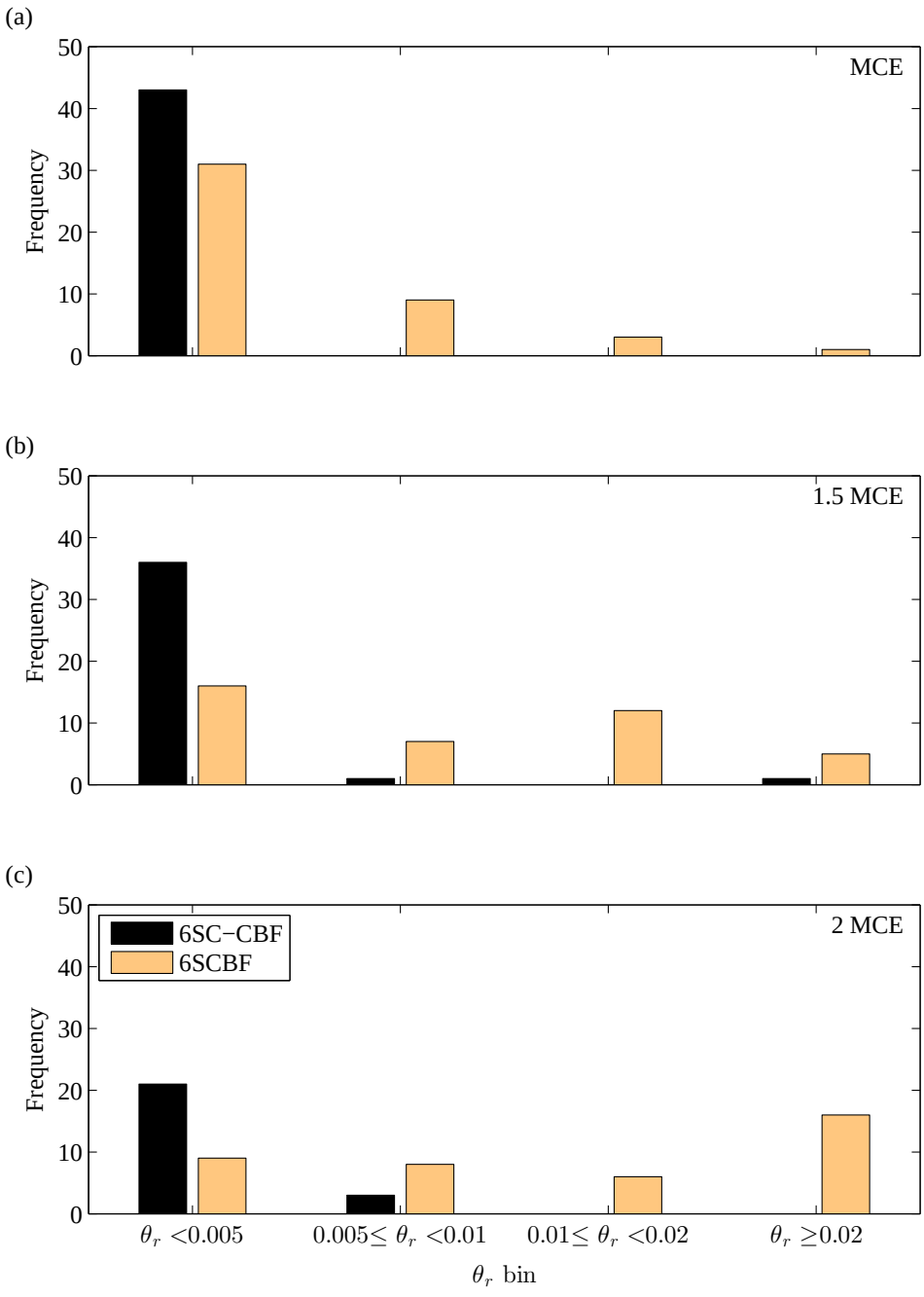

Figure 4.26: Distribution of θ_r for 6-story archetype buildings at: (a) MCE IM value; (b) 1.5 MCE IM value; and (c) 2 MCE IM value

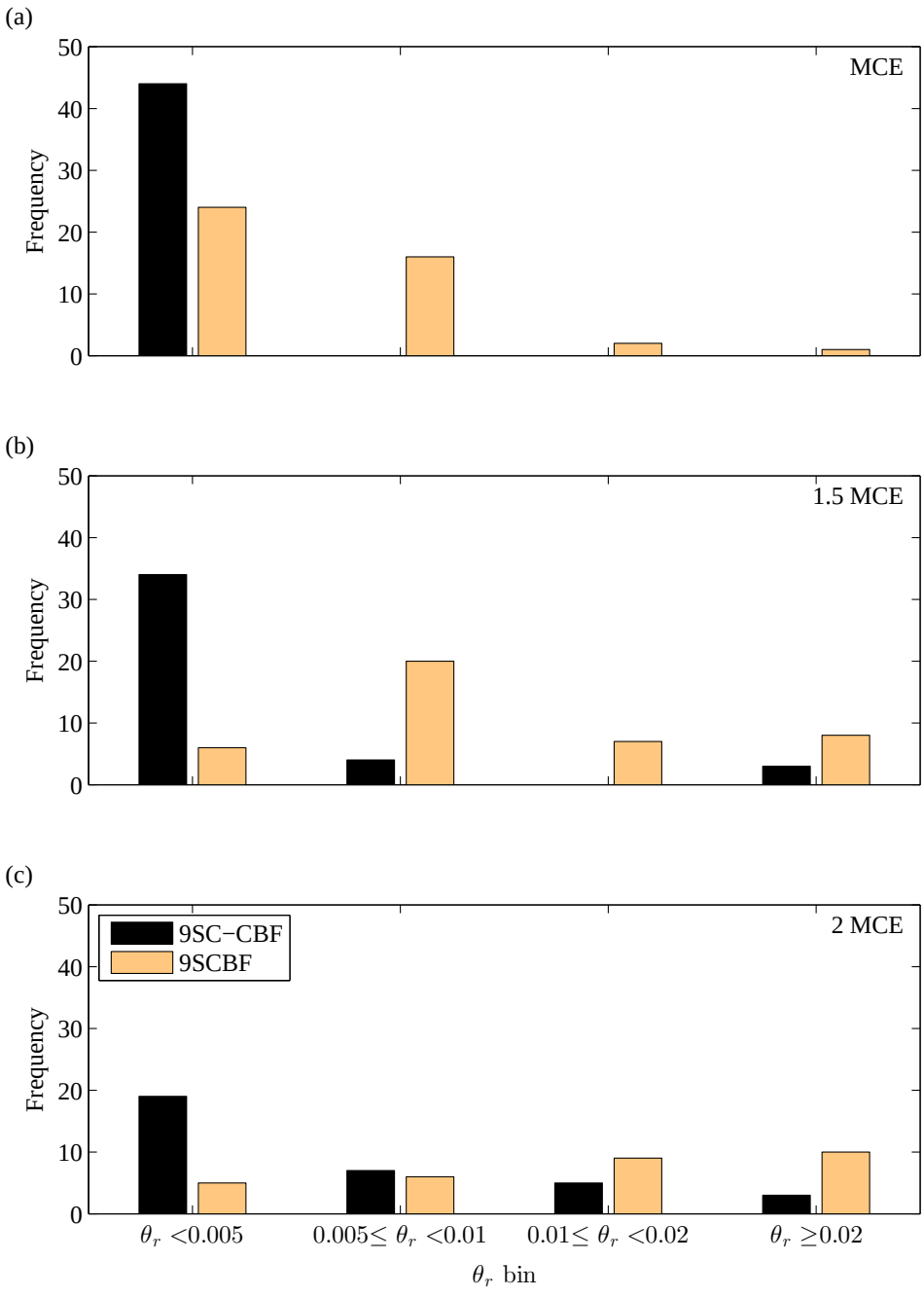

Figure 4.27: Distribution of θ_r for 9-story archetype buildings at: (a) MCE IM value; (b) 1.5 MCE IM value; and (c) 2 MCE IM value

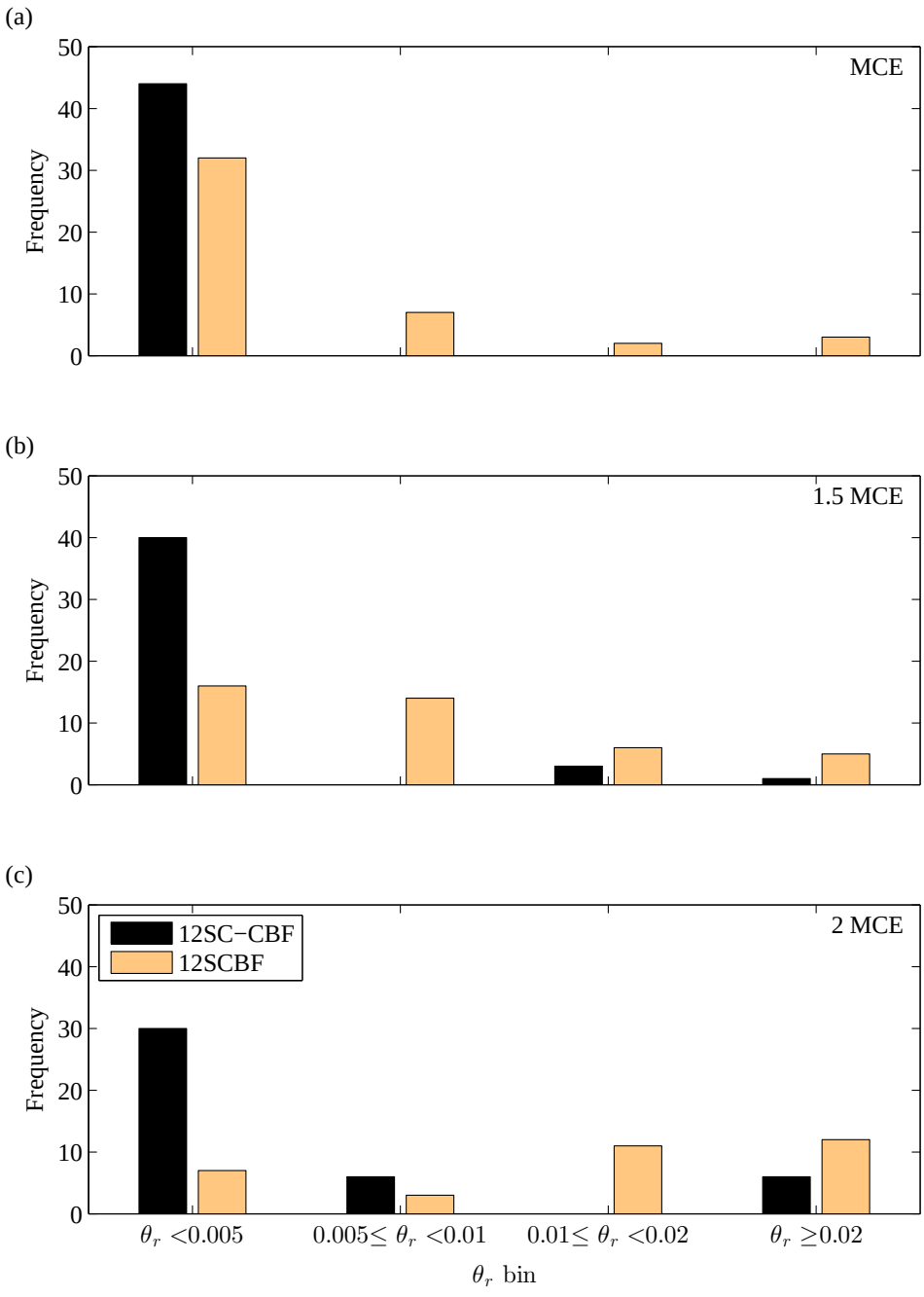

Figure 4.28: Distribution of θ_r for 12-story archetype buildings at: (a) MCE IM value; (b) 1.5 MCE IM value; and (c) 2 MCE IM value

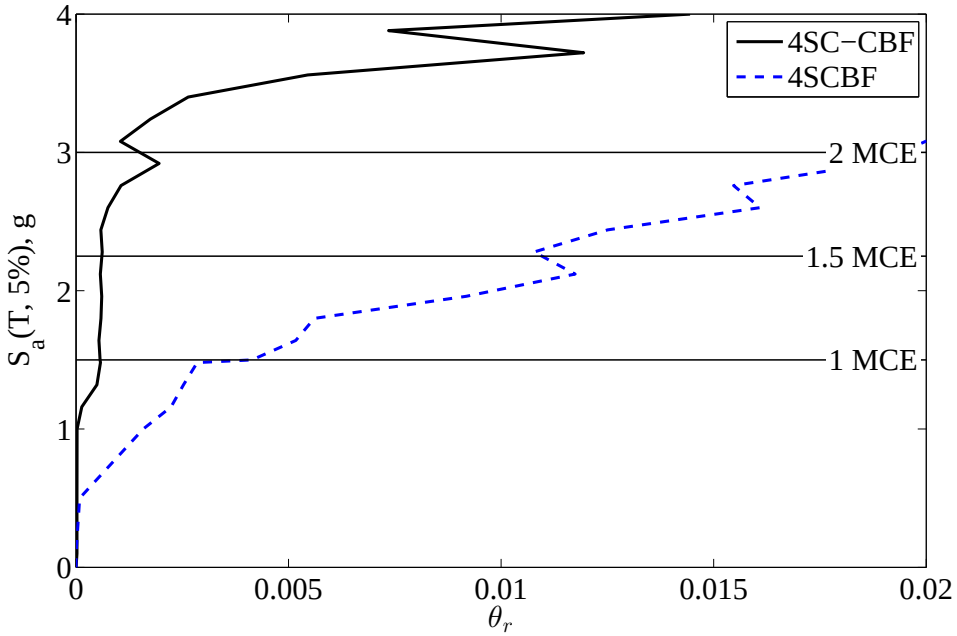

Figure 4.29: Median θ_r for 4-story archetype buildings

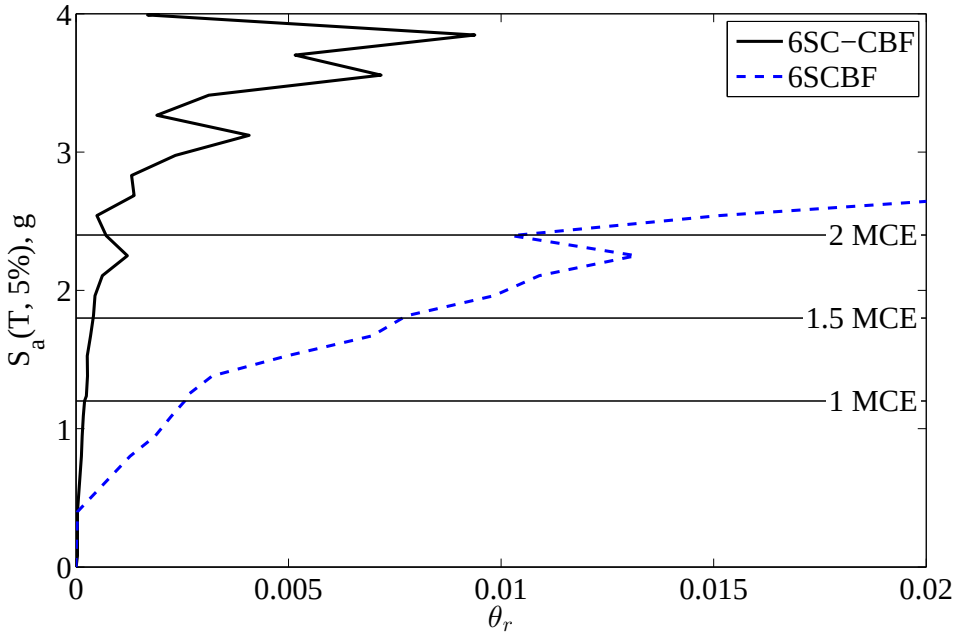

Figure 4.30: Median θ_r for 6-story archetype buildings

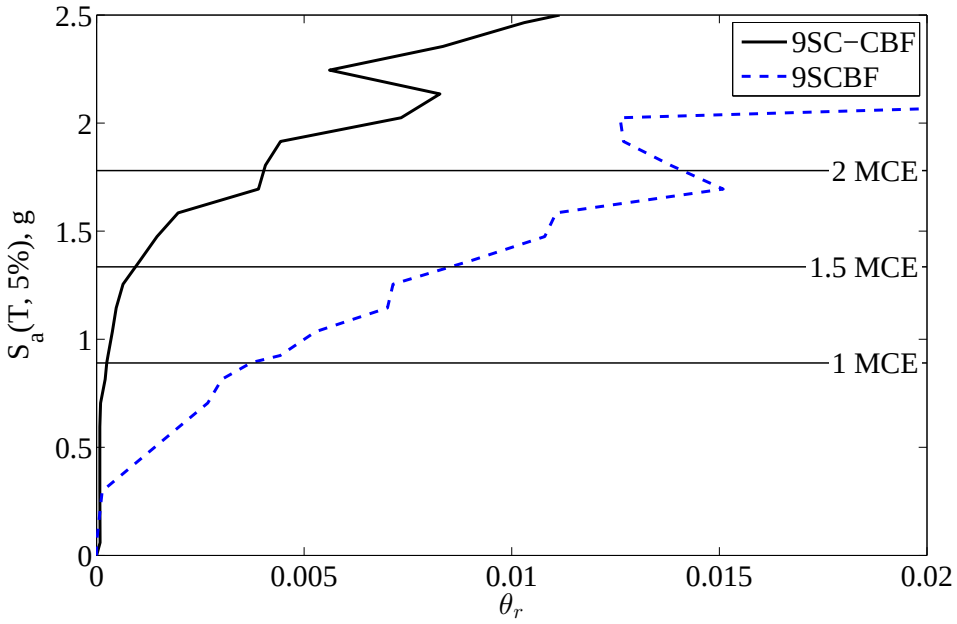

Figure 4.31: Median θ_r for 9-story archetype buildings

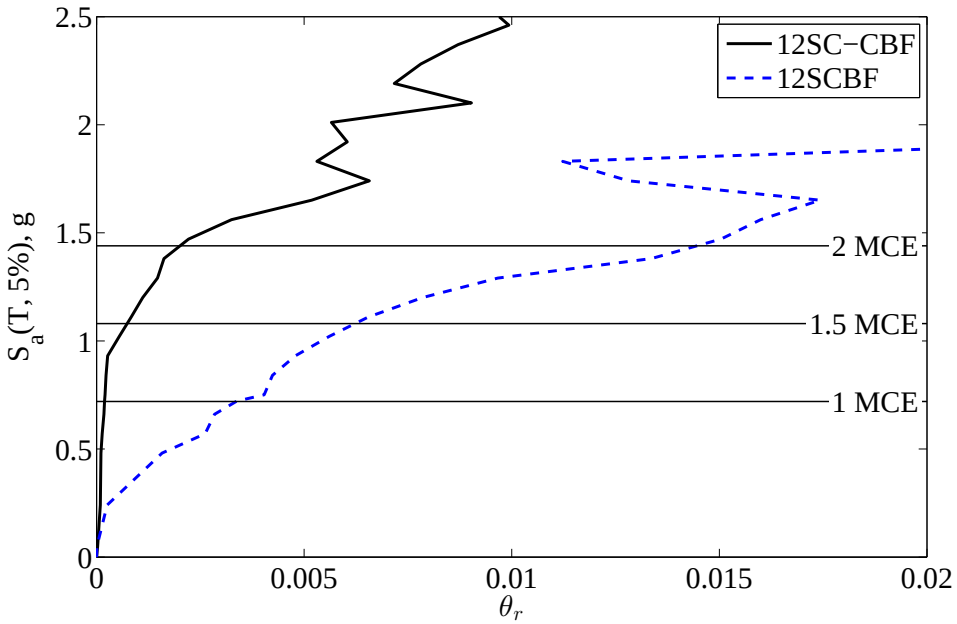

Figure 4.32: Median θ_r for 12-story archetype buildings

4.8 Summary and Findings

The collapse fragility curves and collapse margin ratios for the SCBF and SC-CBF archetype buildings are presented. The adjusted collapse margin ratios (*ACMR*) are also calculated and compared against the acceptable *ACMR* values. The *ACMR* values for all building archetypes were larger than the acceptable *ACMR* values defined by FEMA P695 [23]. It is observed that the margin against collapse for the SC-CBF archetype buildings is larger than the margin against collapse for the SCBF archetype buildings. The larger margin against collapse for the SC-CBF archetype buildings shows that the rocking and self-centering feature of the SC-CBF system, which are the main reasons for the damage-free characteristic of the SC-CBF system, do not reduce the margin against collapse of the system, but actually increases the margin against collapse.

The effect of varying two collapse criteria, slope reduction limit and maximum story drift ratio (θ_m) limit, on the *ACMR* values is explored. It is observed that varying the slope reduction limit in a range of 70% to 90% has a small effect on the *ACMR* values for $\theta_m =$ 0.02, 0.04, and 0.06 for most of the archetype buildings. Varying the slope reduction limit in a range of 70% to 90% has a more significant effect on the variation of the *ACMR* values for $\theta_m = 0.08$ and 0.10. Therefore, changing the slope reduction limit value with $\theta_m = 0.08$ and 0.10, would change the collapse points and the collapse fragility curves.

The distribution of residual story drift ratio (θ_r) values at various hazard intensity measure (IM) values is studied for the SCBF and SC-CBF archetype buildings. It is observed that the number of θ_r values less than 0.005 for the SC-CBF archetype buildings are considerably larger than for the SCBF archetype buildings. In other words, the SCBF archetype buildings have more cases with θ_r values greater than 0.005 compared to the SC-CBF archetype buildings. It is also observed that the median θ_r values, determined at each IM value, start to increase away from zero at IM values that are larger for the SC-CBF

archetype buildings compared to the SCBF archetype buildings. This result shows that damage of the SC-CBF archetype buildings does not occur until greater IM values are reached compared to the SCBF archetype buildings.

Chapter 5

Probabilistic Damage Analysis of Building Using Damage Scenario Tree and Record-By-Record Approach

5.1 Introduction

Chapter 4 presents the collapse capacities of the archetype buildings established using the FEMA P695 [23] approach and incremental dynamic analysis (IDA) results. While the collapse of a building is a major contributor to the estimated earthquake-induced loss for the building, structural damage which does not cause the building to collapse, but results in significant permanent (residual) deformation, is a second major contributor to the earthquake-induced estimated loss [60], because buildings with significant residual deformations are often demolished rather than repaired. The required demolition of numerous reinforced concrete buildings in Mexico City after the 1985 Michoacan, Mexico earthquake [68] and the demolition of numerous reinforced concrete bridge piers after the 1995 Hyogo-ken Nambu earthquake [38] are two examples. In this chapter a framework for conducting probabilistic seismic damage analysis of buildings is presented. In this framework other damage states, in addition to the collapse damage state, are included.

Seismic performance analysis of a building can be organized into four stages: (i) hazard analysis; (ii) structural response analysis; (iii) damage analysis; and (iv) loss estimation. This analysis process involves distinct categories of random variables, including: hazard intensity measures (IM), engineering demand parameters (EDP), damage measures, and decision variables [92, 55, 60]. The results from the structural response history analyses

presented in Chapter 4 are used to conduct the damage analysis in this chapter.

The amplitude of the residual deformations (e.g., the residual story drift ratio) is an important indicator of damage. Increased inelastic deformations in structural components increase the likelihood of residual deformations [13, 39, 50, 51, 57, 70, 71]. Seismic lateral force resisting systems that are designed to have a large inelastic deformation capacity, with the objective of creating a low probability of collapse, are likely to sustain large residual deformations [30].

Previous research has considered the consequences of residual story drift. For example, Uma et al. [81] use the joint distribution of the maximum story drift ratio and the residual story drift ratio to provide a three-dimensional performance matrix. Ramirez and Miranda [60] developed a loss estimation procedure that includes the residual story drift ratio and the resulting probability of demolition in the total estimated loss.

This chapter presents a framework for probabilistic seismic damage analysis of buildings by including damage assessments at the system level, subsystem level, and component level. A damage scenario tree analysis technique is used. EDPs for the system level, subsystem level, and component level damage assessments are considered. Damage scenarios are defined using the damage scenario tree, and the probability of occurrence for damage scenarios are estimated for an example building structure. Two approaches, a record-set approach and a record-by-record approach, for treating the variability of the structural response as the ground motion is varied (so-called ”record-to-record” or RTR variability) are presented and the advantages and disadvantages of the approaches are discussed. Epistemic uncertainty regarding the damage state criteria is considered in estimating the damage scenario probabilities. Engineering demand parameter (EDP)-based and hazard intensity measure (IM)-based methods for quantifying the probability of building collapse are discussed.

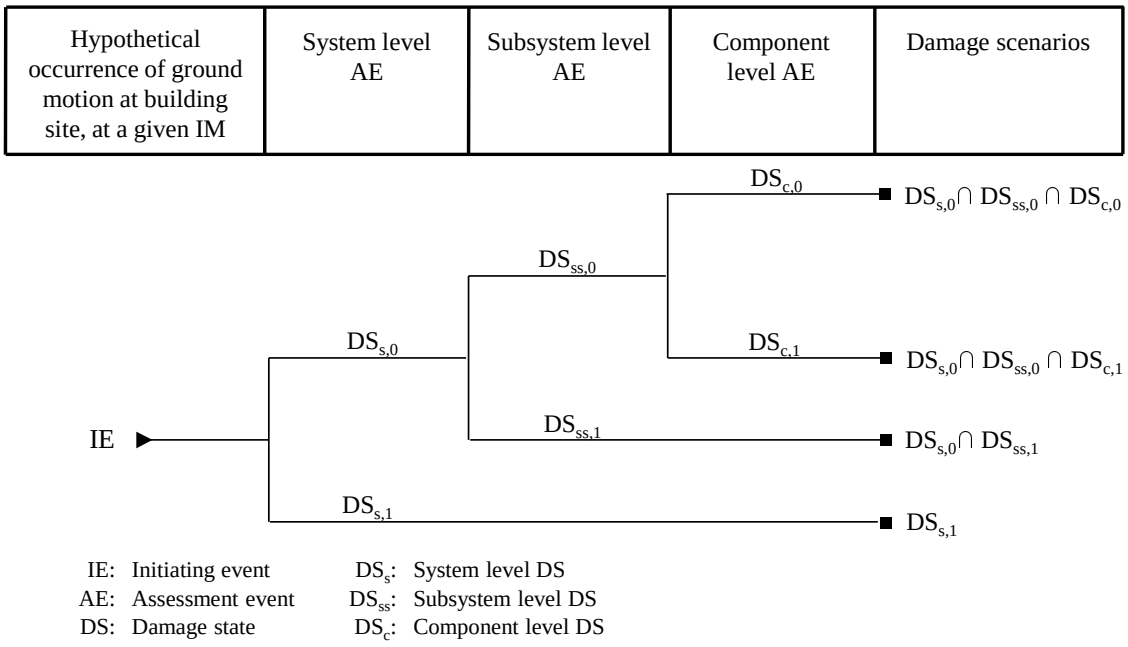

Figure 5.1: Organization of damage analysis for building at system, subsystem, and component levels

5.2 Damage Scenario Tree

5.2.1 Damage scenario tree analysis

A quantitative probabilistic study of a sequence of events resulting from an initiating event can be performed using an event tree analysis (ETA) [21]. In the present study, the ETA technique is adapted to develop a so-called damage scenario tree analysis (DSTA) of the seismic damage to a building. A DSTA uses a hierarchy of levels: (i) the entire system (i.e., the building); (ii) subsystems (e.g., the seismic lateral force resisting system of the building); and (iii) components (e.g., structural components such as columns, braces, and beams, or non-structural components such as cladding and partition walls). Figure 5.1 shows a general damage scenario tree diagram.

The initiating event (IE) for an ETA is usually an undesirable event that has conse-

quences leading to an end state. In a DSTA, the hypothetical occurrence of an earthquake ground motion at the building site, at a given IM value, is treated as the IE for the damage analysis of the building.

In an ETA, pivotal events (PE) are the events that may follow from the IE [21]. In a DSTA, the PE are a sequence of assessment events (AE) at the system level, subsystem level, and component level of the building. Each AE is a probabilistic assessment of the damage state (DS) for the system, a subsystem, or a component.

Each AE has two or more resulting DS which form different branches of the damage scenario tree. The resulting states must be mutually exclusive and collectively exhaustive. A path from the IE to the end of a branch, including all the DS along the path, is called a damage scenario. Different damage scenarios are shown as the intersection of the DS along the path to a branch end in Figure 5.1. In Figure 5.1, the DS are given subscripts where s, ss, and c refer to the system, subsystem, and component levels, and the indices $0, 1, 2, \cdots$ are used to distinguish the different DS. For example, $DS_{ss,1}$ is DS number 1 for subsystem level AE. As it will be seen later, the index 0 is used to distinguish the DS of *no damage* at the system, subsystem, and component levels.

The DS are described qualitatively in terms of the repair action (RA) required to restore the system, subsystem, or component back to an acceptable (e.g., functional) state. A one-to-one correspondence between a DS and the corresponding RA is established, where the RA is used to describe the DS. The probability of being in a DS is assessed quantitatively using one or more related EDP, obtained from structural response analysis. Each EDP is a random variable. Details about the EDPs and the uncertainties contributing to the randomness of the EDPs are given later.

Figure 5.2 shows that the system level DS of the building are non-collapse, $DS_{s,0} = NC$, and collapse, $DS_{s,1} = C$, of the building. The corresponding RA for non-collapse is to

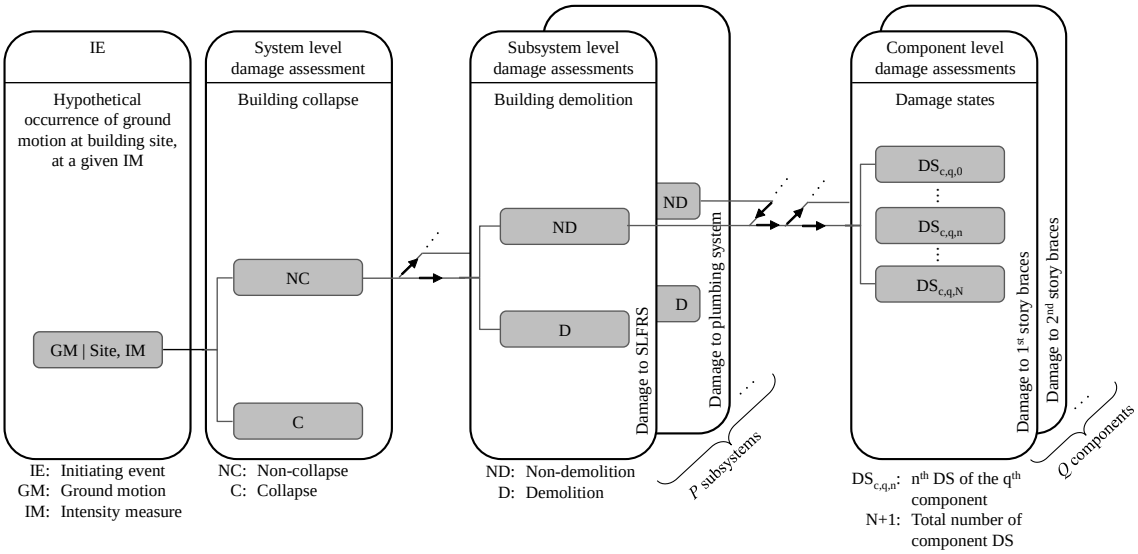

Figure 5.2: Damage scenario tree diagram for probabilistic damage analysis of building

conduct repairs indicated by the subsystem and component DS. The corresponding RA for collapse is to remove the debris and reconstruct the building.

The damage to a subsystem (such as the SLFRS or the plumbing system) of the building is described using the RA of "non-demolition" (ND), and "demolition" and reconstruction (D) of the building corresponding to $DS_{ss,0}$ and $DS_{ss,1}$, respectively. *ND* and *D* were selected as the subsystem-level RA, assuming that it is not feasible to repair a building with a heavily damaged subsystem (see Figure 5.2). Any subsystem that can be damaged to an extent that could lead to demolition and reconstruction of the building could be considered.

The damage to each component can be quantified by different DS, described by the corresponding RA. The identified DS for each component must be mutually exclusive and cover all possible states of the component (i.e., be collectively exhaustive). Figure 5.2 shows N+1 possible damage states for a component level damage assessment.

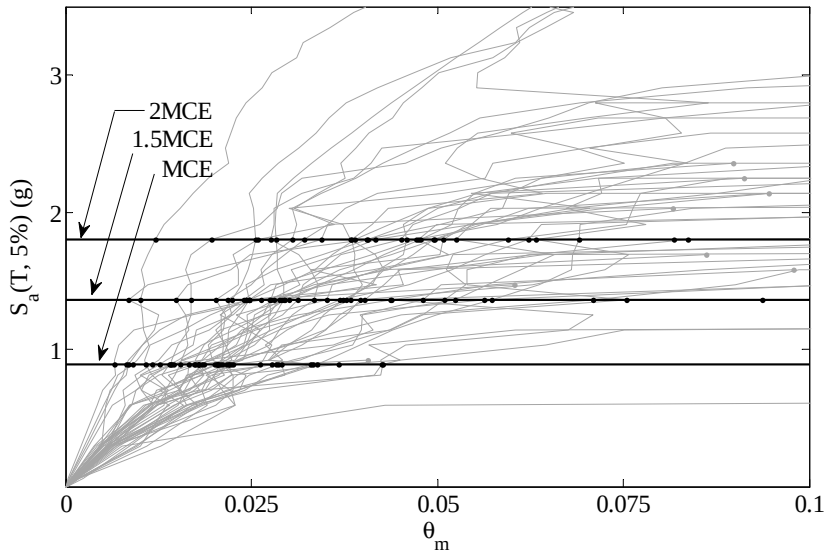

Figure 5.3: IDA for 9SCBF archetype building

5.2.2 Estimation of EDP using IDA

In the present damage analysis, an EDP is a structural response of interest, such as story drift ratio, member deformation, etc. Structural response analyses in the form of IDA [86] are used to estimate the EDP values for a range of IM values. EDP values are obtained from the response of the structure to the set of ground motion records ($GM_l, l = 1 \cdots L$) for a given IM, and the resulting EDP values are considered to be conditioned on the IM.

The set of IDA curves for the Far-Field GM set applied to the 9SCBF archetype building is shown in Figure 5.3. The IM is $S_a(T, 5\%)$, where T = 1.01 seconds is the approximate fundamental period (see Chapter 3), and the EDP is θ_m.

5.2.3 Quantifying damage using EDP

EDP are used to quantify the probability of being in a DS at the system level, subsystem level, and component level. The EDP corresponding to the system level, subsystem

level, and component level damage assessments are denoted by EDP_s, EDP_{ss}, and EDP_c, respectively. EDP_s, EDP_{ss}, and EDP_c are random variables. Three primary sources of EDP uncertainty are the ground motion RTR variability of the structural response, the variability of the building system parameters, and the uncertainty regarding the accuracy of the model of the building used in the nonlinear structural response analyses.

For a specific subsystem, among all P subsystems considered for damage analysis (shown in Figure 5.2), the corresponding EDP is denoted by $EDP_{ss,p}$, where the subscript p indicates the p^{th} subsystem. Similarly, for a specific component, among all Q components considered for damage analysis (shown in Figure 5.2), the corresponding EDP is denoted by $EDP_{c,q}$, where the subscript q indicates the q^{th} component.

EDP limit values ($EDP_{DS,i}$) are used to distinguish between the $(i-1)^{th}$ DS and i^{th} DS for the system, for a subsystem, and for a component. The EDP limit values for the system level, subsystem level, and component level damage assessment are denoted by $EDP_{s,DS,ns}$, $EDP_{ss,p,DS,nss}$, and $EDP_{c,q,DS,n}$, respectively. Indices p and q indicate the p^{th} subsystem and q^{th} component, respectively. The indices $ns = 0,1,\cdots,Ns$; $nss = 0,1,\cdots,Nss$; and $n = 0,1,\cdots,N$ specify the DS number for the system level, subsystem level, and component level damage assessments, respectively. As shown in Figure 5.2, one EDP limit value is required to separate the two DS of non-collapse and collapse at the system level (i.e., $Ns = 1$). The EDP limit value separating the non-collapse DS from the collapse DS is $EDP_{s,DS,1} = EDP_{s,C}$, where the subscript C stands for collapse. Similarly, one EDP limit value is required to separate the two DS of non-demolition and demolition at the subsystem level (i.e., $Nss = 1$). The EDP limit value separating the non-demolition DS from the demolition DS is $EDP_{ss,p,DS,1} = EDP_{ss,p,D}$, where the subscript D stands for demolition. At the component level, N EDP limit values are required to separate the $N+1$ DS. The first component level DS, denoted by $DS_{c,q,0}$ (see Figure 5.2), is the state of having no damage with no required repair action.

In the present analysis, the maximum (over all stories of the building) peak story drift ratio, θ_m, is used as the system level EDP (i.e., $EDP_s = \theta_m$). The θ_m limit value, separating the non-collapse DS from the collapse DS, is $EDP_{s,C} = \theta_{m,C}$. The present study considers the SLFRS as the only subsystem in the damage analysis (i.e., $P = 1$). The maximum (over all stories of the building) residual story drift ratio, θ_r, is used as the subsystem level EDP (i.e., $EDP_{ss} = \theta_r$) for the SLFRS [60]. The θ_r limit value, separating the non-demolition DS from the demolition DS, is $EDP_{ss,1,D} = \theta_{r,D}$. Later in this chapter, where application of DSTA to a the 9SCBF archetype building is discussed, examples of $EDP_{c,q}$ and $EDP_{c,q,DS,n}$ are given.

Recognizing the epistemic uncertainty in the damage state criteria, the EDP limit values (i.e., $EDP_{s,C} = \theta_{m,C}$, $EDP_{ss,1,D} = \theta_{r,D}$, and $EDP_{c,q,DS,n}$) are treated as random variables (rather than deterministic limit values). In other words, the EDP limit values are treated as random variables due to a lack of knowledge of the precise value of an EDP separating two DS. For example, the precise value of θ_r separating the non-demolition DS from the demolition DS is uncertain. Probability distributions for the EDP limit values can be estimated from analytical work, published test data, and post-earthquake reconnaissance reports [55]. The probability of a given EDP value ($EDP = edp$) exceeding an EDP limit value, $EDP_{DS,i}$, is quantified by evaluating the cumulative density function (CDF) of $EDP_{DS,i}$ at edp as follows:

$$P(EDP \geq EDP_{DS,i} | EDP = edp) = F_{EDP_{DS,i}}(EDP = edp) \tag{5.1}$$

where edp is a value of the EDP, $EDP_{DS,i}$ is the i^{th} EDP limit value separating the $(i-1)^{th}$ DS from the i^{th} DS, and $F_{EDP_{DS,i}}$ is the CDF for $EDP_{DS,i}$ which is the i^{th} EDP limit value fragility function. For example, for the system level and the SLFRS subsystem level damage assessment, the collapse fragility function and the demolition fragility function are denoted by $F_{\theta_{m,C}}$ and $F_{\theta_{r,D}}$, respectively. $F_{\theta_{m,C}}$ and $F_{\theta_{r,D}}$ represent the uncertainty in the $\theta_{m,C}$ and $\theta_{r,D}$ limit values, respectively, and are discussed in more detail later.

Figure 5.4 illustrates three damage scenarios from the damage scenario tree in Figure 5.2. The probability of occurrence of a damage scenario (such as those shown in Figure 5.4) is equal to the probability of the intersection of the DS at different levels, which form the damage scenario. The probability of each damage scenario shown in Figure 5.4 can be quantified using the EDP and EDP limit values as follows:

$$P(C|IM) = P(\theta_m \geq \theta_{m,C}|IM) \tag{5.2}$$

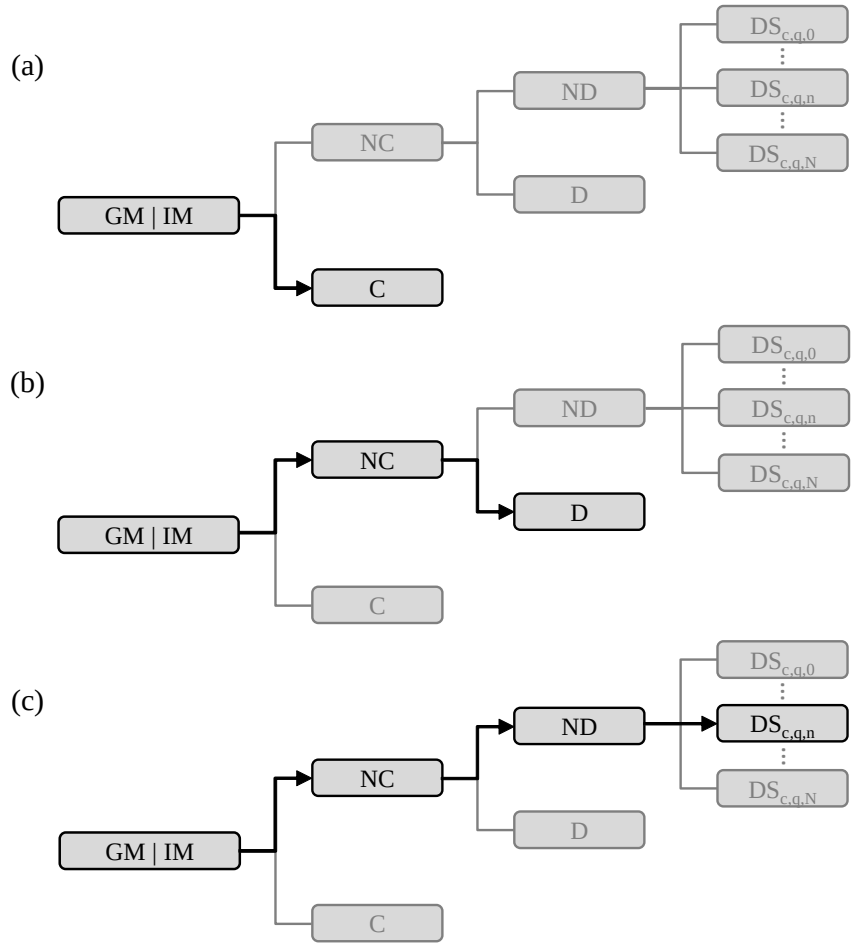

Figure 5.4: Damage scenarios; (a) collapse $(C|IM)$: (b) non-collapse with demolition $(NC \cap D|IM)$; and (c) non-collapse, non-demolition with component damage $(NC \cap ND \cap DS_{c,q,n}|IM)$

$$P(NC \cap D|IM) = P(\theta_m < \theta_{m,C} \cap \theta_r \geq \theta_{r,D}|IM) \tag{5.3}$$

$$P(NC \cap ND \cap DS_{c,q,n}|IM) =$$
$$P(\theta_m < \theta_{m,C} \cap \theta_r < \theta_{r,D} \cap EDP_{c,q,DS,n} \leq EDP_{c,q} < EDP_{c,q,DS,n+1}|IM) \tag{5.4}$$

Equation (5.2) gives the probability of collapse of the building at a given IM value. Equation (5.3) gives the probability of non-collapse with demolition and reconstruction of the building at a given IM value based on the damage assessment of the SLFRS sub-system of the building. Equation (5.4) quantifies the probability of non-collapse and non-demolition with the q^{th} component being in the n^{th} DS.

5.3 EDP-based Damage Scenario Tree Analysis (DSTA)

5.3.1 Overview of damage scenario probability evaluation

Equations (5.2) through (5.4) require probability distributions for the EDPs. As discussed earlier, the primary sources of uncertainty for the EDPs (at a given IM) are: (i) the ground motion RTR variability of the structural response, (ii) the variability of the building system parameters (e.g., stiffness, strength, mass, and damping), and (iii) the uncertain modeling decisions and parameter values used in creating the nonlinear dynamic analysis model for the structural response analyses. In the present study, only the RTR variability is included. In Chapter 6 other uncertainties considered. Two approaches for evaluating the probability of a damage scenario (e.g., Equations (5.2) through (5.4) are discussed. The two approaches differ in their treatment of the ground motion RTR variability.

In the first approach, the so-called "record-set" approach, statistical results for the EDPs from the IDA curves for a set of ground motions, as shown in Figures 5.3 and 5.5, are used to develop EDP probability distributions. In this "record-set" approach, the GM is not treated as a random variable; instead, the ground motion RTR variability of the structural response at a given IM level is represented by EDP probability distributions (based on IDA results for a ground motion record set). In the record-set approach, the structural response analysis results for all GM in the set ($GM_l, l = 1 \cdots L$) are used simultaneously in the DSTA.

In the second approach, the so-called "record-by-record" approach the GM is treated as a random variable; similar to an approach discussed in [85]. In this "record-by-record" approach, the EDP is conditioned on the GM, and the probabilities of being in each DS for the system, the subsystems, and the components are calculated separately for each individual GM in the set. The total probability of a damage scenario is then calculated by combining the damage scenario probabilities for the individual GM. Performing the DSTA for each individual GM is the fundamental advantage of the record-by-record approach over the record-set approach. These two approaches are discussed in more detail in the following sections.

5.3.2 Evaluation of damage scenario probability using record-set approach

The law of total probability is used to evaluate $P(C|IM)$ from Equation (5.2) using the record-set approach by expanding over the relevant θ_m values, for a given IM value, as follows:

$$P(C|IM) = \sum_{all\ \theta_{m_i}} P(\theta_m \geq \theta_{m,C}|\theta_m = \theta_{m_i}, IM) \cdot P(\theta_m = \theta_{m_i}|IM) \tag{5.5}$$

where $P(\theta_m \geq \theta_{m,C}|\theta_m = \theta_{m_i}, IM)$ is the probability of θ_m exceeding $\theta_{m,C}$ given that $\theta_m = \theta_{m_i}$ at a given IM value; and $P(\theta_m = \theta_{m_i}|IM)$ is the probability of θ_m having the value θ_{m_i} at a given IM. Assuming that $\theta_{m,C}$ and θ_{m_i} are statistically independent, $P(\theta_m \geq \theta_{m,C}|\theta_m = \theta_{m_i}, IM)$ is simplified to $P(\theta_{m_i} \geq \theta_{m,C}|IM)$ and $P(\theta_{m_i} \geq \theta_{m,C}|IM)$ can be evaluated using the CDF of $\theta_{m,C}$ which is the collapse fragility function, $F_{\theta_{m,C}}$. Equation(5.5) can be rewritten in terms of $F_{\theta_{m,C}}$ and the probability density function (PDF) for θ_m at a given IM ($f_{\theta_m|IM}$) as follows:

$$P(C|IM) = \sum_{all\ \theta_{m_i}} F_{\theta_{m,C}}(\theta_{m_i}) \cdot f_{\theta_m|IM}(\theta_{m_i}) \Delta\theta_{m_i} \tag{5.6}$$

$f_{\theta_m|IM}$ can be estimated by fitting an assumed probability distribution to the θ_m values from IDA results at a given IM value for the ground motion record set.

An important step in developing Equation (5.6) from Equation (5.5) is the assumption that $\theta_{m,C}$ and θ_{m_i} are statistically independent, as stated previously. This assumption, however, may be questionable if the underlying factors that influence the randomness of $\theta_{m,C}$ (and consequently $F_{\theta_{m,C}}$) also influence the randomness of θ_m.

Similarly, Equation (5.3) can be evaluated using the record-set approach as follows:

$$P(NC \cap D|IM) = \sum_{all\ \theta_{m_i}} \sum_{all\ \theta_{r_j}} P(\theta_m < \theta_{m,C} \cap \theta_r \geq \theta_{r,D}|\theta_m = \theta_{m_i}, \theta_r = \theta_{r_j}, IM) \cdot P(\theta_m = \theta_{m_i}, \theta_r = \theta_{r_j}|IM) \tag{5.7}$$

where $P(\theta_m < \theta_{m,C} \cap \theta_r \geq \theta_{r,D}|\theta_m = \theta_{m_i}, \theta_r = \theta_{r_j}, IM)$ is the probability of θ_m being less than $\theta_{m,C}$ and θ_r exceeding $\theta_{r,D}$ given that $\theta_m = \theta_{m_i}$ and $\theta_r = \theta_{r_j}$ at a given IM value and $P(\theta_m = \theta_{m_i}, \theta_r = \theta_{r_j}|IM)$ is the probability of θ_m having a value of θ_{m_i} and θ_r having a value of θ_{r_j} at a given IM value.

Similar to the development of Equation (5.6), several assumptions are made to simplify

the right hand side of Equation (5.7): (i) θ_{m_i} and $\theta_{m,C}$ are statistically independent; (ii) θ_{r_j} and $\theta_{r,D}$ are statistically independent; and (iii) $\theta_{m,C}$ and $\theta_{r,D}$ are statistically independent. Again, these assumptions may be questionable. With these assumptions, however, Equation (5.7) can be rewritten using the complementary collapse fragility function ($\bar{F}_{\theta_{m,C}} = 1 - F_{\theta_{m,C}}$), the demolition fragility function ($F_{\theta_{r,D}}$), and the joint PDF for θ_m and θ_r at a given IM ($f_{\theta_m\theta_r|IM}$), as follows:

$$P(NC \cap D|IM) = \sum_{all\ \theta_{m_i}} \sum_{all\ \theta_{r_j}} \bar{F}_{\theta_{m,C}}(\theta_{m_i}) \cdot F_{\theta_{r,D}}(\theta_{r_j}) \cdot f_{\theta_m\theta_r|IM}(\theta_{m_i}, \theta_{r_j}) \Delta\theta_{m_i} \Delta\theta_{r_j} \qquad (5.8)$$

where $f_{\theta_m\theta_r|IM}$ is estimated using the θ_m and θ_r values from IDA results at a given IM, for the ground motion record set.

Similarly, Equation (5.4) can be evaluated using the record-set approach for the q^{th} component of the building using the law of total probability by expanding over the relevant θ_m, θ_r, and $EDP_{c,q}$ values. Using a triple summation (for the three random variables: θ_m, θ_r, and $EDP_{c,q}$, Equation (5.4) can be expressed in terms of complementary fragility functions for collapse and demolition, the fragility function for the q^{th} component DS, and the joint PDF of θ_m, θ_r, and $EDP_{c,q}$.

5.3.2.1 Uncertainty in EDP

The ground motion RTR variability is not treated directly in Equation (5.6), rather it is represented within the randomness of θ_m at a given IM as the GM varies, and is included in $f_{\theta_m|IM}$ (as shown in Figure 5.5). Figures 5.3 and 5.5 show the process of estimating $f_{\theta_m|IM}$ from IDA results [94]. Three IM values corresponding to the maximum considered earthquake (MCE), 1.5 times MCE (1.5 MCE), and 2 times MCE (2 MCE) are shown by horizontal lines in Figure 5.3. The intersection of each IDA curve with each horizontal line is shown by a black dot. The projection of the set of black dots on the θ_m axis gives

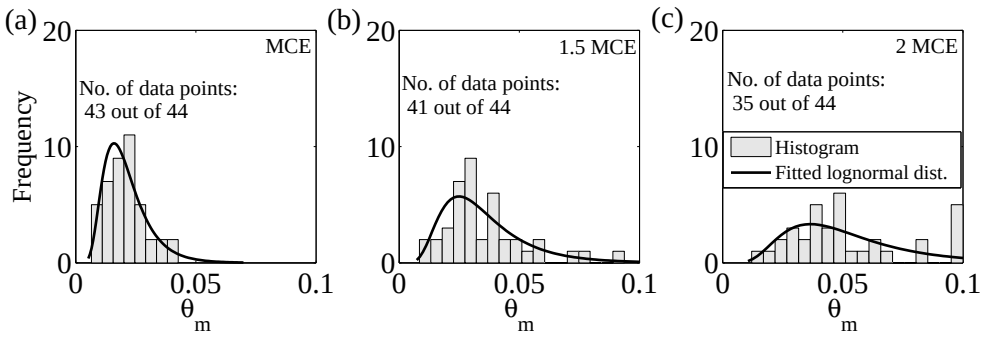

Figure 5.5: Histograms and fitted lognormal distributions for θ_m for 9SCBF archetype building at different IM values: (a) MCE; (b) 1.5 MCE; and (c) 2 MCE

the set of θ_m values for the given IM value, as they vary with GM_l. This set of EDP values for a given IM from the IDA allow statistical results for the EDP to be developed as discussed below. These results, however, include only the RTR variability of the EDP value (for a given IM value). The effects of variability of the building system parameters and of uncertain modeling decisions and parameters used in creating the nonlinear dynamic analysis model are not included in the results from the IDA shown in Figure 5.3.

Histograms of the θ_m values for the three IM values identified in Figure 5.3 (MCE, 1.5 MCE, and 2 MCE) are shown in Figure 5.5. Also shown in Figure 5.5 are fitted lognormal distributions for the θ_m values at each IM value. It can be seen that as the IM value increases, the fitted lognormal distribution becomes less consistent with the histogram of the data. This decreased consistency with the θ_m data is due to an increase in the rate of the increase of θ_m at higher IM values, which can be observed in Figure 5.3, where many of the IDA curves become nearly flat. The increase in the rate of the increase of θ_m is due to an increase in nonlinear structural response and imminence of collapse. In addition, the number of θ_m values in the sample decreases as IM increases due to collapse of the 9-story SCBF building under some GM records. From the 44 GM used in the IDA (shown in Figure 5.3), 43 GM contribute to the θ_m sample at the MCE level, 41 GM contribute to the θ_m sample at the 1.5 MCE level, and 35 GM contribute to the θ_m sample at the 2 MCE level. The number of GM in the sample (those which have not caused collapse of the building)

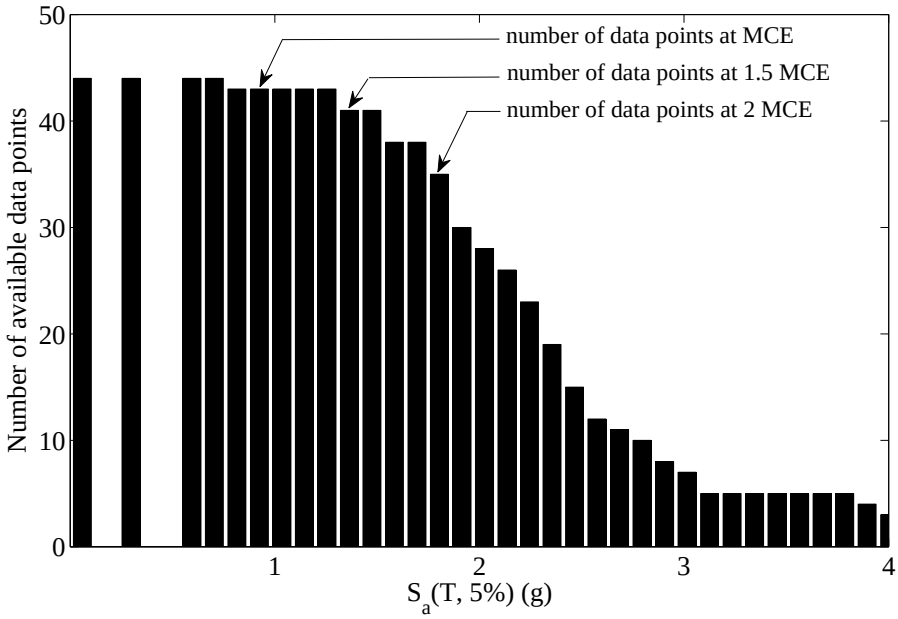

Figure 5.6: Available sample size versus IM value from IDA of 9SCBF archetype building

versus the IM value is shown in Figure 5.6.

Inconsistency is also observed between a fitted lognormal distribution and the θ_r values from a set of IDA, as shown in Figure 5.7. IDA curves with θ_r as the EDP are shown in Figure 5.7(a). The distribution of θ_r values at MCE, 1.5 MCE, and 2 MCE are shown in Figure 5.7(b), (c), and (d), respectively, where the dispersion of θ_r (shown as the logarithmic standard deviation of θ_r, $\sigma_{\ln\theta_r}$) is large. Such large dispersion of θ_r values has also been observed in previous research [60].

5.3.2.2 Uncertainty in EDP limit values

In previous work, $F_{\theta_{m,C}}$ has been established by fitting a distribution to a set of $\theta_{m,C}$ values from a set of IDA curves, e.g., [94]. $F_{\theta_{m,C}}$ established in this way, however, may include only the RTR variability (or other uncertainties included in the IDA results). As noted earlier, epistemic uncertainty in the damage state criteria is an important part of the EDP limit value uncertainty, but this uncertainty is not included within the IDA results.

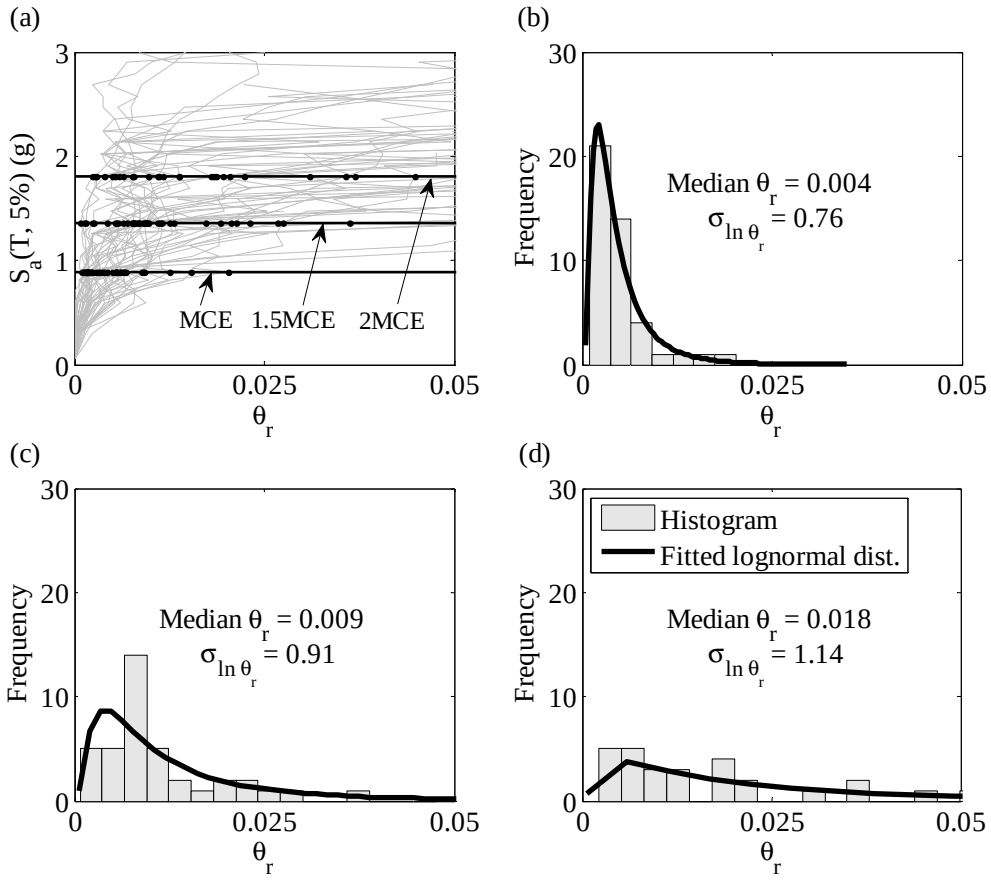

Figure 5.7: θ_r at different IM values for 9SCBF archetype building: (a) IDA results with θ_r as the EDP; (b) histogram and fitted lognormal distribution for θ_r at MCE; (c) histogram and fitted lognormal distribution for θ_r at 1.5 MCE; and (d) histogram and fitted lognormal distribution for θ_r at 2 MCE

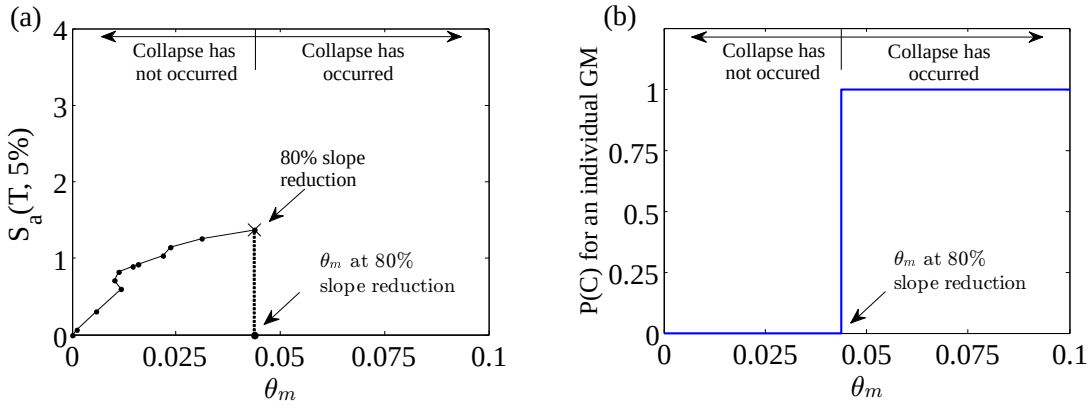

Figure 5.8: Deterministic collapse point using slope reduction of 80% of S_e for a given GM_l: (a) collapse point shown on the IDA curve; (b) EDP-based collapse fragility function

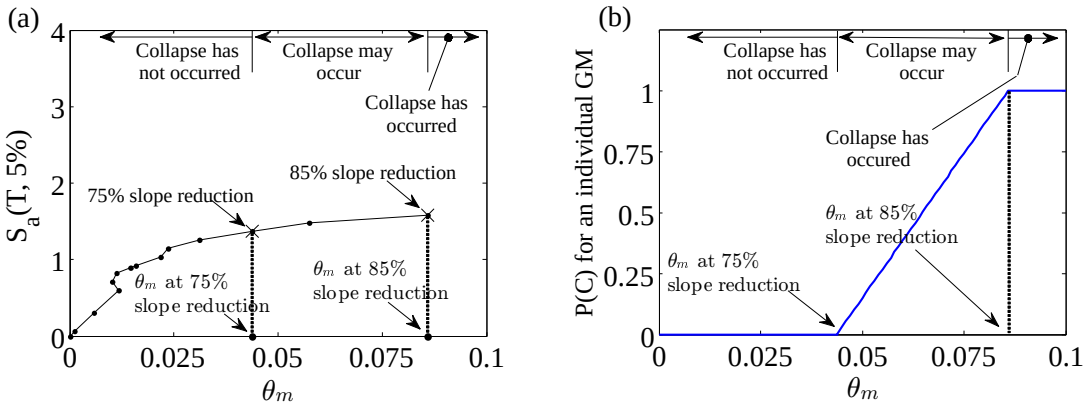

Figure 5.9: Considering epistemic uncertainty in collapse point definition using slope reduction range of 75% to 85% of S_e for a given GM_I: (a) collapse points shown on the IDA curve; (b) EDP-based collapse fragility function

Here, we consider the uncertainty in the θ_m limit value at the collapse damage state (i.e., $\theta_{m,C}$). As discussed in Chapter 4, the collapse point for an IDA curve is defined as the point at which the slope of the curve reduces considerably and the IDA curve flattens. Flattening of the IDA curve (i.e., the collapse point) is quantified in FEMA 355F [22] as a reduction in the slope of the curve with respect to the median initial slope of the IDA curves for the record set (denoted by S_e).

An individual IDA curve for the 9-story SCBF building is shown in Figure 5.8(a). The collapse point shown by "X" in Figure 5.8(a) is determined from the reduction in the slope of $S_a(T,5\%)$ versus θ_m. As discussed in Chapter 4, when the slope is less than 20% of S_e, as described in FEMA F355 [22], and does not increase to more than 20% of S_e for larger $S_a(T,5\%)$ values, the collapse point is established. In the present study, an additional collapse criterion of $\theta_m = 0.1$ from FEMA P695 [23] is used along with the slope reduction criterion, as discussed in Chapter 4. That is, $\theta_m = 0.1$ is the collapse point if the slope is greater than or equal to 20% of S_e up to $\theta_m = 0.1$.

As shown in Figure 5.8(b), using the 80% slope reduction [22] to establish the collapse DS is deterministic and does not consider epistemic uncertainty in the collapse DS defi-

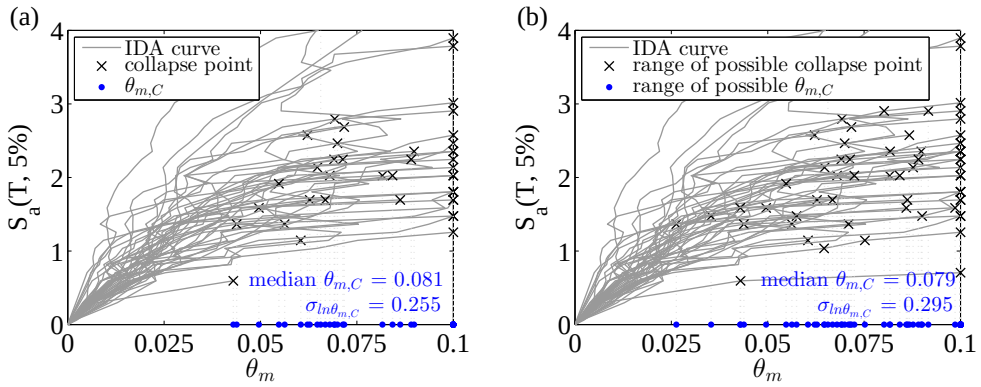

Figure 5.10: Distribution of $\theta_{m,C}$: (a) using slope reduction of 80% of S_e; (b) using slope reduction range between 75% to 85% of S_e

nition. To include epistemic uncertainty in the collapse DS definition, the present study assumes that collapse can occur within a range of slope reduction values rather than at a deterministic value as shown in Figure 5.9. Three ranges are considered for the slope reduction: (i) a range that collapse does not occur; (ii) a range that collapse may occur; and (iii) a range that collapse has certainly occurred. The limit values of 25% of S_e (75% reduction) and 15% of S_e (85% reduction) are selected to separate these three ranges of slope reduction. Thus, it is assumed that when the slope is more than 25% of S_e, collapse has not occurred, when the slope is between 15% of S_e and 25% of S_e, collapse may occur, and when the slope is less than 15% of S_e, collapse has occurred with certainty. These criteria are considered in addition to the limit of $\theta_m = 0.1$ (i.e., when $\theta_m = 0.1$, collapse has occurred).

Considering this uncertainty in the slope reduction criterion, two bounding θ_m values (corresponding to 75% and 85% slope reduction) can be established as shown in Figure 5.9. Three ranges of θ_m values corresponding to the three ranges of slope reduction are shown for an individual GM in Figure 5.9. It is assumed that the PDF for $\theta_{m,C}$ (i.e., θ_m at collapse) is uniform within the two bounding θ_m values, resulting in a probability of collapse (i.e., CDF for $\theta_{m,C}$) that varies linearly from 0% for θ_m at 75% slope reduction to 100% for θ_m at 85% slope reduction, as shown in Figure 5.9(b).

The $\theta_{m,C}$ values obtained from the set of IDA curves for the 9-story SCBF building are shown in Figure 5.10. The collapse points in Figure 5.10(a) are established based on the deterministic 80% slope reduction criterion for each GM (see Figure 5.8(a)). As shown in Figure 5.10(b), a *range* of possible collapse points for each GM (i.e., for each IDA curve) can be established considering that collapse can occur within a range of slope reduction (i.e., between 75% and 85% of S_e) for each GM.

Assuming a lognormal distribution for the $\theta_{m,C}$ values, the resulting median value and dispersion are shown in Figure 5.10(a) and (b). The results show that compared to the RTR variability, the effect of the epistemic uncertainty in the collapse DS criteria is not large (i.e., it changes the logarithmic standard deviation by about 16% from 0.255 to 0.295); and the RTR variability appears to dominate. $F_{\theta_{m,C}}$ can be obtained as the CDF for $\theta_{m,C}$, using the estimated median value and dispersion shown in Figure 5.10. $F_{\theta_{m,C}}$ from Figure 5.10(b) is used in the record-set approach described later in section 5.4 on DSTA application.

As noted earlier, an important step in developing Equation (5.6) from Equation (5.5) is the assumption that $\theta_{m,C}$ and θ_{m_i} are statistically independent. The results presented in this section and the previous section show that RTR variability contributes substantially to the randomness of both $\theta_{m,C}$ and θ_{m_i}. So the assumption that $\theta_{m,C}$ and θ_{m_i} are statistically independent is questionable. In addition, although $F_{\theta_{m,C}}$ is intended to represent the epistemic uncertainty in the collapse DS criteria, RTR variability appears to dominate $F_{\theta_{m,C}}$ established using the record-set approach.

For the demolition DS fragility function (i.e., $F_{\theta_{r,D}}$) it is assumed in this work that $\theta_{r,D}$ has a lognormal distribution and the dispersion in $F_{\theta_{r,D}}$ is due only to the epistemic uncertainty regarding the demolition DS. In this case the RTR variability is not included in $F_{\theta_{r,D}}$. The statistical parameters for $F_{\theta_{r,D}}$ used in the present study are given later in section 5.4 on DSTA application.

5.3.3 Evaluation of damage scenario probability using record-by-record approach

In the record-by-record approach, the probability of a damage scenario is determined in two steps. First, the probability of the damage scenario at a given IM value is determined for each individual GM, using the results of a structural response analysis for the individual GM. Second, the probabilities of the damage scenario at a given IM value, for the individual GM, are combined considering the probability of occurrence of each GM at the given IM value. Using the record-by-record approach, Equation (5.2) is expanded as follows:

$$P(C|IM) = \sum_{all GM_l} \sum_{all \theta_{m_i}} P(\theta_m \geq \theta_{m,C} | \theta_m = \theta_{m_i}, GM = GM_l, IM) \cdot P(\theta_m = \theta_{m_i}, GM = GM_l | IM) \quad (5.9)$$

Similarly, Equation (5.3) is expanded as follows:

$$P(NC \cap D|IM) = \sum_{all\ GM_l} \sum_{all\ \theta_{m_i}} \sum_{all\ \theta_{r_j}} P(\theta_m < \theta_{m,C} \cap \theta_r \geq \theta_{r,D} | GM = GM_l, \theta_m = \theta_{m_i}, \theta_r = \theta_{r_j}, IM) \cdot P(GM = GM_l, \theta_m = \theta_{m_i}, \theta_r = \theta_{r_j} | IM) \quad (5.10)$$

And, Equation (5.4) is expanded as follows:

$$P(NC \cap ND \cap DS_{c,q,n}|IM) = \sum_{all\ GM_l} \sum_{all\ \theta_{m_i}} \sum_{all\ \theta_{r_j}} \sum_{all\ EDP_{(c,q)_k}} P(\theta_m < \theta_{m,C} \cap \theta_r \geq \theta_{r,D} \cap EDP_{c,q,DS_n} \leq EDP_{c,q} < EDP_{c,q,DS_{n+1}} | GM = GM_l, \theta_m = \theta_{m_i}, \theta_r = \theta_{r_j}, EDP_{c,q} = EDP_{(c,q)_k}, IM) \cdot P(GM = GM_l, \theta_m = \theta_{m_i}, \theta_r = \theta_{r_j}, EDP_{c,q} = EDP_{(c,q)_k}|IM) \quad (5.11)$$

5.3.3.1 Uncertainty in EDP

In Equations (5.9), (5.10), and (5.11) each EDP value (e.g., θ_{m_i} or θ_{r_j}) is determined from a structural response analysis for an individual GM (assuming variability of the building system parameters and uncertain modeling decisions and parameters are not considered). As a result, for example, the second expression of the right hand side of Equation (5.9) can be expanded as follows:

$$P(\theta_m = \theta_{m_i}, GM = GM_l|IM) = P(\theta_m = \theta_{m_i}|GM = GM_l, IM) \cdot P(GM = GM_l|IM) \quad (5.12)$$

The first expression of the right hand side of Equation (5.12) can be evaluated as follows:

$$P(\theta_m = \theta_{m_i}|GM = GM_l, IM) = \begin{cases} 1 & \text{if } i = l \\ 0 & \text{otherwise} \end{cases} \quad (5.13)$$

Equation (5.13) shows that the only value for θ_m that must be considered is the value of θ_m from the structural response analysis for GM_l at the given IM value (i.e., $\theta_{m_i} = \theta_m(GM_l, IM)$). Substituting Equation (5.13) into Equation (5.12), and Equation (5.12) into

Equation (5.9), the summation over all θ_{m_i} reduces to one term (when $i = l$) and Equation (5.9) can be simplified as follows:

$$P(C|IM) = \sum_{all\ GM_l} P(\theta_{m_l} \geq \theta_{m,C}|GM = GM_l, IM) \cdot P(GM = GM_l|IM) \tag{5.14}$$

where θ_{m_l} equals $\theta_m(GM_l, IM)$. Finally, Equation (5.14) can be rewritten in terms of the collapse fragility function and probability of occurrence of each GM as follows:

$$P(C|IM) = \sum_{all\ GM_l} F_{\theta_{m,C,l}}(\theta_{m_l}) \cdot P(GM = GM_l|IM) \tag{5.15}$$

where $F_{\theta_{m,C,l}}$ is the collapse fragility function for GM_l.

Similarly, for Equation (5.10) the θ_m and θ_r values are determined from one structural response analysis for an individual GM. As a result, the summations over all θ_{m_i} and all θ_{r_j} reduce to one term (when $i = j = l$), and Equation (5.10) can be simplified using the θ_m and θ_r values for GM_l at a given IM value (i.e., $\theta_{m_i} = \theta_m(GM_l, IM)$ and $\theta_{r_j} = \theta_r(GM_l, IM)$) as follows:

$$P(NC \cap D|IM) = \sum_{all\ GM_l} P(\theta_{m_l} < \theta_{m,C} \cap \theta_{r_l} \geq \theta_{r,D}|GM = GM_l, IM) \cdot P(GM = GM_l|IM) \tag{5.16}$$

where θ_{m_l} and θ_{r_l} equal $\theta_m(GM_l, IM)$ and $\theta_r(GM_l, IM)$, respectively. Equation (5.16) can be expressed in terms of the complementary collapse fragility function ($\bar{F}_{\theta_{m,C,l}} = 1 - F_{\theta_{m,C,l}}$) and the demolition fragility function ($F_{\theta_{r,D,l}}$) for GM_l as follows:

$$P(NC \cap D|IM) = \sum_{all\ GM_l} \bar{F}_{\theta_{m,C,l}}(\theta_{m_l}) \cdot F_{\theta_{r,D,l}}(\theta_{r_l}) \cdot P(GM = GM_l|IM) \tag{5.17}$$

In writing Equation (5.17), it is assumed that $\theta_{m,C}$ and $\theta_{r,D}$ for GM_l are statistically inde-

pendent.

Finally, the θ_m, θ_r, and $EDP_{c,q}$ values for Equation (5.11) are determined from one structural response analysis for an individual GM, so the summations in Equation (5.11) over all θ_{m_i}, all θ_{r_j}, and all $EDP_{(c,q)_k}$ reduce to one term (when $i=j=k=l$). The only values of θ_m, θ_r, and $EDP_{c,q}$ to be considered are the values for GM_l at a given IM value (i.e., $\theta_{m_i}=\theta_m(GM_l,IM)$, $\theta_{r_j}=\theta_r(GM_l,IM)$, and $EDP_{(c,q)_k}=EDP_{c,q}(GM_l,IM)$). Therefore, Equation (5.11) can be simplified as follows:

$$P(NC\cap ND\cap DS_{c,q,n}|IM)=\sum_{all\ GM_l} P(\theta_{m_l}<\theta_{m,C}\cap\theta_{r_l}<\theta_{r,D}$$
$$\cap EDP_{c,q,DS_n}\le EDP_{(c,q)_l}<EDP_{c,q,DS_{n+1}}|GM=GM_l,IM)\cdot P(GM=GM_l|IM) \quad (5.18)$$

where θ_{m_l}, θ_{r_l}, and $EDP_{(c,q)_l}$ equal $\theta_m(GM_l,IM)$, $\theta_r(GM_l,IM)$, and $EDP_{c,q}(GM_l,IM)$, respectively. Equation (5.18) can be expressed in terms of $\bar{F}_{\theta_{m,C,l}}$, the complementary demolition fragility function ($\bar{F}_{\theta_{r,D,l}}=1-F_{\theta_{r,D,l}}$), and the component level damage state fragility function for GM_l as follows:

$$P(NC\cap ND\cap DS_{c,q,n}|IM)=\sum_{all\ GM_l}\bar{F}_{\theta_{m,C,l}}(\theta_{m_l})\cdot\bar{F}_{\theta_{r,D,l}}(\theta_{r_l})$$
$$\cdot\left(F_{EDP_{c,q,DS,n,l}}(EDP_{(c,q)_l})-F_{EDP_{c,q,DS,n+1,l}}(EDP_{(c,q)_l})\right)\cdot P(GM=GM_l|IM) \quad (5.19)$$

where $F_{EDP_{c,q,DS,n,l}}$ is the n^{th} component level damage state fragility function determined for the q^{th} component of the building and GM_l. In writing Equation (5.19), it is assumed that $\theta_{m,C}$, $\theta_{r,D}$, and $EDP_{c,q,DS,n}$ for GM_l are statistically independent.

5.3.3.2 Uncertainty in EDP limit values

The collapse fragility function, $F_{\theta_{m,C,l}}$, in Equation (5.15) represents the epistemic uncertainty in the collapse DS criteria. For the record-by-record approach, this uncertainty is illustrated in Figure 5.9, for a single GM and the subscript l in $F_{\theta_{m,C,l}}$ indicates that it pertains to GM_l. The three ranges of slope reduction with respect to S_e, described previously, are considered in establishing $F_{\theta_{m,C,l}}$ for GM_l. In contrast, $F_{\theta_{m,C}}$, used in the record-set approach pertains to the entire ground motion record set, as illustrated in Figure 5.10, and, as a result, includes RTR variability, as discussed in the previous section. The demolition fragility function, $F_{\theta_{r,D,l}}$, in Equation 5.17, represents the epistemic uncertainty in the demolition DS criteria. Again, the subscript l in $F_{\theta_{r,D,l}}$ indicates that it pertains to GM_l.

Therefore, a significant difference between the fragility functions used in the record-set approach and those of the record-by-record approach is the subscript l in $F_{\theta_{m,C,l}}$, $F_{\theta_{r,D,l}}$, and $F_{EDP_{c,q,DS,n,l}}$, which indicates that for the record-by-record approach, the fragility functions are permitted to be different for each GM_l as opposed to the record-set approach where one fragility function is estimated for all GM (i.e., $F_{\theta_{m,C}}$, $F_{\theta_{r,D}}$, $F_{EDP_{c,q,DS,n}}$). In the present study, although $F_{\theta_{m,C,l}}$ is different for each GM_l because the ranges of slope reduction are different for each GM_l (as shown previously), $F_{\theta_{r,D,l}}$ is assumed to be the same as $F_{\theta_{r,D}}$, and $\theta_{r,D}$ is assumed to have a lognormal distribution. Similarly, at the component level, $F_{EDP_{c,q,DS,n,l}}$ is assumed to be the same as $F_{EDP_{c,q,DS,n}}$ for the ground motion record set. More discussion of $F_{\theta_{m,C,l}}$, $F_{\theta_{r,D,l}}$, and $F_{EDP_{c,q,DS,n,l}}$ are given later in section 5.4 on DSTA application.

Table 5.1: The central value and logarithmic standard deviation of EDP limiting parameters for collapse, demolition, and brace damage states

EDP limit values	Median	Logarithmic std. deviation ($\sigma_{\ln}$)
$\theta_{m,C}$	0.054	0.4
$\theta_{r,D}$	0.01	0.3
$\Delta_{Or,DS,1}$	0.01	0.25
$\Delta_{Or,DS,2}$	0.025	0.3

5.4 Application of DSTA to 9SCBF Archetype Building

5.4.1 Application of record-set approach

The process of constructing the damage scenario fragility results is illustrated in Figure 5.11. The maximum (considering all stories of the building) story drift ratio, θ_m, is used as the EDP for quantifying the collapse DS at the system level. Figure 5.11(a) shows the IDA results for the 9-story SCBF building along with the distribution of θ_m at a given IM value. $f_{\theta_m|IM}$ used in Equation (5.6) is estimated using the θ_m values from all GMs at a given IM (i.e., $S_a(T,5\%)$) value, as shown in Figure 5.11(a). The collapse fragility (i.e., the C damage scenario fragility or $P(C|IM)$), shown in Figure 5.11(b), is developed using Equation (5.6) at various $S_a(T,5\%)$ values. $F_{\theta_{m,C}}$ in Equation (5.6) is estimated using the $\theta_{m,C}$ values shown in Figure 5.10(b). At each given $S_a(T,5\%)$ value, the summation of Equation (5.6) is evaluated using θ_m values for the GMs that have not caused building collapse at smaller $S_a(T,5\%)$ values. As mentioned previously, the number of available θ_m data points decreases as $S_a(T,5\%)$ increases (see Figure 5.6). The IDA results for GMs that have caused collapse at a $S_a(T,5\%)$ value less than the given $S_a(T,5\%)$ are not available for estimating $f_{\theta_m|IM}$, as shown in Figure 5.11(a). Therefore, $P(C|IM)$ calculated using Equation (5.6) becomes increasingly inaccurate as $S_a(T,5\%)$ increases. The inaccuracy of $P(C|IM)$, calculated using the record-set approach can be understood by comparing the IDA results of Figure 5.11(a) with $P(C|IM)$ in Figure 5.11(b); for example Figure 5.11(a)

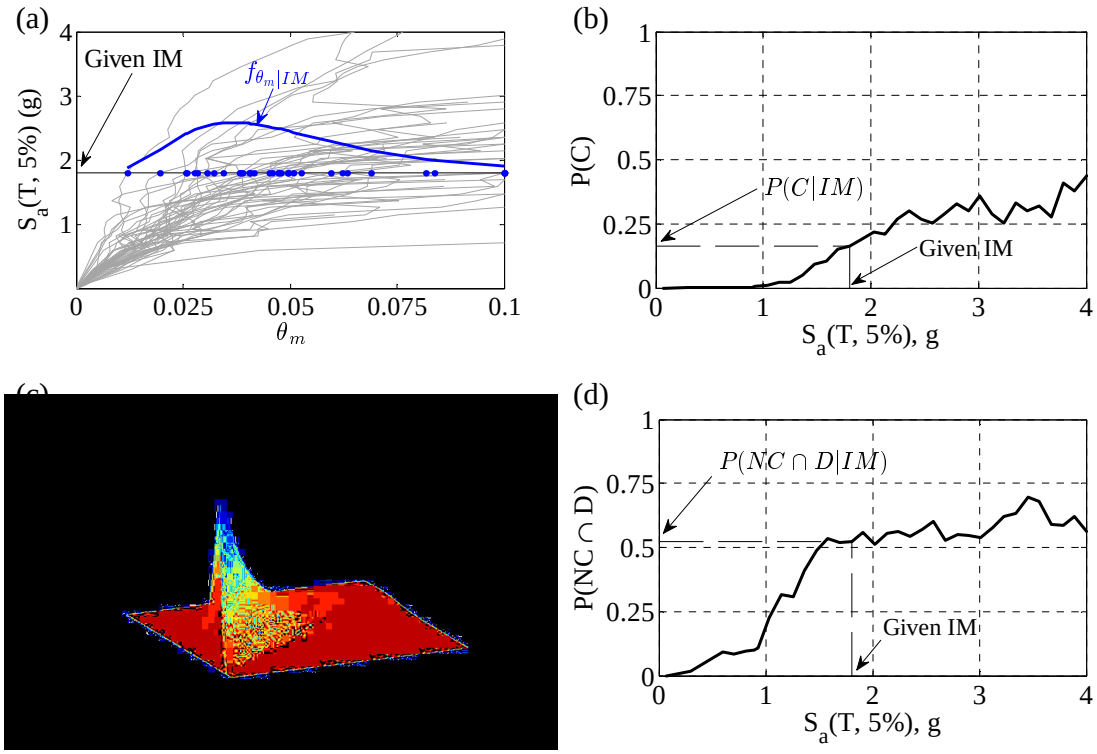

Figure 5.11: Damage scenario fragilities for 9SCBF archetype building using record-set approach: (a) $f_{\theta_m|IM}$ shown with IDA results; (b) fragility for C damage scenario; (c) joint probability density function for θ_m and θ_r at arbitrary IM value; and (d) fragility for $NC \cap D$ damage scenario

shows that most of the GMs have caused collapse for $S_a(T,5\%) \leq 3.5g$ and therefore the probability of collapse at $S_a(T,5\%) = 3.5g$ is expected be close to 1. But $P(C|IM)$ is much less than 1 at $S_a(T,5\%) = 3.5g$ because results for GMs which have caused collapse at $S_a(T,5\%) < 3.5g$ are not included in estimating $f_{\theta_m|IM}$ at $S_a(T,5\%) = 3.5g$.

The non-collapse with demolition ($NC \cap D$) damage scenario fragility (or $P(NC \cap D|IM)$) is evaluated using Equation (5.8) at various IM (i.e., $S_a(T,5\%)$) values. The SLFRS (i.e., the SCBF) is the only building subsystem considered in this example. The EDP used for the damage assessment of the SCBF is the maximum (considering all stories of the building) residual story drift ratio, θ_r. The median value and dispersion of the demolition fragility function, $F_{\theta_{r,D}}$, are given in Table 5.1. $f_{\theta_m\theta_r|IM}$ must be estimated as an intermediate step when applying Equation (5.8) at each $S_a(T,5\%)$ value. Figure 5.11(c) shows $f_{\theta_m\theta_r|IM}$ for

an arbitrary $S_a(T,5\%)$ value. The $NC \cap D$ damage scenario fragility, constructed using the record-set approach, is shown in Figure 5.11(d). Similar to $P(C)$ shown in Figure 5.11(b), $P(NC \cap D)$ becomes increasingly inaccurate as $S_a(T,5\%)$ increases due to missing IDA results for GMs that have cause collapse at $S_a(T,5\%)$ values less than the given $S_a(T,5\%)$. $P(NC \cap D)$ should decrease to zero as $P(C)$ increases to 1 (i.e., as $P(NC)$ decreases to zero). It can be seen from Figure 5.11(d) that $P(NC \cap D)$ does not decreases to zero as $S_a(T,5\%)$ increases because $P(C)$ does not increase to 1.

5.4.2 Application of record-by-record approach

The IDA curve for a given GM_l and $F_{\theta_{m,C,l}}$ as a function of θ_m is shown in Figure 5.12(a). The IM (i.e., $S_a(T,5\%)$) values are shown on the left side vertical axis for the IDA curve and the $F_{\theta_{m,C,l}}$ values are shown on the right side vertical axis of Figure 5.12(a). As discussed previously, the PDF for $\theta_{m,C}$ for each GM_l is assumed to be uniform between the bounding values of θ_m at 75% slope reduction and θ_m at 85% slope reduction. Therefore, $F_{\theta_{m,C,l}}$, which is the CDF for $\theta_{m,C}$, varies linearly from 0 for θ_m at 75% slope reduction criterion to 1 for θ_m at 85% slope reduction (see Figure 5.12(a)). The process of calculating $P(C|GM_l,IM)$ is illustrated in Figures 5.12(a) and 5.12(b). As shown in Equation (5.15), the probability of collapse for GM_l, at a given $S_a(T,5\%)$ value, is calculated by evaluating $F_{\theta_{m,C,l}}$ at the specific θ_m value determined from the structural analysis for GM_l at the given $S_a(T,5\%)$ value. The collapse fragility for GM_l is shown in Figure 5.12(b). The collapse fragility for other GMs can be developed similarly. The collapse fragility for each GM_l is multiplied by $P(GM = GM_l|IM)$ and then summed as shown in Equation (5.15). Each GM in the ground motion set is assumed to be equally probable at all $S_a(T,5\%)$ values [85]. Therefore $P(GM = GM_l|IM) = 1/L$ where L is the total number of GMs.

The C fragility, constructed using the record-by-record approach, is shown with solid line in Figure 5.12(c). The C fragility, constructed using the record-set approach and shown

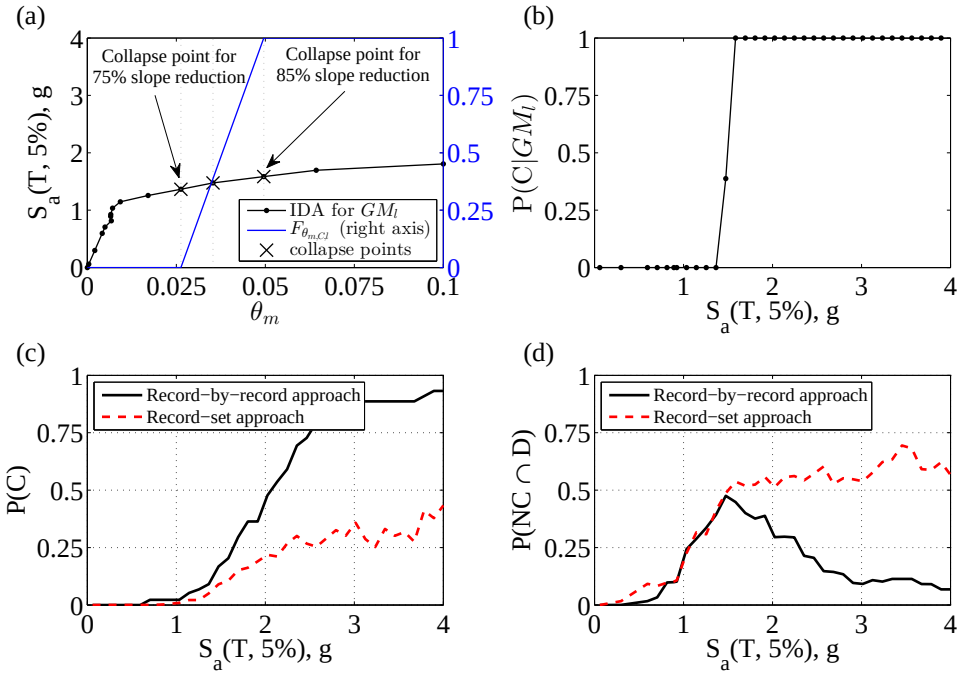

Figure 5.12: Damage scenario fragilities for 9SCBF archetype building using the record-by-record approach: (a) single GM record IDA with probability of collapse calculated from collapse fragility function; (b) collapse fragility curve for single GM record; (c) fragility for C damage scenario; and (d) fragility for $NC \cap D$ damage scenario

previously in Figure 5.11(b), is shown with a dashed line in Figure 5.12(c) for comparison. In the record-by-record approach, $P(C|IM)$ is calculated for each GM_l individually, and combined to estimate $P(C|IM)$ for the GM set, at each $S_a(T,5\%)$ value. Therefore, the effect of all GMs are considered in the probability of collapse at all $S_a(T,5\%)$ values. This can be seen from Figure 5.12(c) by comparing the C damage scenario fragility obtained using the record-by-record approach and the record-set approach, where $P(C)$ for record-by-record approach increases to 1 as $S_a(T,5\%)$ increases.

The process of calculating the fragility for other damage scenarios is similar to the process for C damage scenario. The $NC \cap D$ damage scenario is calculated using Equations (5.17). It is assumed that $F_{\theta_{r,D,l}}$ is equal to $F_{\theta_{r,D}}$ as mentioned earlier. The median value and dispersion of $\theta_{r,D}$ are given in Table 5.1. The $NC \cap D$ fragility, calculated us-

ing the record-by-record approach is shown with solid line in Figure 5.12(d). The $NC \cap D$ fragility, calculated using the record-set approach and shown previously in Figure 5.11(d), is shown with a dashed line in Figure 5.12(d) for comparison. It can be seen that the $NC \cap D$ fragility (calculated using the record-by-record approach) increases from zero to its peak at $S_a(T,5\%) \approx 1.5g$ and then decreases as $S_a(T,5\%)$ increases. The small values of $P(NC \cap D)$ at small $S_a(T,5\%)$ values are due to the small probability of damage requiring demolition. The considerable values of $P(NC \cap D)$ (e.g., around the peak) occur at $S_a(T,5\%)$ values where non-collapse and demolition have significant probabilities. The small values of $P(NC \cap D)$ at large $S_a(T,5\%)$ values are due to the large probability of collapse (so that probability of non-collapse is small). The $NC \cap D$ fragility, calculated by the record-set approach, does not decrease to zero as $S_a(T,5\%)$ increases because the probability of non-collapse (calculated using the record-set approach) does not become zero as $S_a(T,5\%)$ increases.

At the component level, the probability of $NC \cap ND \cap DS_{c,q}$ is calculated for the braces of the SCBF. The EDP used to quantify the brace damage is the normalized residual out-of-plane deformation at the mid-length of the braces (Δ_{Or}). Δ_{Or} is the residual out-of-plane deformation of the brace divided by the initial length of the brace. Three brace DS with corresponding repair actions of: (i) no repair, *NR* (corresponds to $DS_{c,q,0}$); (ii) brace straightening, *BS* (corresponds to $DS_{c,q,1}$); and (iii) brace replacement *BR* (corresponds to $DS_{c,q,2}$) are considered [3]. The median value and dispersion of the two fragility functions $F_{\Delta_{Or,DS,1}}$ and $F_{\Delta_{Or,DS,2}}$, separating the three brace DS, are given in Table 5.1. These values are selected based on experimental results by Powell [59] and analytical studies by Akbas [3].

For the brace damage assessment, it is assumed that the brace DS fragility functions, $F_{EDP_{c,q,DS,n,l}}$, are the same for all GM_l in the GM set, and are the same for all brace components (i.e., $F_{EDP_{c,q,DS,n,l}} = F_{EDP_{c,DS,n}}$ where $EDP_{c,DS,n} = \Delta_{Or,DS,n}$). The two fragility functions $F_{\Delta_{Or,DS,1}}$ and $F_{\Delta_{Or,DS,2}}$ separating the three brace damage states are shown in Figure 5.13(a).

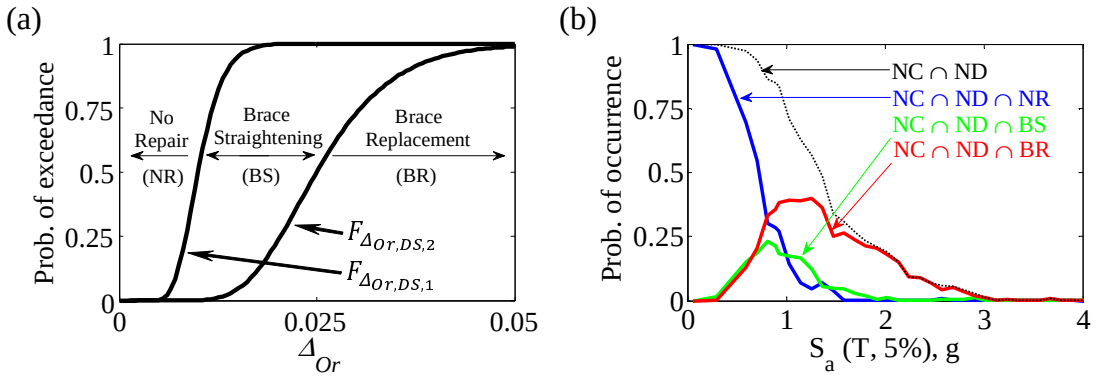

Figure 5.13: Brace damage assessment: (a) fragility functions separating brace DS; and (b) brace damage scenario fragilities constructed using record-by-record approach for 3^{rd} story right side brace of 9SCBF archetype building

Using these fragility functions, the damage scenario fragility for $NC \cap ND \cap DS_{c,q,n}$ for the three damage scenarios involving the three brace DS are calculated for the 3^{rd} story right side brace (i.e., $q = 3^{rd}$ story right side brace and $n = 1,2,3$), and shown in Figure 5.13(b).

It can be seen that the probability of no collapse and no demolition of the building without the need to repair the 3^{rd} story right side brace (i.e. $P(NC \cap ND \cap NR)$) decreases and becomes small at $S_a(T,5\%) \approx 1.5g$. The probability of no collapse and no demolition but having to straighten the 3^{rd} story right side brace (i.e., $P(NC \cap ND \cap BS)$) increases to about 25% at $S_a(T,5\%) \approx 0.9g$ and then decreases to nearly zero at $S_a(T,5\%) \approx 2.0g$. The probability of no collapse and no demolition but having to replace the 3^{rd} story right side brace (i.e. $P(NC \cap ND \cap BR)$) increases to about 40% at $S_a(T,5\%) \approx 1.5g$ and then becomes nearly zero at $S_a(T,5\%) \approx 3.0g$. The $NC \cap ND \cap BS$ and $NC \cap ND \cap BR$ damage scenarios have a considerable probability at the MCE IM level (where $S_a(T,5\%) = 0.89g$). The $NC \cap ND$ fragility is also shown in Figure 5.13(b). The sum of $P(NC \cap ND \cap NR)$, $P(NC \cap ND \cap BS)$, and $P(NC \cap ND \cap BR)$ at each $S_a(T,5\%)$ value is equal to $P(NC \cap ND)$ due to the collective exhaustiveness of the brace DS.

Similar damage scenario fragility results can be constructed for other braces of the 9-

story SCBF. Figure 5.14 shows the $NC \cap ND \cap NR$, $NC \cap ND \cap BS$, and $NC \cap ND \cap BR$ fragilities for all 18 braces of the 9SCBF archetype building. The $NC \cap ND$ fragility is also shown in Figure 5.14. Among the $NC \cap ND \cap NR$ fragilities shown in Figure 5.14(a) and (d), those that are closer to the $NC \cap ND$ fragility correspond to braces with less damage. Among the $NC \cap ND \cap BS$ and $NC \cap ND \cap BR$ fragilities, the smallest fragilities, closer to the $S_a(T, 5\%)$ axis represent less damage. The $NC \cap ND \cap BS$ fragilities reach a peak near the DBE IM level (where, $S_a(T, 5\%) = 0.59g$), while the $NC \cap ND \cap BR$ fragilities reach a peak near the MCE IM level (where, $S_a(T, 5\%) = 0.89g$). The 9^{th} story braces did not have any damage and thus the $NC \cap ND \cap NR$ fragilities for the 9^{th} story braces are identical to the $NC \cap ND$ fragility. The 8^{th} story brace damage is small for most GM, and the $NC \cap ND \cap NR$ fragilities for the 8^{th} story braces are close to the $NC \cap ND$ fragility. The 3^{rd} story braces are the most heavily damaged braces for most GM, and the $NC \cap ND \cap NR$ fragilities for the 3^{rd} story braces are farthest from the $NC \cap ND$ fragility.

5.4.3 Advantages of the record-by-record approach

The record-by-record approach avoids the shortcomings and inaccuracies of the record-set approach by performing the DSTA for each GM individually. The main advantages of the record-by-record approach over the record-set approach are: (i) eliminating the need to estimate (joint) PDF of the EDPs *at each IM value*; (ii) including the correlation between different EDPs directly within the structural response analysis results for each GM_l and at each given IM value; (iii) enabling the use of GM-specific DS fragility functions for each GM if needed; and (iv) separating the epistemic uncertainty in the collapse DS fragility function from the RTR variability in structural response. These advantages are discussed in more detail below.

Estimating the the (joint) PDF of the EDPs (e.g., $f_{\theta_m|IM}$ or $f_{\theta_m\theta_r|IM}$) *at each IM value*, which is required for the record-set approach, is computationally expensive (especially

when the number of EDPs is large, for example, when many components are included in the damage analysis). The record-by-record approach eliminates the need to estimate these PDFs because the damage scenario probabilities are evaluated for each GM individually. The estimated PDFs used in the record-set approach introduce inaccuracy in the probability of damage scenarios, because they approximate both the actual probability distribution and the correlation among the EDPs. In the record-by-record approach, correlations among

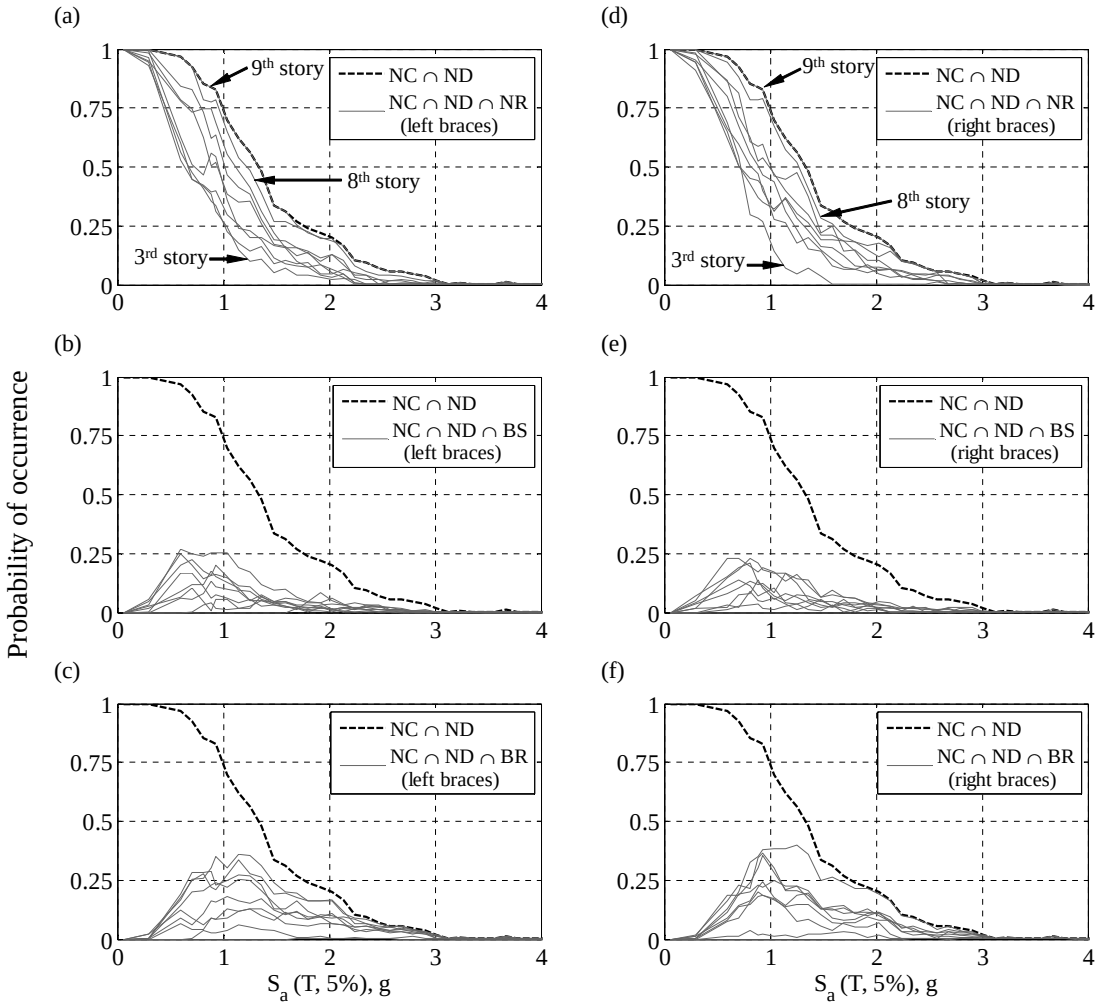

Figure 5.14: Damage scenario fragility results for all braces of 9SCBF archetype building: (a) $NC \cap ND \cap NR$ for left side braces; (b) $NC \cap ND \cap BS$ for left side braces; (c) $NC \cap ND \cap BR$ for left side braces; (d) $NC \cap ND \cap NR$ for right side braces; (e) $NC \cap ND \cap BS$ for right side braces; and (f) $NC \cap ND \cap BR$ for right side braces;

the EDPs are included directly within the structural response analysis results for each individual GM. For example, when calculating $P(NC \cap D|IM)$, θ_{m_l} and θ_{r_l} determined by the structural response analysis for GM_l are used to calculate $P(NC \cap D|GM_l, IM)$.

The record-by-record approach enables the use of GM-specific DS fragility function, determined for each individual GM separately. This advantage is specifically useful for the collapse DS where it was shown that the collapse fragility functions representing only the epistemic uncertainty in the collapse DS criteria, vary with the ground motion. For the record-set approach, the collapse DS fragility function $F_{\theta_{m,C}}$ (which represents $\theta_{m,C}$) is dominated by RTR variability, and the effect of epistemic uncertainty in the collapse DS criteria is small.

At the same time, RTR variability dominates the uncertainty in the EDP used to quantify the collapse DS, θ_m. As a result, the assumption of statistical independence of θ_m and $\theta_{m,C}$ in the record-set approach is questionable.

5.5 Damage Analysis with IM-based Collapse Fragility Function

In Equation (5.5) and the related equations, the probability of the collapse DS was quantified by comparing θ_m (i.e., an EDP) with $\theta_{m,C}$ (i.e., the EDP limit value for the collapse DS, or the EDP-based collapse capacity). Ultimately an EDP-based collapse fragility function $F_{\theta_{m,C,l}}$ (e.g., Figure 5.12(a)) is used for this comparison. This method is known as an EDP-based method for quantifying collapse [94]. An alternative method for quantifying the collapse DS probability is to use the record-by-record approach with an IM-based collapse capacity, which is the IM value at which the building collapses (denoted by IM_C) [94, 33] as shown in Figure 5.15(a). As discussed in Chapter 4, an IM-based method of

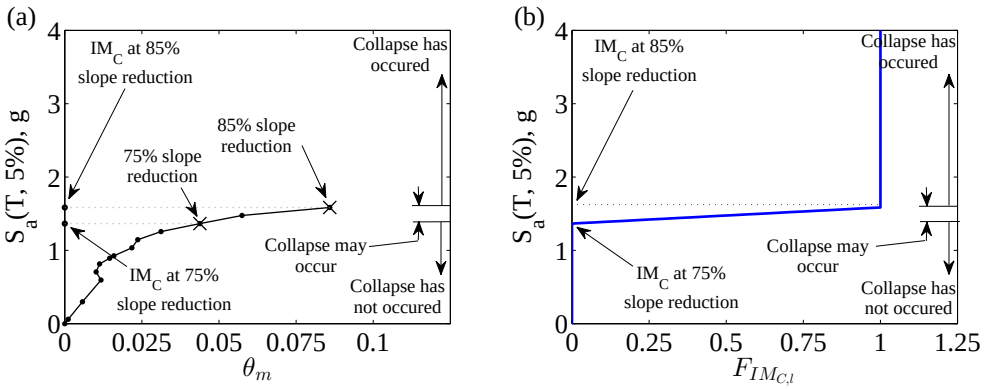

Figure 5.15: IM-based method of quantifying collapse DS probability for a given GM_l with epistemic uncertainty in collapse DS criteria: (a) IDA for GM_l; and (b) probability of collapse for GM_l (i.e., $F_{IM_{C,l}}$)

quantifying the collapse DS probability is used by FEMA P695 [23]. In the present study, an IM-based method of quantifying the collapse DS probability is included in a DSTA and combined with the EDP-based method of quantifying other DS probabilities to evaluate the damage scenario probabilities.

In the IM-based method presented here, the ground motion RTR variability of the structural response and the epistemic uncertainty in the collapse DS criteria are included in evaluating the probability of collapse. Including the effect of building system parameter variability and uncertain modeling decisions and parameters in a DSTA is discussed in Chapter 6. Using the law of total probability, $P(C|IM)$ is evaluated using the record-by-record approach with the IM-based method for quantifying the collapse DS probability as follows:

$$P(C|IM) = \sum_{all\ GM_l} P(IM \geq IM_C|GM = GM_l, IM) \cdot P(GM = GM_l|IM) \tag{5.20}$$

where $P(IM \geq IM_C|GM = GM_l, IM)$ is the probability of the given IM value exceeding IM_C, for the given GM_l.

Equation (5.20) can be rewritten using the IM-based collapse fragility function for GM_l

as follows:

$$P(C|IM) = \sum_{all\ GM_l} F_{IM_{C,l}}(IM) \cdot P(GM = GM_l|IM) \tag{5.21}$$

where $F_{IM_{C,l}}$ is the CDF for IM_C determined for GM_l. $F_{IM_{C,l}}$ represents the epistemic uncertainty in the collapse DS criteria. $F_{IM_{C,l}}$ for a given GM_l is shown in Figure 5.15(b). Similar to $F_{\theta_{m,C,l}}$ used in the EDP-based method for quantifying the collapse DS probability (shown in Figure 5.12(a)), the PDF for IM_C for each GM_l is assumed to be uniform between the bounding value of IM at 75% slope reduction and IM at 85% slope reduction for the IDA curve for GM_l. Therefore, $F_{IM_{C,l}}(IM)$, which is the CDF for IM_C, varies linearly from 0 for the IM value at 75% slope reduction to 1 for the IM value at 85% slope reduction, as shown in Figure 5.15(b). Evaluation of $P(C|IM)$ using the IM-based method represented by Equation (5.21) is comparable to the EDP-based method represented by Equation (5.15). $F_{\theta_{m,C,l}}(\theta_m)$ in Equation (5.15) is replaced by $F_{IM_{C,l}}(IM)$ in Equation (5.21).

Other damage scenarios can be evaluated using the record-by-record approach with the IM-based method for the collapse DS and the EDP-based method for the other DS. Equation (5.3) can be expressed as follows:

$$P(NC \cap D|IM) = \sum_{all\ GM_l} P(IM < IM_C \cap \theta_r \geq \theta_{r,D}|GM = GM_l, IM) \cdot P(GM = GM_l|IM) \tag{5.22}$$

Equation (5.22) can be expressed in terms of the complementary IM-based collapse fragility function ($\bar{F}_{IM_{C,l}} = 1 - F_{IM_{C,l}}$) for GM_l and $F_{\theta_{r,D,l}}$ as follows:

$$P(NC \cap D|IM) = \sum_{all\ GM_l} \bar{F}_{IM_{C,l}}(IM) \cdot F_{\theta_{r,D,l}}(\theta_{r_l}) \cdot P(GM = GM_l|IM) \tag{5.23}$$

In writing Equation (5.23), it is assumed that IM_C and $\theta_{r,D}$ are statistically independent.

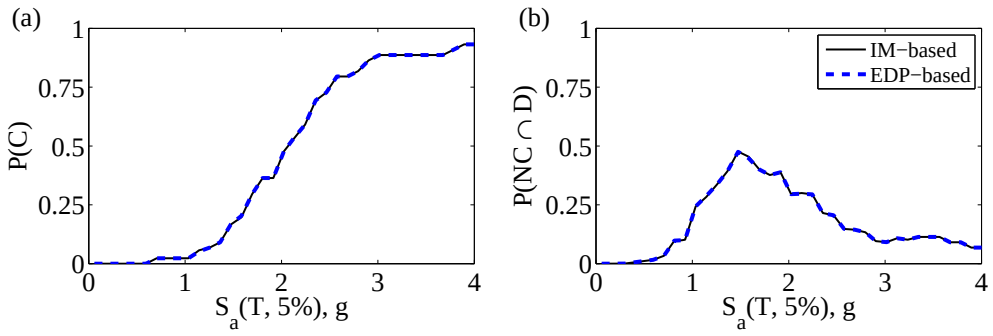

Figure 5.16: Comparison of the fragilities between EDP-based and IM-based method of quantifying collapse for 9SCBF archetype building: (a) collapse damage scenario; and (b) non-collapse with demolition damage scenario

Similarly, Equation (5.4) can be expressed as follows:

$$P(NC \cap ND \cap DS_{c,q,n}|IM) = \sum_{all\ GM_l} \bar{F}_{IM_{C,l}}(IM) \cdot \bar{F}_{\theta_{r,D,l}}(\theta_{r_l}) \cdot \left(F_{EDPc,q,DS,n,l}(EDP_{(c,q)_l}) - F_{EDPc,q,DS,n+1,l}(EDP_{(c,q)_l})\right) \cdot P(GM = GM_l|IM) \quad (5.24)$$

The fragilities for the C and $NC \cap D$ damage scenarios, calculated using the record-by-record approach with either the IM-based or the EDP-based method of quantifying the collapse DS probability for the 9SCBF archetype building are shown in Figure 5.16. The damage scenario fragilities calculated with the IM-based method are quite similar to those calculated with the EDP-based method. The use of the record-by-record approach enables the similarity of these results.

5.6 Summary and Findings

Damage scenario tree analysis (DSTA) for building system seismic damage is presented in this chapter. A DSTA organizes the damage analysis of a building into system, subsystem, and component level damage assessments. Collapse and non-collapse of the building are

the two damage states (DS) considered for the system level damage assessment. Demolition and reconstruction, and non-demolition of the building are the two DS considered at the subsystem level damage assessment. At the component level, different DS can be considered depending on the type of component. Various damage scenarios are developed using these damage states. The three damages scenarios of interest, that are discussed, are: (i) collapse (C); (ii) non-collapse with demolition ($NC \cap D$); and (iii) non-collapse, non-demolition, with component damage ($NC \cap ND \cap DS_c$). The different DS considered for each damage assessment are mutually exclusive and collectively exhaustive. As a result, a DSTA provides a rigorous framework for calculating the fragilities for various damage scenarios.

Two approaches for calculating the damage scenario probabilities in a DSTA were considered: (i) a record-set aproach; and (ii) a record-by-record approach. It is shown that the record-by-record approach is effective and avoids several disadvantages of the record-set approach. The record-by-record approach avoids the expensive (and potentially inaccurate) process of estimating the joint probability density function (PDF) of the engineering demand parameters (EDPs) from a set of incremental dynamic analysis (IDA) results for the ground motion record set being considered. The record-by-record approach calculates the damage scenario probabilities for each ground motion record (GM) in the set individually. Therefore, the correlations between various EDPs, needed for damage assessment at different levels in the DSTA, are directly considered because the EDP values for the given GM are obtained from one structural response analysis for that GM. The record-by-record approach enables the use of GM-specific damage state (DS) fragility functions in the DSTA, which was shown to be useful for including the epistemic uncertainty in the collapse DS criteria, as the criteria are applied to the IDA results for an individual GM. In contrast for the record-set approach, the collapse DS fragility function is dominated by RTR variability. The record-by-record approach was shown to be flexible in using EDP-based, IM-based, or

a combination of EDP-based and IM-based methods for the DS fragility functions.

Chapter 6

Incorporating System Parameter Variability and Modeling Uncertainty in Damage Analysis of Buildings Using DSTA

6.1 Introduction

Damage scenario tree analysis (DSTA), presented in Chapter 5, provides a robust framework for developing earthquake-induced damage scenario fragilities for a building. Three distinct damage assessments are performed in a DSTA: (i) system level damage assessment; (ii) subsystem level damage assessment; and (iii) component level damage assessment. At the system level, the damage state of building collapse is evaluated. At the subsystem level, the damage to the subsystems of the building is evaluated and the possible outcomes are demolition and reconstruction of the building or non-demolition and repair of damaged components. At the component level, the damage state for one or more components is evaluated. By combining these three damage assessment levels in a damage scenario tree, three types of damage scenarios can be considered for a building: (i) building collapse (C); (ii) non-collapse with demolition and building reconstruction ($NC \cap D$); and (iii) non-collapse, non-demolition, with possible component damage ($NC \cap ND \cap DS_c$).

Three primary sources of uncertainty when evaluating the probability of a damage scenario for a given building are: (i) the record-to-record (RTR) variability in structural response; (ii) the variability of the building system parameters; and (iii) the uncertainty regarding the numerical modeling decisions and parameters. Only the RTR variability in structural response is considered in the DSTA presented in Chapter 5. In this chapter,

the variability of system parameters, and uncertain modeling decisions and parameters are included in the DSTA. The variability of system parameters, and uncertain modeling decisions and parameters are treated together in this chapter, and are referred to generally as the "system parameter variability and modeling uncertainty". The set of system parameters and modeling decisions and parameters that are treated in this chapter are referred to as "random system and modeling parameters". An approach, conceptually similar to the record-by-record approach presented in Chapter 5, is developed for treating the random system and modeling parameters to include system parameter variability and modeling uncertainty in the DSTA.

6.2 Damage Analysis Approach

The use of the record-by-record approach in a DSTA is described in Chapter 5. In the record-by-record approach, the probability of a damage scenario is evaluated for each individual GM separately. The probability of the damage scenario is then evaluated by expanding over all GM. For example, $P(C|IM)$ is evaluated using the record-by-record approach as follows:

$$P(C|IM) = \sum_{all\ GM_l} P(C|GM = GM_l, IM) \cdot P(GM = GM_l|IM) \tag{6.1}$$

The effect of system parameter variability and modeling uncertainty can be considered in a DSTA by performing a full Monte Carlo (MC) simulation. In a conventional full MC simulation, all random parameters are sampled simultaneously and therefore the number of samples is the same for all random parameters. In the present study, however, the sampling for a full MC simulation is conducted by separating the sampling of the GM from the sampling of the random system and modeling parameters. The sampling for the GM is done by assembling and using a GM set (e.g., the Far-Field GM set in FEMA P695 [23]), and treat-

ing each GM, denoted by GM_l, as equally probable. The sampling for the random system and modeling parameters is conducted by developing and using probability distributions for the random system and modeling parameters, and applying a technique for sampling from these distributions (e.g., random sampling or Latin Hypercube sampling).

Assuming that samples of the random system and modeling parameters have been taken, a numerical model developed using the i^{th} set of samples for the random system and modeling parameters is denoted by MDL_i. Structural response history analyses are then conducted for each sampled GM (i.e., each GM_l from the assembled GM set) and each numerical model MDL_i. Therefore, the total number of analyses required for a full MC simulation in the present study will be the number of GM_l in the GM set (e.g., L GMs) multiplied by the number of numerical models MDL_i (e.g., I numerical models). Note that in a conventional full MC simulation the total number of analyses is equal to the number of samples (e.g., I) from the sampling technique.

The system parameter variability and modeling uncertainty is included in the probability of a damage scenario by treating the results for each structural response history analysis (conducted for GM_l, and MDL_i at a given IM value) separately. This approach is similar in concept to the record-by-record approach discussed in Chapter 5, and is presented in this chapter as an extension to the record-by-record approach to include system parameter variability and modeling uncertainty in the damage analysis. For example, in Chapter 5, the probability of collapse is evaluated separately for each GM_l using the record-by-record approach, while here, the probability of collapse can be evaluated separately for each GM_l and MDL_i pair. Therefore, $P(C|GM = GM_l, IM)$ in Equation (6.1) can be evaluated using the results of structural response history analyses conducted for each GM_l and all MDL_i at a

given IM value, using the law of total probability and expanding over all MDL_i as follows:

$$P(C|GM = GM_l, IM) = \sum_{all\ MDL_i} P(C|MDL = MDL_i, GM = GM_l, IM) \cdot P(MDL = MDL_i|GM = GM_l, IM) \quad (6.2)$$

where $P(C|MDL = MDL_i, GM = GM_l, IM)$ is the probability of collapse given that the numerical model MDL_i is developed for the i^{th} set of samples (of the random system and modeling parameters) and for GM_l at a given IM value; and $P(MDL = MDL_i|GM = GM_l, IM)$ is the probability of having MDL_i (i.e., of having the i^{th} set of samples) for GM_l at a given IM value. Assuming MDL_i is independent of GM_l and IM, $P(MDL = MDL_i|GM = GM_l, IM)$ is simplified to $P(MDL = MDL_i)$. Therefore, Equation 6.2 can be simplified as follows:

$$P(C|GM = GM_l, IM) = \sum_{all\ MDL_i} P(C|MDL = MDL_i, GM = GM_l, IM) \cdot P(MDL = MDL_i) \quad (6.3)$$

Substituting Equation (6.3) in Equation (6.1), $P(C|IM)$ can be stated as follows:

$$P(C|IM) = \sum_{all\ GM_l} \sum_{all\ MDL_i} P(C|MDL = MDL_i, GM = GM_l, IM) \cdot P(MDL = MDL_i) \cdot P(GM = GM_l|IM) \quad (6.4)$$

It can be seen from Equation (6.4) that the probability of collapse is being evaluated for each pair of GM_l and MDL_i and then multiplied by $P(MDL = MDL_i)$ and $P(GM = GM_l|IM)$. $P(C|IM)$ is then determined by summing the probabilities for all GM_l and MDL_i pairs. Similarly, the probabilities of other damage scenarios such as $P(NC \cap D)$ and $P(NC \cap ND \cap DS_{c,q,n})$ can be evaluated considering system parameter variability and

modeling uncertainty as follows:

$$P(NC \cap D|IM) = \sum_{all\ GM_l} \sum_{all\ MDL_i} P(NC \cap D|MDL = MDL_i, GM = GM_l, IM) \cdot P(MDL = MDL_i) \cdot P(GM = GM_l|IM) \quad (6.5)$$

$$P(NC \cap ND \cap DS_{c,q,n}|IM) = \sum_{all\ GM_l} \sum_{all\ MDL_i} P(NC \cap ND \cap DS_{c,q,n}|MDL = MDL_i, GM = GM_l, IM) \cdot P(MDL = MDL_i) \cdot P(GM = GM_l|IM) \quad (6.6)$$

Chapter 5 presents two methods for quantifying the probability of a damage scenario: (i) using the EDP-based method for all DS; and (ii) using a combination of the IM-based method for the collapse DS and the EDP-based method for the other DS. In the following sections, these two methods are used to evaluate Equations (6.4), (6.5), and (6.6).

6.2.1 EDP-based method

In the EDP-based method for quantifying the probability of being in a DS, the EDP value from structural response history analysis is compared against an EDP limit value, separating two DS. The maximum story drift ratio, θ_m, is used for quantifying the probability of the collapse DS. In the EDP-based method, the collapse DS is reached when $\theta_m \geq \theta_{m,C}$, where $\theta_{m,C}$ is the θ_m limit value separating the non-collapse DS from the collapse DS.

Using the EDP-based method of quantifying the collapse DS, Equation (6.4) can be

written as follows:

$$P(C|IM) = \sum_{all\ GM_l} \sum_{all\ MDL_i} P(\theta_m \geq \theta_{m,C}|MDL = MDL_i, GM = GM_l, IM) \cdot P(MDL = MDL_i) \cdot P(GM = GM_l|IM) \quad (6.7)$$

Only one θ_m value is obtained from the structural response analysis conducted for each MDL_i and GM_l pair at each given IM value. As shown in Chapter 5, a range of possible collapse points can be determined from the IDA curve (developed for each MDL_i and GM_l pair) using the 75% and 85% slope reduction criteria. Using the cumulative density function (CDF) for the $\theta_{m,C}$ values established from the IDA curve for MDL_i and GM_l (i.e., $F_{\theta_{m,C,l,i}}$) to quantify $P(\theta_m \geq \theta_{m,C}|MDL = MDL_i, GM = GM_l, IM)$, Equation 6.7 can be written as follows:

$$P(C|IM) = \sum_{all\ GM_l} \sum_{all\ MDL_i} F_{\theta_{m,C,l,i}}(\theta_m) \cdot P(MDL = MDL_i) \cdot P(GM = GM_l|IM) \quad (6.8)$$

The collapse fragility function $F_{\theta_{m,C,l,i}}$ represents the uncertainty in the collapse point on the IDA curve for the given GM_l and MDL_i due to epistemic uncertainty in the collapse DS criteria. It is assumed that the underlying random variable for $F_{\theta_{m,C,l,i}}$, i.e., $\theta_{m,C,l,i}$, follows a uniform distribution between the two bounding values of θ_m corresponding to 75% and 85% slope reduction of the IDA curve for the given GM_l and MDL_i pair. Therefore, the collapse fragility function $F_{\theta_{m,C,l,i}}$ is the CDF for a uniform distribution, varying linearly from 0 at θ_m corresponding to 75% slope reduction to 1.0 at θ_m corresponding to 85% slope reduction. Extensive discussion of this epistemic uncertainty in the collapse DS criteria, considering the IDA curve slope reduction is presented in Chapter 5.

Quantifying $P(NC \cap D|IM)$ considering system parameter variability and modeling uncertainty is similar to quantifying $P(C|IM)$ using Equation (6.4). The maximum (over all

stories of the building) residual story drift ratio, θ_r, is used for quantifying the damage to the SLFRS of the building and for quantifying the probability of demolition. Therefore, the damage scenario $NC \cap D$ is quantified by $\theta_m < \theta_{m,C} \cap \theta_r \geq \theta_{r,D}$, where $\theta_{r,D}$ is the θ_r limit value separating two DS of the SLFRS corresponding, respectively, to the non-demolition and the demolition and reconstruction of the building. Equation (6.5) can be written using the EDP-based method of quantifying the probability of each DS as follows:

$$P(NC \cap D|IM) = \sum_{all\ GM_l} \sum_{all\ MDL_i} P(\theta_m < \theta_{m,C} \cap \theta_r \geq \theta_{r,D}|MDL = MDL_i, GM = GM_l, IM) \cdot P(MDL = MDL_i) \cdot P(GM = GM_l|IM) \quad (6.9)$$

One θ_m value and one θ_r value are obtained from the structural response history analysis conducted for each MDL_i and GM_l pair at each given IM value. Assuming $\theta_{m,C}$ and $\theta_{r,D}$ are statistically independent, $P(\theta_m < \theta_{m,C} \cap \theta_r \geq \theta_{r,D}|MDL = MDL_i, GM = GM_l, IM)$ can be quantified as the complementary CDF of $\theta_{m,C}$ (for MDL_i and GM_l) evaluated at θ_m multiplied by the CDF of $\theta_{r,D}$ (i.e., $F_{\theta_{r,D}}$) evaluated at θ_r. Therefore, Equation (6.9) can be written as follows:

$$P(NC \cap D|IM) = \sum_{all\ GM_l} \sum_{all\ MDL_i} \bar{F}_{\theta_{m,C,l,i}}(\theta_m) \cdot F_{\theta_{r,D}}(\theta_r) \cdot P(MDL = MDL_i) \cdot P(GM = GM_l|IM) \quad (6.10)$$

where $\bar{F}_{\theta_{m,C,l,i}} = 1 - F_{\theta_{m,C,l,i}}$ and $F_{\theta_{r,D}}$ is the CDF of $\theta_{r,D}$.

Similarly, $P(NC \cap ND \cap DS_{c,q,n}|IM)$ can be evaluated including system parameter vari-

ability and modeling uncertainty using θ_m, θ_r, and $EDP_{c,q}$ as follows:

$$P(NC \cap ND \cap DS_{c,q,n}|IM) = \sum_{all\ GM_l} \sum_{all\ MDL_i} P(\theta_m < \theta_{m,C} \cap \theta_r < \theta_{r,D} \cap EDP_{c,q} \geq EDP_{c,q,DS,n}|MDL = MDL_i, GM = GM_l, IM) \cdot P(MDL = MDL_i) \cdot P(GM = GM_l|IM) \quad (6.11)$$

Only one θ_m value, one θ_r value, and one $EDP_{c,q}$ value are obtained from the structural response history analysis conducted for each MDL_i and GM_l pair at each given IM value. Assuming $\theta_{m,C}$, $\theta_{r,D}$, and $EDP_{c,q,DS,n}$ are statistically independent, Equation (6.11) can be written as follows:

$$P(NC \cap ND \cap DS_{c,q,n}|IM) = \sum_{all\ GM_l} \sum_{all\ MDL_i} \bar{F}_{\theta_{m,C,l,i}}(\theta_m) \cdot \bar{F}_{\theta_{r,D}}(\theta_r) \cdot \left(F_{EDP_{c,q,DS,n}}(EDP_{c,q}) - F_{EDP_{c,q,DS,n+1}}(EDP_{c,q})\right) \cdot P(MDL = MDL_i) \cdot P(GM = GM_l|IM) \quad (6.12)$$

where $\bar{F}_{\theta_{r,D}} = 1 - F_{\theta_{r,D}}$ and $F_{EDP_{c,q,DS,n}}$ is the fragility function for the q^{th} component separating the n^{th} DS from the $n+1^{th}$ DS.

6.2.2 IM-based method

In the IM-based method for quantifying the probability of the collapse DS, a given IM is compared against the IM at collapse, IM_C [94, 23]. Therefore, the probability of collapse is quantified as P($IM \geq IM_C$) in the IM-based method.

Equation (6.4) can be written using the IM-based method of quantifying the probability

of collapse DS as follows:

$$P(C|IM) = \sum_{all\ GM_l} \sum_{all\ MDL_i} P(IM \geq IM_C|MDL = MDL_i, GM = GM_l, IM) \cdot P(MDL = MDL_i) \cdot P(GM = GM_l|IM) \quad (6.13)$$

IM_C in Equation (6.13) is determined from the IDA results developed for each MDL_i and GM_l pair. $P(IM \geq IM_C|MDL = MDL_i, GM = GM_l, IM)$ can be quantified using the CDF of IM_C (determined for the MDL_i and GM_l pair), evaluated at the given IM, i.e., $F_{IM_{C,l,i}}(IM)$. Equation (6.13) can be written in terms of $F_{IM_{C,l,i}}$ as follows:

$$P(C|IM) = \sum_{all\ GM_l} \sum_{all\ MDL_i} F_{IM_{C,l,i}}(IM) \cdot P(MDL = MDL_i) \cdot P(GM = GM_l|IM) \quad (6.14)$$

The collapse fragility function $F_{IM_{C,l,i}}$ represents the uncertainty in the collapse point on the IDA curve for the given GM_l and MDL_i pair. Similar to the development of $F_{IM_{C,l}}$ in Chapter 5, due to the epistemic uncertainty in the collapse DS criteria, $F_{IM_{C,l,i}}$ is based on the bounding values of IM at 75% and at 85% slope reduction of the IDA curve for the GM_l and MDL_i pair. It is assumed that $IM_{C,l,i}$ (the underlying random variable for $F_{IM_{C,l,i}}$) follows a uniform distribution between the two bounding IM values and therefore $F_{IM_{C,l,i}}$ varies linearly from 0 at the IM value corresponding to 75% slope reduction to 1.0 at the IM value corresponding to 85% slope reduction. Extensive discussion about the bounding collapse points corresponding to the 75% and 85% slope reduction is given in Chapter 5.

Similarly, $P(NC \cap D|IM)$ can be evaluated including system parameter variability and modeling uncertainty using the IM-based method of quantifying the probability of the collapse DS and the EDP-based method of quantifying the probability of demolition. There-

fore, Equation (6.5) can be evaluated as follows:

$$P(NC \cap D|IM) = \sum_{all\ GM_l} \sum_{all\ MDL_i} P(IM < IM_C \cap \theta_r \geq \theta_{r,D}|MDL = MDL_i, GM = GM_l, IM) \cdot P(MDL = MDL_i) \cdot P(GM = GM_l|IM) \quad (6.15)$$

Only one θ_r value is obtained from the structural response history analysis conducted for each MDL_i and GM_l pair at each given IM value. Also, only one CDF for IM_C is determined from the IDA results for each MDL_i and GM_l pair (i.e., $F_{IM_{C,l,i}}$). Assuming that $IM_{C,l,i}$ and $\theta_{r,D}$ are statistically independent, $P(IM < IM_C \cap \theta_r \geq \theta_{r,D}|MDL = MDL_i, GM = GM_l, IM)$ can be quantified using the complementary CDF for $IM_{C,l,i}$ (i.e., $\bar{F}_{IM_{C,l,i}}$), evaluated at the given IM, multiplied by the CDF of $\theta_{r,D}$ (i.e., $F_{\theta_{r,D}}$) evaluated at θ_r. Therefore, Equation (6.15) can be written as follows:

$$P(NC \cap D|IM) = \sum_{all\ GM_l} \sum_{all\ MDL_i} \bar{F}_{IM_{C,l,i}}(IM) \cdot F_{\theta_{r,D}}(\theta_r) \cdot P(MDL = MDL_i) \cdot P(GM = GM_l|IM) \quad (6.16)$$

where $\bar{F}_{IM_{C,l,i}} = 1 - F_{IM_{C,l,i}}$.

Similarly, Equation (6.6) can be evaluated using the IM-based method of quantifying the probability of the collapse DS, the EDP-based method of quantifying the probability of demolition, and the EDP-based method of quantifying the probability of component level DS as follows:

$$P(NC \cap ND \cap DS_{c,q,n}|IM) = \sum_{all\ GM_l} \sum_{all\ MDL_i} P(IM < IM_C \cap \theta_r < \theta_{r,D} \cap EDP_{c,q,DS,n} \leq EDP_{c,q} < EDP_{c,q,DS,n+1}) \cdot P(MDL = MDL_i) \cdot P(GM = GM_l|IM) \quad (6.17)$$

Only one θ_r value and one $EDP_{c,q}$ value are obtained from the structural response history analysis conducted for each MDL_i and GM_l pair at each given IM value. Also, only one CDF for IM_C is determined from the IDA results for each MDL_i and GM_l pair (i.e., $F_{IM_{C,l,i}}$). Assuming that $IM_{C,l,i}$, $\theta_{r,D}$, and $EDP_{c,q,DS,n}$ are statistically independent, $P(IM < IM_C \cap \theta_r < \theta_{r,D} \cap EDP_{c,q,DS,n} \leq EDP_{c,q} < EDP_{c,q,DS,n+1})$ can be quantified using $\bar{F}_{IM_{C,l,i}}$, $\bar{F}_{\theta_{r,D}}$, and the CDF for the component EDP limit value for the n^{th} DS of the q^{th} component (i.e., $F_{EDP_{c,q,DS,n}}$). Therefore, Equation (6.17) can be rewritten as follows:

$$P(NC \cap ND \cap DS_{c,q,n}|IM) = \sum_{all\ GM_l} \sum_{all\ MDL_i} \bar{F}_{IM_{C,l,i}}(IM) \cdot \bar{F}_{\theta_{r,D}}(\theta_r) \cdot \left(F_{EDP_{c,q,DS,n}}(EDP_{c,q}) - F_{EDP_{c,q,DS,n+1}}(EDP_{c,q})\right) \cdot P(MDL = MDL_i) \cdot P(GM = GM_l|IM) \quad (6.18)$$

where, $\bar{F}_{\theta_{r,D}} = 1 - F_{\theta_{r,D}}$ and $F_{EDP_{c,q,DS,n}}$ is the CDF for the component EDP limit value for the n^{th} DS of the q^{th} component.

6.3 Application to Damage Analysis of 9SCBF Archetype Building

A damage scenario tree analysis (DSTA) using the record-by-record approach and including system parameter variability and modeling uncertainty is presented for the 9SCBF archetype building in this section. This DSTA, including system parameter variability and modeling uncertainty, has five main steps:

1. Assembling a GM set (i.e., sampling the GMs)
2. Identifying and developing probability distributions for the random system and modeling parameters, and sampling the parameters

3. Developing a numerical model MDL_i for the building for each set (i) of the sampled values of the random system and modeling parameters

4. Conducting structural response history analyses (in the form of an IDA) for each MDL_i and GM_l pair

5. Completing the DSTA using the results of the structural response analyses (IDAs) and Equations (6.14), (6.16), and (6.18)

Steps 1, 2, 3, and 4 represent a full MC simulation of the uncertain aspects of the damage analysis including the GM and the system parameter variability and modeling uncertainty. In this full MC simulation, the GM sampling and the sampling of random system and modeling parameters are conducted in two separate steps; specifically, the GMs are not varied simultaneously with random system and modeling parameters, as discussed in Section 6.2. After the IDA is completed for each GM_l and MDL_i pair, the DSTA is completed in step 5.

In this section, the DSTA includes an MC simulation using a subset of GMs from the Far-Field GM set to show how system parameter variability and modeling uncertainty is included using Equations (6.14), (6.16), and (6.18). This type of MC simulation is referred to as a "GM subset MC simulation". The earthquake names and recording stations for the five GMs included in the GM subset MC simulation are given in Table 6.1. The five GMs shown in Table 6.1 are called the "GM subset". The individual GMs of the GM subset are denoted by GM_x, where the subscript x is used to distinguish between an individual GM from the GM subset from an individual GM and the GM set (denoted by GM_l). The 5 GMs of the GM subset are selected based on two criteria: (i) minimizing the difference between the median collapse capacity of the 9SCBF archetype building under the 44 GMs of the Far-Field GM set and the median collapse capacity of the 9SCBF archetype building under the 5 GMs of the GM subset; and (ii) minimizing the difference between the logarithmic standard deviation of collapse capacity of the 9SCBF archetype building under the 44 GMs

Table 6.1: Earthquake ground motions used for the GM subset

Earthquake name	Recording station	Component	GM identifier
Friuli, Italy 2000	Tolmezzo	270	TMZ-270
Chi-Chi, Taiwan 1999	TCU045	E	TCU045-E
Manjil, Iran 1990	Manjil	T	ABBAR-T
Superstition Hills, CA 1987	El Centro Imp Co Center	000	ICC-000
Cape Mendocino, CA 1992	Rio Dell overpass	270	RIO-270

of the Far-Field GM set and the logarithmic standard deviation of collapse capacity of the 9SCBF archetype building under the 5 GMs of the GM subset.

6.3.1 Random system parameters

Among all possible random system and modeling parameters for the 9SCBF archetype building, a few random system parameters were selected for this study. Uncertainty regarding the modeling decisions and parameters (i.e., random modeling parameters) are not treated in the examples presented in this research, however, random modeling parameters can be treated similar to the random system parameters. The random system parameters considered for the 9SCBF archetype buildings are: (i) the initial out-of-straightness of the SCBF braces; and (ii) the live load at each floor level of the 9SCBF archetype building. The parameter representing the initial out-of-straightness of the braces is Δ_{Oi}; which is the amplitude of initial out-of-straightness of the SCBF braces divided by the initial brace length (normalized). The live load at different floor levels is denoted by *LL*.

It is assumed that Δ_{Oi} follows a lognormal distribution with a median of 1/1000. Because there is no documented data regarding the dispersion of Δ_{Oi}, a coefficient of variation of 0.3 is assumed for Δ_{Oi}. Correlation between the Δ_{Oi} values ($\rho_{\Delta_{Oi}}$) for different braces is considered. Since there is no documented data regarding the correlation coefficient between two Δ_{Oi} values (for any two braces in the SCBF), the $\rho_{\Delta_{Oi}}$ values between any two Δ_{Oi} values for the 18 braces of the SCBF are assumed to be 0.5. Perfect correlation (i.e.,

$\rho_{\Delta_{Oi}} = 1$) is not considered as it is deemed highly unlikely for all braces to have the same Δ_{Oi} due to random error (or inaccuracy) in the fabrication process for the braces. Zero correlation (i.e., $\rho_{\Delta_{Oi}} = 0$) is also not considered to account for some systematic error (or inaccuracy) in the fabrication process for the braces.

The *LL* at each floor level of the 9SCBF archetype building is assumed to follow a lognormal distribution with the median values as given in Table 3.2 and a coefficient of variation of 0.25 [20, 54]. Perfect correlation is assumed between the *LL* values (i.e., $\rho_{LL} = 1$) at any two floors (of the 8 floors with live load) in the 9SCBF archetype building. Perfect correlation results from assuming that all floors are occupied similarly during the business hours of the archetype building and unoccupied at other times. Also, it is assumed that an accumulation of office contents over time is similar for all floors of the building. Live load is not included at the roof level.

The Δ_{Oi} values and the *LL* values are assumed to be uncorrelated ($\rho_{\Delta_{Oi},LL} = 0$). The total number of random system parameters are $2 \times 9 = 18$ (number of braces) $+ 8$ (number of floors with live load) $= 26$. The total correlation matrix for the above 26 random system parameters is as follows:

$$\boldsymbol{\rho}_{TOT} = \begin{bmatrix} \boldsymbol{\rho}_{\Delta_{Oi}} & \boldsymbol{\rho}_{\Delta_{Oi},LL} \\ \boldsymbol{\rho}_{LL,\Delta_{Oi}} & \boldsymbol{\rho}_{LL} \end{bmatrix} \tag{6.19}$$

where $\boldsymbol{\rho}_{\Delta_{Oi}}$ is the correlation matrix between the 18 Δ_{Oi} values of the SCBF, $\boldsymbol{\rho}_{LL}$ is the correlation matrix between the 8 *LL* values at the floors of the 9SCBF archetype building with live load, and $\boldsymbol{\rho}_{\Delta_{Oi},LL} = \boldsymbol{\rho}^{T}_{LL,\Delta_{Oi}}$ is the correlation matrix between the Δ_{Oi} values of the SCBF braces and the *LL* values at building floors. $\boldsymbol{\rho}_{\Delta_{Oi}}$, $\boldsymbol{\rho}_{LL}$, $\boldsymbol{\rho}_{\Delta_{Oi},LL}$, and $\boldsymbol{\rho}_{LL,\Delta_{Oi}}$ are as

follows:

$$\boldsymbol{\rho}_{\Delta_{Oi}} = \begin{bmatrix} 1 & 0.5 & \cdots & 0.5 \\ 0.5 & 1 & \cdots & 0.5 \\ \vdots & \vdots & \ddots & \vdots \\ 0.5 & 0.5 & \cdots & 1 \end{bmatrix}_{18\times 18} \tag{6.20}$$

$$\boldsymbol{\rho}_{LL} = [\mathbf{1}]_{8\times 8} \tag{6.21}$$

$$\boldsymbol{\rho}_{\Delta_{Oi},LL} = \boldsymbol{\rho}^{T}_{LL,\Delta_{Oi}} = [\mathbf{0}]_{18\times 8} \tag{6.22}$$

The random system parameters are sampled using the Latin Hypercube sampling (LHS) technique [52]. 100 samples are generated for the 18 Δ_{Oi} values and the 8 LL values using the previously described probability distributions for Δ_{Oi} and LL and using the $\boldsymbol{\rho}_{TOT}$ matrix. One numerical model is developed for each set of random system parameter samples. A model created for a set of random system parameter samples is denoted as a "sample model" (and is also denoted by MDL_i). The model created using the median values of the random system parameters is denoted as the "base model". The base model is identical to the numerical model used for the structural response history analyses presented in Chapter 5.

6.3.2 Damage scenario fragilities

The IDA results for the base model of the 9SCBF archetype building using the Far-Field GM set, are shown in Figure 6.1(a). The IDA results for the base model of the 9SCBF archetype building using the GM subset are shown in Figure 6.1(b). The collapse points shown by "X" in Figure 6.1 correspond to 85% slope reduction in each individual IDA

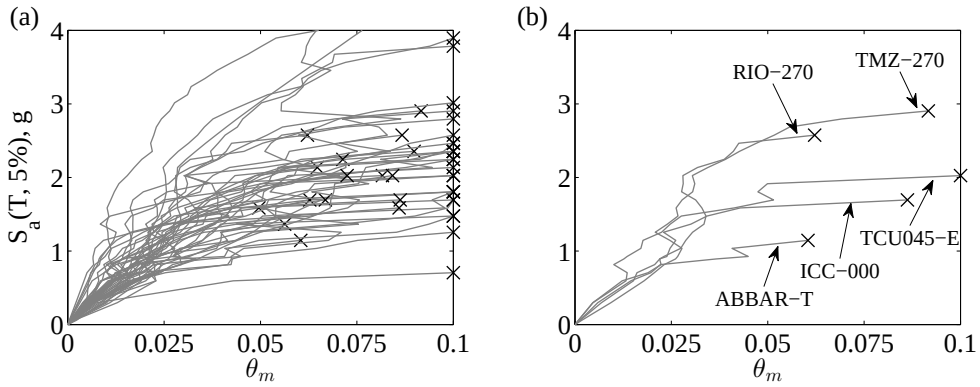

Figure 6.1: IDA results for 9SCBF archetype building: (a) for the far-field GM set; and (b) for the GM subset

curve which is the upper limit value for the slope reduction collapse criterion, as described in Chapter 5. The IDA curves stop at the collapse points shown by "X" in Figure 6.1, as it is assumed that collapse has occurred with certainty for IM (i.e., $S_a(T,5\%)$) values greater than the $S_a(T,5\%)$ value corresponding to the 85% slope reduction. The IM-based collapse fragility function (denoted by $F_{IM_{C,l}}$ in Chapter 5) is used to quantify the probability of collapse for each individual IDA curve. The IM-based collapse fragility function $F_{IM_{C,l}}$ is assumed to be the CDF of a uniform distribution, which varies linearly from the $S_a(T,5\%)$ value corresponding to 75% slope reduction to the $S_a(T,5\%)$ value corresponding to 85% slope reduction, as presented in Section 5.5.

Two collapse (C) damage scenario fragilities, developed for the base model using Equation (5.21), are shown in Figure 6.2. The C damage scenario fragility for the Far-Field GM set is developed using the IDA results from the 44 GMs of the Far-Field GM set. The C damage scenario fragility for the GM subset, on the other hand, is developed using the IDA results from the 5 GMs of the GM subset. Therefore, $P(GM = GM_l) = 1/44$ for the Far-Field GM set and $P(GM = GM_x) = 1/5$ for the GM subset. The effect of using a limited number of GMs (in the GM subset) compared to using the larger Far-Field GM set is a sharp increase of the C damage scenario fragility curve over the range of $S_a(T,5\%)$ values where $F_{IM_{C,x}}$ is defined for each GM_x. This result can be clearly seen from the C damage

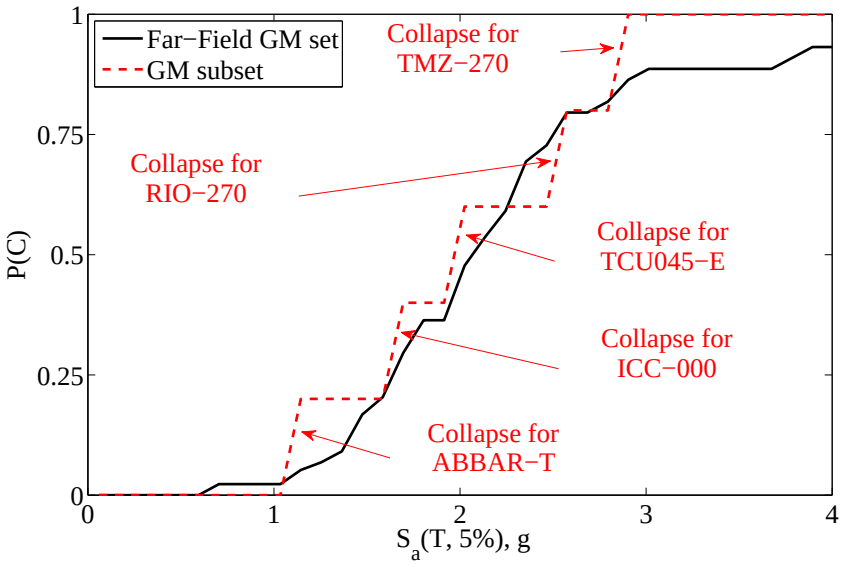

Figure 6.2: The C damage scenario fragility for 9SCBF archetype building determined using the base model and the Far-Field GM set or the GM subset

scenario fragility for the GM subset. Each of the five sharp increases in the C damage scenario fragility for the GM subset in Figure 6.2 occurs over the range of $S_a(T,5\%)$ values corresponding to the collapse range for one GM_x in the GM subset.

The GM subset MC simulation is performed using the five GM_x of the GM subset. For each GM_x of the GM subset, an IDA is performed for each sample model MDL_i (i.e., each numerical model created using the sampled values of the random system parameters). The IDA results for the 9SCBF archetype building using the GM subset are shown in Figure 6.3 for the sample models. The IDA results using the GM subset for the base model are also shown in Figure 6.3. It can be seen that the variation of the random system parameters causes variation in the IDA curves for each GM_x of the GM subset.

As shown by Equation (6.1), $P(C|IM)$ is quantified by evaluating $P(C|GM = GM_l, IM)$ for each GM_l, multiplying by $P(GM = GM_l|IM)$ and then summing the products of these probabilities for all GM_l. In this GM subset MC simulation only the 5 GM_x of the GM subset are used. $P(C|IM)$ is quantified by evaluating $P(C|GM = GM_x, IM)$ for each GM_x of the

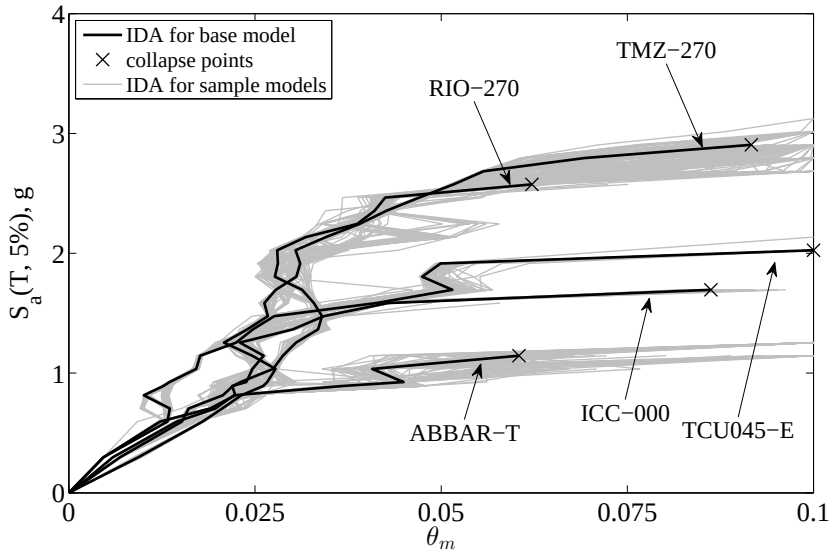

Figure 6.3: IDA results for 9SCBF archetype building using the GM subset and the base model or the sample models

GM subset, multiplying by $P(GM = GM_x|IM) = 1/5$ and then summing the products for the 5 GM_x of the GM subset. Similarly as shown by Equation (6.3), $P(C|GM = GM_l, IM)$ is determined by evaluating $P(C|MDL = MDL_i, GM = GM_l, IM)$ for each MDL_i, multiplying by $P(MDL = MDL_i)$, and then summing the products for all sample models. In the GM subset MC simulation, $P(C|GM = GM_x, IM)$ is determined by evaluating $P(C|MDL = MDL_i, GM = GM_x, IM)$ for each MDL_i, multiplying by $P(MDL = MDL_i) = 1/100$ (assuming all numerical models are equally likely) and then summing the products for all sample models. Comparing Equations (6.4) and (6.14), it can be seen that $P(C|MDL = MDL_i, GM = GM_l, IM)$ is quantified by $F_{IM_{C,l,i}}(IM)$, where $F_{IM_{C,l,i}}$ is determined using the IDA curve for sample model MDL_i and GM_l. In the present GM subset MC simulation, $P(C|MDL = MDL_i, GM = GM_x, IM)$ is quantified by $F_{IM_{C,x,i}}(IM)$, where $F_{IM_{C,x,i}}$ is determined using the IDA curve for sample model MDL_i and GM_x.

Figure 6.4 shows $P(C|GM = GM_x)$ for GM_x = TMZ-270. Three types of curves are shown in Figure 6.4: (i) results for GM_x for the base model; (ii) results for GM_x for the sample models; and (iii) the GM_x MC simulation, which includes the results for all the

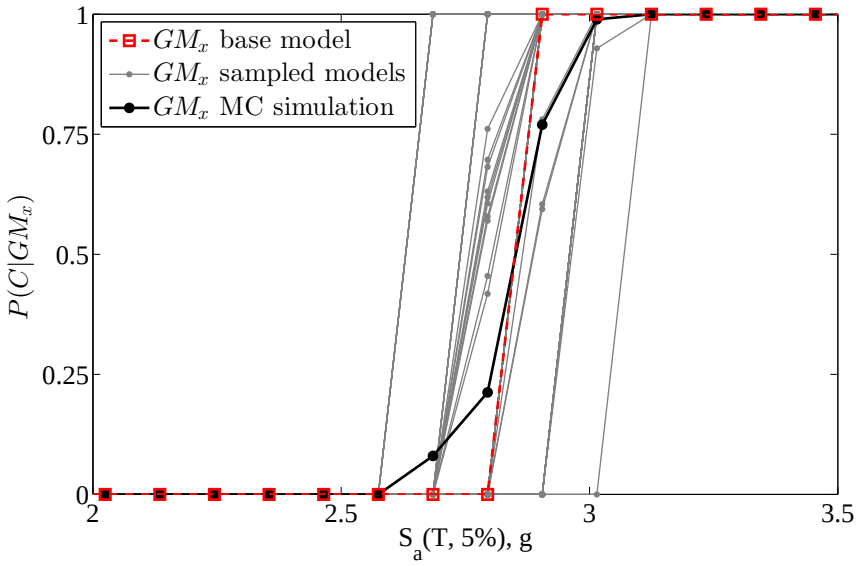

Figure 6.4: $P(C|GM_x)$ for 9SCBF archetype building using GM_x = TMZ-270

sample models. The curve for GM_x for the base model shows $P(C|GM = GM_x)$ calculated for the base model at each IM value, which can be stated as $P(C|GM = GM_x, MDL_{BM}, IM)$, and is quantified by $F_{IM_{C,x,BM}}(IM)$, where $F_{IM_{C,x,BM}}$ is determined using the IDA curve for the base model and GM_x. The curves for the sample models show $P(C|GM = GM_x)$ calculated for GM_x for each sample model MDL_i at each IM value, which can be stated as $P(C|GM = GM_x, MDL_i, IM)$ and is quantified by $F_{IM_{C,x,i}}(IM)$. Finally, the GM_x MC simulation curve is quantified using Equation (6.3) where $P(C|MDL = MDL_i, GM = GM_x, IM)$ is quantified by $F_{IM_{C,x,i}}(IM)$. Therefore, the curve for the GM_x MC simulation in Figure 6.4 is developed by multiplying the $P(C|GM_x)$ values for each sample model MDL_i by $P(MDL_i) = 1/100$ and then summing the products for all sample models.

Equation (6.3) is in fact part of a MC simulation, but it includes only one GM sample, GM_l (or GM_x in the present GM subset MC simulation). The effect of including random system parameters in evaluating $P(C|GM_x)$ can be seen by comparing the curve for the base model with the curve for the GM_x MC simulation in Figure 6.4. It can be seen that the effect of the variation of the random system parameters is an increase in the dispersion in

$P(C|GM_x)$.

The C damage scenario fragility, $P(C|IM)$, for the 9SCBF archetype building, calculated using the GM subset MC simulation and Equation (6.14), is shown in Figure 6.5(a). $P(C|GM_x)$ for each GM_x of the GM subset, calculated using a GM_x MC simulation is also shown in Figure 6.5(a). The contribution of each GM_x to the C fragility can be seen as a sharp increase in $P(C)$, as mentioned previously.

The C fragility calculated using Equation (5.21) for the base model and the 5 GM_x of the GM subset is shown in Figure 6.5(b). Also shown in Figure 6.5(b) is the C fragility calculated using Equation (6.14) for the sample models and the 5 GM_x of the GM subset. It can be seen that the effect of considering system parameter variability, calculated through the GM subset MC simulation, is a smoothing of $P(C)$ at $S_a(T,5\%) \approx 1.2g$ and $S_a(T,5\%) \approx 2.7g$. This smoothing effect is due to the increased dispersion in $P(C|GM_x)$ when the system parameter variability is included (see Figure 6.4).

6.3.3 Variation of EDP due to system parameter variability

By including system parameter variability and modeling uncertainty in a DSTA through a full MC simulation, the variation in the EDP values (i.e., the uncertainty in the EDP values due to the system parameter variability and modeling uncertainty) can be obtained for a given GM_l at each given IM. In other words, various EDP values are obtained from structural response analyses for the given GM_l using various sample models, MDL_i. The variation of different EDPs considered in this study (i.e., θ_m, θ_r, and Δ_{Or}) due to the variation of Δ_{Oi} and LL is presented and discussed in this section. Before discussing the variation of the EDP values, the relationship between the EDP and IM values is described based on an understanding of IDA results.

A "one-to-one" relationship between the IM, the "independent" variable, and the EDP,

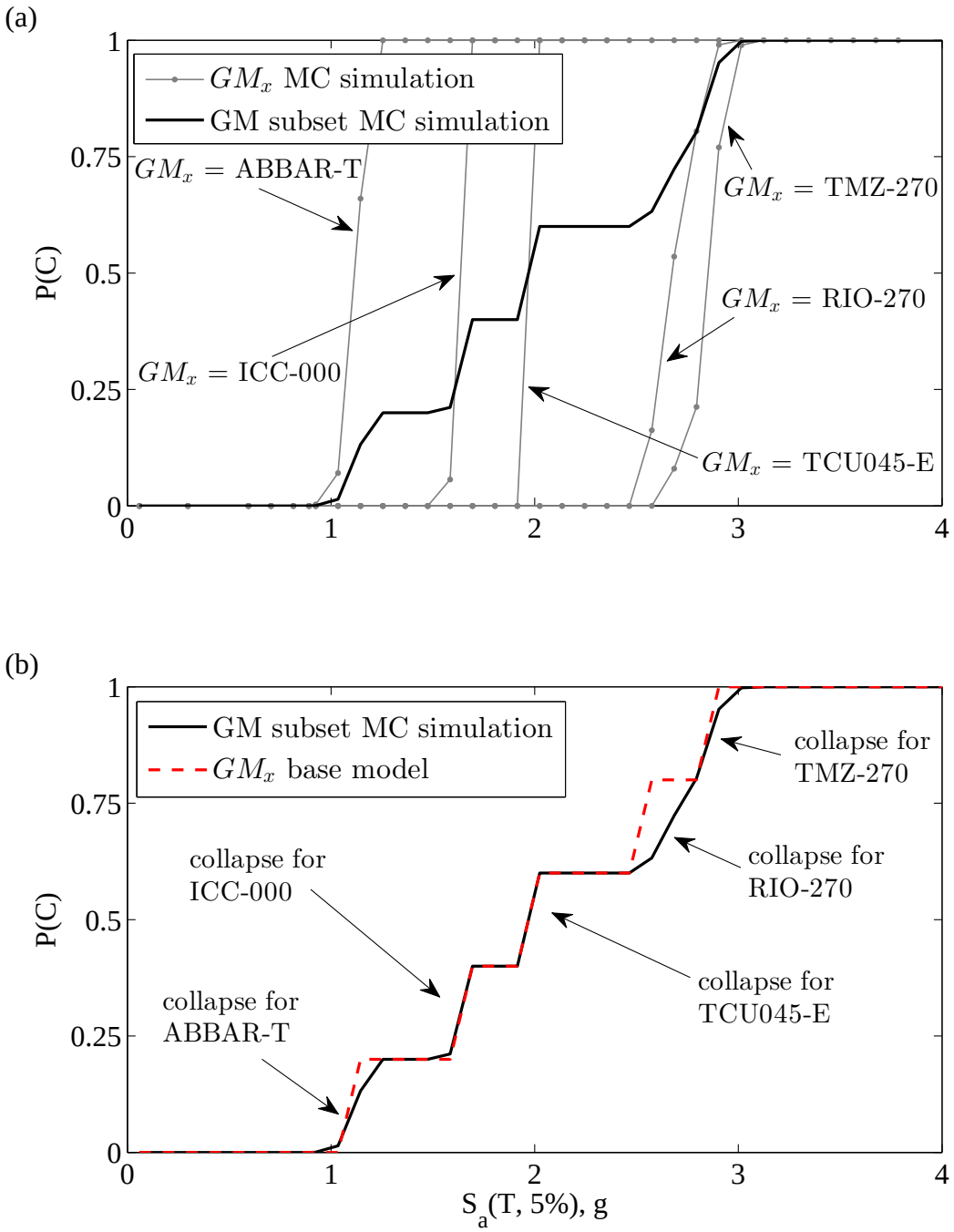

Figure 6.5: Fragility for C damage scenario determined using the five GM_x of the GM subset: (a) construction of $P(C)$ from the five $P(C|GM_x)$; and (b) comparison of $P(C)$ for the GM subset for the base model and GM subset MC simulation

the "dependent" variable, is represented by an IDA curve. The structural response history analysis conducted using a specific GM and a specific numerical model at a given IM value (e.g., $S_a(T,5\%)$), results in a specific value for each EDP (e.g., θ_m or θ_r). Because of nonlinearity in the response during a structural response history analysis (especially at IM values close to collapse), it is difficult to predict the one-to-one relationship between the IM value and EDP value; therefore, this one-to-one relationship is usually estimated by conducting an IDA. The one-to-one relationship between the IM and EDP for GM_x and numerical model MDL_i, estimated using an IDA, can be symbolically stated as follows:

$$EDP_{x,i} = fcn_{x,i}(IM) \tag{6.23}$$

where $EDP_{x,i}$ is the EDP value obtained from the structural response history analysis for GM_x and numerical model MDL_i and $fcn_{x,i}$ is the one-to-one relationship between $EDP_{x,i}$ and IM, defined numerically by the IDA curve for GM_x and numerical model MDL_i. Equation (6.23) is used in the remainder of this section to distinguish between different one-to-one relationships between the IM and EDP, defined by different IDA curves. The indices x, for GM_x, and i, for numerical model MDL_i, in $EDP_{x,i}$ indicates the EDP values for GM_x and MDL_i. For example $EDP_{x,BM} = fcn_{x,BM}(IM)$ shows the one-to-one relationship between the IM and EDP, defined by the IDA curve developed using GM_x and the base model (indicated by the subscript BM).

Values of θ_m obtained from the structural response history analyses for GM_x and the sample model MDL_i, denoted as $\theta_{m_{x,i}}$, are shown in Figures 6.6 through 6.10 for the 5 GM_x of the GM subset at different IM values. Also shown in Figures 6.6 through 6.10, are θ_m values from structural response history analysis for GM_x and the base model, denoted as $\theta_{m_{x,BM}}$, and the median of the $\theta_{m_{x,i}}$ values, denoted as $\tilde{\theta}_{m_{x,i}}$. It can be seen that dispersion of the $\theta_{m_{x,i}}$ values due to variation of the random system parameters (i.e., Δ_{Oi} and LL) is small at most IM values. It can also be seen that the $\theta_{m_{x,i}}$ values are closely distributed

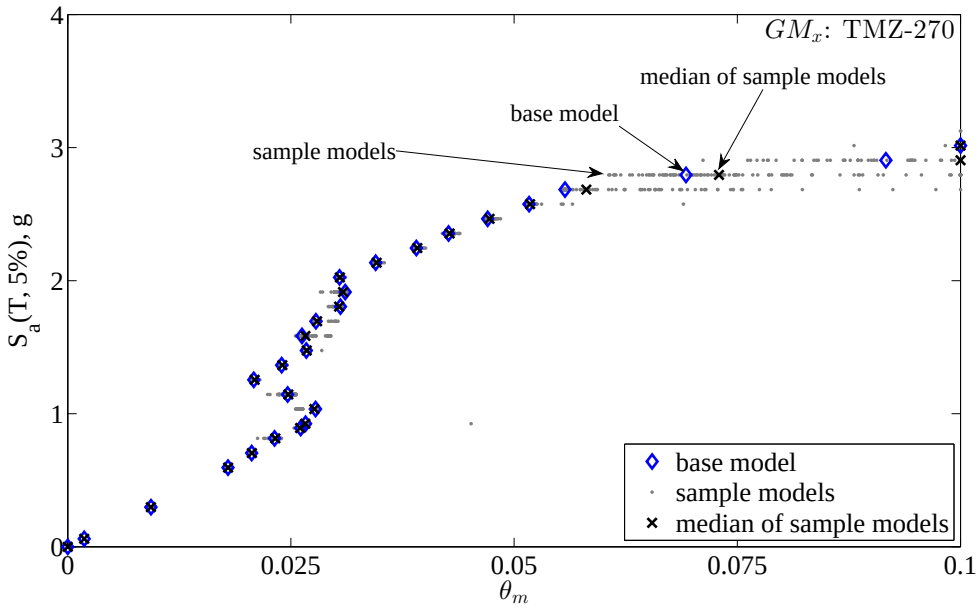

Figure 6.6: Variation of θ_m due to variation of random system parameters at different IM values for GM_x = TMZ-270

around the $\theta_{m_{x,BM}}$ values at most IM values. As a result, the difference between $\theta_{m_{x,BM}}$ and $\tilde{\theta}_{m_{x,i}}$ is negligible. This means that the θ_m value obtained from a numerical model with the median values of the random system parameters (i.e., $\theta_{m_{x,BM}}$ from the base model) is close to the median of the $\theta_{m_{x,i}}$ values obtained from a set of sample models with varying values of random system parameters (i.e., $\tilde{\theta}_{m_{x,i}}$).

The $\theta_{m_{x,BM}}$ and $\tilde{\theta}_{m_{x,i}}$ values are similar at most IM values, except for IM values close to the IM value at collapse, IM_C. The dispersion of the $\theta_{m_{x,i}}$ values increases at IM values close to IM_C. In addition to the increase in the dispersion of the $\theta_{m_{x,i}}$ values, the difference between the $\theta_{m_{x,BM}}$ value and the $\tilde{\theta}_{m_{x,i}}$ value is not negligible at some IM values close to IM_C. An example of considerable difference between the $\theta_{m_{x,BM}}$ value and the $\tilde{\theta}_{m_{x,i}}$ value can be seen in Figure 6.6 at $S_a(T, 5\%) \approx 3g$. Increased dispersion of the $\theta_{m_{x,i}}$ values at IM values close to IM_C, however, is not always accompanied by a considerable difference between the $\tilde{\theta}_{m_{x,i}}$ values and the $\theta_{m_{x,BM}}$ values, as shown in Figures 6.7 and 6.9.

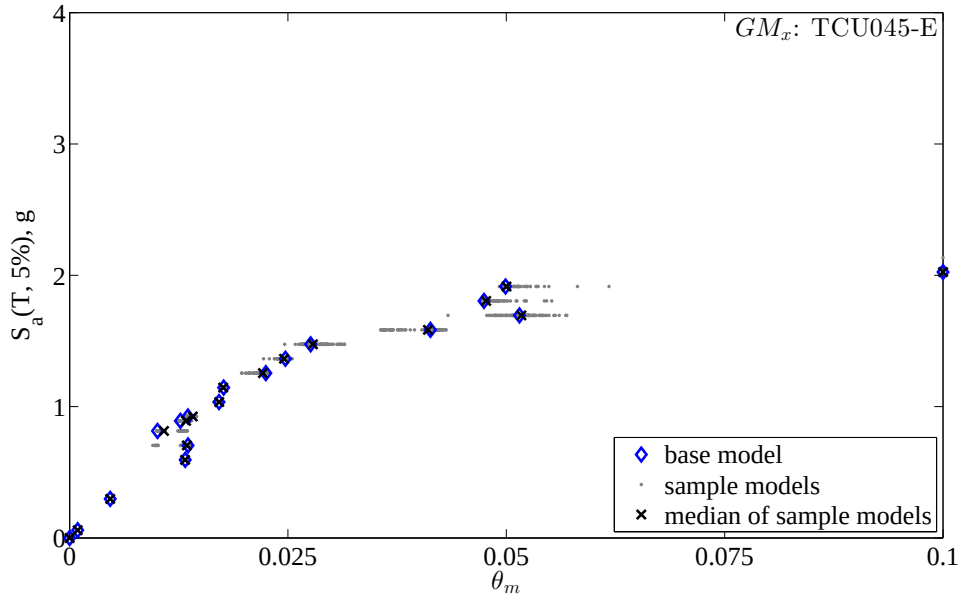

Figure 6.7: Variation of θ_m due to variation of random system parameters at different IM values for GM_x = TCU045-E

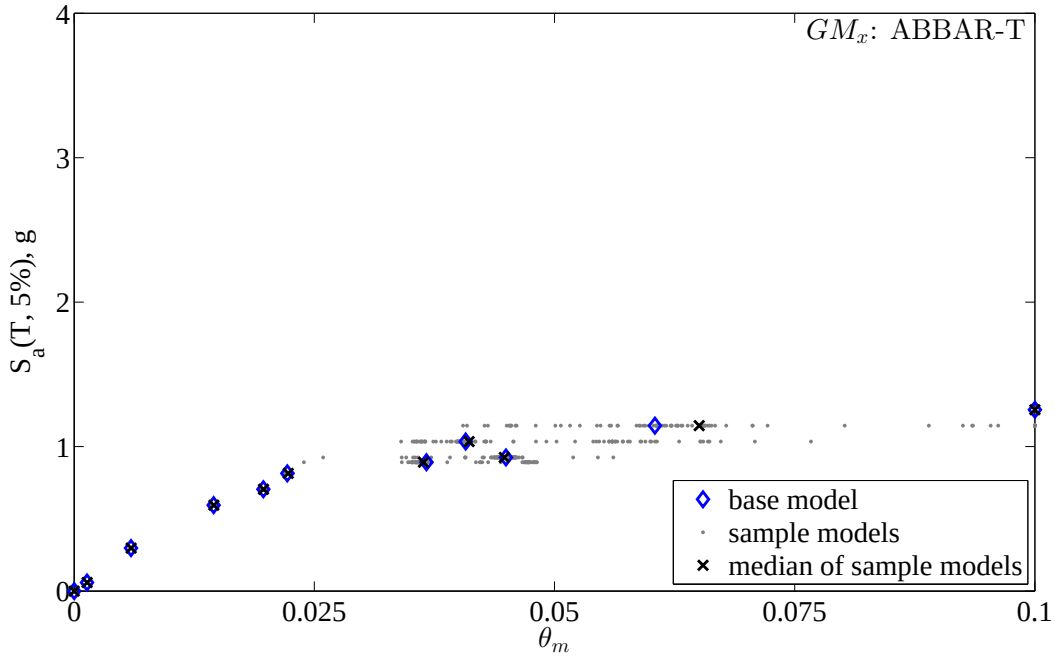

Figure 6.8: Variation of θ_m due to variation of random system parameters at different IM values for GM_x = ABBAR-T

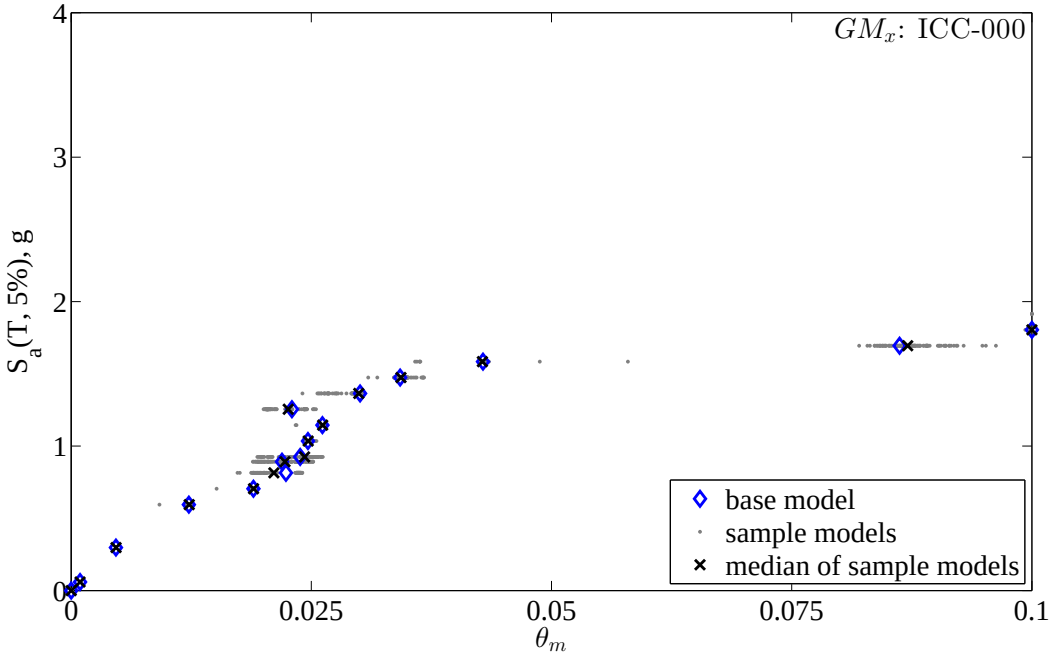

Figure 6.9: Variation of θ_m due to variation of random system parameters at different IM values for GM_x = ICC-000

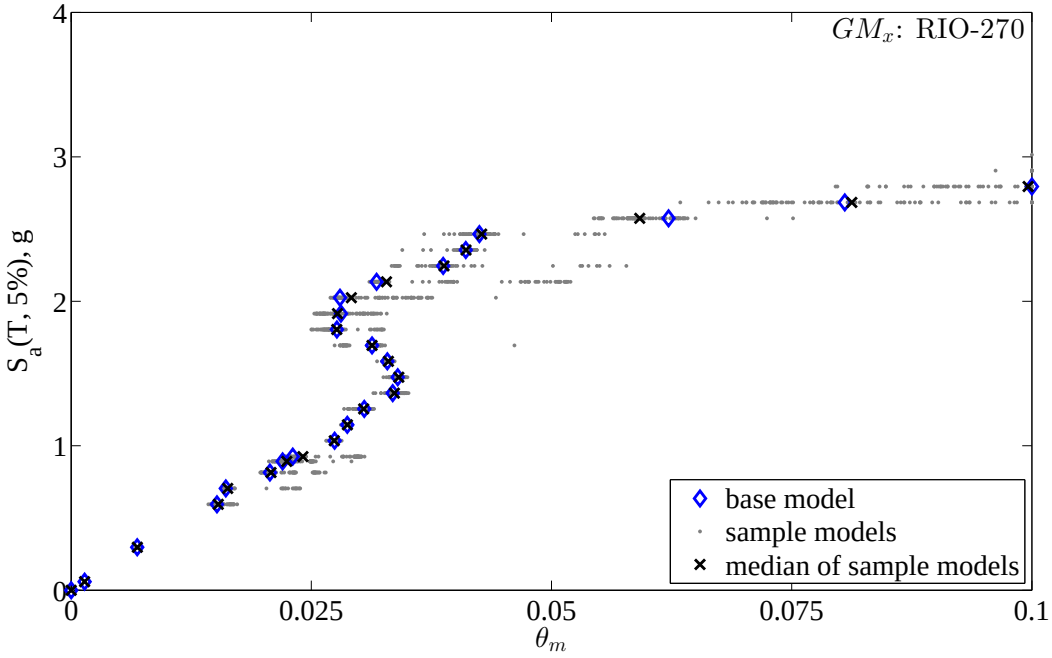

Figure 6.10: Variation of θ_m due to variation of random system parameters at different IM values for GM_x = RIO-270

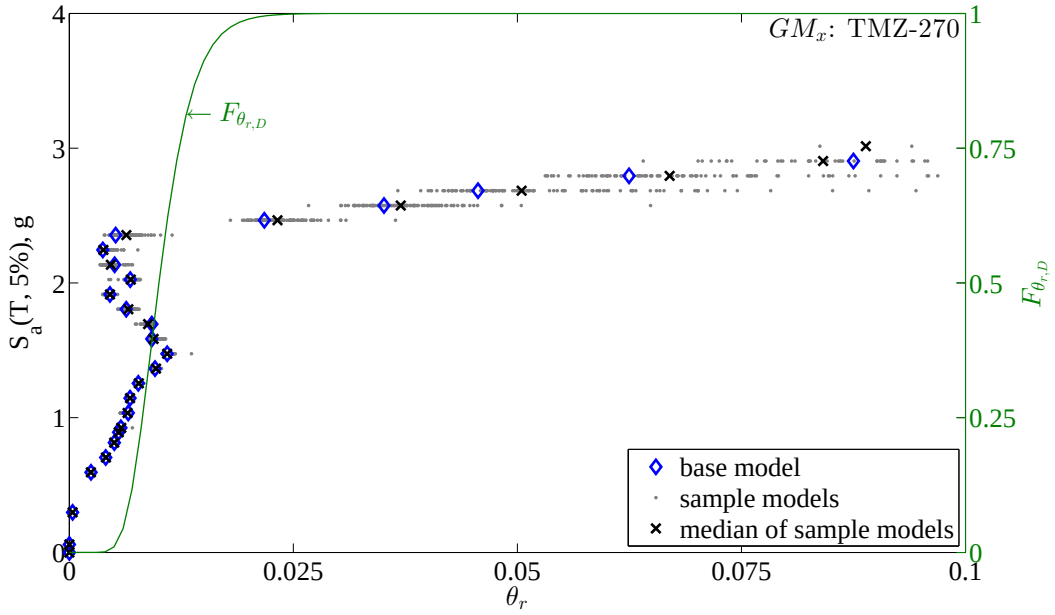

Figure 6.11: Variation of θ_r due to variation of random system parameters at different IM values for GM_x = TMZ-270

Values of θ_r obtained from the structural response history analyses for GM_x and the sample models MDL_i, denoted as $\theta_{r_{x,i}}$, are shown in Figures 6.11 through 6.15 for the 5 GMs of the GM subset at different IM values. Also shown in Figures 6.11 through 6.15, are θ_r from structural response history analyses for GM_x and the base model, denoted as $\theta_{r_{x,BM}}$, and the median of the $\theta_{r_{x,i}}$ values for sample models, denoted as $\tilde{\theta}_{r_{x,i}}$. Similar to the $\theta_{m_{x,i}}$ values, the dispersion of the $\theta_{r_{x,i}}$ values is small and $\theta_{r_{x,BM}}$ and $\tilde{\theta}_{r_{x,i}}$ values are nearly the same at IM values which are not close to IM_C. At IM values close to IM_C, the dispersion of θ_r increases and some $\tilde{\theta}_{r_{x,i}}$ values are different than $\theta_{r_{x,BM}}$ (see Figures 6.11 and 6.15).

The demolition fragility function, $F_{\theta_{r,D}}$, is shown on the right side vertical axis of Figures 6.11 through 6.15. It can be seen that at IM values close to IM_C where $\tilde{\theta}_{r_{x,i}}$ and $\theta_{r_{x,BM}}$ have different values, $F_{\theta_{r,D}}$ is almost equal to 1. At IM values where $F_{\theta_{r,D}} < 1$, $\theta_{r,BM}$ and $\tilde{\theta}_{r,MDL}$ have similar values. This observation is discussed later in this chapter when an approximate method for considering system parameter variability is presented.

Values of Δ_{Or} obtained from the structural response history analyses for GM_x and the

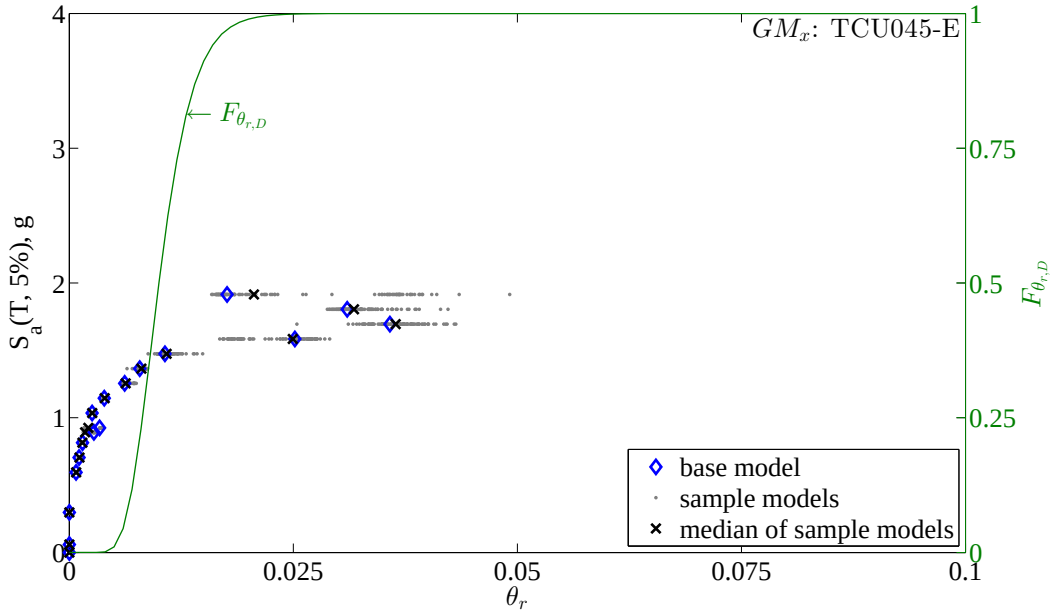

Figure 6.12: Variation of θ_r due to variation of random system parameters at different IM values for GM_x = TCU045-E

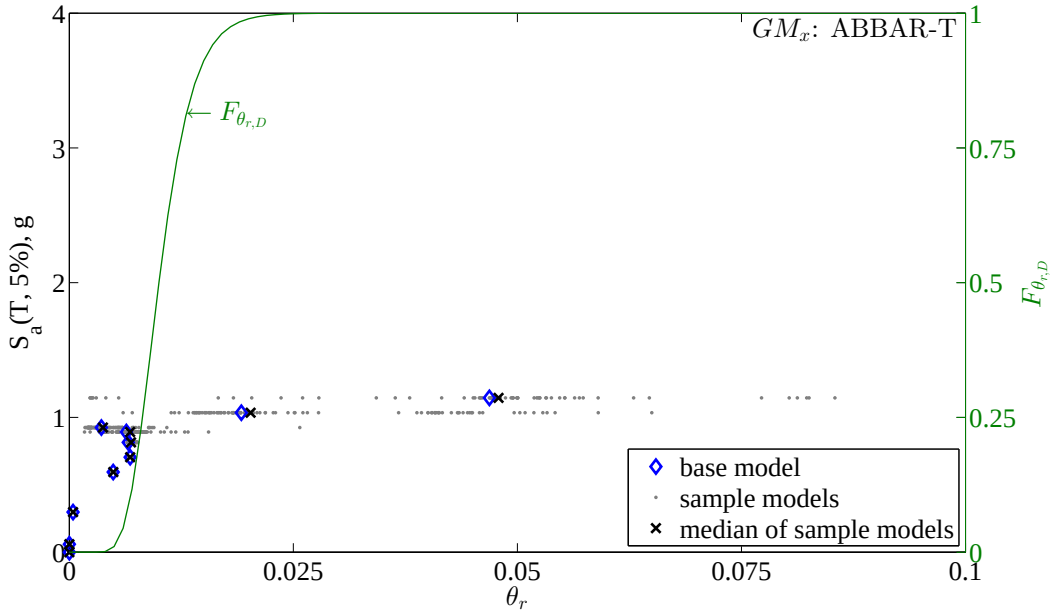

Figure 6.13: Variation of θ_r due to variation of random system parameters at different IM values for GM_x = ABBAR-T

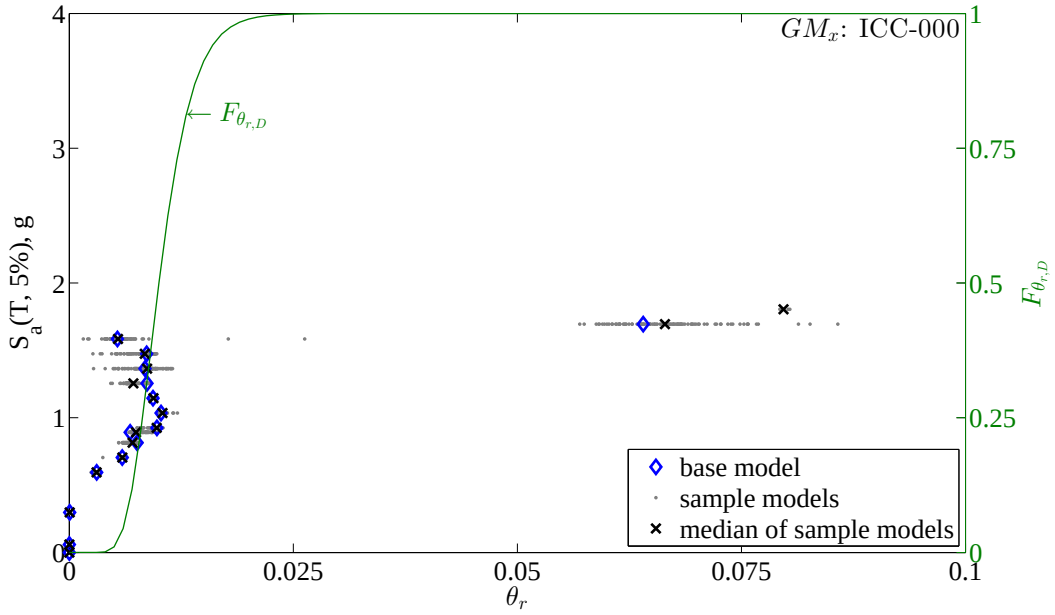

Figure 6.14: Variation of θ_r due to variation of random system parameters at different IM values for GM_x = ICC-000

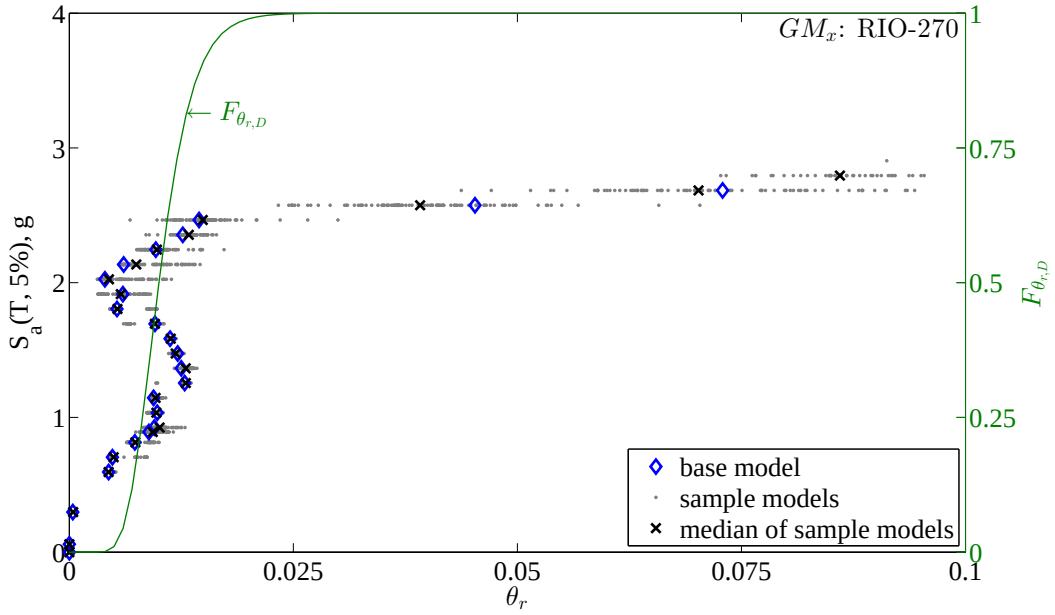

Figure 6.15: Variation of θ_r due to variation of random system parameters at different IM values for GM_x = RIO-270

sample models MDL_i, are denoted as $\Delta_{Or_{x,i}}$. Results for the $\Delta_{Or_{x,i}}$ values for the third story braces of the 9SCBF archetype building are shown in Figures 6.16 through 6.20 for the 5 GM_x of the GM subset at different IM values. Also shown in Figures 6.16 through 6.20, are Δ_{Or} values obtained from the structural response history analyses for GM_x and the base model, denoted as $\Delta_{Or_{x,BM}}$, and the median of the $\Delta_{Or_{x,i}}$ values, denoted as $\tilde{\Delta}_{Or_{x,i}}$. The dispersion of the $\Delta_{Or_{x,i}}$ values is larger than the dispersion of the $\theta_{m_{x,i}}$ and $\theta_{r_{x,i}}$ values discussed earlier. Furthermore, considerable dispersion of the $\Delta_{Or_{x,i}}$ values occurs at IM values not close to IM_C. For example, in Figure 6.19 considerable dispersion of the $\Delta_{Or_{x,i}}$ values can be seen at $S_a(T,5\%) < 1g$ which is far less than the IM_C under $GM_x =$ ICC-000. In addition to the large dispersion of $\Delta_{Or_{x,i}}$ values, the difference between $\tilde{\Delta}_{Or_{x,i}}$ and $\Delta_{Or_{x,BM}}$ is also considerable. This result means that the Δ_{Or} value obtained for a model with the median values of the random system parameters (i.e., $\Delta_{Or_{x,BM}}$ from the base model) is not necessarily close to the median of the Δ_{Or} values obtained for models with varying values of random system parameters (i.e., $\tilde{\Delta}_{Or_{x,i}}$). There are GM_x, however, for which the dispersion of the $\Delta_{Or_{x,i}}$ values is not large at IM values not close to IM_C, and the large dispersion occurs only at IM values near IM_C (i.e., the trend is similar to the trend for θ_m and θ_r). Figure 6.16, plotted for $GM_x =$ TMZ-270, is an example of this small $\Delta_{Or_{x,i}}$ dispersion (compared to other GM_x).

The large dispersion in the $\Delta_{Or_{x,i}}$ values shows the sensitivity of Δ_{Or} to the variation of the random system parameters (i.e., Δ_{Oi} and LL). As described earlier, the brace initial out-of-straightness, Δ_{Oi}, is one of the random system parameters considered. The effect of Δ_{Oi} on the axial force-deformation response of a compression member (i.e., the braces of the 9SCBF archetype building) is considerable [10, 84]. Therefore, the considerable sensitivity of the $\Delta_{Or_{x,i}}$ values appears to result from the variation of Δ_{Oi}.

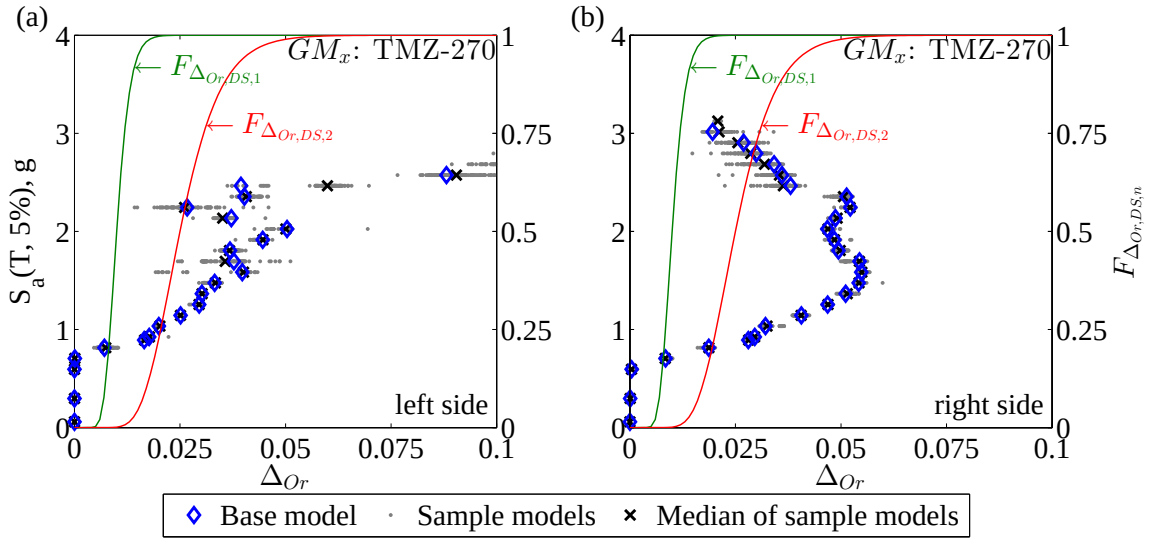

Figure 6.16: Variation of Δ_{Or} for the third story brace of 9SCBF archetype building at different IM values due to variation of system parameters for GM_x: TMZ-270: (a) left side brace; and (b) right side brace

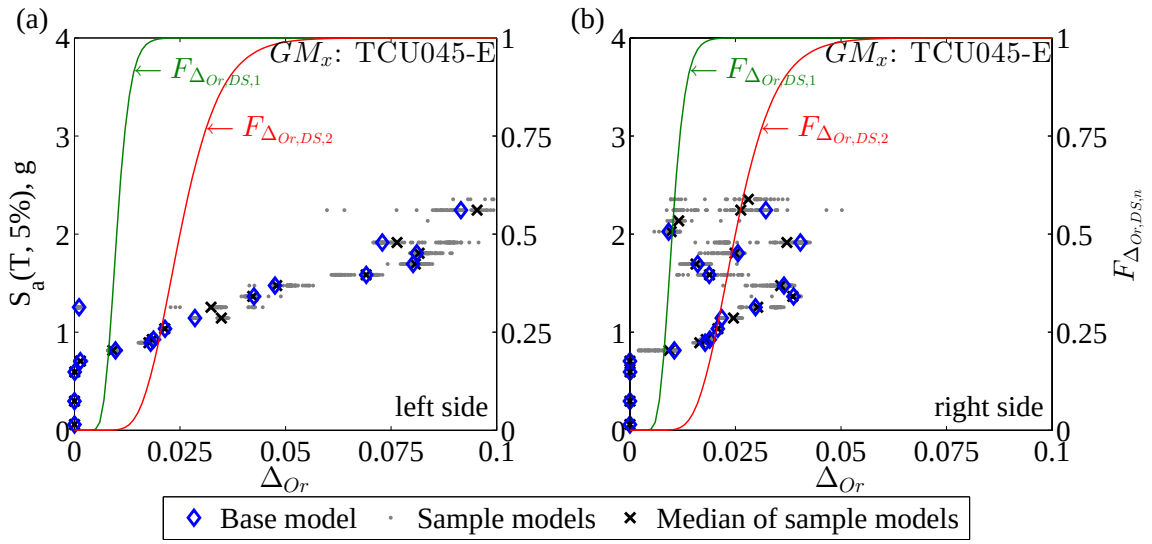

Figure 6.17: Variation of Δ_{Or} for the third story brace of 9SCBF archetype building at different IM values due to variation of system parameters for GM_x: TCU045-E: (a) left side brace; and (b) right side brace

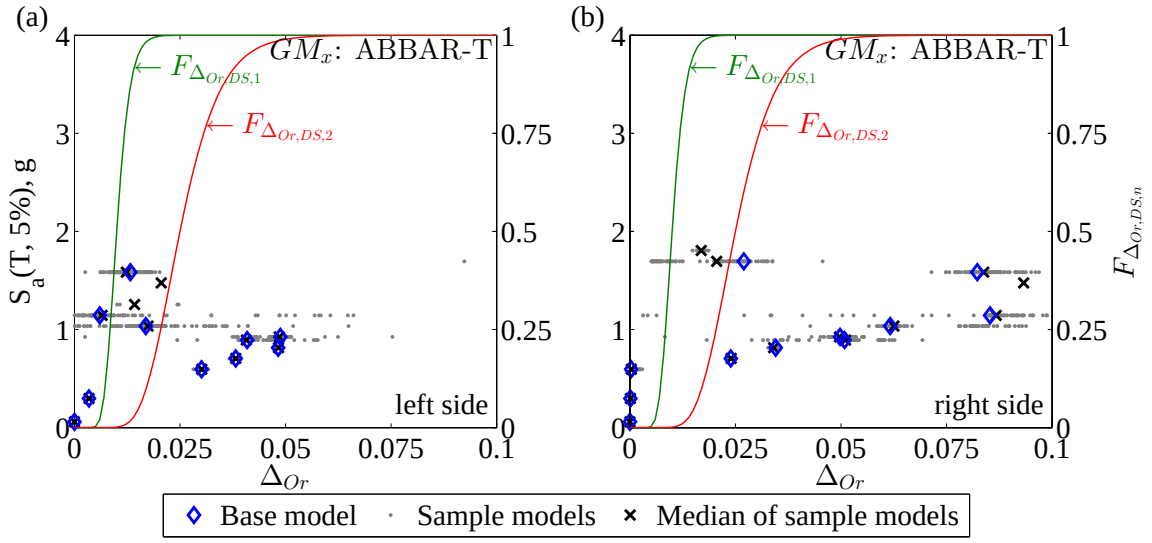

Figure 6.18: Variation of Δ_{Or} for the third story brace of 9SCBF archetype building at different IM values due to variation of system parameters for GM_x: ABBAR-T: (a) left side brace; and (b) right side brace

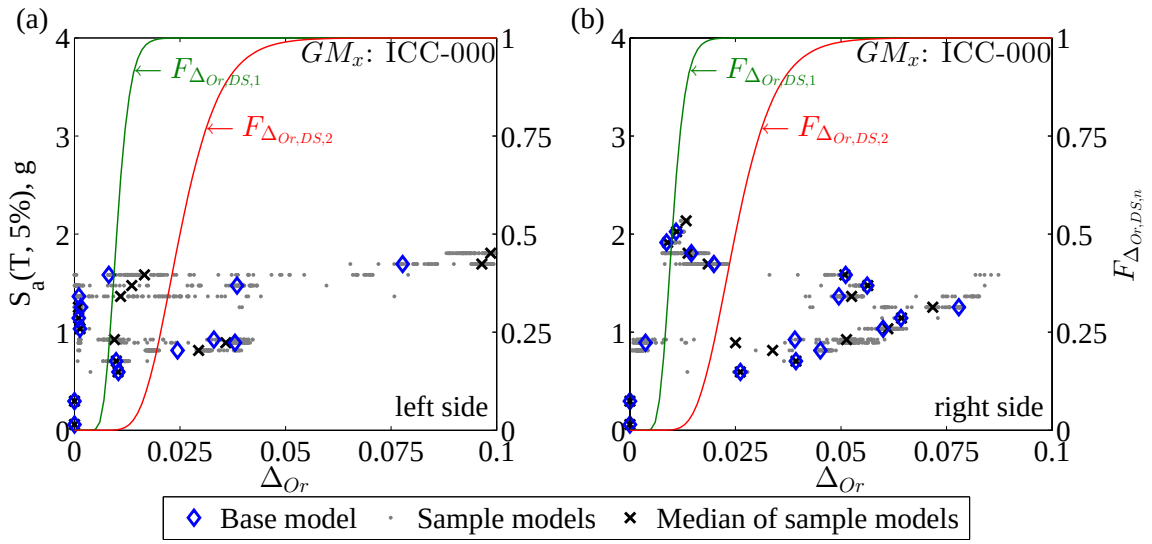

Figure 6.19: Variation of Δ_{Or} for the third story brace of 9SCBF archetype building at different IM values due to variation of system parameters for GM_x: ICC-000: (a) left side brace; and (b) right side brace

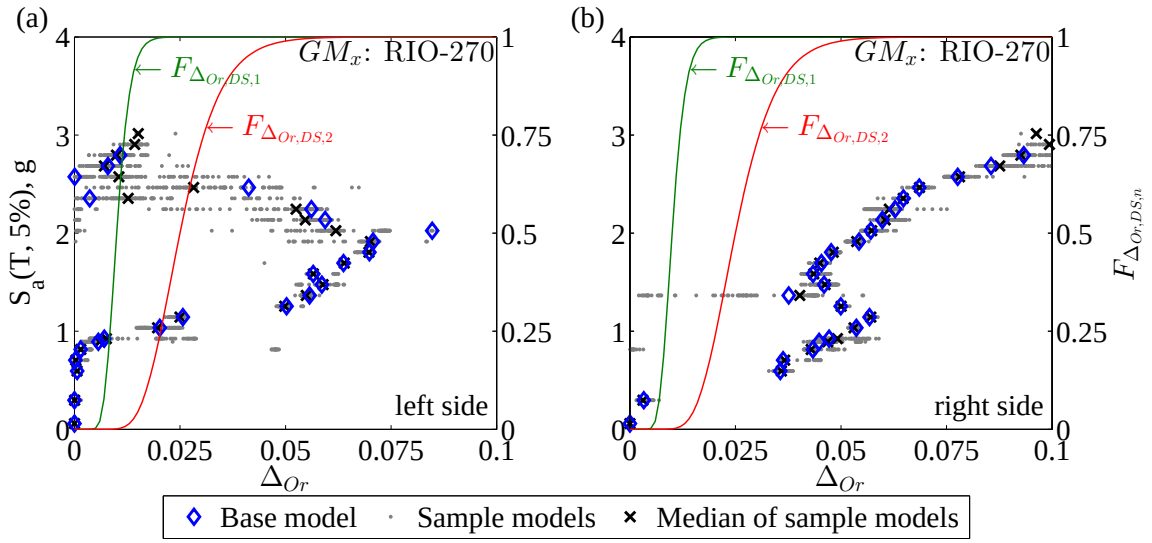

Figure 6.20: Variation of Δ_{Or} for the third story brace of 9SCBF archetype building at different IM values due to variation of system parameters for GM_x: RIO-270: (a) left side brace; and (b) right side brace

6.4 Estimating Effect of System Parameter Variability and Modeling Uncertainty Using Monte Carlo Simulation

An approximate method for including system parameter variability and modeling uncertainty in damage scenario fragilities is discussed in this section. In this approximate method, the results of a GM subset MC simulation are used to modify the damage state (DS) fragility functions. The *modified* DS fragility functions are assumed to represent two sources of uncertainty: (i) the uncertainty in the corresponding DS (similar to the unmodified DS fragility function used previously); and (ii) the uncertainty from including the system parameter variability and modeling uncertainty (using the GM subset MC simulation results). The modified DS fragility functions are then used for all GMs of the full GM set.

The results from the GM subset MC simulation and the one-to-one relationship between

IM and EDP, shown in Equation (6.23), are used to estimate the effect of system parameter variability and modeling uncertainty for all GM_l of the full GM set. The approximate method includes fitting a CDF to the MC simulation results for GM subset for the collapse DS, demolition DS, and component DS.

6.4.1 Estimating demolition DS fragility function with system parameter variability

Figure 6.21(a) shows the IDA results for the sample models and the base model for $GM_x =$ RIO-270. The EDP in Figure 6.21(a) is θ_r. Figure 6.21(a) is identical to Figure 6.15 except that the data points are connected by lines in Figure 6.21(a).

The probability of demolition, $P(D)$ (i.e., the probability of θ_r exceeding $\theta_{r,D}$) for an individual IDA curve, developed for a given GM and a given numerical model (e.g., the base model or a sample model), can be determined by evaluating $F_{\theta_{r,D}}(\theta_r)$ at various IM values. It is important to recognize the difference between $P(D)$ and $P(NC \cap D)$ as explained in Chapter 5. $P(NC \cap D)$ is the probability of the $NC \cap D$ damage scenario from a DSTA. In evaluating $P(NC \cap D)$, the probability of both collapse and demolition occurring (i.e., $C \cap D$) is not included; only the cases of non-collapse with demolition are of interest. In contrast, $P(D)$ is the probability of demolition, regardless of the collapse criteria. The relationship between $P(D)$ and $P(NC \cup D)$ can be stated as: $P(D) = P(NC \cap D) + P(C \cap D)$, where it is understood that $P(C) + P(NC) = 1$.

Figure 6.21(b) shows $P(D)$ for $GM_x =$ RIO-270. The curves for the base model and the sample models in Figure 6.21(b) are developed using the IDA results shown in Figure 6.21(a). The sharp decrease in $P(D|GM_x)$ for $S_a(T,5\%)$ between 1.5g to 2g in Figure 6.21(b) is due to the decrease of θ_r for $S_a(T,5\%)$ between 1.5g to 2g in Figure 6.21(a), where it is shown that θ_r decreases to values with a low probability of demolition (i.e.,

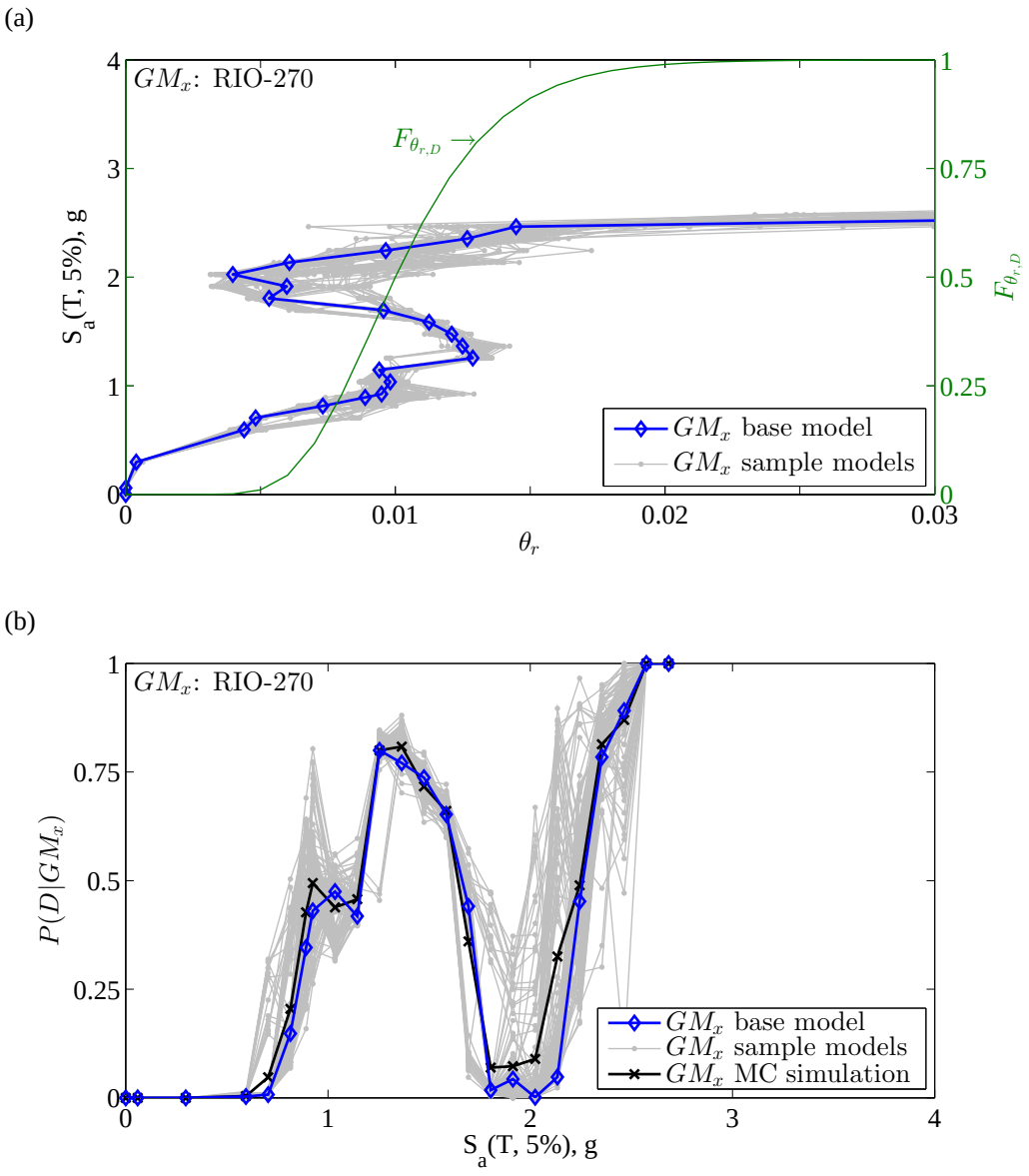

Figure 6.21: Demolition for 9SCBF archetype building and GM_x = RIO-270 : (a) IDA results with $EDP = \theta_r$; and (b) probability of demolition for GM_x

$F_{\theta_{r,D}}(\theta_r)$ is small). While intuition suggests that a continuously increasing IM should lead to continuously increasing EDP values, a decrease in the EDP as the IM increases can occur due to the nonlinearity of the system with possible redistribution of damage (e.g., plasticity or fracture) in structural components. Decreasing EDP with increasing IM has been observed by Vamvatsikos and Cornell [86].

$P(D)$ for a given GM_x including system parameter variability can be evaluated at a given IM value using the MC simulation results for GM_x as follows:

$$\begin{aligned} P(D|GM_x, IM) &= P(\theta_r \geq \theta_{r,D}|GM_x, IM) \\ &= \sum_{all\ MDL_i} P(\theta_r \geq \theta_{r,D}|MDL_i, GM_x, IM) \cdot P(MDL_i|GM_x, IM) \end{aligned} \quad (6.24)$$

where $P(MDL_i|GM_x, IM)$ is the probability of the random system and modeling parameter values used to create MDL_i (i.e., the probability of MDL_i) for a given GM_x and at a given IM. $P(\theta_r \geq \theta_{r,D}|MDL_i, GM_x, IM)$ is evaluated using $F_{\theta_{r,D}}(\theta_{r_{x,i}})$. Note that the subscript x refers to GM_x from the GM subset (e.g., GM_x = RIO-270 in Figure 6.21) and the subscript i refers to the sample model MDL_i. Assuming that the random system and modeling parameter values are independent of GM_x and IM, $P(MDL_i|GM_x, IM)$ simplifies to $P(MDL_i)$. Equation (6.24) can be written as follows:

$$P(D|GM_x, IM) = \sum_{all\ MDL_i} F_{\theta_{r,D}}(\theta_{r_{x,i}}) \cdot P(MDL_i) \quad (6.25)$$

where $\theta_{r_{x,i}}$ is the θ_r value determined from the structural response history analysis for GM_x and MDL_i. The one-to-one relationship between $\theta_{r_{x,i}}$ and IM is obtained from the IDA results (i.e., the IDA curve) for GM_x and MDL_i, as shown symbolically by Equation (6.23), where $EDP_{x,i} = \theta_{r_{x,i}}$.

The GM_x MC simulation results, determined using Equation (6.25), are shown in Figure

6.21(b). It can be seen from Figure 6.21(b) that the $P(D|GM_x)$ curve for the MC simulation for GM_x (which includes system parameter variability) is close, but not identical, to the $P(D|GM_x)$ curve for the base model. The small effect of the system parameter variability can be explained using Figure 6.15, which shows that the variation of θ_r as the sample model varies is small for $S_a(T,5\%) < 2.5g$, but the variation of θ_r as the sample model varies increases for $S_a(T,5\%) > 2.5g$. However, for $S_a(T,5\%) > 2.5g$ the θ_r values are large enough so that $F_{\theta_{r,D}}(\theta_{r_{x,i}}) \approx 1$, therefore, the variation of θ_r at $S_a(T,5\%) > 2.5g$ does not cause a significant difference between $P(D|GM_x,IM)$ for the MC simulation for GM_x, calculated using Equation (6.25), and $P(D|GM_x,IM)$ for the base model and GM_x. $P(D|GM_x,IM)$ for the base model is calculated by evaluating $F_{\theta_{r,D}}(\theta_{r_{x,BM}})$ where $\theta_{r_{x,BM}}$ is the θ_r value obtained from the one-to-one relationship between θ_r and IM using the IDA curve for the base model and GM_x (i.e., from Equation (6.23) where $EDP_{x,BM} = \theta_{r_{x,BM}}$ and the subscript BM refers to the base model).

The remainder of this section discusses a modification to $F_{\theta_{r,D}}$ to enables the uncertain effects of system parameter variability, in addition to the epistemic uncertainty associated with the demolition DS to be included in the modified $F_{\theta_{r,D}}$ based on the GM subset MC simulation results. The modified $F_{\theta_{r,D}}$ is denoted by $F_{\theta_{r,D,MDL}}$ which is treated as unknown. The random variable for $F_{\theta_{r,D,MDL}}$ is denoted by $\theta_{r,D,MDL}$. To be useful, $F_{\theta_{r,D,MDL}}$ is defined so that when evaluated at $\theta_{r_{x,BM}}$, the resulting probability is equivalent to the result from Equation (6.25). Therefore, $F_{\theta_{r,D,MDL}}$ is estimated by setting $P(D|GM_x,IM)$ equal to $F_{\theta_{r,D,MDL}}(\theta_{r_{x,BM}})$ and then finding $F_{\theta_{r,D,MDL}}$ from the results, as follows:

$$P(D|GM_x,IM) = F_{\theta_{r,D,MDL}}(\theta_{r_{x,BM}}) \tag{6.26}$$

where the value of $P(D|GM_x,IM)$ at each IM is determined from Equation (6.25) and the value of $\theta_{r_{x,BM}}$ at each IM is determined using the one-to-one relationship between θ_r and IM for GM_x and the base model (symbolically stated as $\theta_{r_{x,BM}} = fcn_{x,BM}(IM)$).

Once $F_{\theta_{r,D,MDL}}$ is determined it can be used for all GM_l of the GM set. Note that the dispersion in $F_{\theta_{r,D}}$ is due to the epistemic uncertainty in the demolition DS, while the dispersion in $F_{\theta_{r,D,MDL}}$ is due to: (i) the epistemic uncertainty in the demolition DS; and (ii) the effect of system parameter variability and modeling uncertainty. While modeling uncertainty is not considered in the present example, the procedure for including modeling uncertainty is exactly the same as the procedure for including system parameter variability, as shown in this section.

It is possible to plot the $P(D|GM_x)$ values from Equation (6.25) versus the $\theta_{r_{x,BM}}$ values from $\theta_{r_{x,BM}} = fcn_{x,BM}(IM)$, at each IM, as shown for GM_x = Rio-270 in Figure 6.22 by the "X" symbols. An estimation of $F_{\theta_{r,D,MDL}}$ can be determined by fitting a CDF to the $\theta_{r_{x,BM}}$ and $P(D|GM_x, IM)$ pairs shown by the "X" sumbols in Figure 6.22. It is assumed that $F_{\theta_{r,D,MDL}}$ follows a lognormal distribution, the same as $F_{\theta_{r,D}}$. The fitted lognormal CDF and $F_{\theta_{r,D}}$ are also plotted in Figure 6.22. It can be seen in Figure 6.22 that, as expected, the fitted lognormal CDF has a larger dispersion compared to $F_{\theta_{r,D}}$. This larger dispersion is a result of the system parameter variability included in the GM_x MC simulation.

The fitted lognormal CDF shown in Figure 6.22 is a solution for the unknown $F_{\theta_{r,D,MDL}}$ from Equation (6.26), found using only the GM_x MC simulation results for GM_x = RIO-270. This solution does not consider the GM_x MC simulation results for other GM_x of the GM subset. Therefore, the fitted lognormal CDF based on the MC simulation results for GM_x is denoted by $\hat{F}_{\theta_{r,D,MDL,x}}$. The "$\hat{hat}$" symbol above F shows that it is an estimate of $F_{\theta_{r,D,MDL,x}}$. The random variable for $F_{\theta_{r,D,MDL,x}}$ is $\theta_{r,D,MDL}$ for GM_x which is denoted by $\theta_{r,D,MDL,x}$. A solution for $\hat{F}_{\theta_{r,D,MDL,x}}$ was determined for each GM_x of the GM subset and the results are shown in Figures 6.23 through 6.26. It can be seen that the difference between $F_{\theta_{r,D}}$ and each $\hat{F}_{\theta_{r,D,MDL,x}}$ is small. Such a small difference is mainly due to the small sensitivity of θ_r to the variation of random system parameters (i.e., Δ_{Oi}, LL). Looking at Figures 6.22 through 6.26, it can be said that the contribution of system parameter variability to

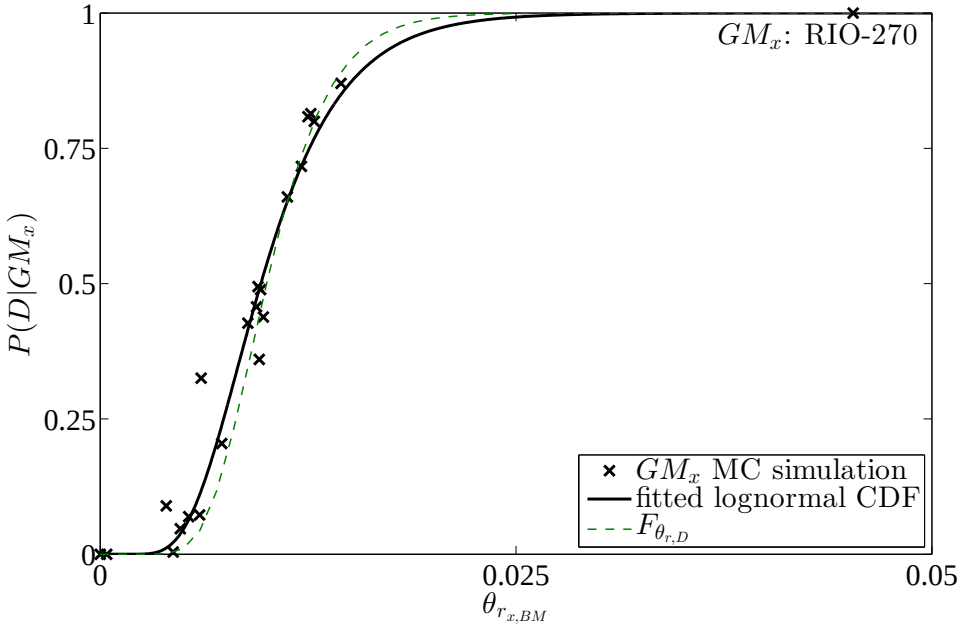

Figure 6.22: Estimating $F_{\theta_{r,D,MDL,x}}$ for GM_x = RIO-270

the dispersion of $\hat{F}_{\theta_{r,D,MDL,x}}$ is considerably smaller than the contribution of the epistemic uncertainty included in the original demolition DS fragility $F_{\theta_{r,D}}$.

The median and the logarithmic standard deviation of $\theta_{r,D,MDL,x}$ for the five GMs of the GM subset are given in Table 6.2. As assumed in Chapter 5, the median of $\theta_{r,D}$ is 0.01 and logarithmic standard deviation of $\theta_{r,D}$ is 0.3. Comparing the logarithmic standard deviations given in Table 6.2 with the logarithmic standard deviation of $\theta_{r,D}$, it can be seen that the effect of including the system parameter variability is small. The difference between the median values of $\theta_{r,D,MDL,x}$ and the median value of $\theta_{r,D}$ is also small. No clear trend of increase or decrease in the median $\theta_{r,D,MDL,x}$ values can be observed from Table 6.2. Some median $\theta_{r,D,MDL,x}$ values are slightly smaller and some are slightly larger than the median $\theta_{r,D}$ value.

The $\hat{F}_{\theta_{r,D,MDL,x}}$, determined for the five GM_x of the GM subset were used to estimate $F_{\theta_{r,D,MDL}}$ which can be used for all GM_l of the GM set. Since the median $\theta_{r,D,MDL,x}$ values are similar to the median $\theta_{r,D}$ value for five GM_x of the GM subset, the median $\theta_{r,D,MDL}$ is

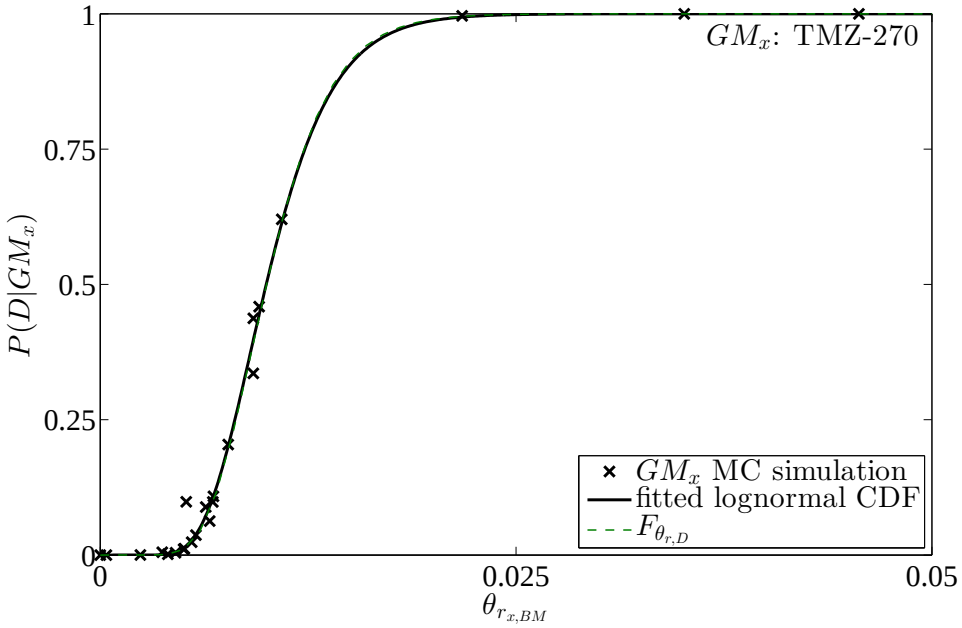

Figure 6.23: Estimating $F_{\theta_{r,D,MDL,x}}$ for GM_x = TMZ-270

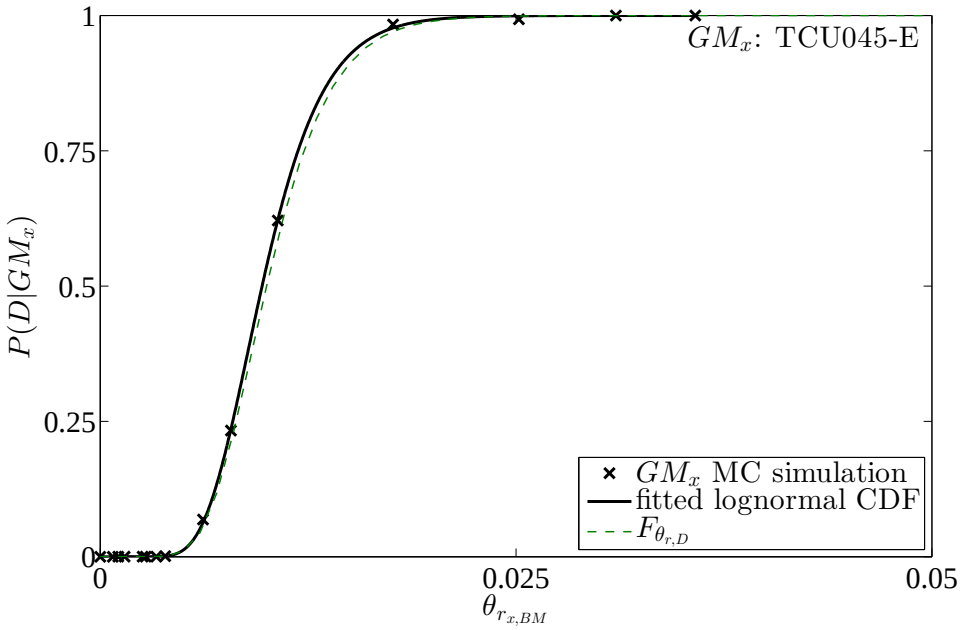

Figure 6.24: Estimating $F_{\theta_{r,D,MDL,x}}$ for GM_x = TCU045-E

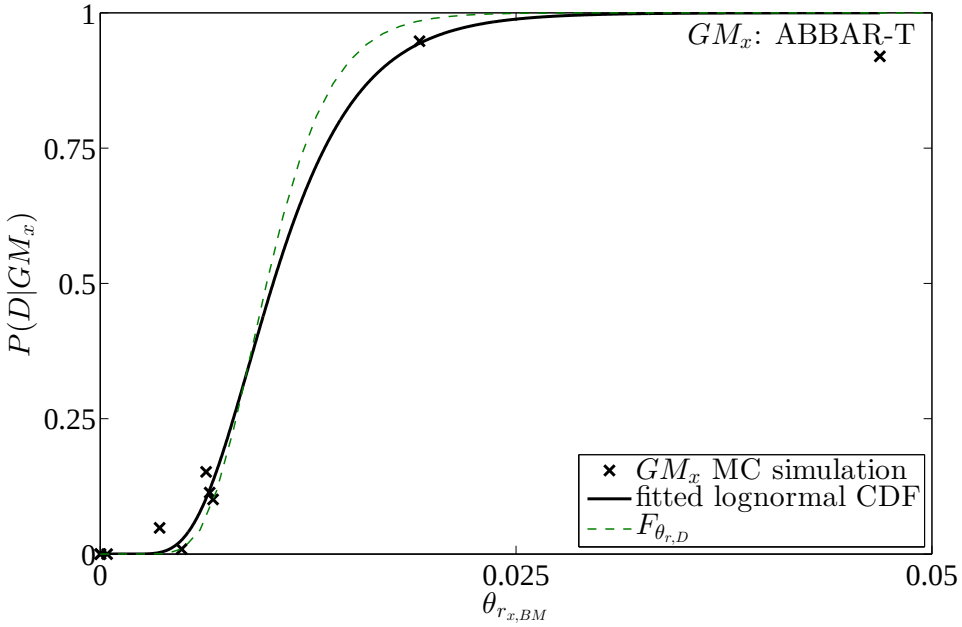

Figure 6.25: Estimating $F_{\theta_{r,D,MDL,x}}$ for GM_x = ABBAR-T

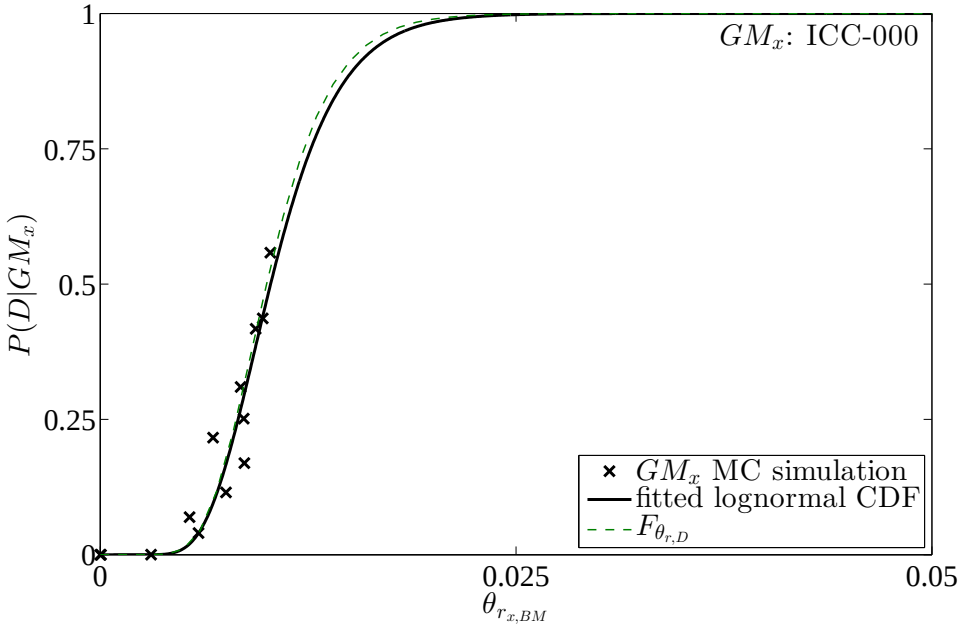

Figure 6.26: Estimating $F_{\theta_{r,D,MDL,x}}$ for GM_x = ICC-000

Table 6.2: Median and dispersion of $\theta_{r,D,MDL,x}$ for the GMs of the GM subset

GM_x	$med\ \theta_{r,D,MDL,x}$	$\sigma_{\ln \theta_{r,D,MDL,x}}$
TMZ-270	0.00998	0.311
TCU045-E	0.00973	0.300
ABBAR-T	0.0104	0.387
ICC-000	0.0102	0.314
RIO-270	0.00966	0.391

selected to be the same as the median $\theta_{r,D}$, i.e., median $\theta_{r,D,MDL} = 0.01$. An estimate of the dispersion for $\theta_{r,D,MDL}$ is also required to define $F_{\theta_{r,D,MDL}}$. One choice is the expected value (mean value) of the $\sigma_{\ln \theta_{r,D,MDL,x}}$ values given in Table 6.2, i.e., which is 0.341. Another choice is to conservatively use the maximum value of $\sigma_{\ln \theta_{r,D,MDL,x}}$ from Table 6.2, which is 0.391. Both of these values were used to generate an estimate of $F_{\theta_{r,D,MDL}}$ (denoted by $\hat{F}_{\theta_{r,D,MDL}}$) to evaluate $P(D)$ using all GM_l of the GM set as follows:

$$P(D|IM) = \sum_{all\ GM_l} \hat{F}_{\theta_{r,D,MDL}}(\theta_{r_{l,BM}}) \cdot P(GM_l) \tag{6.27}$$

where $\theta_{r_{l,BM}}$ is the θ_r value obtained from structural response analysis for GM_l and the base model.

Figure 6.27 shows the effect of including system parameter variability on the demolition DS fragility by comparing the results for the base model (i.e., without system parameter variability) and the result developed using Equation (6.27) (i.e., with system parameter variability). The two demolition fragility curves (with and without system parameter variability) are so close to each other, that it is difficult to see their difference in Figure 6.27. To show the effect of including system parameter variability on the demolition fragility curve in Figure 6.27, a demolition fragility curve is developed using an arbitrary $\hat{\sigma}_{\ln \theta_{r,D,MDL}}$ value of 0.9 and is shown in Figure 6.27 for comparison. As expected, the effect of the significant increase in $\hat{\sigma}_{\ln \theta_{r,D,MDL}}$ is a slight increase in the dispersion of the demolition fragility function.

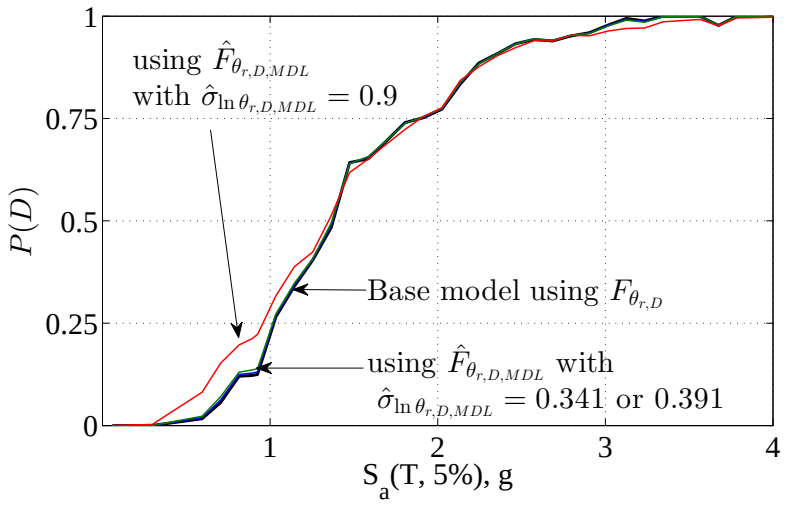

Figure 6.27: Comparing demolition fragility with and without including system parameter variability using $\hat{F}_{\theta_{r,D,MDL}}$

The small difference between the demolition fragility curves with and without system parameter variability (shown in Figure 6.27) is due to two main reasons: (i) the expected value or the maximum value of $\hat{\sigma}_{\ln\theta_{r,D,MDL}}$ (i.e., 0.341 or 0.391) is not much larger than $\sigma_{\ln\theta_{r,D}} = 0.3$; and (ii) the small increase in $\hat{\sigma}_{\ln\theta_{r,D,MDL}}$ is small compared to the effect of RTR variability in the structural response. The RTR variability in the structural response is included when all GM_l of the full Far-Field GM set are considered in Equation (6.27).

6.4.2 Estimating brace DS fragility functions with system parameter variability

Similar to the demolition DS, the brace DS fragility functions (i.e., $F_{\Delta_{Or,DS,1}}$ and $F_{\Delta_{Or,DS,2}}$) can be modified using the GM subset MC simulation results to include the system parameter variability in addition to the epistemic uncertainty associated with each brace DS. The system parameter variability can be included in the probability of exceeding the EDP limit

value for the n^{th} DS based on the results of the GM_x MC simulation as follows:

$$P(Br_{DS,n}|GM_x,IM) = P(\Delta_{Or} \geq \Delta_{Or,DS,n}|GM_x,IM)$$
$$= \sum_{all\ MDL_i} P(\Delta_{Or} \geq \Delta_{Or,DS,n}|MDL_i,GM_x,IM) \cdot P(MDL_i|GM_x,IM) \quad (6.28)$$

where $P(Br_{DS,n}|GM_x,IM)$ is the probability of exceeding the EDP limit value for the n^{th} brace DS for GM_x, at a given IM value. $P(\Delta_{Or} \geq \Delta_{Or,DS,n}|MDL_i,GM_x,IM)$ can be evaluated by $F_{\Delta_{Or,DS,n}}(\Delta_{Or_{x,i}})$, where $F_{\Delta_{Or,DS,n}}$ is the n^{th} brace DS fragility function. Subscripts x and i show that $\Delta_{Or_{x,i}}$ is obtained using the one-to-one relationship between Δ_{Or} and IM from the IDA results (i.e., the IDA curve) developed for GM_x and MDL_i. Assuming that the system parameter variability is independent of GM_x and IM, $P(MDL_i|GM_x,IM)$ simplifies to $P(MDL_i)$, and Equation 6.28 can be written as follows:

$$P(Br_{DS,n}|GM_x,IM) = \sum_{all\ MDL_i} F_{\Delta_{Or,DS,n}}(\Delta_{Or_{x,i}}) \cdot P(MDL_i) \quad (6.29)$$

Similar to the demolition fragility function, the objective is to modify $F_{\Delta_{Or,DS,n}}$ in a way that includes the uncertain effects of system parameter variability, in addition to the epistemic uncertainty associated with the n^{th} brace DS, using the GM subset MC simulation results. The modified $F_{\Delta_{Or,DS,n}}$ is denoted by $F_{\Delta_{Or,DS,MDL,n}}$ which is unknown and needs to be determined. The random variable for $F_{\Delta_{Or,DS,MDL,n}}$ is denoted by $\Delta_{Or,DS,MDL,n}$. To be useful, $F_{\Delta_{Or,DS,MDL,n}}$ is defined so that when evaluated at $\Delta_{Or_{x,BM}}$, the resulting probability is equivalent to the result from Equation (6.29). Therefore, $F_{\Delta_{Or,DS,MDL,n}}$ is estimated by setting $P(Br_{DS,n}|GM_x,IM)$ equal to $F_{\Delta_{Or,DS,MDL,n}}(\Delta_{Or_{x,BM}})$ and then finding $F_{\Delta_{Or,DS,MDL,n}}$ from the results, as follows:

$$P(Br_{DS,n}|GM_x,IM) = F_{\Delta_{Or,DS,MDL,n}}(\Delta_{Or_{x,BM}}) \quad (6.30)$$

where the value of $P(Br_{DS,n}|GM_x, IM)$ at each IM is determined from Equation (6.29) and the value of $\Delta_{Or_{x,BM}}$ at each IM is determined using the one-to-one relationship between Δ_{Or} and IM for GM_x and the base model (symbolically stated as $\Delta_{Or_{x,BM}} = fcn_{x,BM}(IM)$).

Once $F_{\Delta_{Or,DS,MDL,n}}$ is determined it can be used for all GM_l of the full Far-Field GM set. Note that the dispersion in $F_{\Delta_{Or,DS,n}}$ is due to the epistemic uncertainty in the EDP limit value for the n^{th} brace DS, while the dispersion in $F_{\Delta_{Or,DS,MDL,n}}$ is due to: (i) the epistemic uncertainty in the EDP limit value for the n^{th} brace DS; and (ii) the effect of system parameter variability. While modeling uncertainty is not considered in the present example, the procedure for including modeling uncertainty is exactly the same as the procedure for including system parameter variability.

The $P(Br_{DS,1}|GM_x)$ values obtained from Equation (6.29) are plotted against the $\Delta_{Or_{x,BM}}$ values obtained from $\Delta_{Or_{x,BM}} = fcn_{x,BM}(IM)$, at each IM for the third story braces of 9SCBF archetype building and GM_x = TMZ-270 in Figure 6.28, shown by the "X" symbols. Also shown in Figure 6.28 is the fitted lognormal CDF to the results and $F_{\Delta_{Or,DS,1}}$. The small difference between the fitted lognormal CDF and $F_{\Delta_{Or,DS,1}}$ shows that effect of the system parameter variability is negligible on the first DS (corresponding to brace straightening) for the third story braces for GM_x = TMZ-270. It can be seen from Figure 6.28 that the $P(Br_{DS,1}|GM_x)$ values are mostly close to 0 and 1 and there is only one data point with $0 < P(Br_{DS,1}|GM_x) < 1$. This result can be explained using Figure 6.16, where the Δ_{Or} values are either zero (i.e., no residual out-of-plane displacement) or are large enough for which $F_{\Delta_{Or,Ds,1}}(\Delta_{Or}) \approx 1$. There is only one Δ_{Or} values for which $0 < F_{\Delta_{Or,Ds,1}}(\Delta_{Or}) < 1$.

Similarly, $P(Br_{DS,2}|GM_x)$ values for the second brace DS (corresponding to brace replacement) are plotted against the $\Delta_{Or_{x,BM}}$ values for the third story braces and GM_x = TMZ-270 in Figure 6.29, shown by the "X" symbols. Also shown in Figure 6.29 is the fitted lognormal CDF to the results (i.e., $\hat{F}_{\Delta_{Or,DS,MDL,2}}$) and $F_{\Delta_{Or,DS,2}}$. The difference between

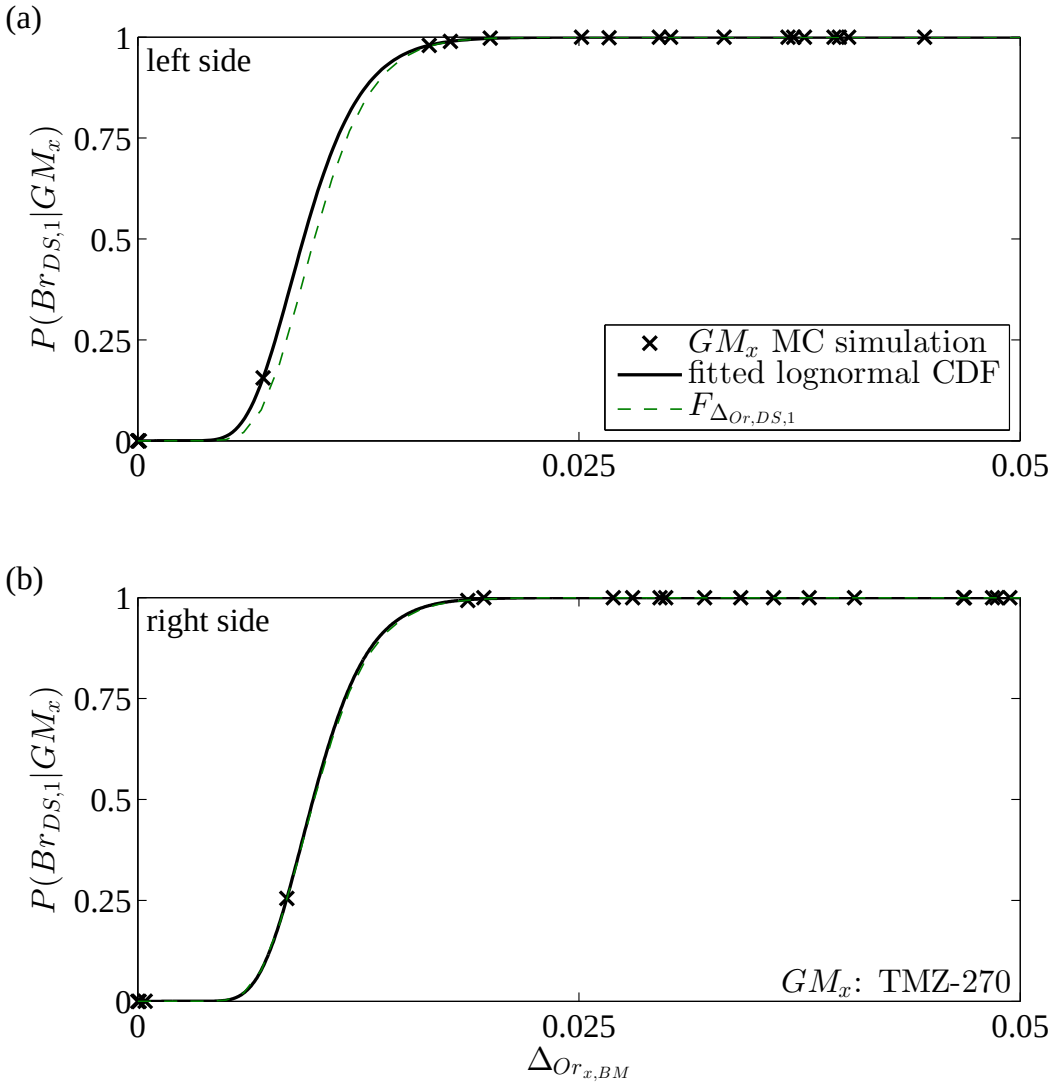

Figure 6.28: Estimating $F_{\Delta_{Or,DS,1,MDL,x}}$ for (brace straightening of) third story braces and GM_x = TMZ-270: (a) left side brace; and (b) right side brace

$F_{\Delta_{Or,DS,2}}$ and the fitted lognormal CDF is small for the left side brace. This small difference is due to the small variability of the Δ_{Or} values over the approximate range of at $1g < S_a(T,5\%) < 2.25g$, as shown in Figure 6.16(a).

The variation of the $\Delta_{Or_{x,i}}$ values in the regions where $F_{\Delta_{Or,DS,2}}(\Delta_{Or_{x,i}}) \approx 0$ or 1 (i.e., at the tail regions of $F_{\Delta_{Or,DS,2}}$), does not affect the $P(Br_{DS,2}|GM_x)$ values from Equation (6.29) because of the small sensitivity of $F_{\Delta_{Or,DS,2}}$ in those regions. Therefore, although the variation of the $\Delta_{Or_{x,i}}$ values increases in the range of $2.25g < S_a(T,5\%) < 3g$ in Figure 6.16(a), the difference between the $P(Br_{DS,2}|GM_x)$ values from Equation (6.29) and $F_{\Delta_{Or,DS,2}}$ evaluated at $\Delta_{Or_{x,BM}}$ in the range of $2.25g < S_a(T,5\%) < 3g$ is small. As a result, the fitted lognormal CDF (i.e., $\hat{F}_{\Delta_{Or,DS,MDL,2}}$) is close to $F_{\Delta_{Or,DS,2}}$ for the left side third story brace of the 9SCBF archetype building, as shown in Figure 6.29(a).

The difference between the fitted lognormal CDF (i.e., $\hat{F}_{\Delta_{Or,DS,MDL,2}}$) and $F_{\Delta_{Or,DS,2}}$ is not small for the right side third story brace of the 9SCBF archetype building, as shown in Figure 6.29(b). Looking at Figure 6.16(b), it can be seen that variation of the $\Delta_{Or_{x,i}}$ values increase as IM increases. The variation of $\Delta_{Or_{x,i}}$ becomes considerable when $S_a(T,5\%) \approx 2.5g$. This variation of the $\Delta_{Or_{x,i}}$ values at $S_a(T,5\%) \geq 2.5g$ causes a considerable difference between the $P(Br_{DS,2}|GM_x)$ values from Equation (6.29) and $F_{\Delta_{Or,DS,2}}(\Delta_{Or_{x,BM}})$. This considerable difference is the main contributor to the observed difference between the fitted lognormal CDF (i.e., $\hat{F}_{\Delta_{Or,DS,MDL,2}}$) and $F_{\Delta_{Or,DS,2}}$ in Figure 6.29(b).

An interesting observation from Figure 6.16(b) at $S_a(T,5\%) \geq 2.5g$ is the decreased amplitude of the Δ_{Or} values for the right side brace and the increased Δ_{Or} values for the left side brace, as the IM increases. This result indicates that while both the left side and right side braces buckle at $S_a(T,5\%) \geq 2.5g$, the buckling is more severe for the left side brace. Note that while the $\Delta_{Or_{x,i}}$ values for the right side brace decreases at $S_a(T,5\%) \geq 2.5g$, they are away from the tail regions of $F_{\Delta_{Or,DS,2}}$ and therefore $P(Br_{DS,2}|GM_x)$ is sensitive to this

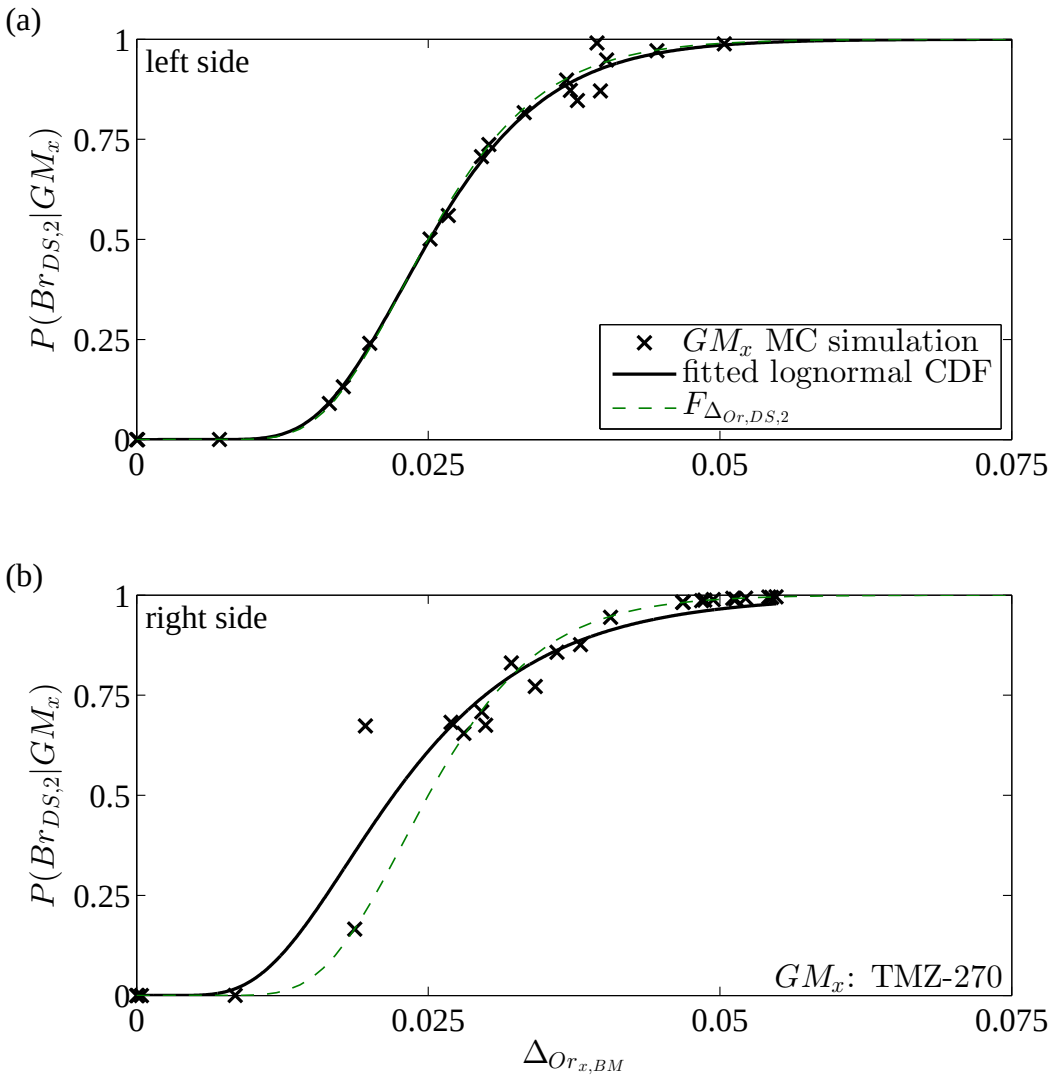

Figure 6.29: Estimating $F_{\Delta_{Or,DS,,2,MDL,x}}$ for (brace replacement of) third story braces and GM_x = TMZ-270: (a) left side brace; and (b) right side brace

variation of $\Delta_{Or_{x,i}}$ values.

The $P(Br_{DS,1}|GM_x)$ and $\Delta_{Or_{x,BM}}$ values are plotted and the fitted lognormal CDF (i.e., $\hat{F}_{\Delta_{Or,DS,MDL,1}}$) is shown for the first DS (corresponding to brace straightening) of the third story braces and the remaining GM_x of the GM subset in Figures 6.30 through 6.33. The $P(Br_{DS,2}|GM_x)$ and $\Delta_{Or_{x,BM}}$ values are plotted and the fitted lognormal CDF (i.e., $\hat{F}_{\Delta_{Or,DS,MDL,2}}$) is shown for the second DS (corresponding to brace replacement) of the third story braces and the remaining GM_x of the GM subset in Figures 6.34 through 6.37. It can be seen that for most GM_x of the GM subset the difference between the fitted lognormal CDF and $F_{\Delta_{Or,DS,n}}$ is significant. In many cases the fitted lognormal CDF is not a reasonable fit to the $P(Br_{DS,n}|GM_x)$ and $\Delta_{Or_{x,BM}}$ data. The main reason for a large difference between the fitted lognormal CDF and the $P(Br_{DS,n}|GM_x)$ and $\Delta_{Or_{x,BM}}$ data is the large variability of the $\Delta_{Or_{x,i}}$ values due to the variability of random system parameters as was discussed above for $GM_x =$ TMZ-270 using Figure 6.16.

One reason for poor fit to the $P(Br_{DS,n}|GM_x)$ data is the considerable difference between the $\Delta_{Or_{x,BM}}$ value and the median of $\Delta_{Or_{x,i}}$ values. For example, in Figures 6.19(a) and 6.20(a) it can be seen that at some IM values, the $\Delta_{Or_{x,BM}}$ value is close to zero (i.e., indicating no residual deformation due to buckling for the base model) while $\Delta_{Or_{x,i}}$ values vary over a large range, between values corresponding to no damage and values corresponding to 100% probability of brace replacement. In such cases, using $\Delta_{Or_{x,BM}} \approx 0$ and a non-zero $P(Br_{DS,n}|GM_x)$ value from Equation (6.29) in the data used to fit a lognormal CDF, results in an unreliable estimation for $\hat{F}_{\Delta_{Or,DS,n,MDL}}$.

The large variability of the $\Delta_{Or_{x,i}}$ values due to the variability of the random system parameters (i.e., Δ_{Oi} and LL) makes it impractical to estimate the effect of the system parameter variability in $F_{\Delta_{Or,DS,n}}$ by fitting a lognormal CDF to the $P(Br_{DS,n}|GM_x)$ versus $\Delta_{Or_{x,BM}}$ data. For the example of brace damage (with the initial brace out-of-straightness as

a random system parameter), a full MC simulation is needed to study the effect of system parameter variability on the probability of damage scenarios which include brace damage. Equation 6.6 can be used to evaluate the probability of such damage scenarios using the results of the full MC simulation.

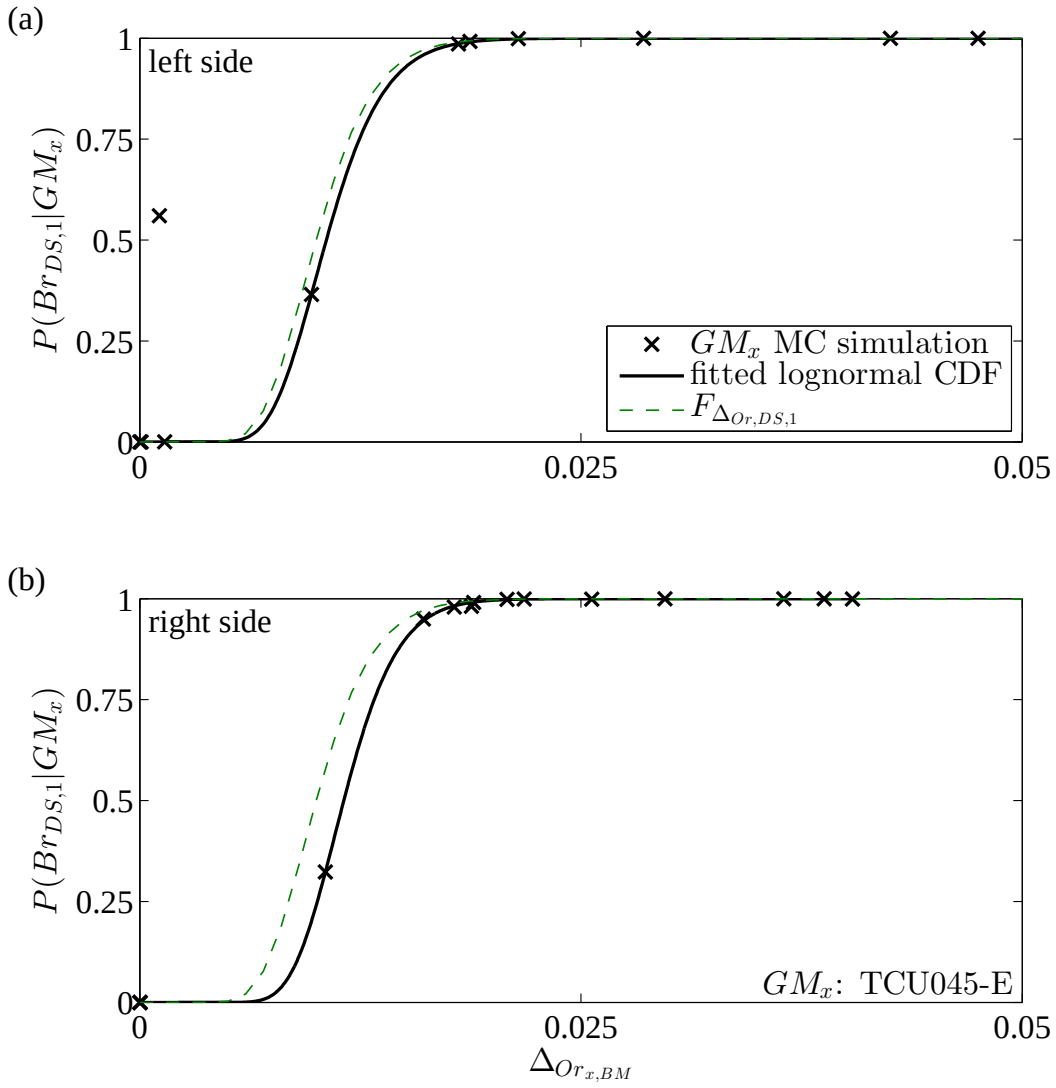

Figure 6.30: Estimating $F_{\Delta_{Or,DS,1,MDL,x}}$ for (brace straightening of) third story braces and GM_x = TCU045-E: (a) left side brace; and (b) right side brace

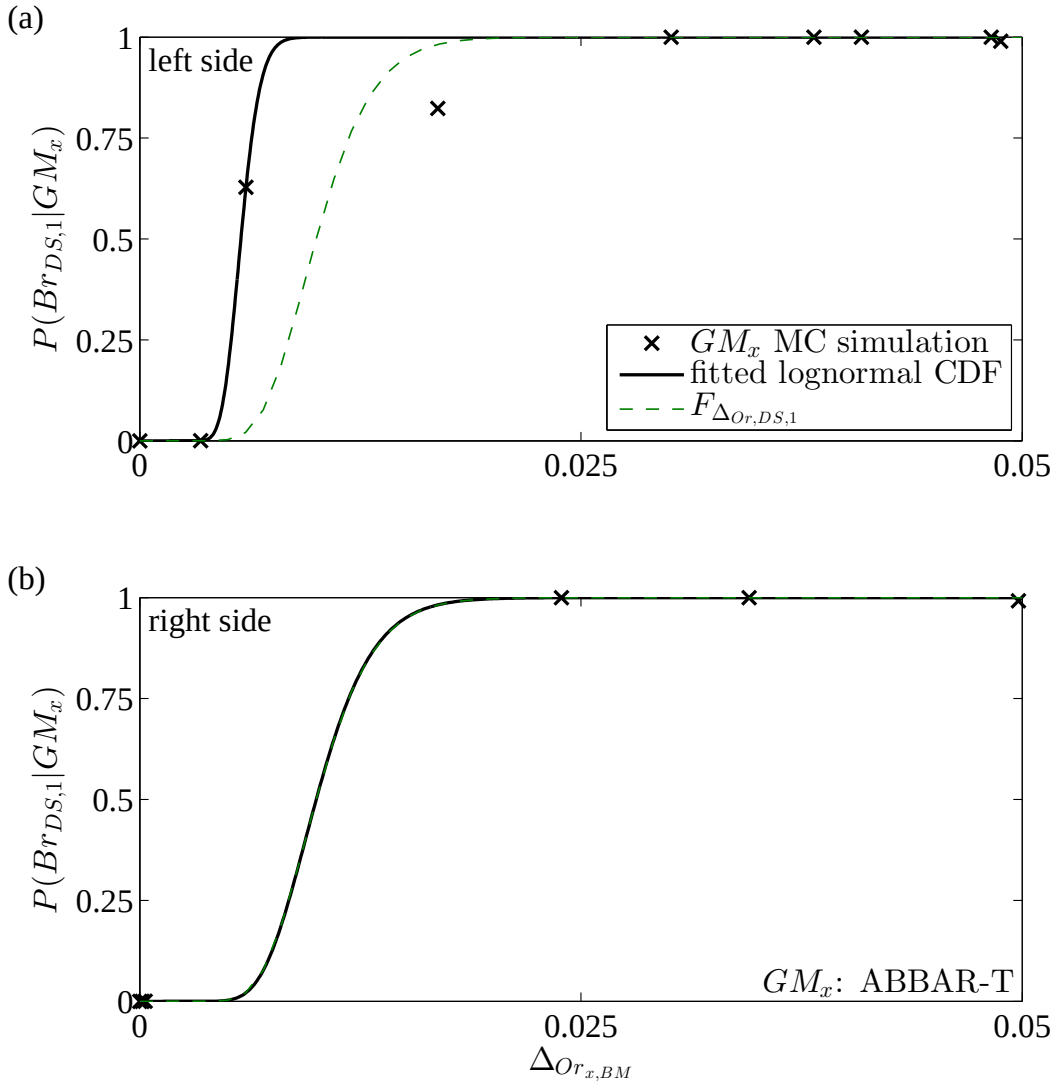

Figure 6.31: Estimating $F_{\Delta_{Or,DS,1,MDL,x}}$ for (brace straightening of) third story braces and GM_x = ABBAR-T: (a) left side brace; and (b) right side brace

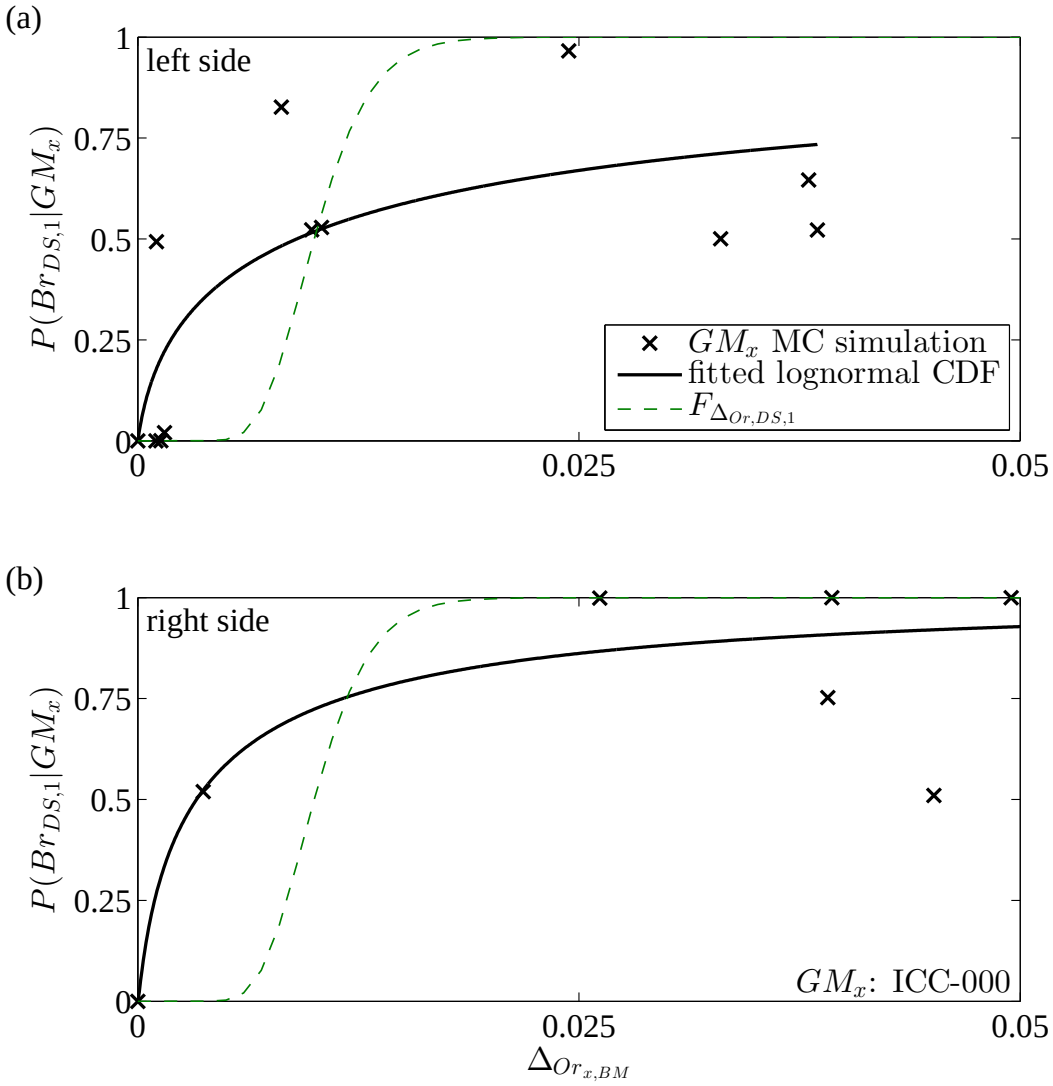

Figure 6.32: Estimating $F_{\Delta_{Or,DS,1,MDL,x}}$ for (brace straightening of) third story braces and GM_x = ICC-000: (a) left side brace; and (b) right side brace

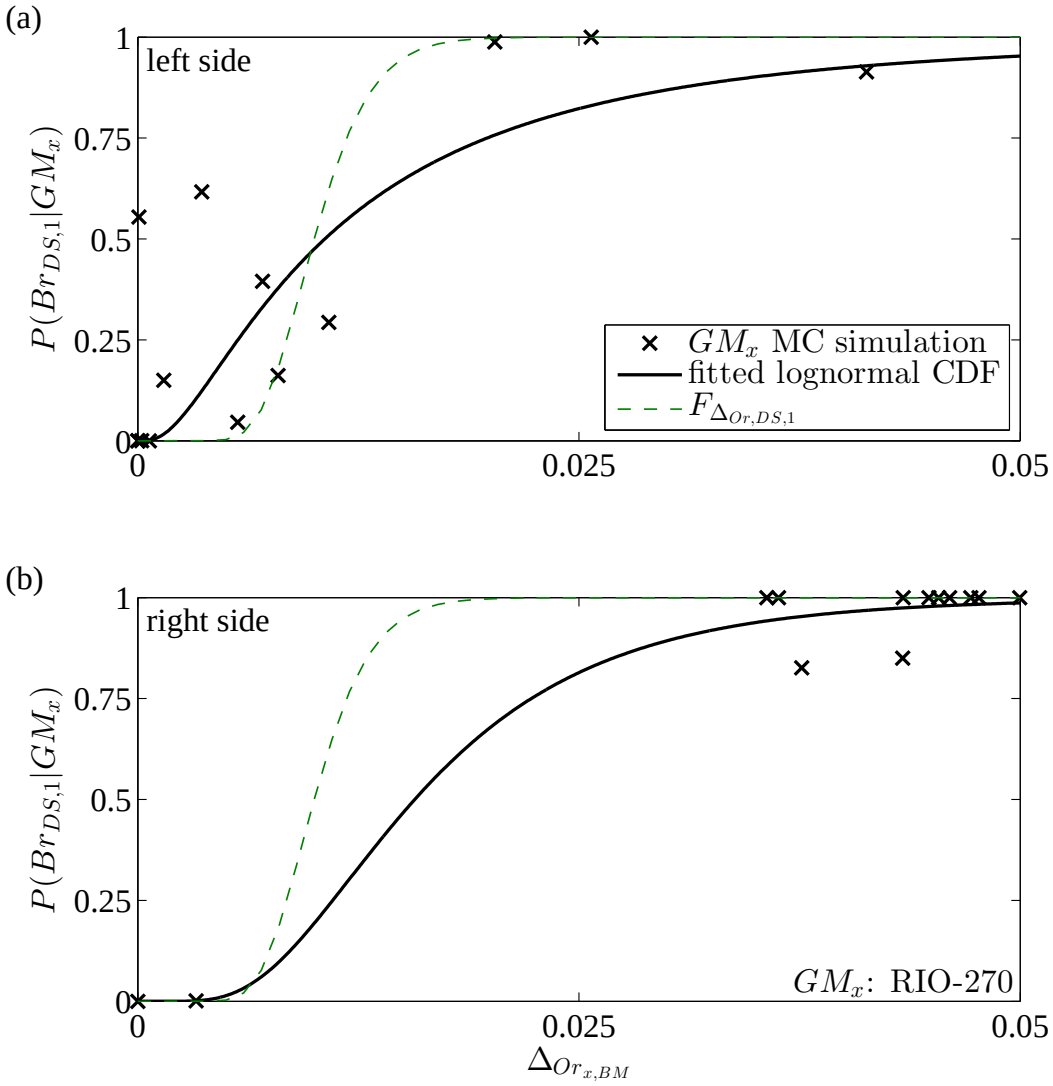

Figure 6.33: Estimating $F_{\Delta_{Or,DS,1,MDL,x}}$ for (brace straightening of) third story brace and GM_x = RIO-270: (a) left side brace; and (b) right side brace

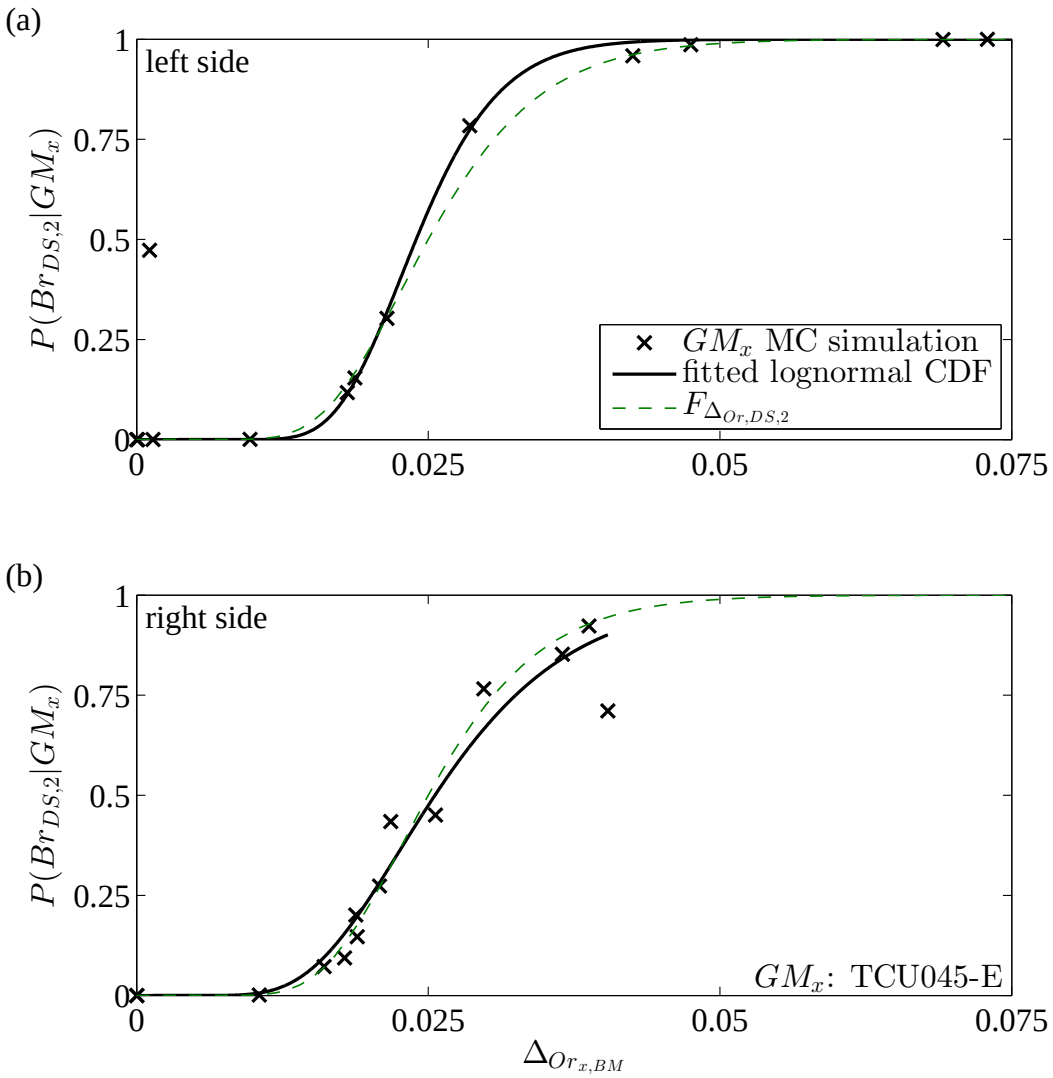

Figure 6.34: Estimating $F_{\Delta_{Or,DS,2,MDL,x}}$ for (brace replacement of) third story braces and GM_x = TCU045-E: (a) left side brace; and (b) right side brace

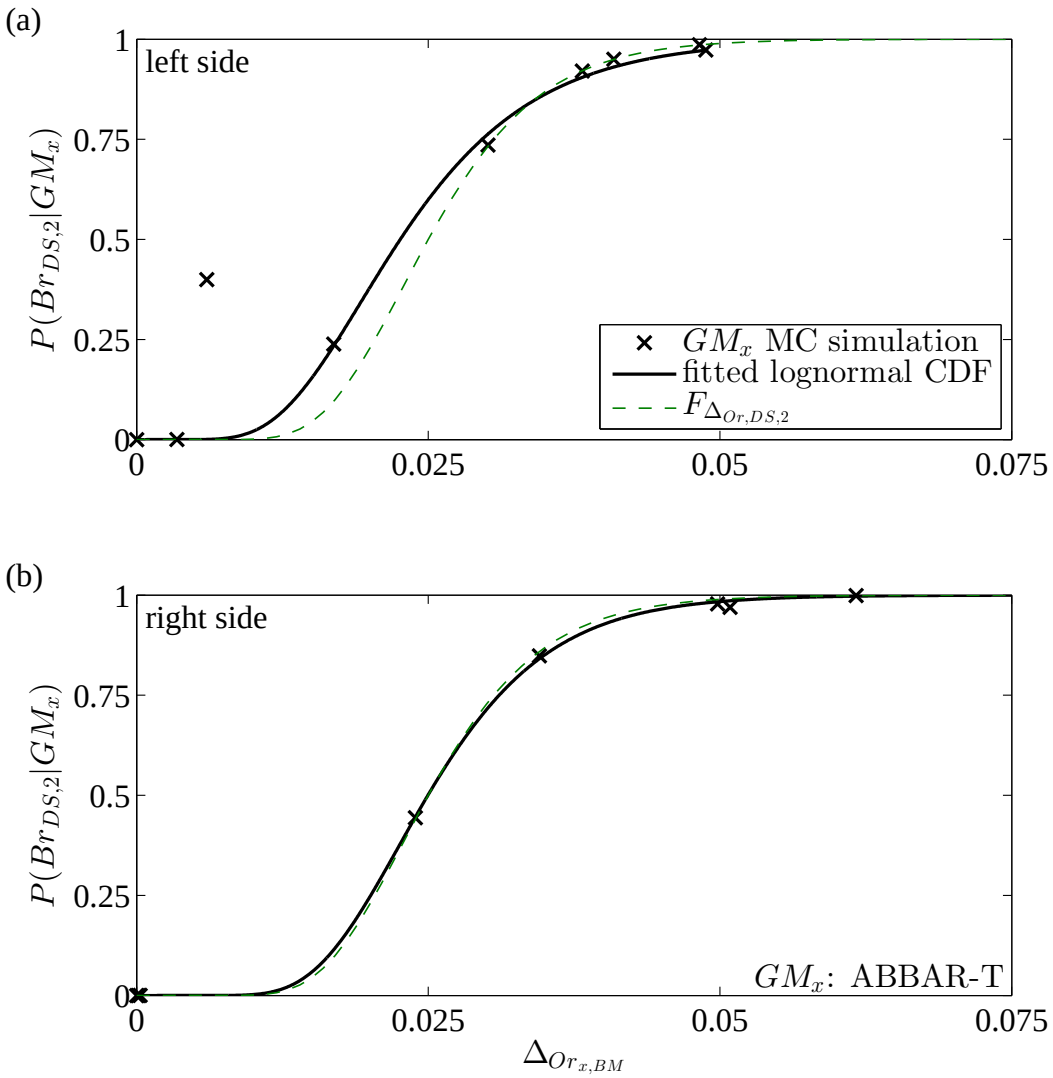

Figure 6.35: Estimating $F_{\Delta_{Or,DS,2,MDL,x}}$ for (brace replacement of) third story braces and GM_x = ABBAR-T: (a) left side brace; and (b) right side brace

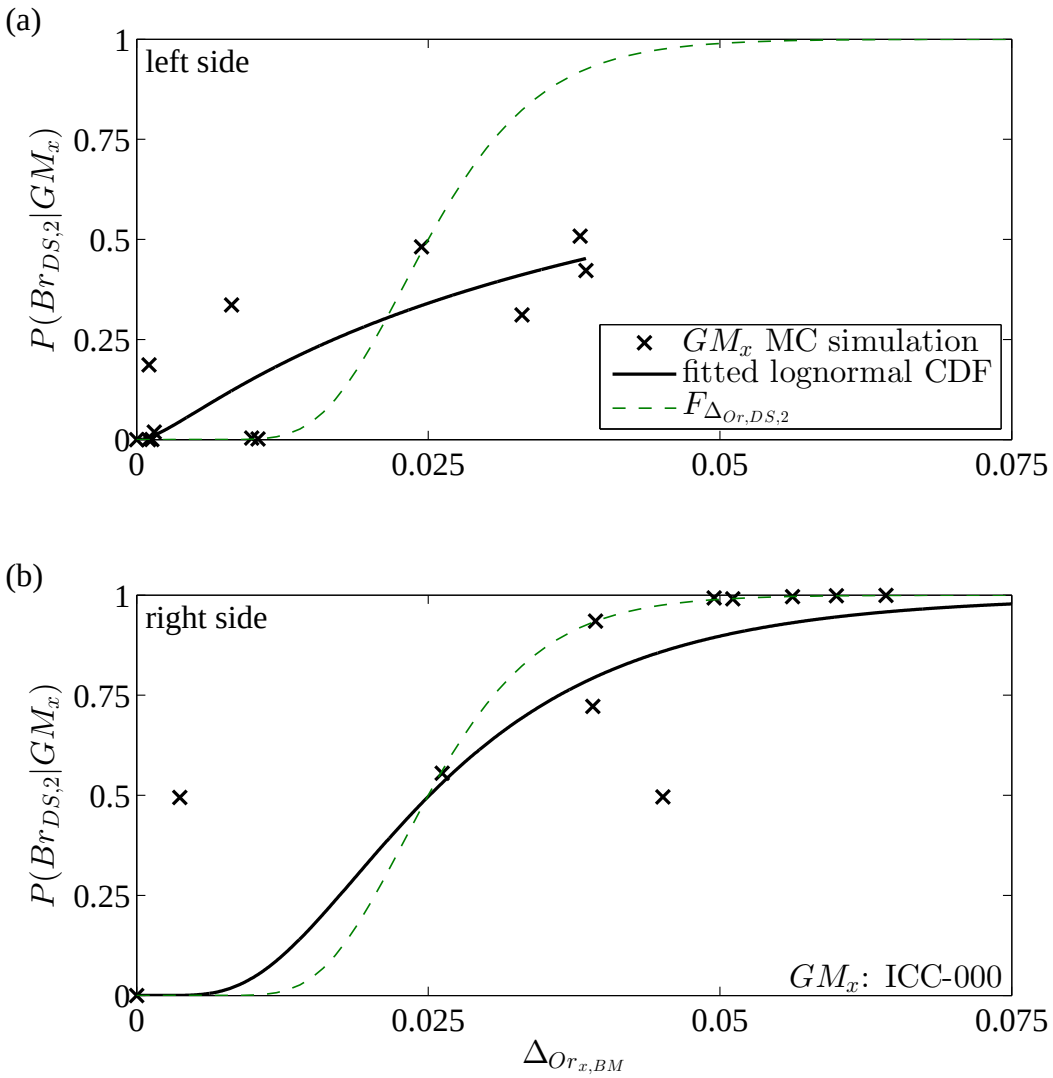

Figure 6.36: Estimating $F_{\Delta_{Or,DS,2,MDL,x}}$ for (brace replacement of) third story braces and GM_x = ICC-000: (a) left side brace; and (b) right side brace

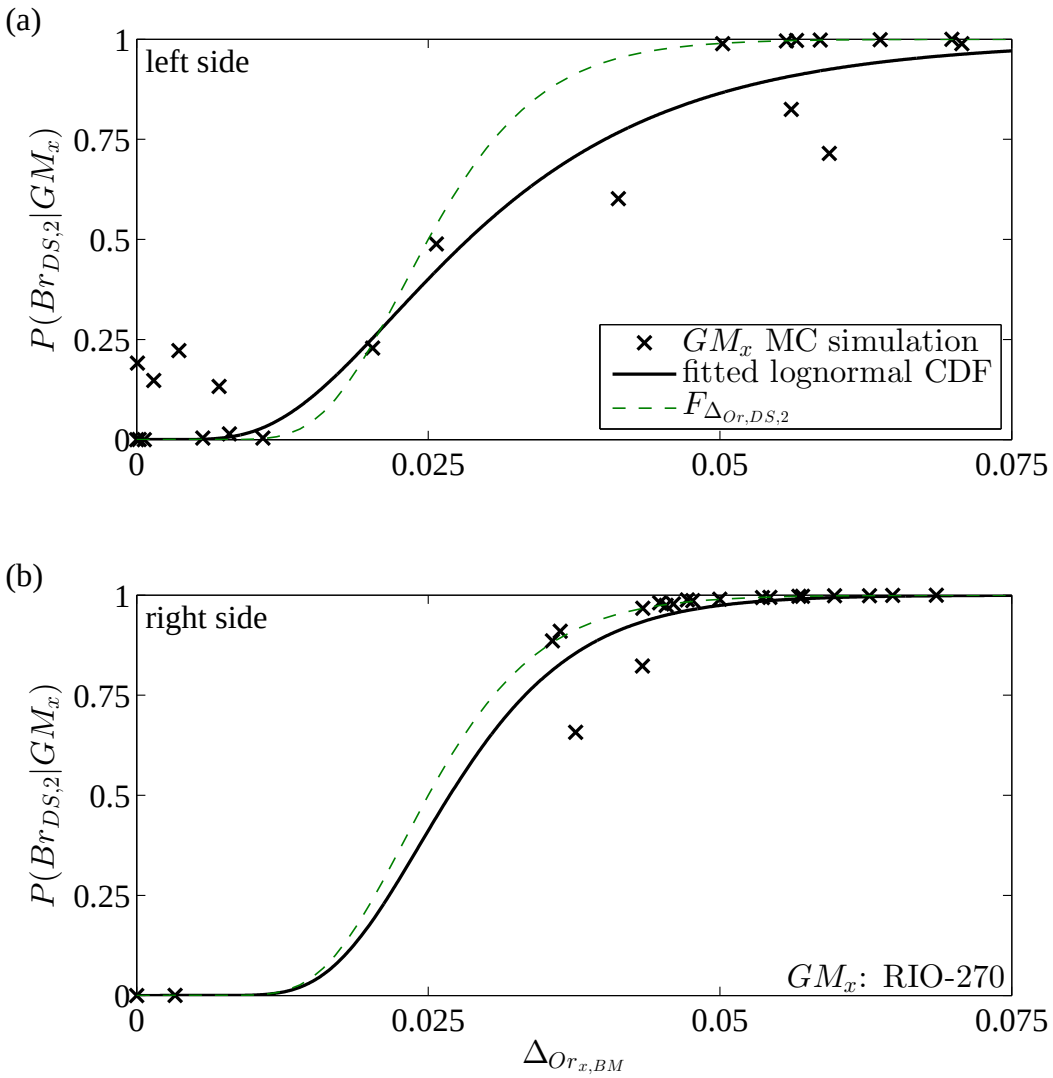

Figure 6.37: Estimating $F_{\Delta_{Or,DS,2,MDL,x}}$ for (brace replacement of) third story brace and GM_x = RIO-270: (a) left side brace; and (b) right side brace

6.4.3 Estimating collapse DS fragility function with system parameter variability

The effect of system parameter variability is estimated for the collapse DS by fitting a lognormal CDF to the GM_x MC simulation results. In contrast to the demolition DS and brace DS (which are quantified using a single fragility function to express the random EDP limit value for the DS, such as $F_{\theta_{r,D}}(\theta_r)$), the probability of collapse at various IM values for an individual IDA curve is quantified using the IM-based collapse fragility function (see Section 5.5). As stated previously, two criteria are used to establish collapse: (i) a reduction in the slope of the $S_a(T,5\%)$ versus θ_m IDA curves; and (ii) a maximum story drift ratio, θ_m, of 0.1. The slope reduction criterion is defined in a probabilistic manner for each IDA curve as discussed in Chapter 5.

The probability of collapse at a given IM value for an individual IDA curve can be stated as $P(IM \geq IM_C)$ using the IM-based method for quantifying collapse (see Section 5.5). IM_C is the IM limit value that separates the non-collapse DS from the collapse DS and is defined as a random variable. $P(IM \geq IM_C)$ can be quantified by $F_{IM_C}(IM)$, where F_{IM_C} is the collapse fragility function (i.e., CDF of IM_C). As mentioned previously, an IM versus EDP ($S_a(T,5\%)$ versus θ_m) IDA curve is plotted for each numerical model and GM pair. Since the collapse fragility function is defined for each IDA curve separately, F_{IM_C} is expressed as $F_{IM_{C,x,i}}$ for the IDA curve plotted for each given GM_x and numerical model MDL_i. Similarly, $F_{IM_{C,x,BM}}$ is the collapse fragility function defined for the IDA curve plotted for GM_x and the base model. Therefore, the probability of collapse for GM_x and a sample model MDL_i at a given IM value can be quantified as follows:

$$P(C|MDL_i, GM_x, IM) = P(IM \geq IM_C|MDL_i, GM_x, IM) = F_{IM_{C,x,i}}(IM) \tag{6.31}$$

The system parameter variability can be included in $P(C|GM_x)$ at any given IM value, using the GM_x MC simulation results as follows:

$$P(C|GM_x, IM) = \sum_{all\ MDL_i} P(C|MDL_i, GM_x, IM) \cdot P(MDL_i|GM_x, IM) \tag{6.32}$$

Assuming that the random system parameter values, for which the numerical model MDL_i is developed, are independent of GM_x and IM, $P(MDL_i|GM_x, IM)$ simplifies to $P(MDL_i)$. Substituting for $P(C|MDL_i, GM_x, IM)$ from Equation (6.31), Equation (6.32) can be written as follows:

$$P(C|GM_x, IM) = \sum_{all\ MDL_i} F_{IM_{C,x,i}}(IM) \cdot P(MDL_i) \tag{6.33}$$

Equation (6.33) is one term from the summation over all GM_l in Equation (6.14). The subscript l is replaced by subscript x, to refer to an individual GM from the GM subset.

Similar to the approach taken for the demolition DS and the brace DS , the approach here is to include the effect of the system parameter variability on the collapse DS fragility function by modifying F_{IM_C} to represent the effect of the system parameter variability in addition to the epistemic uncertainty associated with the collapse criteria. The modified F_{IM_C} is denoted by $F_{IM_{C,MDL}}$. Similar to the demolition DS and brace DS, $F_{IM_{C,MDL}}$ can be estimated by fitting a CDF to the $P(C|GM_x, IM)$ values calculated using Equation (6.33) and the GM subset MC simulation results.

The probability of collapse for each individual GM_x of the GM subset is shown in part (a) of Figures 6.38 through 6.42 for the individual sample models and the base model. These probabilities are calculated using Equation (6.31). Also shown in part (a) of Figures 6.38 through 6.42, are the $P(C|GM_x, IM)$ values, calculated using Equation (6.33) and the GM_x MC simulation results. It can be seen that the effect of including system parameter variability is slight increase in the dispersion of $P(C|GM_x)$ from the GM_x MC simulation compared to $P(C|GM_x)$ from the base model (i.e., without system parameter variability).

The effect of including system parameter variability on the results for the collapse DS is different for different GM_x. For example, $P(C|GM_x)$ is identical for the base model and the sample models (and therefore for the GM_x MC simulation) for GM_x = TCU045-E as shown in Figure 6.39(a). The identical $P(C|GM_x)$ values for the base model and the sample models are due to the small sensitivity of the collapse DS under GM_x = TCU045-E to the variation of random system parameters as shown in Figure 6.3. The 75% and 85% slope reduction limits occur at the same $S_a(T,5\%)$ value for GM_x = TCU045-E, for the base model and the sample models. Therefore, the variation of random system parameters does not change the collapse fragility function for GM_x = TCU045-E, i.e., $F_{IM_{C,x,BM}} = F_{IM_{C,x,i}}$.

Part (b) of Figures 6.38 through 6.42 show the fitted lognormal CDF to the GM_x MC simulation results from Equation (6.33). Also shown in Part (b) of Figures 6.38 through 6.42 is $F_{IM_{C,x,BM}}$, based on the IDA curve for GM_x and the base model. As discussed in Chapter 5, $F_{IM_{C,x,BM}}$ is a uniform CDF that starts from 0 at the IM value corresponding to 75% slope reduction and increases linearly to 1.0 at the IM value corresponding to 85% slope reduction. The probability distribution for the fitted CDF to the GM_x MC simulation results is assumed to be lognormal. The fitted lognormal CDF includes the epistemic uncertainty due to the collapse criteria and the uncertainty due to the system parameter variability. The fitted lognormal CDF is in fact estimation of $F_{IM_{C,MDL,x}}$ for the IDA results for GM_x and is denoted by $\hat{F}_{IM_{C,MDL,x}}$.

From part (b) of Figures 6.38 through 6.42, it can be seen that for most GM_x the fitted lognormal CDF (i.e., $\hat{F}_{IM_{C,MDL,x}}$) is close to $F_{IM_{C,x,BM}}$. This result is due to the small sensitivity of the collapse DS to the variation of the random system parameters. For GM_x = RIO-270, however, the difference between $\hat{F}_{IM_{C,MDL,x}}$ and $F_{IM_{C,x,BM}}$ is not small as it can be seen in Figure 6.42(b). The dispersion of $\hat{F}_{IM_{C,MDL,x}}$ is larger than that of $F_{IM_{C,x,BM}}$ for GM_x = RIO-270 and the median value of $IM_{C,MDL,x}$ (the underlying random variable for $F_{IM_{C,MDL,x}}$) is different than the median value of $IM_{C,x,BM}$ (the underlying random variable

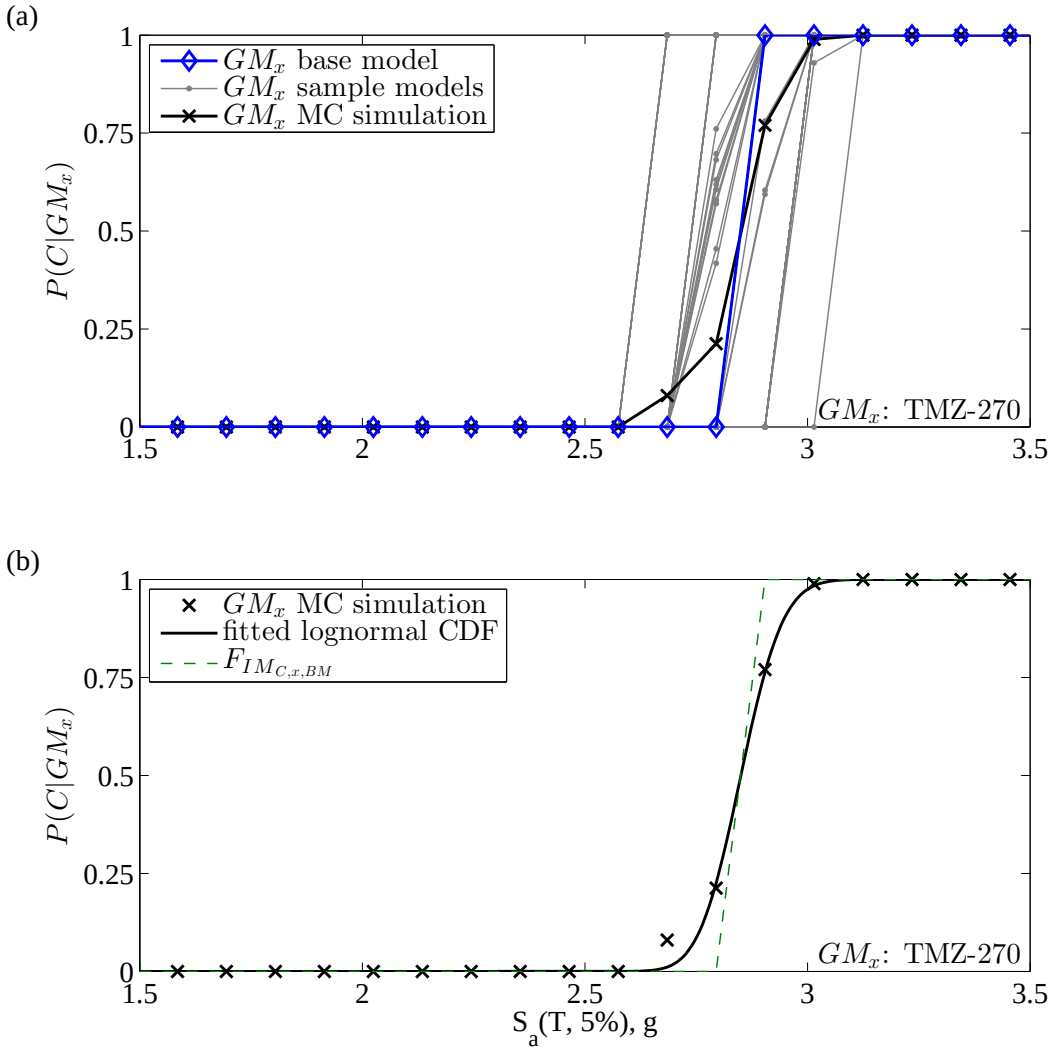

Figure 6.38: Probability of collapse for GM_x = TMZ-270: (a) for base model, sample models, and GM_x MC simulation results; and (b) estimating the effect of system parameter variability by fitting lognormal CDF to GM_x MC simulation results

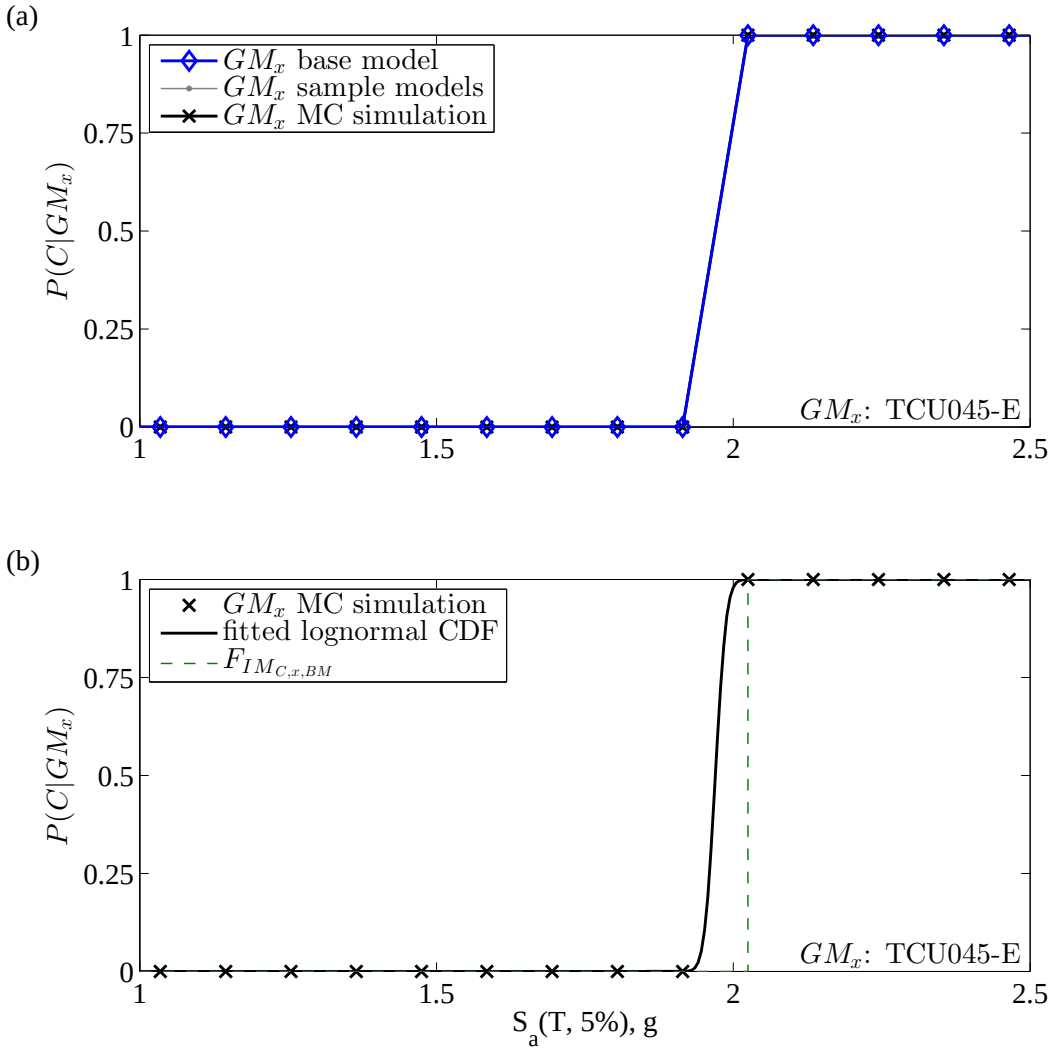

Figure 6.39: Probability of collapse for GM_x = TCU045-E: (a) for base model, sample models, and GM_x MC simulation results; and (b) estimating the effect of system parameter variability by fitting lognormal CDF to GM_x MC simulation results

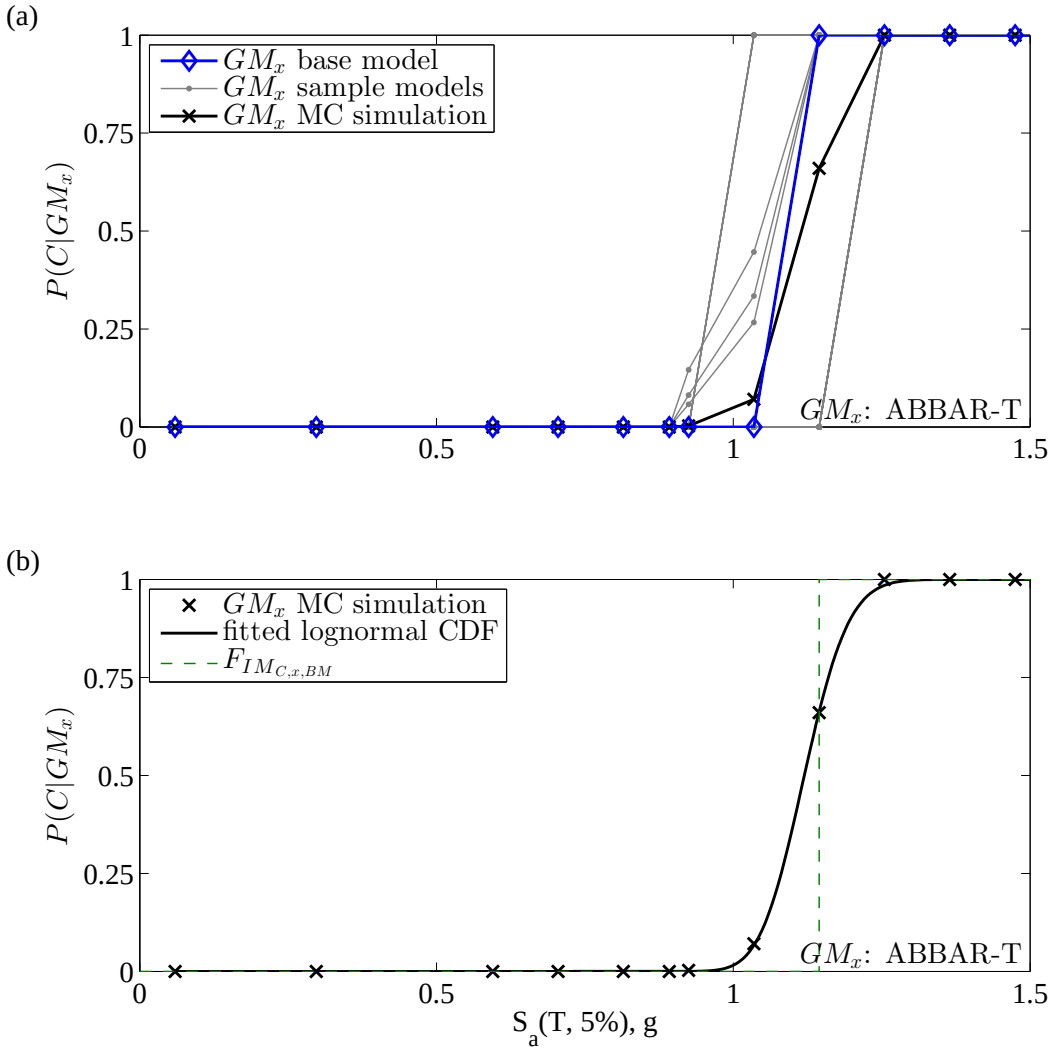

Figure 6.40: Probability of collapse for GM_x = ABBAR-T: (a) for base model, sample models, and GM_x MC simulation results; and (b) estimating the effect of system parameter variability by fitting lognormal CDF to GM_x MC simulation results

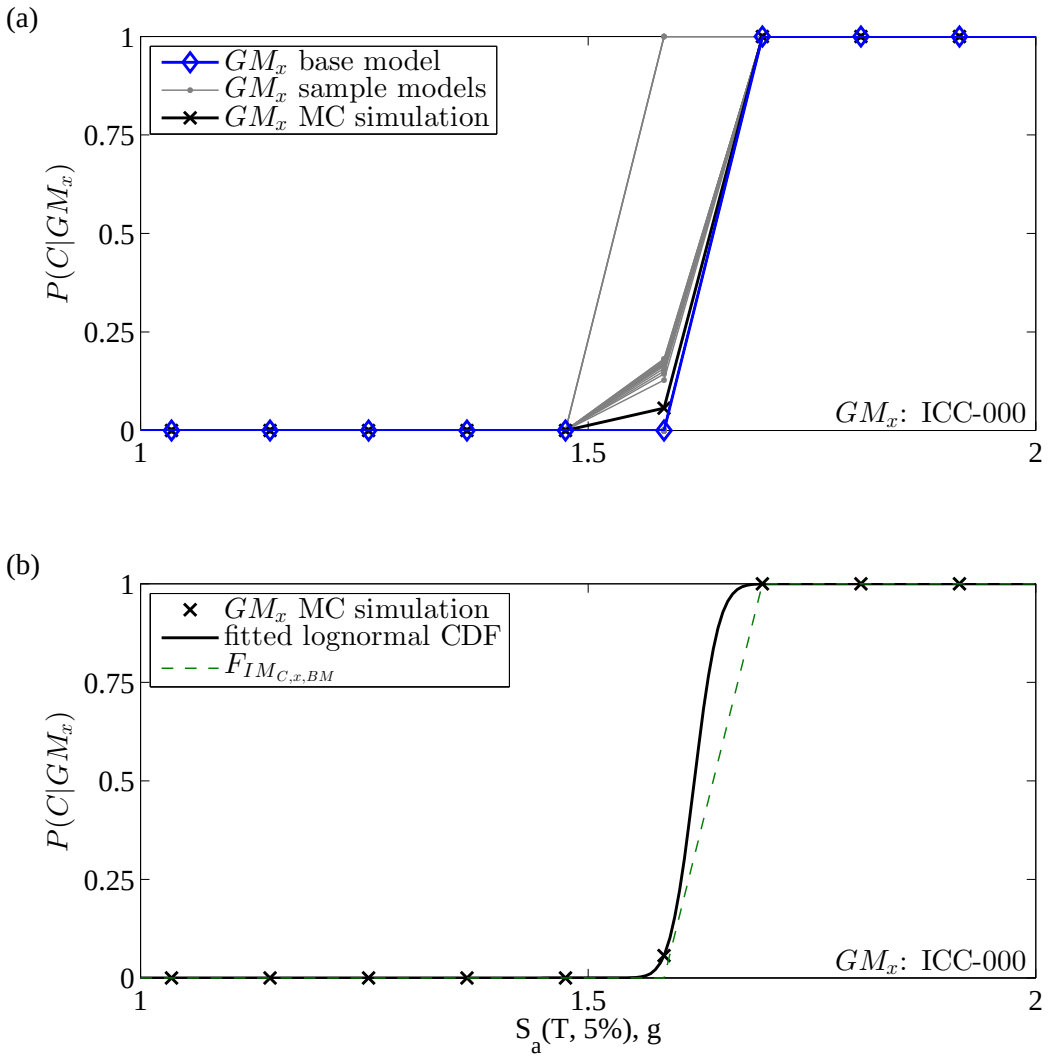

Figure 6.41: Probability of collapse for GM_x = ICC-000: (a) for base model, sample models, and GM_x MC simulation results; and (b) estimating the effect of system parameter variability by fitting lognormal CDF to GM_x MC simulation results

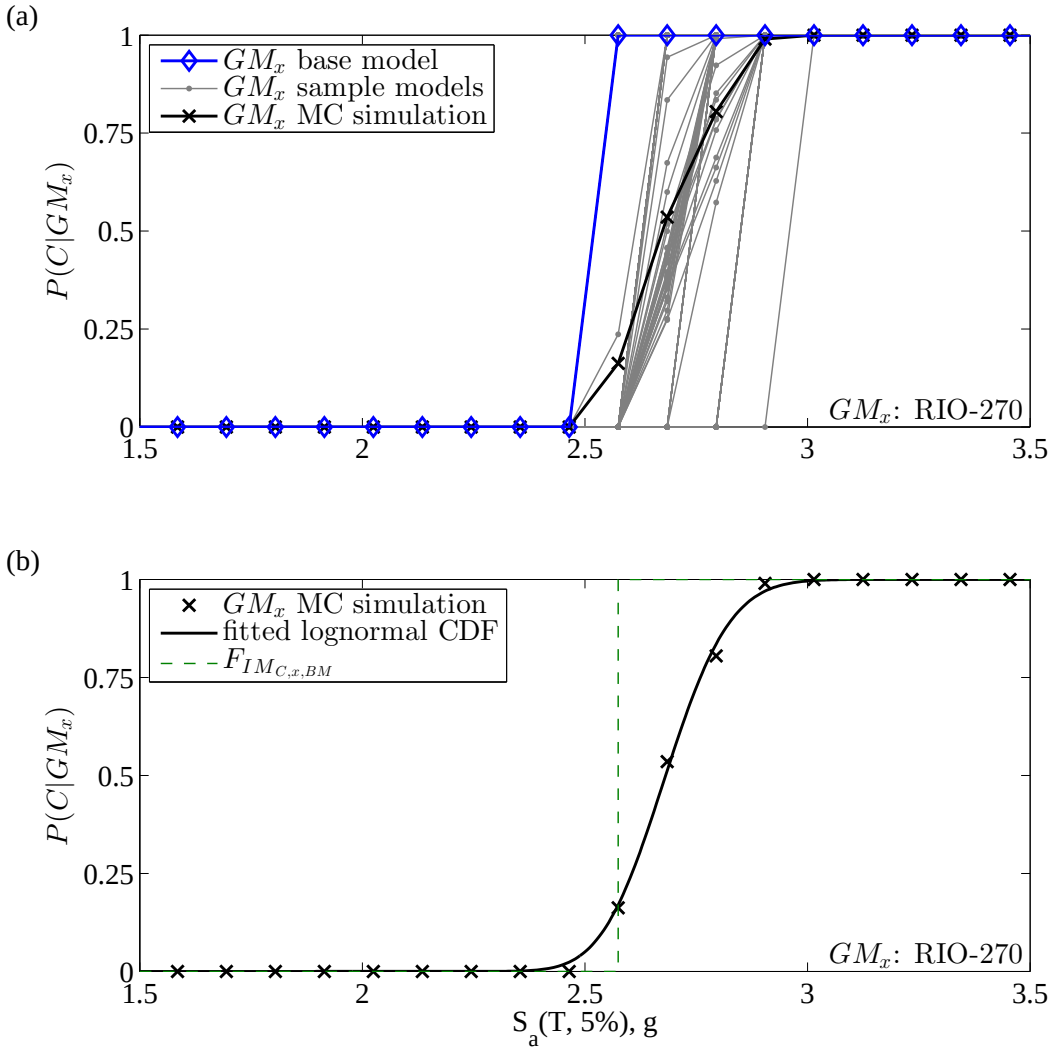

Figure 6.42: Probability of collapse for GM_x = RIO-270: (a) for base model, sample models, and GM_x MC simulation results; and (b) estimating the effect of system parameter variability by fitting lognormal CDF to GM_x MC simulation results

Table 6.3: Median and dispersion of $\hat{F}_{IM_{C,MDL,x}}$ and $F_{IM_{C,x,BM}}$

GM_x	*med* $IM_{C,MDL,x}$ (g)	*med* $IM_{C,x,BM}$ (g)	$\sigma_{\ln IM_{C,MDL,x}}$	$\sigma_{IM_{C,x,BM}}$
TMZ-270	2.85	2.85	0.026	0.011
TCU045-E	1.97	2.02	0.007	0
ABBAR-T	1.12	1.14	0.053	0
ICC-000	1.62	1.64	0.013	0.019
RIO-270	2.68	2.57	0.043	0

for $F_{IM_{C,x,BM}}$). For the other GM_x of the GM subset, the median value of $IM_{C,MDL,x}$ is close to the median value of $IM_{C,x,BM}$. The median value and logarithmic standard deviation of $IM_{C,MDL,x}$ and the median value and dispersion of $IM_{C,x,BM}$ are given in Table 6.3. $\sigma_{IM_{C,x,BM}}$ is zero for $GM_x =$ TCU045-E, ABBAR-T, and RIO-270, as shown in Table 6.3. $\sigma_{IM_{C,x,BM}} = 0$ occurs when the IM_C corresponding to 75% slope reduction is the same as the IM_C corresponding to 85% slope reduction.

As stated previously, the collapse fragility function is determined for each IDA curve separately, corresponding to a given GM_x and MDL_i. As a result, the median $IM_{C,x,BM}$ values are different for each GM_x as shown in Table 6.3. To use the GM subset MC simulation results as the basis for estimating the effect of system parameter variability for each GM_l of the Far-Field GM set, it is assumed that the median $IM_{C,l,BM}$ values are the same as $IM_{C,MDL,l}$ as developed in Chapter 5 without system parameter variability and the $\sigma_{IM_{C,l,BM}}$ values increase when system parameter variability is included. It should be noted that $IM_{C,l,BM}$ is the random variable for $F_{IM_{C,l,BM}}$, defined for GM_l and the base model as shown in Chapter 5. $IM_{C,l,BM}$ follows a uniform probability distribution between the IM_C value at 75% slope reduction and the IM_C value at 85% slope reduction on the ($S_a(T,5\%)$ versus θ_m) IDA curve for GM_l and the base model. $IM_{C,MDL,l}$, however, is the random variable for $F_{IM_{C,MDL,l}}$ and follows a lognormal probability distribution. The median value of $IM_{C,MDL,l}$ is assumed to be the same as the median value of $IM_{C,l,BM}$ for each GM_l, while the standard deviation of $IM_{C,MDL,l}$ is assumed to be greater than the standard deviation of

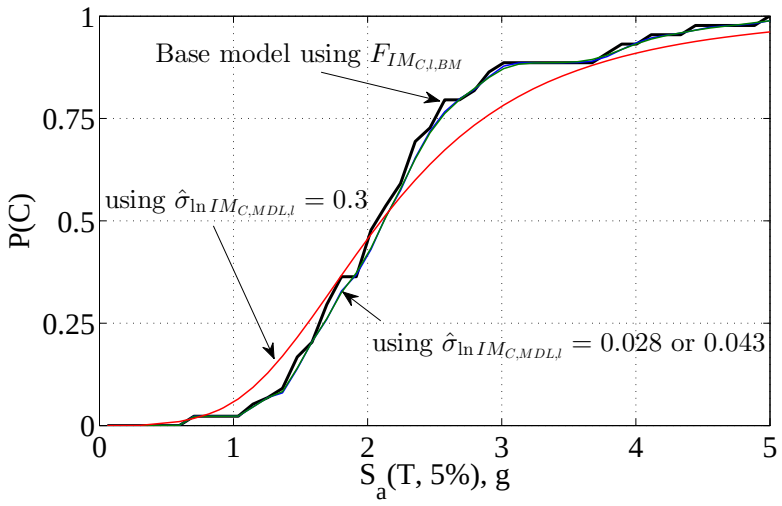

Figure 6.43: Probability of collapse (C) with system parameter variability

$IM_{C,l,BM}$ (due to the system parameter variability).

The GM subset MC simulation results are used to estimate the dispersion for $IM_{C,MDL,l}$. In this study it is observed that the $\hat{\sigma}_{\ln IM_{C,MDL,x}}$ values (shown in Table 6.3) are small compared to the other DS fragilities (e.g., $\sigma_{\ln \theta_{r,D}} = 0.3$). Treating $\hat{\sigma}_{\ln IM_{C,MDL,x}}$ as a random variable itself, both the expected value for $\hat{\sigma}_{\ln IM_{C,MDL,x}}$ (i.e., 0.028) and the maximum value for $\hat{\sigma}_{\ln IM_{C,MDL,x}}$ (i.e., 0.043) from Table 6.3 are used to estimate $F_{IM_{C,MDL,l}}$ for all GM_l of the Far-Field GM subset. Figure 6.43 shows $P(C)$ calculated using the Far-Field GM set. It can be seen that $P(C)$ for the base model (i.e., without system parameter variability) is very close to $P(C)$ with system parameter variability when $\hat{\sigma}_{\ln IM_{C,MDL,l}} = 0.028$ or 0.043 are used. The small difference between the two curves is expected as the collapse DS was not observed to be sensitive to the variation of random system parameters.

$P(C)$ was also calculated using $\hat{\sigma}_{\ln IM_{C,MDL,l}} = 0.3$ for all GM_l of the Far-Field GM set, for comparison, and is shown in Figure 6.43. The $\hat{\sigma}_{\ln IM_{C,MDL,l}}$ value of 0.3 is approximately 10 times greater than the $\hat{\sigma}_{\ln IM_{C,MDL,l}}$ value of 0.028. It can be seen that this increase in the standard deviation of $IM_{C,MDL,l}$ increases the dispersion of $P(C)$. This increase in the dispersion of $P(C)$ is not considerable compared to the total dispersion of $P(C)$ for the

base model. Note that the total dispersion of $P(C)$ for the base model is mainly due to the record-to-record (RTR) variability in structural response. Therefore, the contribution of RTR variability to the total dispersion of $P(C)$ is considerably greater than the contribution of system parameter variability to the total dispersion of $P(C)$.

6.4.4 Effect of system parameter variability on $NC \cap D$ damage scenario fragility

The effect of system parameter variability on the $NC \cap D$ damage scenario fragility is shown in Figure 6.44. It can be seen that effect of including the system parameter variability on the $NC \cap D$ damage scenario fragility is not significant. This result is due to the small effect of the system parameter variability on both the collapse DS and the demolition DS. In general, the $NC \cap D$ damage scenario fragility increases from zero at small IM values, reaches a maximum point, and then decreases to zero for large IM values. The left tail of the $NC \cap D$ damage scenario fragility at small IM values is affected more by the demolition DS, since the probability of non-collapse (NC) is close to 1 at small IM values. The right

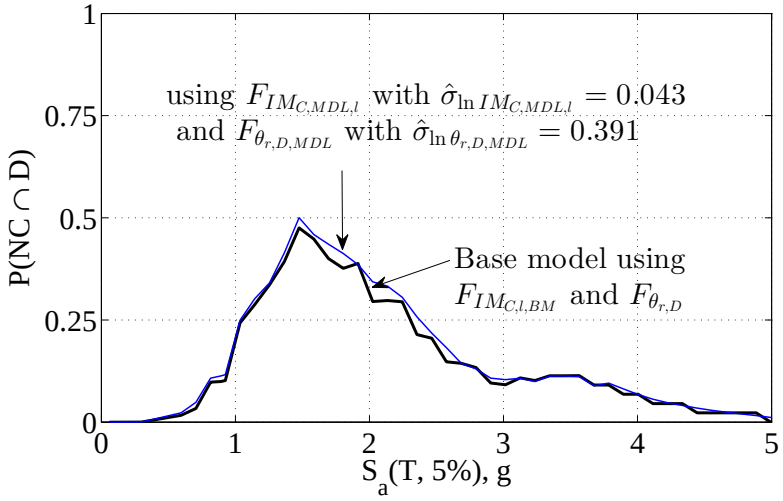

Figure 6.44: Probability of non-collapse with demolition ($NC \cap D$) with system parameter variability

tail of the $NC \cap D$ damage scenario fragility is affected more by the collapse DS, since the probability of demolition (D) is close to 1 at large IM values. The region between the tails where the peak of the $NC \cap D$ fragility occurs, is affected by both the collapse DS and the demolition DS.

The effect of including the system parameter variability on the $NC \cap D$ damage scenario fragility is shown for the collapse DS and the demolition DS separately in Figure 6.45. The $\hat{\sigma}_{\ln IM_{C,MDL,l}} = 0.3$ and $\hat{\sigma}_{\ln \theta_{r,D,MDL}} = 0.9$ used to generate the results shown in Figure 6.45 are considerably larger than the values estimated using the GM subset MC simulation results, and used to illustrate the effect of system parameter variability on the $NC \cap D$ fragility. It can be seen that when the system parameter variability is included only for the demolition DS, the effect is more evident around the left tail of the $NC \cap D$ damage scenario fragility at small IM values, as shown in Figure 6.45(a). When the system parameter variability is included only for the collapse DS, the effect is more evident around the right tail of $NC \cap D$ damage scenario fragility at large IM values, as shown in Figure 6.45(b). The left tail of the $NC \cap D$ fragility corresponds to IM values at the DBE and MCE hazard levels. Therefore, considering the system parameter variability in the demolition DS can

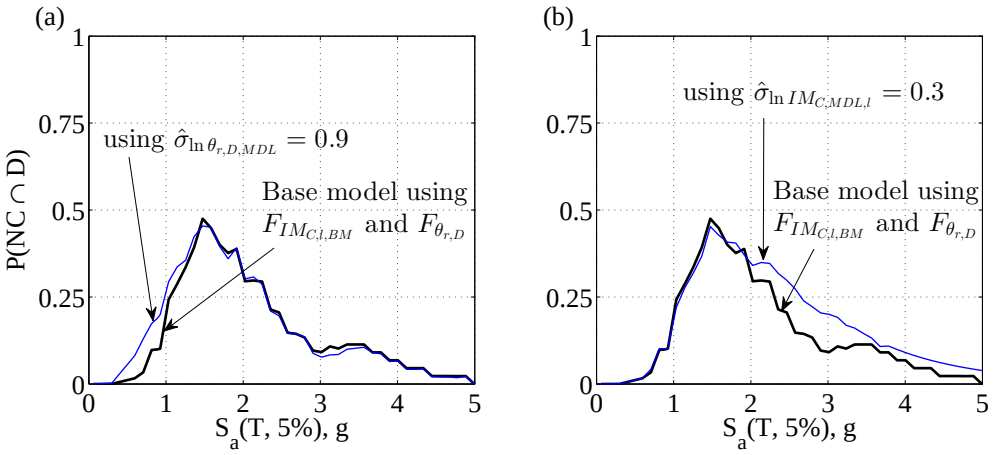

Figure 6.45: Effect of including system parameter variability on $NC \cap D$ damage scenario fragility: (a) $\hat{\sigma}_{\ln \theta_{r,D,MDL}} = 0.9$ with no system parameter variability for collapse DS; and (b) $\hat{\sigma}_{\ln IM_{C,MDL,l}} = 0.3$ with no system parameter variability for demolition DS

increase the probability of $NC \cap D$ damage scenario at the the DBE and MCE hazard levels. However, as shown in Figure 6.44, the effect appears to be small.

6.5 Summary and Findings

The effect of system parameter variability and modeling uncertainty is included in the damage scenario tree analysis (DSTA) framework. A Monte Carlo (MC) simulation approach is taken and sampling of the ground motion records and sampling of the random system and modeling parameters are conducted in two separate processes. The results of MC simulation in the form of incremental dynamic analysis (IDA) results, conducted using the sampled ground motion records and the random system parameter values, are combined using an approach similar to the record-by-record approach presented in Chapter 5. The probability of a damage scenario is determined for each ground motion record using the MC simulation results for the given ground motion record. The probabilities for individual ground motion records are then combined to determine the total probability for the damage scenario.

The approach is demonstrated by conducting MC simulation using a subset of the full FEMA P695 Far-Field ground motion record set. The initial out-of-straightness of the braces of the 9SCBF archetype building and the live load acting on each floor of the 9SCBF archetype building are used as random system parameters and sampled using the Latin Hypercube technique. Numerical models are developed for each set of sampled values for the random system parameters. MC simulation is performed using the sampled ground motion records and sampled random system parameters.

It is observed that the variation of the maximum story drift ratio and maximum (over all stories) residual story drift ratio due to the variation of the random system parameters is small. The variation of the brace residual out-of-straightness (Δ_{Or}) due to the variation

of the random system parameters is observed to be considerable. The effect of including the system parameter variability is observed to be slight increase in the dispersion of the probability of collapse and demolition.

An approximate method for including the effect of system parameter variability observed from the MC simulation results for the subset of ground motions is presented. The damage state (DS) fragility functions are modified to include the uncertainty due to the system parameter variability in addition to the epistemic uncertainty associated with the DS. A modified demolition fragility function is developed using the MC simulation results for subset of the ground motions. The difference between the modified demolition fragility function and the unmodified demolition fragility function (which does not include uncertainty due to the system parameter variability) is observed to be small.

It is observed that modifying the brace DS fragility functions to include the uncertainty due to the system parameter variability was not practical for all cases. The large variability in the Δ_{Or} values due to the variability in the random system parameters leads to unreasonable (and incorrect) modified brace DS fragility functions. The main reason for the inaccuracy is that the Δ_{Or} values for the numerical model with median values of the random system parameters were considerably different from the median Δ_{Or} values for the sample numerical models.

The IM-based collapse fragility function is modified to include the uncertainty due to the system parameter variability using the MC simulation results for the subset of ground motions. The effect of the system parameter variability on the collapse DS fragility function is observed to be a small increase of the dispersion in the collapse damage scenario fragility curve.

The effect of system parameter variability is studied on the non-collapse with demolition ($NC \cap D$) damage scenario, using the modified collapse and demolition fragility func-

tions. It is observed that the effect of the system parameter variability on the demolition fragility function is more evident for the $NC \cap D$ damage scenario at small IM values; and the effect of the system parameter variability on the collapse fragility function is more evident for the $NC \cap D$ damage scenario at large IM values.

Chapter 7

Comparison of Damage Scenario Fragilities for SCBF and SC-CBF Archetype Buildings

7.1 Introduction

In this chapter, the damage scenario fragilities are presented for all archetype buildings described in Chapter 3. The fragilities are based on the damage scenario tree analysis (DSTA) technique presented in Chapter 5. Specifically, the damage scenarios shown in Figure 5.4 are of interest. Incremental dynamic analysis (IDA) results were used to conduct the DSTA.

For the system level damage assessment, the damage state (DS) of building collapse is considered as discussed in Chapter 5. The maximum story drift ratio, θ_m, is used as the EDP to establish the collapse points on the individual IDA curves. The collapse point for an IDA curve is based on two criteria: (i) the reduction in the slope of the IDA curve; and (ii) θ_m reaching a limit value of 0.10. For the slope reduction criterion, the reduction in the slope of an individual $S_a(T,5\%)$ versus θ_m curve from the IDA, is quantified with respect to the median of the initial slopes of the IDA curves for the record set, denoted by S_e, as defined by FEMA [22], and explained previously in Chapter 3.

The slope reduction collapse criterion is a probabilistic criterion as described in Chapter 5. Two bounding slope reduction values of 75% and 85% are used to defined three ranges of slope reduction: (i) collapse has not occurred if the slope reduction is less than 75% (i.e.,

the slope is greater than or equal to 0.25 S_e); (ii) collapse may occur if the slope reduction is greater than or equal to 75% and less than 85% (i.e., the slope is less than or equal to 0.25 S_e and greater than 0.15 S_e); and (iii) collapse has occurred with certainty if the slope reduction is greater than or equal to 85% (i.e., the slope is less than or equal to 0.15 S_e).

The probability of collapse is quantified using the IM-based method as presented in Section 5.5. It is assumed that the IM value at collapse, IM_C, is uniformly distributed between the IM values corresponding to the 75% and 85% slope reduction. Therefore, the IM-based collapse fragility function F_{IM_C} is defined for each individual IDA curve (developed for a ground motion record and an archetype building) as shown in Figure 5.15(b).

For the subsystem level damage assessment, the SLFRS of the archetype buildings (i.e., the SCBF or the SC-CBF) is the only subsystem that is considered, as shown in the example in Chapter 5. Two DS, corresponding to non-demolition and demolition of the building, are considered for the SLFRS of the archetype buildings. The damage to the SLFRS of the archetype buildings is quantified using an EDP-based method, where the maximum (over all stories) residual story drift ratio, θ_r, is the EDP. Demolition is quantified using the θ_r limit value, $\theta_{r,D}$. The demolition fragility function $F_{\theta_{r,D}}$ is based on a lognormal distribution for $\theta_{r,D}$ with the median and logarithmic standard deviation for $\theta_{r,D}$ as given in Table 5.1.

At the component level, damage to the braces of the SCBF and SC-CBF are considered. Three DS are considered for each brace: (i) no damage (brace DS 0), corresponding to no repair action (denoted by *NR*); (ii) brace DS 1, corresponding to the brace straightening repair action (denoted by *BS*); and (iii) brace DS 2, corresponding to the brace replacement repair action (denoted by *BR*). The brace DS are quantified using an EDP-based method, where the normalized brace residual out-of-plane deformation, denoted by Δ_{Or}, is the EDP. The three brace DS are separated using two Δ_{Or} limit values $\Delta_{Or,DS,1}$ and $\Delta_{Or,DS,2}$.

Two brace DS fragility functions $F_{\Delta_{Or,DS,1}}$ and $F_{\Delta_{Or,DS,2}}$ are used to quantify the probability of exceeding the Δ_{Or} limit values of $\Delta_{Or,DS,1}$ and $\Delta_{Or,DS,2}$, respectively. The median and logarithmic standard deviation of $\Delta_{Or,DS,1}$ and $\Delta_{Or,DS,2}$ are given in Table 5.1.

Five damage scenarios are considered for the SCBF and SC-CBF archetype buildings: (i) building collapse, C; (ii) non-collapse with demolition, $NC \cap D$; (iii) non-collapse with non-demolition and no brace repair, $NC \cap ND \cap NR$; (iv) non-collapse with non-demolition and brace straightening, $NC \cap ND \cap BS$; and (v) non-collapse with non-demolition and brace replacement, $NC \cap ND \cap BR$. In addition, the possibility of damage to the PT bars of the SC-CBF archetype buildings is considered. Fragilities for damage scenarios involving damage to the PT bars are presented in Section 7.6.

$P(C|IM)$ is calculated using Equation (5.21) as follows:

$$P(C|IM) = \sum_{all\ GM_l} F_{IM_{C,l}}(IM) \cdot P(GM = GM_l|IM) \tag{7.1}$$

$P(NC \cap D)$ is calculated using Equation (5.23) as follows:

$$P(NC \cap D|IM) = \sum_{all\ GM_l} \bar{F}_{IM_{C,l}}(IM) \cdot F_{\theta_{r,D}}(\theta_{r_l}) \cdot P(GM = GM_l|IM) \tag{7.2}$$

where $F_{\theta_{r,D,l}}$ in Equation (5.23) is replaced by $F_{\theta_{r,D}}$ since one demolition fragility function (i.e., $F_{\theta_{r,D}}$) is used for all ground motion records. $P(NC \cap ND \cap NR)$, $P(NC \cap ND \cap BS)$, and $P(NC \cap ND \cap BR)$ are calculated using Equation (5.24) as follows:

$$P(NC \cap ND \cap NR|IM) = \sum_{all\ GM_l} \bar{F}_{IM_{C,l}}(IM) \cdot \bar{F}_{\theta_{r,D}}(\theta_{r_l}) \cdot \left(1 - F_{\Delta_{Or,DS,1}}(\Delta_{Or_l})\right) \cdot P(GM = GM_l|IM) \tag{7.3}$$

$$P(NC \cap ND \cap BS|IM) = \sum_{all\ GM_l} \bar{F}_{IM_{C,l}}(IM) \cdot \bar{F}_{\theta_{r,D}}(\theta_{r_l}) \cdot \left(F_{\Delta_{Or,DS,1}}(\Delta_{Or_l}) - F_{\Delta_{Or,DS,2}}(\Delta_{Or_l})\right) \cdot P(GM = GM_l|IM) \quad (7.4)$$

$$P(NC \cap ND \cap BR|IM) = \sum_{all\ GM_l} \bar{F}_{IM_{C,l}}(IM) \cdot \bar{F}_{\theta_{r,D}}(\theta_{r_l}) \cdot F_{\Delta_{Or,DS,2}}(\Delta_{Or_l}) \cdot P(GM = GM_l|IM) \quad (7.5)$$

The damage scenario fragilities are developed using the IDA results for each archetype building. To enable the fragility of the SCBF system to be comparable with the fragility of the SC-CBF system, the fragilities for the SCBF and SC-CBF archetype buildings with the same numbers of stories are compared in a single plot. The discussion of the damage scenario fragilities for 4-story, 6-story, 9-story, and 12-story archetype buildings is presented separately in Sections 7.2, 7.3, 7.4, and 7.5, respectively.

7.2 Comparison of Damage Scenario Fragilities for 4-story Archetype Buildings

The damage scenario fragilities for the 4SCBF and 4SC-CBF archetype buildings are presented and discussed in this section. The C damage scenario fragility is shown in Figure 7.1. It can be seen from Figure 7.1 that $P(C)$ for the 4SC-CBF archetype building is smaller than $P(C)$ for the 4SCBF archetype building at all $S_a(T,5\%)$ values. It can also be seen that the $S_a(T,5\%)$ value at 50% probability of collapse is close to $\hat{S}_{CT} = 4.68g$ for the 4SC-CBF archetype building and $\hat{S}_{CT} = 3.72g$ for the 4SCBF archetype building, presented previously in Chapter 4, Table 4.2, based on the performance evaluation methodology of FEMA P695 document [23]. The $P(C)$ values are negligible at the DBE and MCE hazard levels

for the 4SCBF and 4SC-CBF archetype buildings.

The $NC \cap D$ damage scenario fragility, calculated using Equation (7.2), is shown in Figure 7.2 for the 4SCBF and 4SC-CBF archetype buildings. It can be seen that $P(NC \cap D)$ for the 4SCBF archetype building starts from approximately 0 at $S_a(T,5\%) \approx 1.0g$, increases to approximately 63% at $S_a(T,5\%) \approx 3.0g$, and then decreases to less than 10% at $S_a(T,5\%) \approx 5.0g$. The $P(NC \cap D)$ value for the 4SC-CBF archetype building starts from approximately 0 at $S_a(T,5\%) \approx 2.0g$, increases to approximately 50% at $S_a(T,5\%) \approx 4.3g$, and then decreases to less than 10% at $S_a(T,5\%) \approx 6.0g$. It can clearly be seen from Figure 7.2 that the $NC \cap D$ damage scenario fragility for the 4SC-CBF archetype building is shifted towards larger values of $S_a(T,5\%)$, compared to the 4SCBF archetype building. This shift of the $NC \cap D$ damage scenario fragility shows that a larger $S_a(T,5\%)$ value (i.e., a more intense GM or greater hazard) is needed to produce the same $P(NC \cap D)$ (i.e., probability of damage leading to demolition when collapse has not occurred) for the 4SC-CBF archetype building. It can also be seen that the maximum $P(NC \cap D)$ value is smaller for the 4SC-CBF archetype building. The $P(NC \cap D)$ value is negligible at the DBE and MCE hazard levels for the 4SC-CBF archetype building. The $P(NC \cap D)$ value is negligible at the DBE hazard level but is considerable at the MCE hazard level for the 4SCBF archetype building.

The brace damage scenario fragilities for the 4SCBF archetype building and the 4SC-CBF archetype building, calculated using Equations (7.3), (7.4), and (7.5), are shown in Figure 7.3 through Figure 7.6 for the 1st story through the 4th story, respectively. The $NC \cap ND \cap NR$ damage scenario fragilities for all braces are shown in parts (a) and (b) of Figure 7.3 through Figure 7.6. It can be seen that for all braces, the $P(NC \cap ND \cap NR)$ value (i.e., the probability of no damage to the braces) is greater for the 4SC-CBF archetype building than for the 4SCBF archetype building at all $S_a(T,5\%)$ values. For the 4SC-CBF archetype building, the probability of no brace damage is approximately 100% for all braces at the DBE hazard level and close to 100% for all braces at the MCE hazard level.

For the 4SCBF archetype building, the probability of no brace damage is much lower for the 1st and 2nd story braces at the DBE and MCE hazard levels.

The $NC \cap ND \cap BS$ damage scenario fragilities for all braces of the 4SCBF and 4SC-CBF archetype buildings are shown in parts (c) and (d) of Figure 7.3 through Figure 7.6. It can be seen from Figure 7.3(c) and (d) and Figure 7.4(c) and (d) that a non-negligible $P(NC \cap ND \cap BS)$ value (i.e., a non-negligible probability of brace straightening) is seen at a much smaller $S_a(T, 5\%)$ value for the 1st and 2nd story braces of the 4SCBF archetype building than for the 4SC-CBF archetype building. The maximum $P(NC \cap ND \cap BS)$ value for the 1st story left side brace is larger for the 4SCBF (about 25%) than for the 4SC-CBF (about 10%). The maximum $P(NC \cap ND \cap BS)$ value for the 1st story right side brace is larger for the 4SC-CBF (about 25%) than for the 4SCBF (about 20%). The maximum $P(NC \cap ND \cap BS)$ value for the 2nd story braces is negligible for the 4SC-CBF but is non-negligible for the 4SCBF. The $P(NC \cap ND \cap BS)$ value is negligible for the 3rd and 4th story braces for the 4SC-CBF and the 4SCBF, as can be seen from Figure 7.5(c) and (d) and Figure 7.6(c) and (d). The $P(NC \cap ND \cap BS)$ value is negligible at the DBE and MCE hazard levels for all braces of the 4SC-CBF archetype building. The $P(NC \cap ND \cap BS)$ value is considerable at the DBE and MCE hazard levels for the 1st and 2nd story braces of the 4SCBF archetype building.

The $NC \cap ND \cap BR$ damage scenario fragilities for all braces of the 4SCBF and 4SC-CBF archetype buildings are shown in parts (e) and (f) of Figure 7.3 through Figure 7.6. The $P(NC \cap ND \cap BR)$ value for the 4SC-CBF is small for the 1st story braces and is negligible for braces at all other stories. The $P(NC \cap ND \cap BR)$ value for the 4SCBF is considerable for the 1st and 2nd story braces, but is negligible for the 3rd and 4th story braces. Therefore, it can be seen that the probability of replacing the braces is negligible for the 4SC-CBF archetype building, while it is considerable for 1st and 2nd story braces of the 4SCBF archetype building. The $P(NC \cap ND \cap BR)$ value is negligible at the DBE and MCE

hazard levels for all the braces of the 4SC-CBF archetype building. The $P(NC \cap ND \cap BR)$ value is considerable at the DBE and MCE hazard levels for the 1st and 2nd story braces of the 4SCBF archetype building.

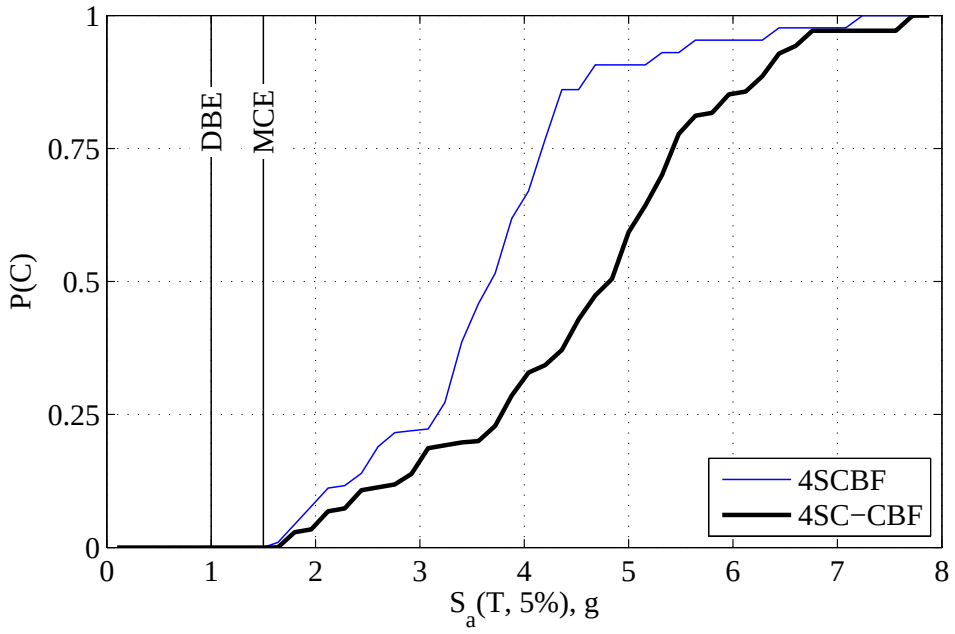

Figure 7.1: Comparison of *C* damage scenario fragility for 4-story archetype buildings

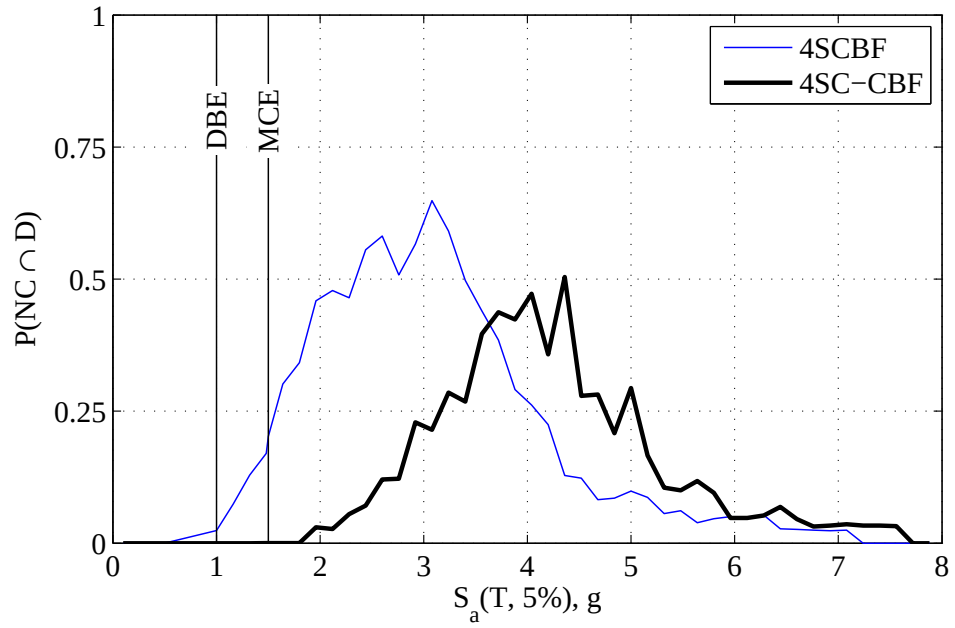

Figure 7.2: Comparison of $NC \cap D$ damage scenario fragility for 4-story archetype buildings

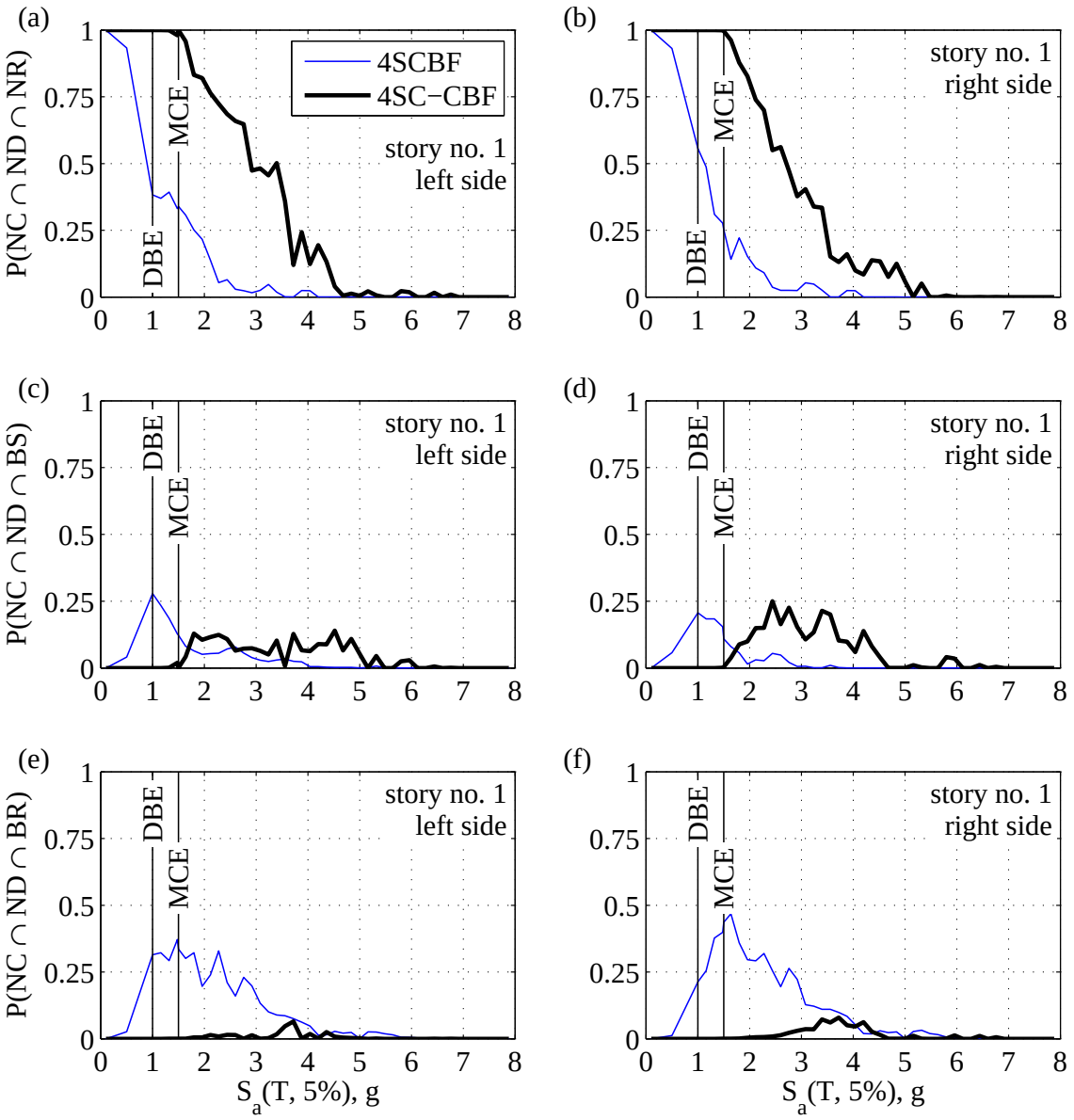

Figure 7.3: Comparison of brace damage scenario fragilities for 1st story of 4-story archetype buildings: (a) $NC \cap ND \cap NR$ for left side brace; (b) $NC \cap ND \cap NR$ for right side brace; (c) $NC \cap ND \cap BS$ for left side brace; (d) $NC \cap ND \cap BS$ for right side brace; (e) $NC \cap ND \cap BR$ for left side brace; and (f) $NC \cap ND \cap BR$ for right side brace;

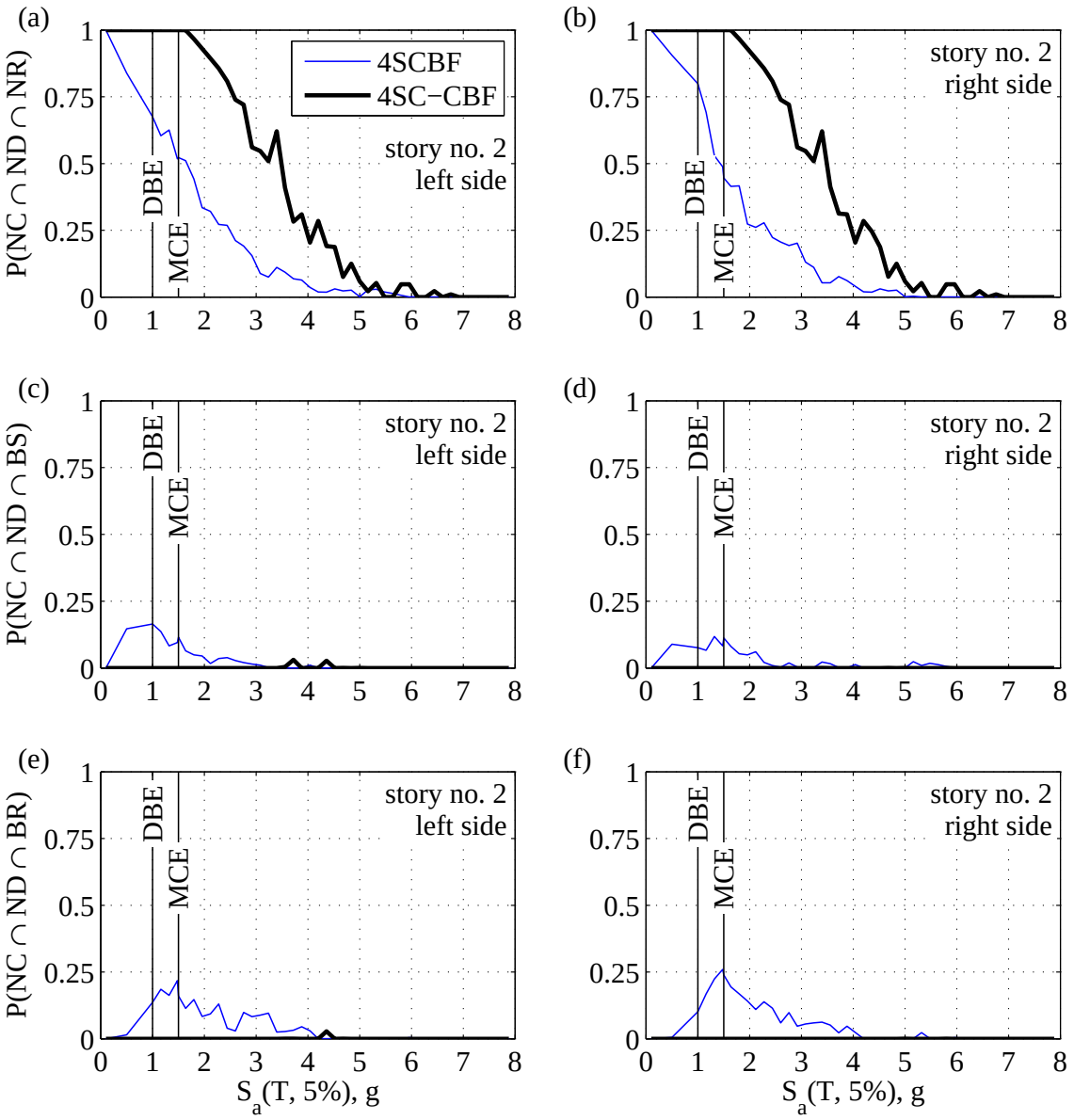

Figure 7.4: Comparison of brace damage scenario fragilities for 2nd story of 4-story archetype buildings: (a) $NC \cap ND \cap NR$ for left side brace; (b) $NC \cap ND \cap NR$ for right side brace; (c) $NC \cap ND \cap BS$ for left side brace; (d) $NC \cap ND \cap BS$ for right side brace; (e) $NC \cap ND \cap BR$ for left side brace; and (f) $NC \cap ND \cap BR$ for right side brace;

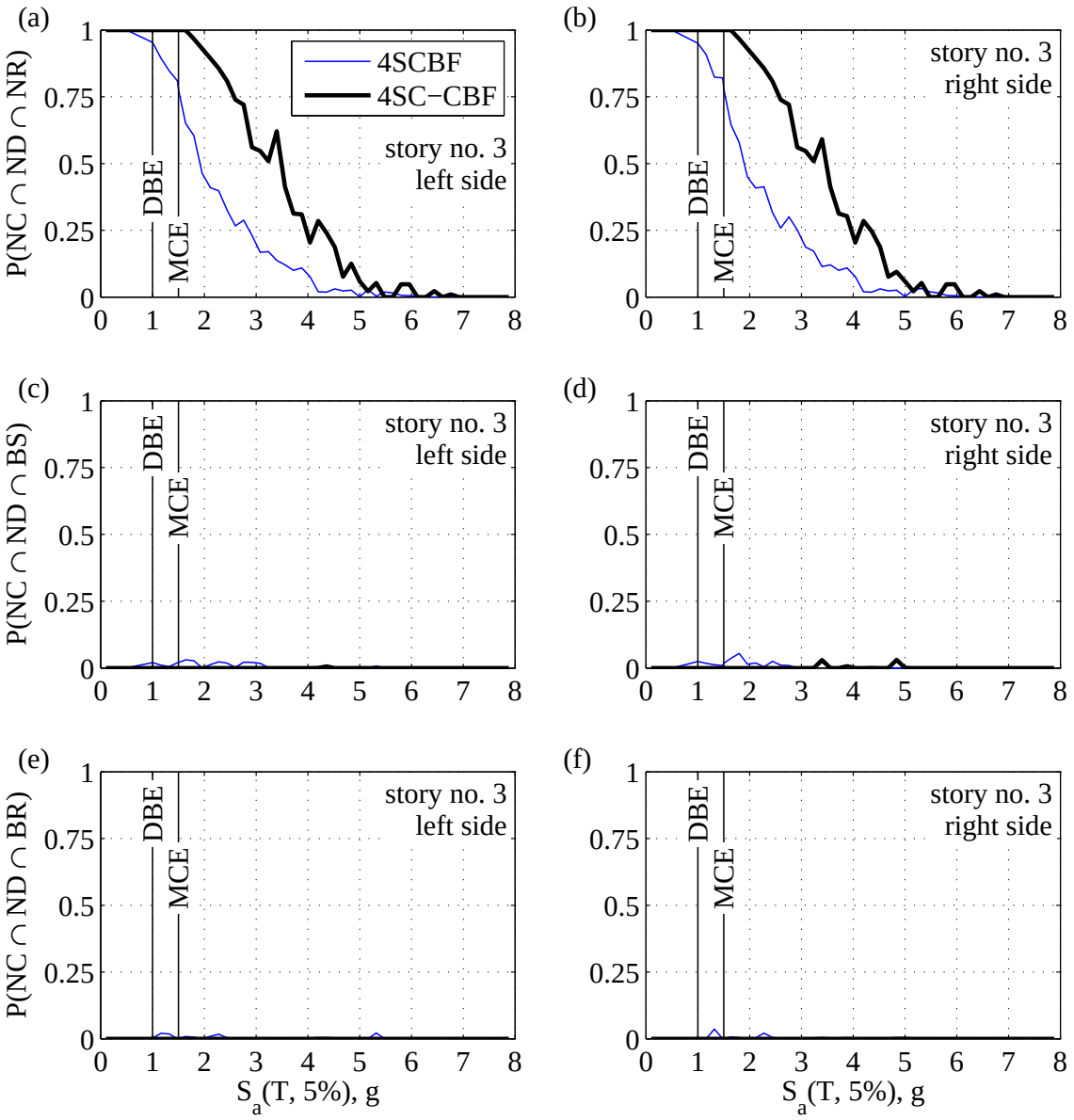

Figure 7.5: Comparison of brace damage scenario fragilities for 3rd story of 4-story archetype buildings: (a) $NC \cap ND \cap NR$ for left side brace; (b) $NC \cap ND \cap NR$ for right side brace; (c) $NC \cap ND \cap BS$ for left side brace; (d) $NC \cap ND \cap BS$ for right side brace; (e) $NC \cap ND \cap BR$ for left side brace; and (f) $NC \cap ND \cap BR$ for right side brace;

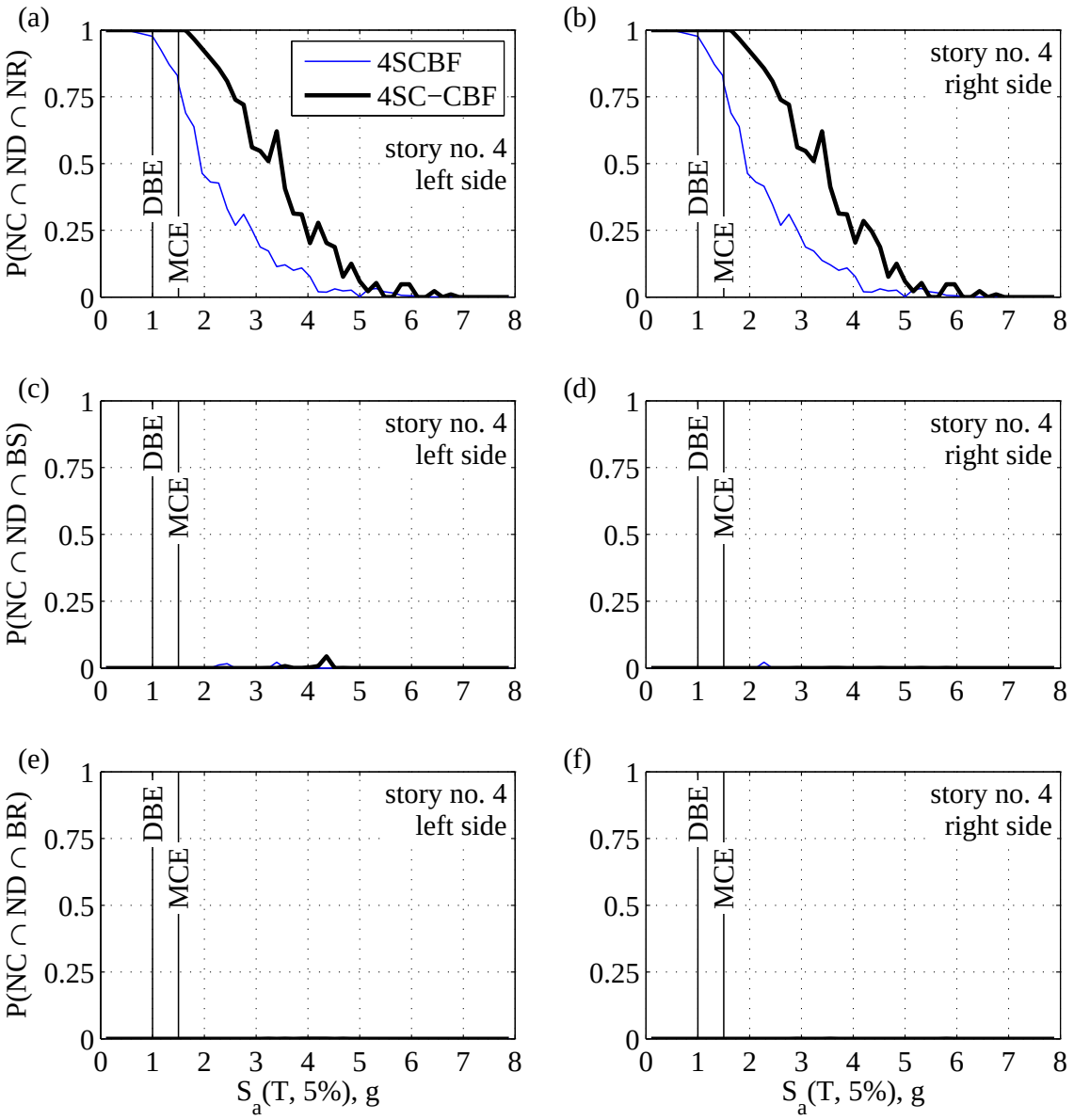

Figure 7.6: Comparison of brace damage scenario fragilities for 4th story of 4-story archetype buildings: (a) $NC \cap ND \cap NR$ for left side brace; (b) $NC \cap ND \cap NR$ for right side brace; (c) $NC \cap ND \cap BS$ for left side brace; (d) $NC \cap ND \cap BS$ for right side brace; (e) $NC \cap ND \cap BR$ for left side brace; and (f) $NC \cap ND \cap BR$ for right side brace;

7.3 Comparison of Damage Scenario Fragilities for 6-story Archetype Buildings

The damage scenario fragilities for the 6SCBF and 6SC-CBF archetype buildings are presented and discussed in this section. The C damage scenario fragility is shown in Figure 7.7. It can be seen from Figure 7.7 that $P(C)$ for the 6SC-CBF archetype building is smaller than $P(C)$ for the 6SCBF archetype building at all $S_a(T,5\%)$ values. It can also be seen that the $S_a(T,5\%)$ value at 50% probability of collapse is close to $\hat{S}_{CT} = 4.43g$ for the 6SC-CBF archetype building and $\hat{S}_{CT} = 3.41g$ for the 6SCBF archetype building, presented previously in Chapter 4, Table 4.2, based on the performance evaluation methodology of FEMA P695 document [23]. The $P(C)$ values are negligible at the DBE and MCE hazard levels for the 6SCBF and 6SC-CBF archetype buildings.

The $NC \cap D$ damage scenario fragility, calculated using Equation (7.2), is shown in Figure 7.8 for the 6SCBF and 6SC-CBF archetype buildings. It can be seen that $P(NC \cap D)$ for the 6SCBF archetype building starts from approximately 0 at $S_a(T,5\%) \approx 1.0g$, increases to approximately 55% at $S_a(T,5\%) \approx 2.8g$, and then decreases to less than 10% at $S_a(T,5\%) \approx 5.0g$. The $P(NC \cap D)$ value for the 6SC-CBF archetype building starts from approximately 0 at $S_a(T,5\%) \approx 1.5g$, increases to approximately 50% at $S_a(T,5\%) \approx 3.1g$, and then decreases to less than 10% at $S_a(T,5\%) \approx 6.0g$. It can clearly be seen from Figure 7.8 that the $NC \cap D$ damage scenario fragility for the 6SC-CBF archetype building is shifted towards larger values of $S_a(T,5\%)$, compared to the 6SCBF archetype building. This shift of the $NC \cap D$ damage scenario fragility shows that a larger $S_a(T,5\%)$ value (i.e., a more intense GM or greater hazard) is needed to produce the same $P(NC \cap D)$ (i.e., probability of damage leading to demolition when collapse has not occurred) for the 6SC-CBF archetype building. It can also be seen that the maximum $P(NC \cap D)$ value is slightly greater for the 6SCBF archetype building. The $P(NC \cap D)$ value is negligible at the DBE and MCE

hazard levels for the 6SC-CBF archetype building. The $P(NC \cap D)$ value is negligible at the DBE hazard level but is not negligible at the MCE hazard level for the 6SCBF archetype building.

The brace damage scenario fragilities for the 6SCBF archetype building and the 6SC-CBF archetype building, calculated using Equations (7.3), (7.4), and (7.5), are shown in Figure 7.9 through Figure 7.14 for the 1st story through the 6th story, respectively. The $NC \cap ND \cap NR$ damage scenario fragilities for all braces are shown in parts (a) and (b) of Figure 7.9 through Figure 7.14. It can be seen that for all braces, the $P(NC \cap ND \cap NR)$ value (i.e., the probability of no damage to the braces) is greater for the 6SC-CBF archetype building than for the 6SCBF archetype building at most $S_a(T, 5\%)$ values. For the 6SC-CBF archetype building, the probability of no brace damage is approximately 100% for all braces at the DBE hazard level and close to 100% for all braces at the MCE hazard level. For the 6SCBF archetype building, the probability of no brace damage is much lower for the 1st through the 5th story braces at the DBE and MCE hazard levels.

The $NC \cap ND \cap BS$ damage scenario fragilities for all braces of the 6SCBF and 6SC-CBF archetype buildings are shown in parts (c) and (d) of Figure 7.9 through Figure 7.14. It can be seen from Figure 7.9(c) and (d) and Figure 7.11(c) and (d) that a non-negligible $P(NC \cap ND \cap BS)$ value (i.e., a non-negligible probability of brace straightening) is seen at a much smaller $S_a(T, 5\%)$ values for the 1st and the 3rd story braces of the 6SCBF compared to that of the 6SC-CBF. The $P(NC \cap ND \cap BS)$ value is negligible for braces at the 2nd, 4th, 5th, and 6th story for the 6SC-CBF archetype building. The $P(NC \cap ND \cap BS)$ value is considerable for the 1st through the 5th story braces and is negligible for the 6th story braces for the 6SCBF archetype building. The $P(NC \cap ND \cap BS)$ value is negligible at the DBE and MCE hazard levels for all braces of the 6SC-CBF archetype building. The $P(NC \cap ND \cap BS)$ value is considerable at the DBE and MCE hazard levels for the 1st story through 5th story braces of the 6SCBF archetype building.

The $NC \cap ND \cap BR$ damage scenario fragilities for all braces of the 6SCBF and 6SC-CBF archetype buildings are shown in parts (e) and (f) of Figure 7.9 through Figure 7.14. The $P(NC \cap ND \cap BR)$ value for the 1st, 3rd, and 4th story braces are considerably smaller for the 6SC-CBF archetype building than those of the 6SCBF archetype building. It can be seen from Figure 7.9(e) and (f), Figure 7.11(e) and (f), and Figure 7.12(e) and (f) that a non-negligible $P(NC \cap ND \cap BS)$ value (i.e., a non-negligible probability of brace straightening) is seen at much smaller $S_a(T, 5\%)$ values for the 1st, 3rd, and 4th story braces of the 6SCBF archetype building than for the 6SC-CBF archetype building. The $P(NC \cap ND \cap BR)$ value is negligible for the 2nd, 5th, and 6th story braces for the 6SC-CBF archetype building. The $P(NC \cap ND \cap BR)$ value is considerable for braces at all stories except for the 6th story for the 6SCBF archetype building. The $P(NC \cap ND \cap BR)$ value is negligible at the DBE and MCE hazard levels for all the braces of the 6SC-CBF archetype building. The $P(NC \cap ND \cap BR)$ value is considerable at the DBE and MCE hazard levels for the 1st story through 5th story braces of the 6SCBF archetype building.

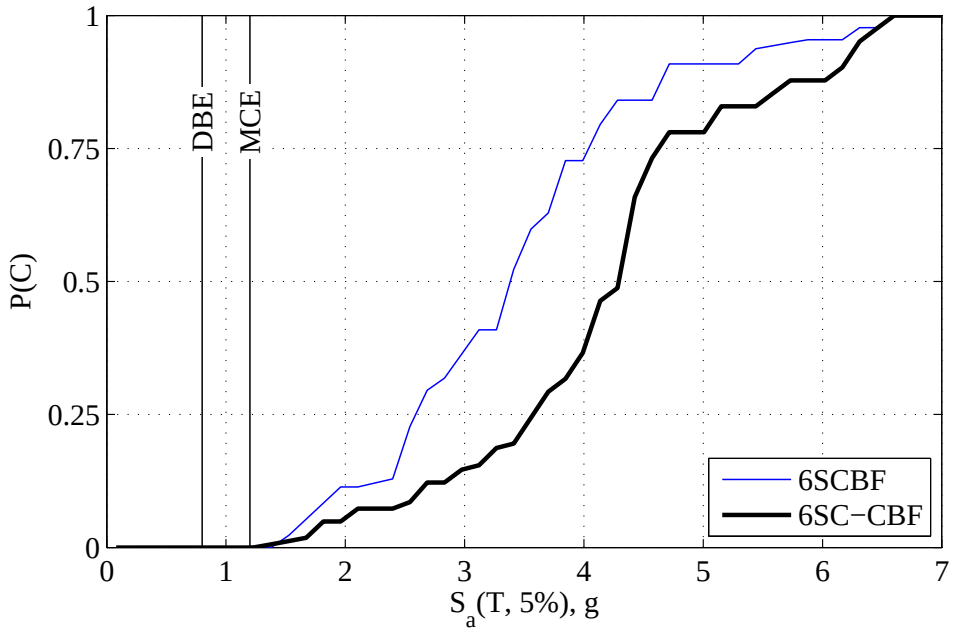

Figure 7.7: Comparison of *C* damage scenario fragility for 6-story archetype buildings

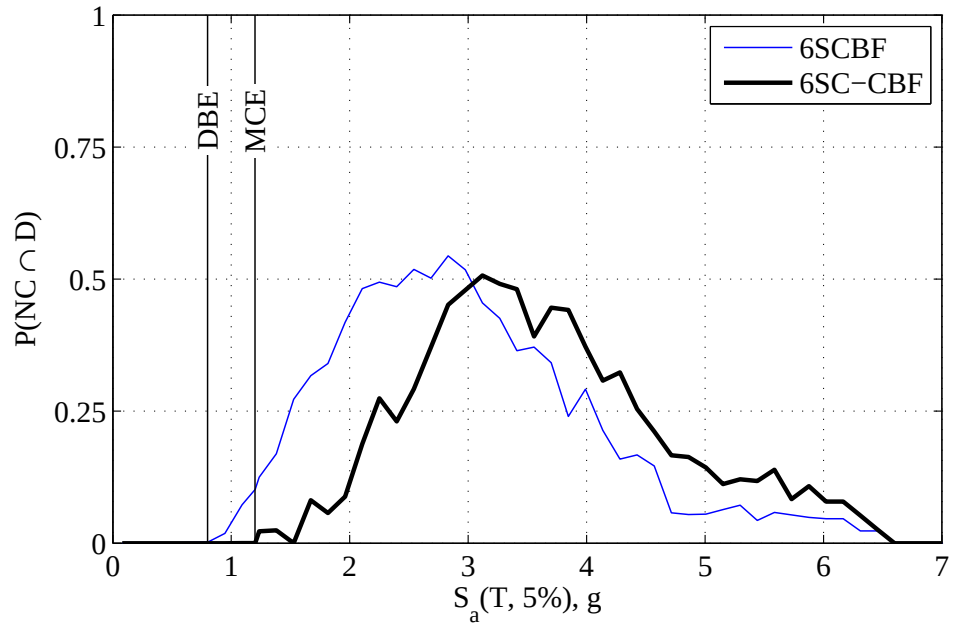

Figure 7.8: Comparison of $NC \cap D$ damage scenario fragility for 6-story archetype buildings

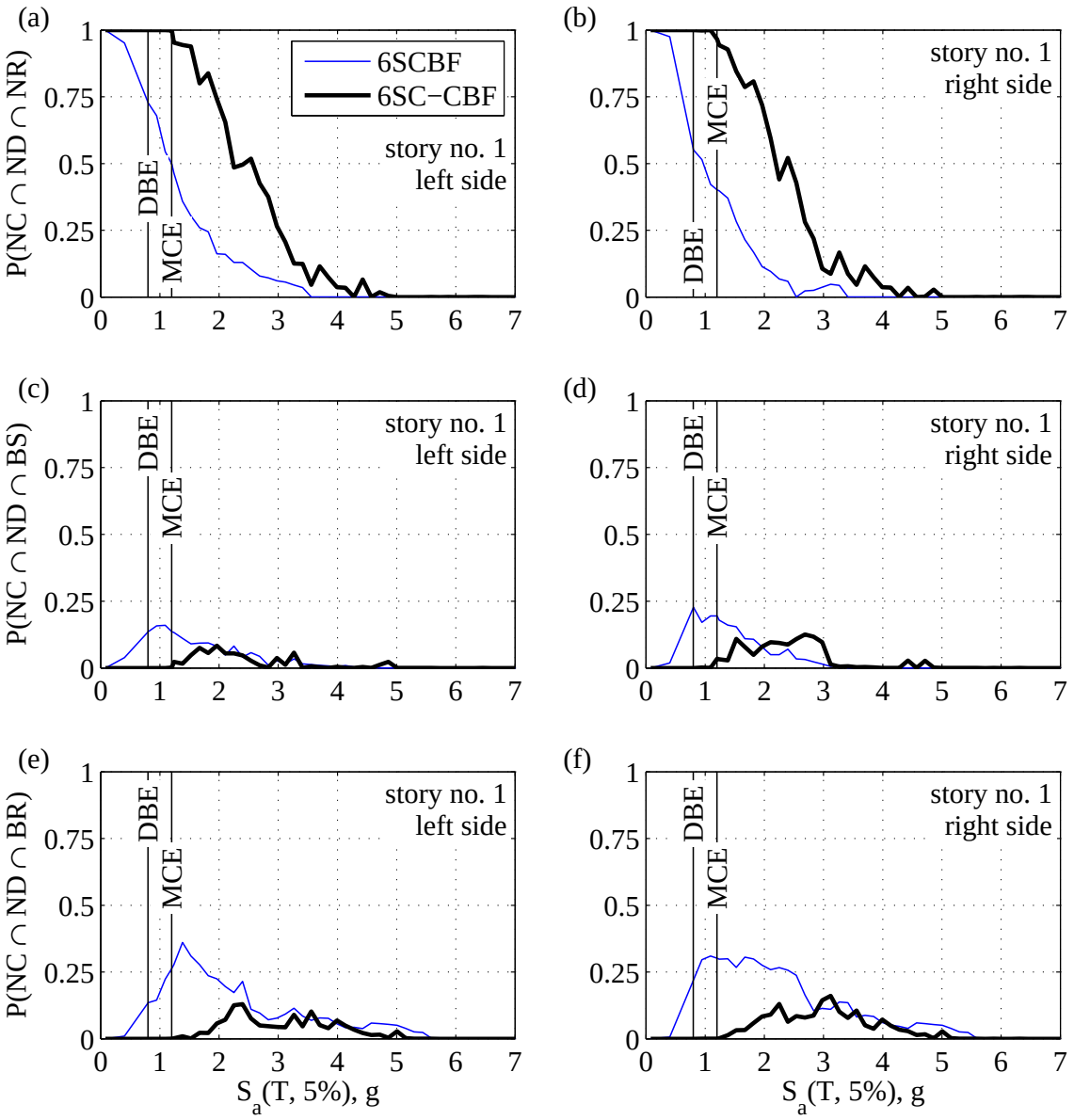

Figure 7.9: Comparison of brace damage scenario fragilities for 1st story of 6-story archetype buildings: (a) $NC \cap ND \cap NR$ for left side brace; (b) $NC \cap ND \cap NR$ for right side brace; (c) $NC \cap ND \cap BS$ for left side brace; (d) $NC \cap ND \cap BS$ for right side brace; (e) $NC \cap ND \cap BR$ for left side brace; and (f) $NC \cap ND \cap BR$ for right side brace;

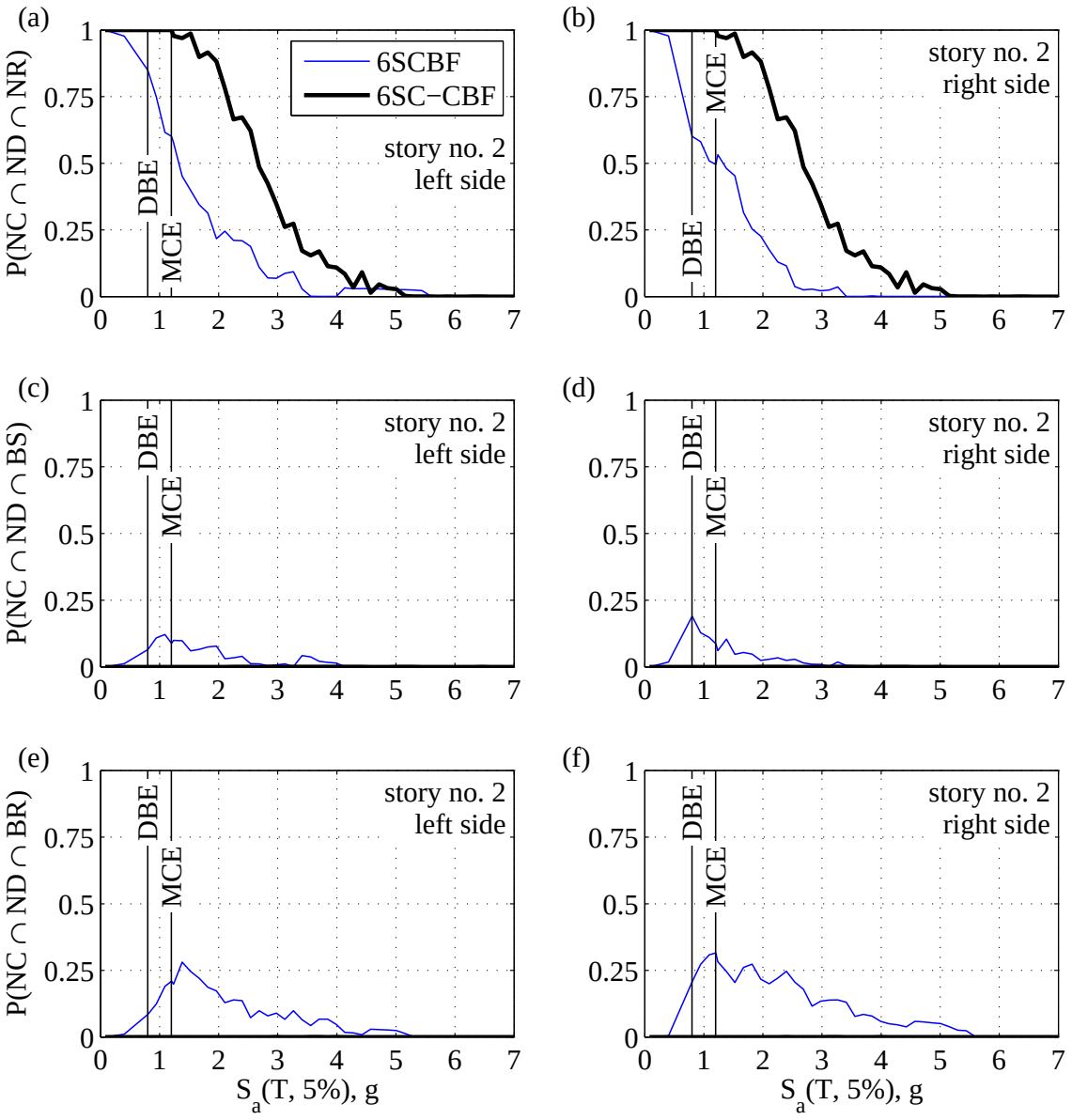

Figure 7.10: Comparison of brace damage scenario fragilities for 2nd story of 6-story archetype buildings: (a) $NC \cap ND \cap NR$ for left side brace; (b) $NC \cap ND \cap NR$ for right side brace; (c) $NC \cap ND \cap BS$ for left side brace; (d) $NC \cap ND \cap BS$ for right side brace; (e) $NC \cap ND \cap BR$ for left side brace; and (f) $NC \cap ND \cap BR$ for right side brace;

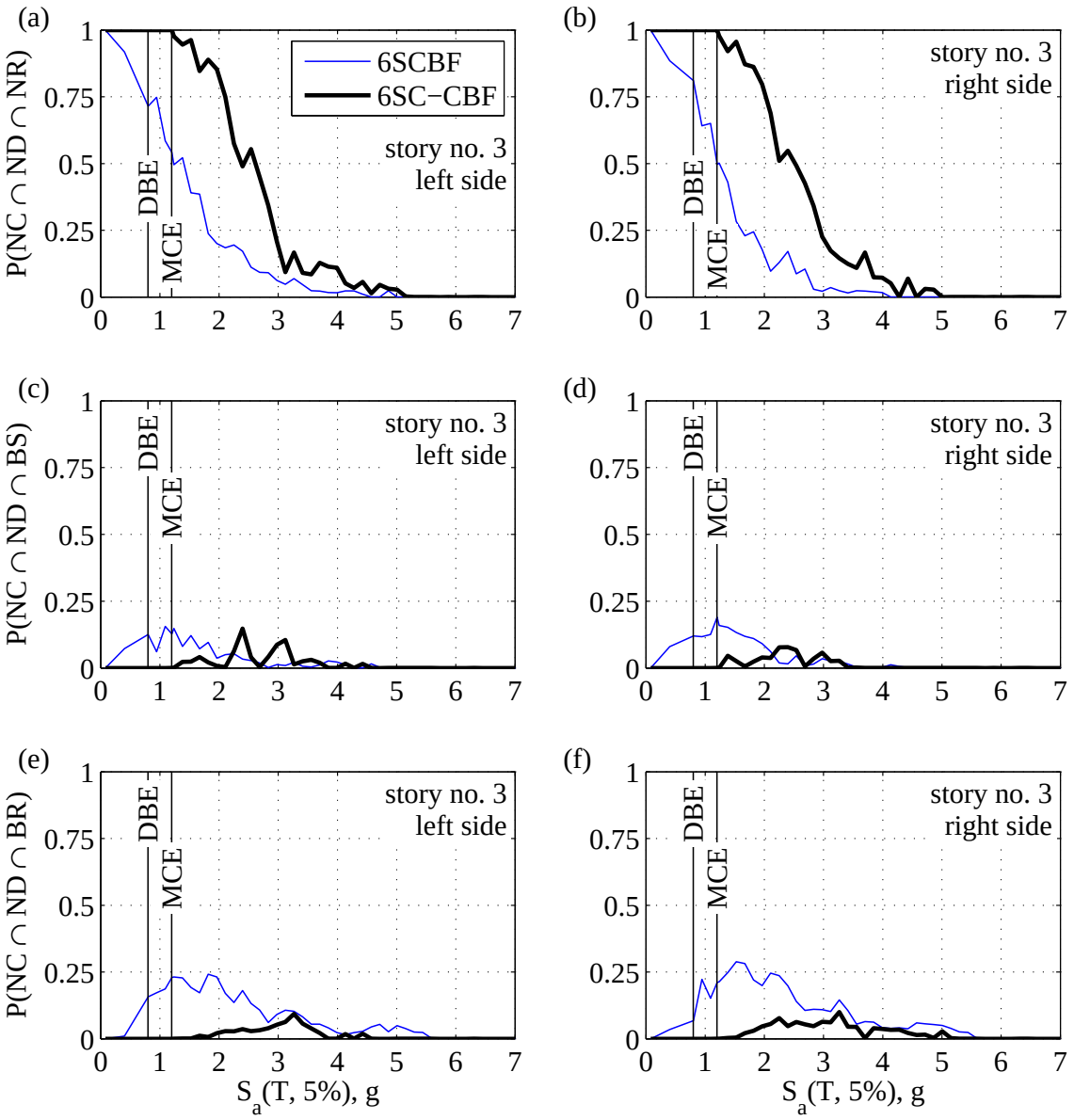

Figure 7.11: Comparison of brace damage scenario fragilities for 3rd story of 6-story archetype buildings: (a) $NC \cap ND \cap NR$ for left side brace; (b) $NC \cap ND \cap NR$ for right side brace; (c) $NC \cap ND \cap BS$ for left side brace; (d) $NC \cap ND \cap BS$ for right side brace; (e) $NC \cap ND \cap BR$ for left side brace; and (f) $NC \cap ND \cap BR$ for right side brace;

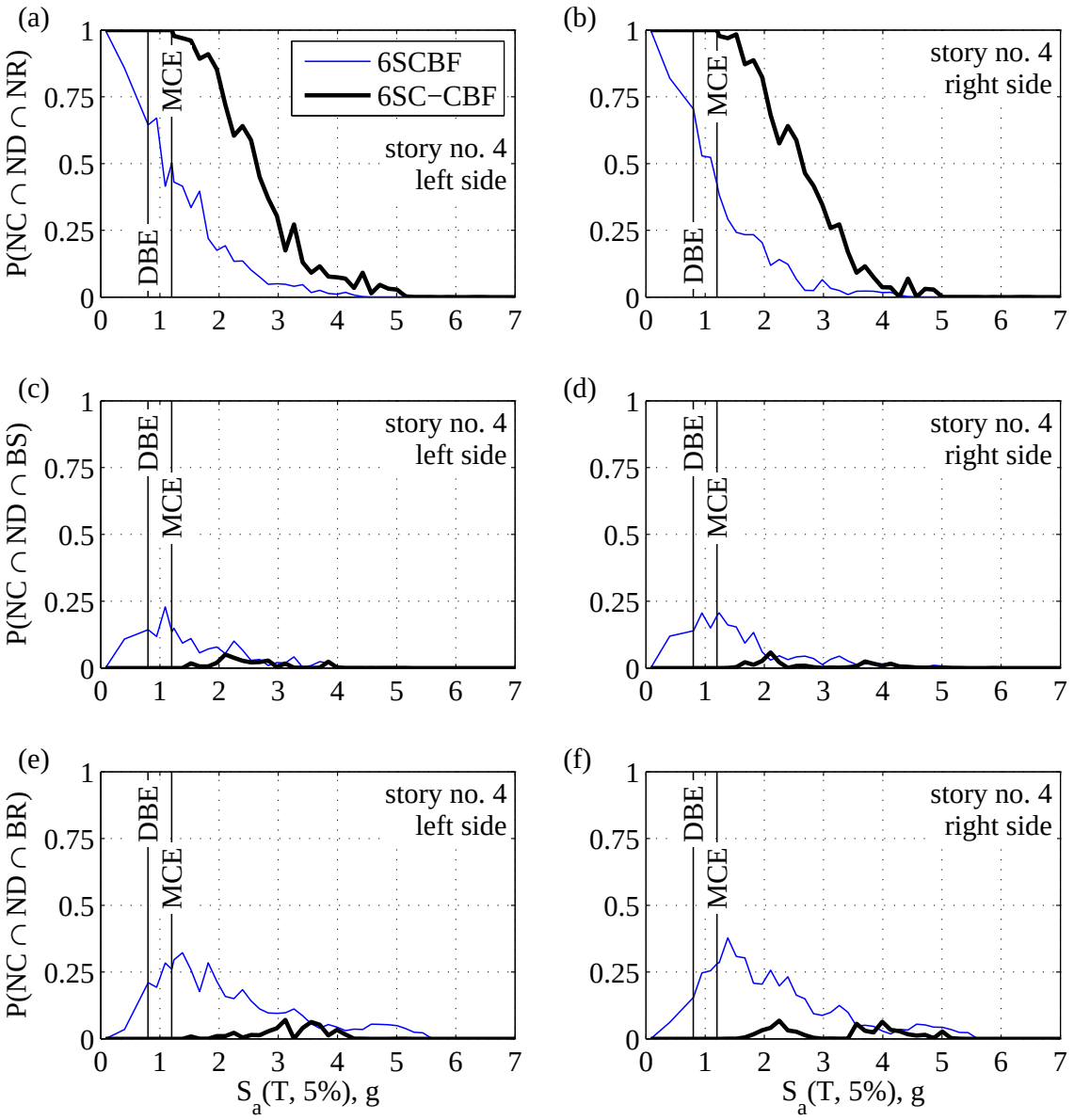

Figure 7.12: Comparison of brace damage scenario fragilities for 4th story of 6-story archetype buildings: (a) $NC \cap ND \cap NR$ for left side brace; (b) $NC \cap ND \cap NR$ for right side brace; (c) $NC \cap ND \cap BS$ for left side brace; (d) $NC \cap ND \cap BS$ for right side brace; (e) $NC \cap ND \cap BR$ for left side brace; and (f) $NC \cap ND \cap BR$ for right side brace;

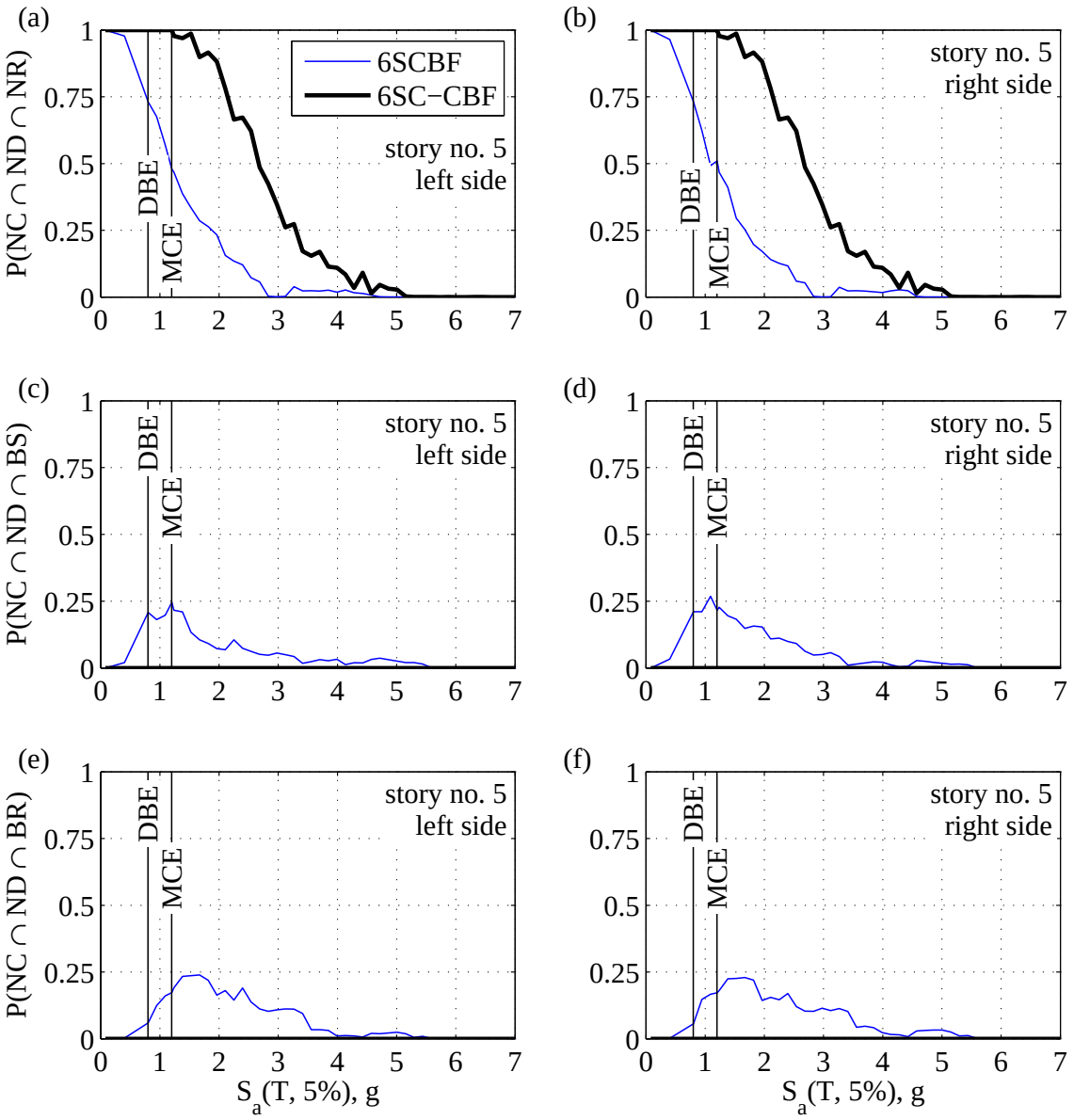

Figure 7.13: Comparison of brace damage scenario fragilities for 5th story of 6-story archetype buildings: (a) $NC \cap ND \cap NR$ for left side brace; (b) $NC \cap ND \cap NR$ for right side brace; (c) $NC \cap ND \cap BS$ for left side brace; (d) $NC \cap ND \cap BS$ for right side brace; (e) $NC \cap ND \cap BR$ for left side brace; and (f) $NC \cap ND \cap BR$ for right side brace;

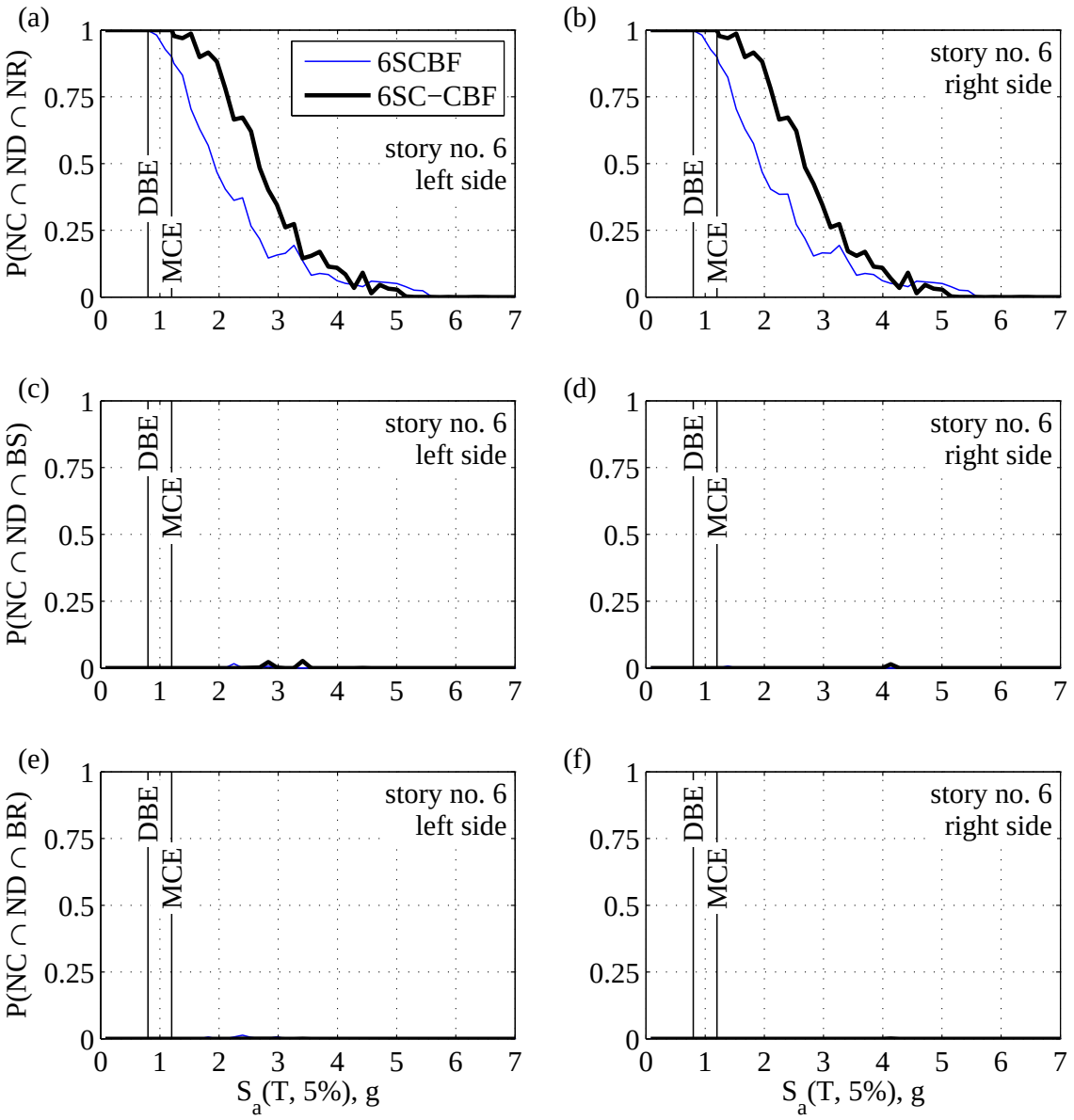

Figure 7.14: Comparison of brace damage scenario fragilities for 6th story of 6-story archetype buildings: (a) $NC \cap ND \cap NR$ for left side brace; (b) $NC \cap ND \cap NR$ for right side brace; (c) $NC \cap ND \cap BS$ for left side brace; (d) $NC \cap ND \cap BS$ for right side brace; (e) $NC \cap ND \cap BR$ for left side brace; and (f) $NC \cap ND \cap BR$ for right side brace;

7.4 Comparison of Damage Scenario Fragilities for 9-story Archetype Buildings

The damage scenario fragilities for the 9SCBF and 9SC-CBF archetype buildings are presented and discussed in this section. The C damage scenario fragility is shown in Figure 7.15. It can be seen from Figure 7.15 that $P(C)$ for the 9SC-CBF archetype building is smaller than $P(C)$ for the 9SCBF archetype building at all $S_a(T,5\%)$. It can also be seen that the $S_a(T,5\%)$ value at 50% probability of collapse is close to $\hat{S}_{CT} = 2.68g$ for the 9SC-CBF archetype building and $\hat{S}_{CT} = 2.02g$ for the 9SCBF archetype building, presented previously in Chapter 4, Table 4.2, based on the performance evaluation methodology of FEMA P695 document [23]. The $P(C)$ values are negligible at the DBE and MCE hazard levels for the 9SCBF and 9SC-CBF archetype buildings.

The $NC \cap D$ damage scenario fragility, calculated using Equation (7.2), is shown in Figure 7.16 for the 9SCBF and 9SC-CBF archetype buildings. It can be seen that $P(NC \cap D)$ for the 9SCBF archetype building starts from approximately 0 at $S_a(T,5\%) \approx 0.5g$, increases to approximately 50% at $S_a(T,5\%) \approx 1.5g$, and then decreases to less than 10% at $S_a(T,5\%) \approx 4.0g$. The $P(NC \cap D)$ value for the 9SC-CBF archetype building starts from approximately 0 at $S_a(T,5\%) \approx 1g$, increases to approximately 37% at $S_a(T,5\%) \approx 2.2g$, and then decreases to less than 10% at $S_a(T,5\%) \approx 4.0g$. It can clearly be seen from Figure 7.16 that the $NC \cap D$ damage scenario fragility for the 9SC-CBF archetype building is shifted towards larger values of $S_a(T,5\%)$, compared to the 9SCBF archetype building. This shift of the $NC \cap D$ damage scenario fragility shows that a larger $S_a(T,5\%)$ value (i.e., a more intense GM or greater hazard) is needed to produce the same $P(NC \cap D)$ (i.e., probability of damage leading to demolition when collapse has not occurred) for the 9SC-CBF archetype building. It can also be seen that the maximum $P(NC \cap D)$ value is smaller for the 9SC-CBF archetype building. The $P(NC \cap D)$ value is negligible at the

DBE and MCE hazard levels for the 9SC-CBF archetype building. The $P(NC \cap D)$ value is negligible at the DBE hazard level but is considerable at the MCE hazard level for the 9SCBF archetype building.

The brace damage scenario fragilities for the 9SCBF archetype building and the 9SC-CBF archetype building, calculated using Equations (7.3), (7.4), and (7.5), are shown in Figure 7.17 through Figure 7.25 for the 1st story through the 9th story, respectively. The $NC \cap ND \cap NR$ damage scenario fragilities for all braces are shown in parts (a) and (b) of Figure 7.17 through Figure 7.25. It can be seen that for all braces, the $P(NC \cap ND \cap NR)$ value (i.e., the probability of no damage to the braces) is greater for the 9SC-CBF archetype building than for the 9SCBF archetype building at all $S_a(T, 5\%)$ values. For the 9SC-CBF archetype building, the probability of no brace damage is approximately 100% for all braces at the DBE hazard level and close to 100% for all braces at the MCE hazard level. For the 9SCBF archetype building, the probability of no brace damage is much lower for the 1st through the 7th story braces at the DBE and MCE hazard levels.

The $NC \cap ND \cap BS$ damage scenario fragilities for all braces of the 9SCBF and 9SC-CBF archetype buildings are shown in parts (c) and (d) of Figure 7.17 through Figure 7.25. It can be seen from Figure 7.17(c) and (d) that a non-negligible $P(NC \cap ND \cap BS)$ value (i.e., a non-negligible probability of brace straightening) starts at much smaller $S_a(T, 5\%)$ values for the 1st story braces of the 9SCBF archetype buildings compared to that of the 9SC-CBF archetype buildings. The $P(NC \cap ND \cap BS)$ value is negligible for braces at the 2nd story through 9th story for the 9SC-CBF archetype building. For the 9SCBF archetype building, however, the $P(NC \cap ND \cap BS)$ value is considerable for braces at the 1st story through 7th story and is negligible for the 8th and 9th story braces. The $P(NC \cap ND \cap BS)$ value is negligible at the DBE and MCE hazard levels for all braces of the 9SC-CBF archetype building. The $P(NC \cap ND \cap BS)$ value is non-negligible at the DBE and MCE hazard levels for the 1st story through 7th story braces of the 9SCBF archetype building.

The $NC \cap ND \cap BR$ damage scenario fragilities for all braces of the 9SCBF and 9SC-CBF archetype buildings are shown in parts (e) and (f) of Figure 7.17 through Figure 7.25. The maximum $P(NC \cap ND \cap BR)$ value for the 1st story braces is smaller for the 9SC-CBF archetype building than those of the 9SCBF archetype building. Non-negligible $P(NC \cap ND \cap BR)$ values (i.e., non-negligible probability of brace replacement) for the 1st story braces are seen at much smaller $S_a(T, 5\%)$ values for the 1st story braces of the 9SCBF archetype building than for the 9SC-CBF archetype building. The $P(NC \cap ND \cap BR)$ value is negligible for the 2nd story through the 9th story braces for the 9SC-CBF archetype building. The $P(NC \cap ND \cap BR)$ value, however, is non-negligible for the 1st story through 7th story braces, but is negligible for the 8th and 9th story braces for the 9SCBF archetype building. The $P(NC \cap ND \cap BR)$ value is negligible at the DBE and MCE hazard levels for all the braces of the 9SC-CBF archetype building. The $P(NC \cap ND \cap BR)$ value is non-negligible at the DBE and MCE hazard levels for the 1st story through the 7th story braces of the 9SCBF archetype building.

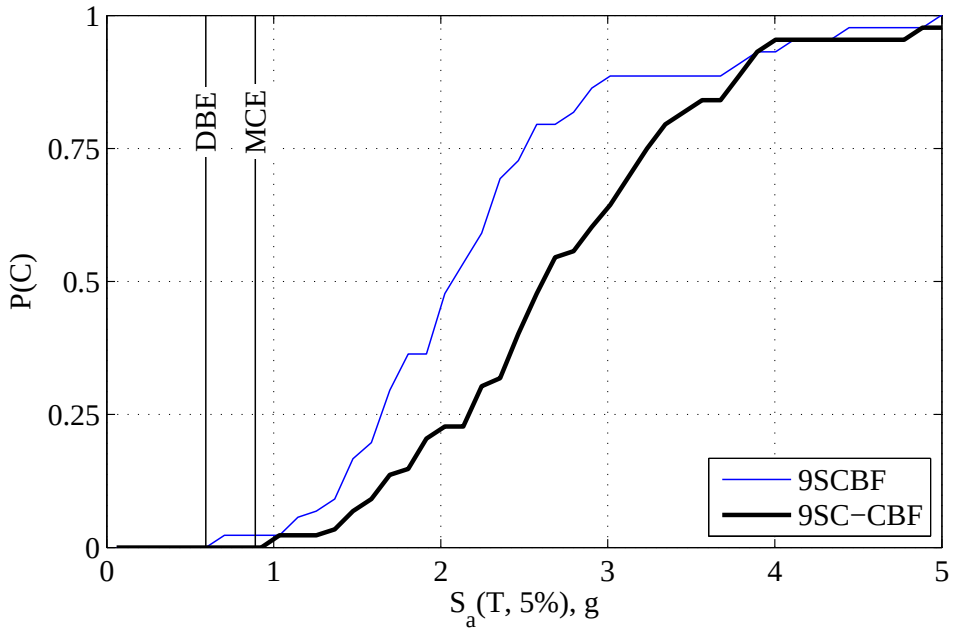

Figure 7.15: Comparison of *C* damage scenario fragility for 9-story archetype buildings

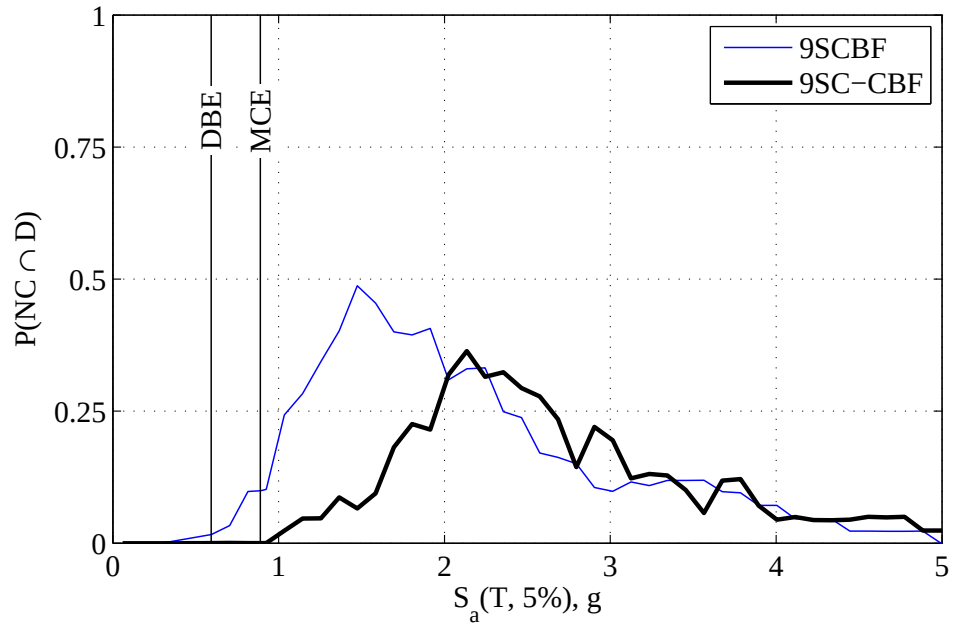

Figure 7.16: Comparison of $NC \cap D$ damage scenario fragility for 9-story archetype buildings

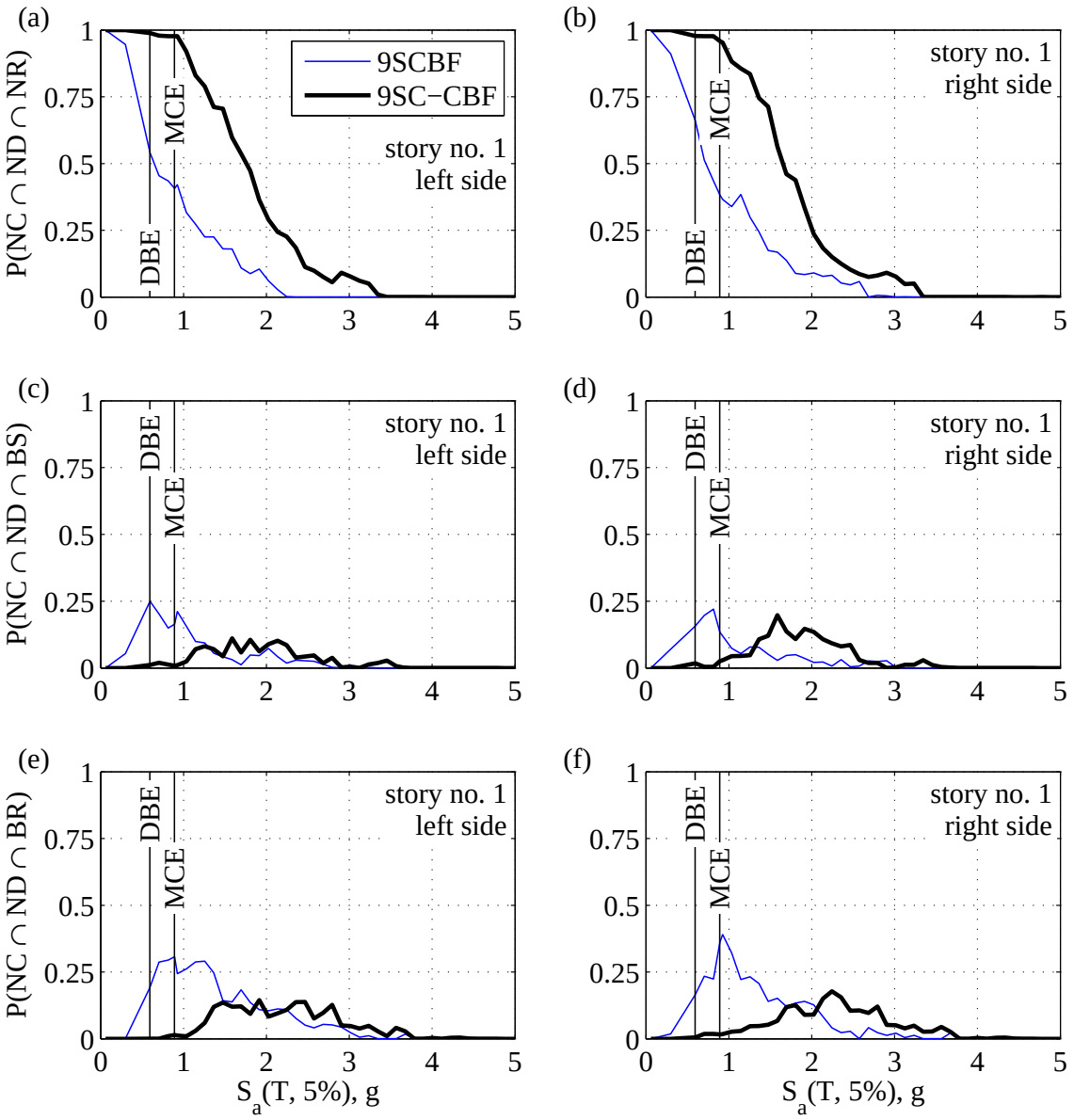

Figure 7.17: Comparison of brace damage scenario fragilities for 1st story of 9-story archetype buildings: (a) $NC \cap ND \cap NR$ for left side brace; (b) $NC \cap ND \cap NR$ for right side brace; (c) $NC \cap ND \cap BS$ for left side brace; (d) $NC \cap ND \cap BS$ for right side brace; (e) $NC \cap ND \cap BR$ for left side brace; and (f) $NC \cap ND \cap BR$ for right side brace;

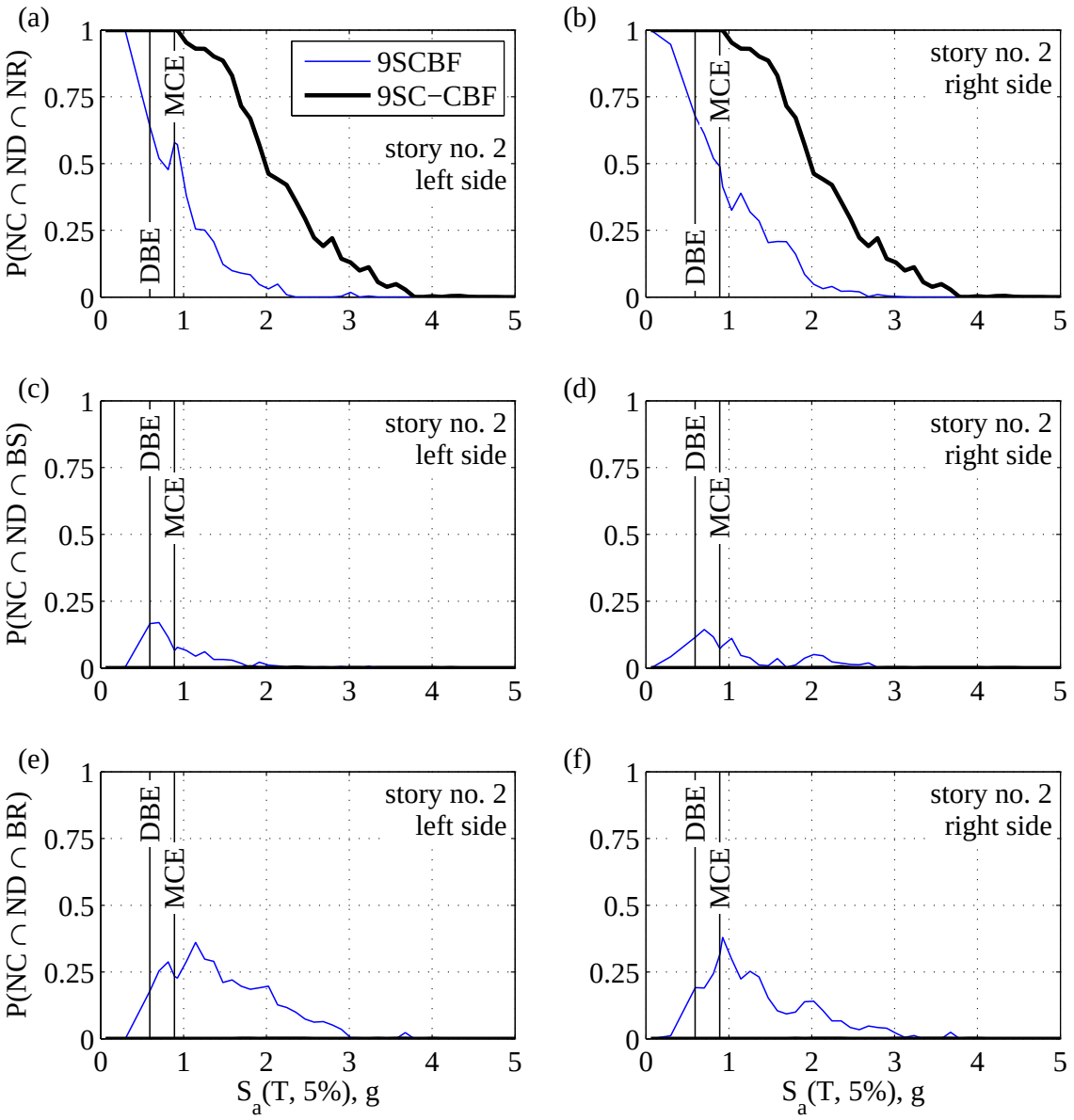

Figure 7.18: Comparison of brace damage scenario fragilities for 2nd story of 9-story archetype buildings: (a) $NC \cap ND \cap NR$ for left side brace; (b) $NC \cap ND \cap NR$ for right side brace; (c) $NC \cap ND \cap BS$ for left side brace; (d) $NC \cap ND \cap BS$ for right side brace; (e) $NC \cap ND \cap BR$ for left side brace; and (f) $NC \cap ND \cap BR$ for right side brace;

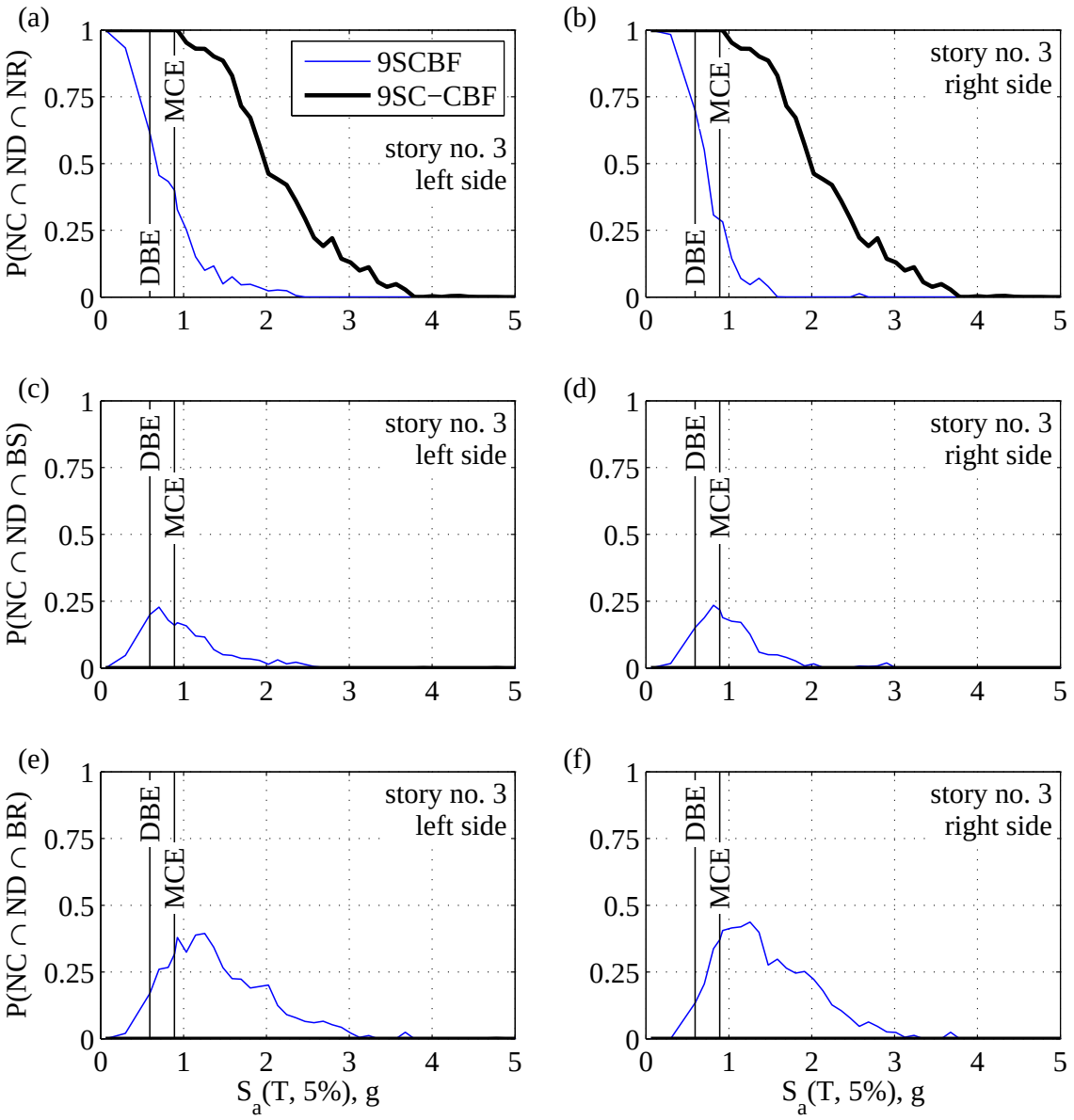

Figure 7.19: Comparison of brace damage scenario fragilities for 3rd story of 9-story archetype buildings: (a) $NC \cap ND \cap NR$ for left side brace; (b) $NC \cap ND \cap NR$ for right side brace; (c) $NC \cap ND \cap BS$ for left side brace; (d) $NC \cap ND \cap BS$ for right side brace; (e) $NC \cap ND \cap BR$ for left side brace; and (f) $NC \cap ND \cap BR$ for right side brace;

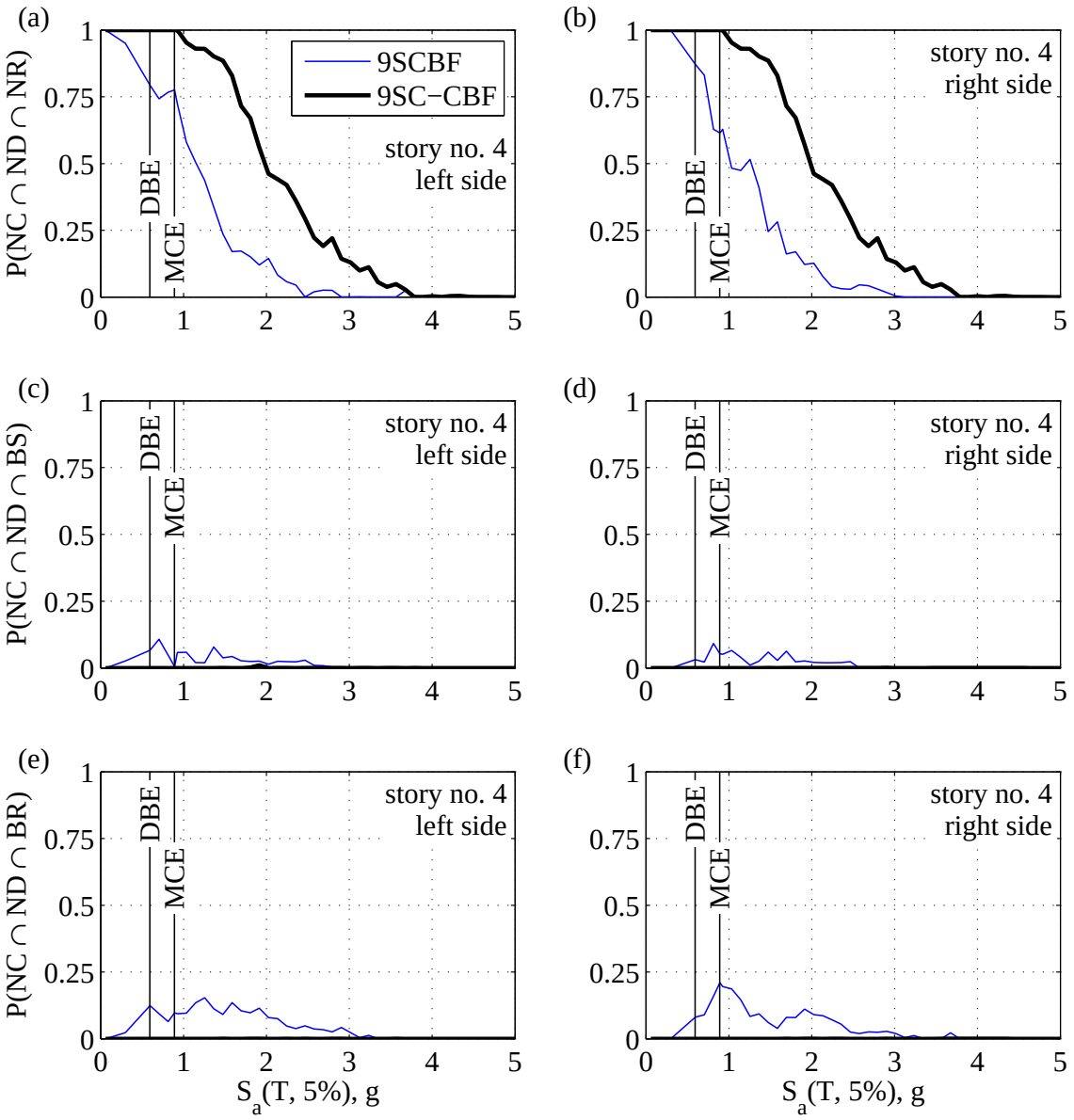

Figure 7.20: Comparison of brace damage scenario fragilities for 4th story of 9-story archetype buildings: (a) $NC \cap ND \cap NR$ for left side brace; (b) $NC \cap ND \cap NR$ for right side brace; (c) $NC \cap ND \cap BS$ for left side brace; (d) $NC \cap ND \cap BS$ for right side brace; (e) $NC \cap ND \cap BR$ for left side brace; and (f) $NC \cap ND \cap BR$ for right side brace;

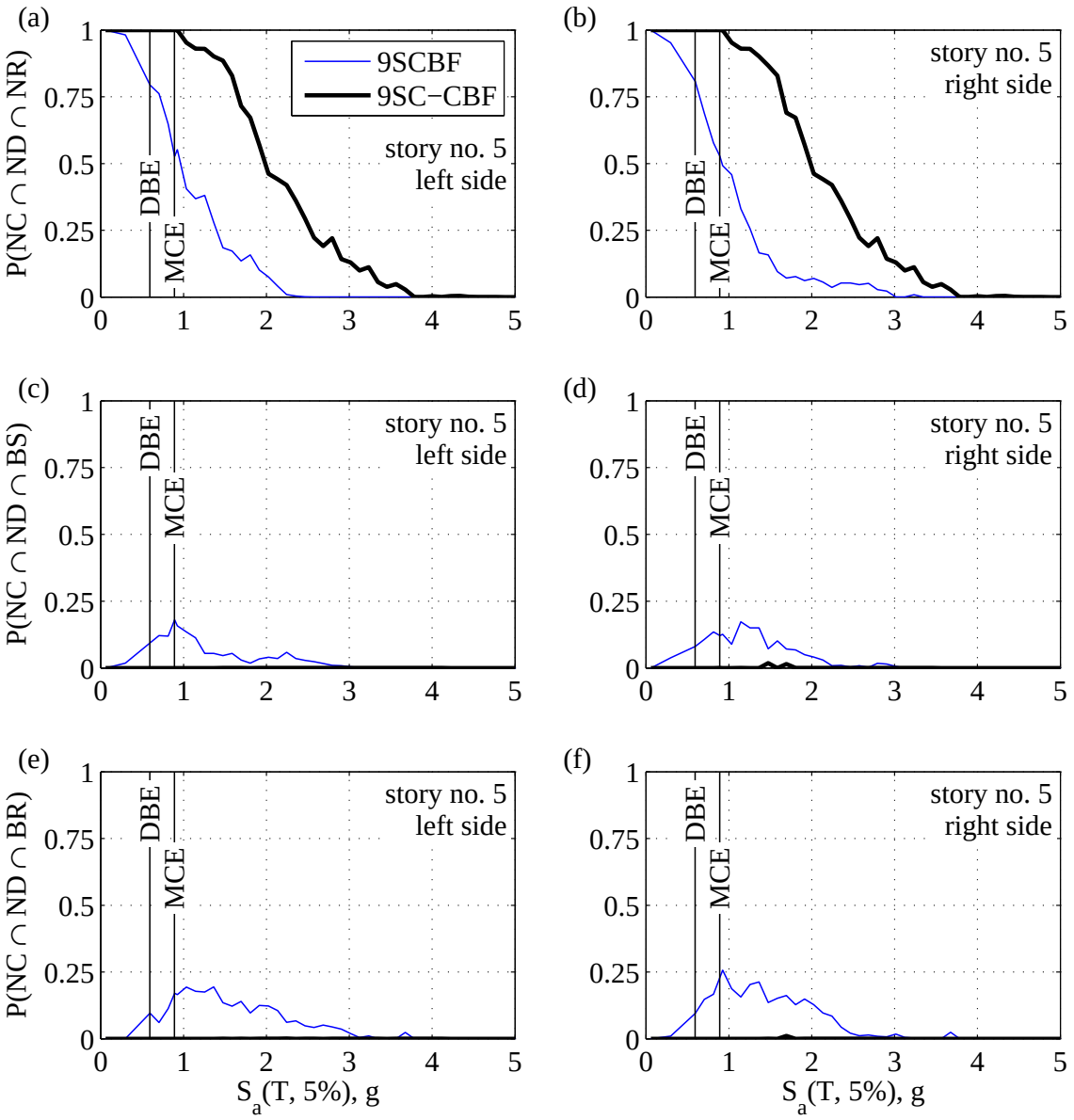

Figure 7.21: Comparison of brace damage scenario fragilities for 5th story of 9-story archetype buildings: (a) $NC \cap ND \cap NR$ for left side brace; (b) $NC \cap ND \cap NR$ for right side brace; (c) $NC \cap ND \cap BS$ for left side brace; (d) $NC \cap ND \cap BS$ for right side brace; (e) $NC \cap ND \cap BR$ for left side brace; and (f) $NC \cap ND \cap BR$ for right side brace;

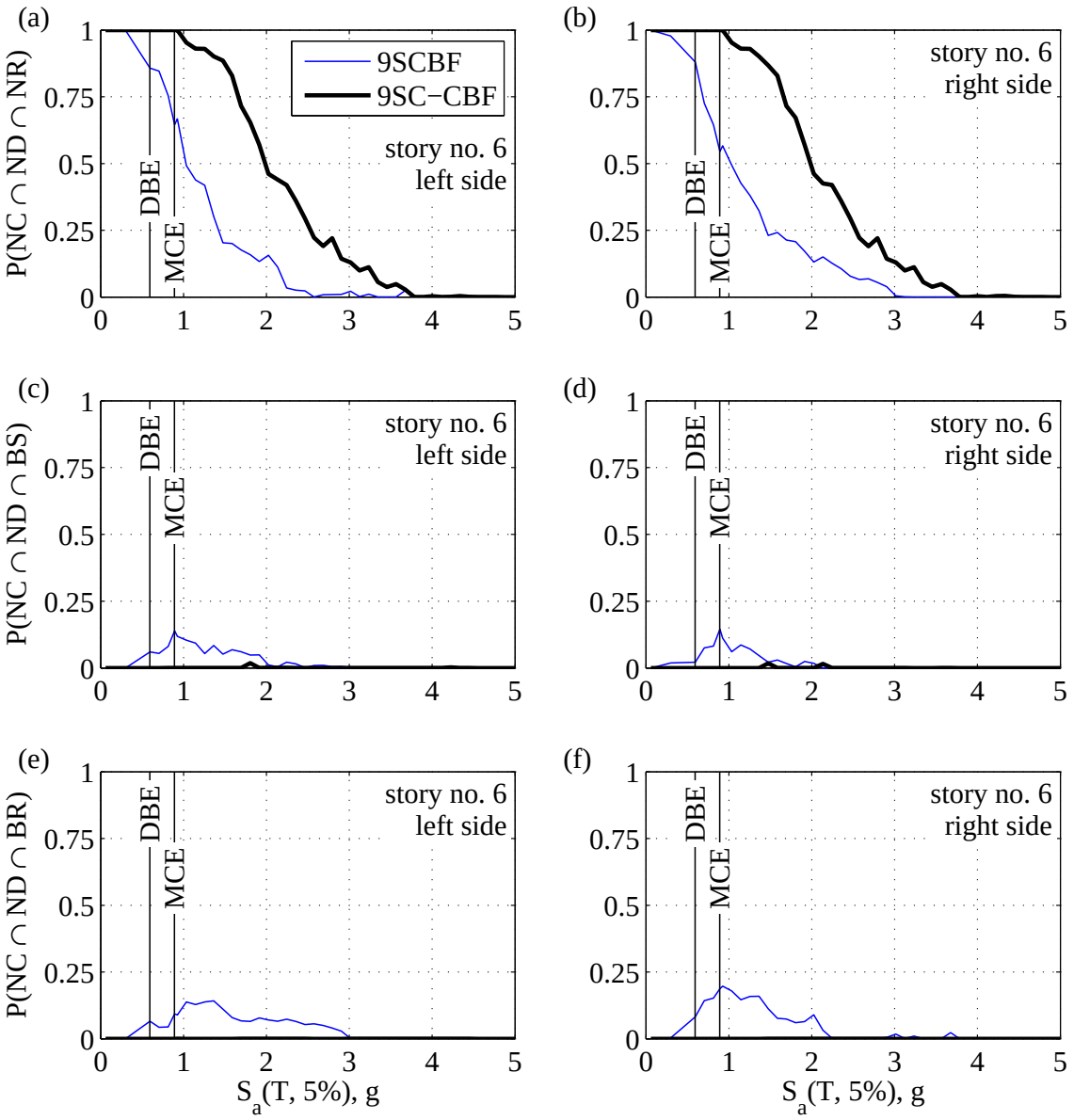

Figure 7.22: Comparison of brace damage scenario fragilities for 6th story of 9-story archetype buildings: (a) $NC \cap ND \cap NR$ for left side brace; (b) $NC \cap ND \cap NR$ for right side brace; (c) $NC \cap ND \cap BS$ for left side brace; (d) $NC \cap ND \cap BS$ for right side brace; (e) $NC \cap ND \cap BR$ for left side brace; and (f) $NC \cap ND \cap BR$ for right side brace;

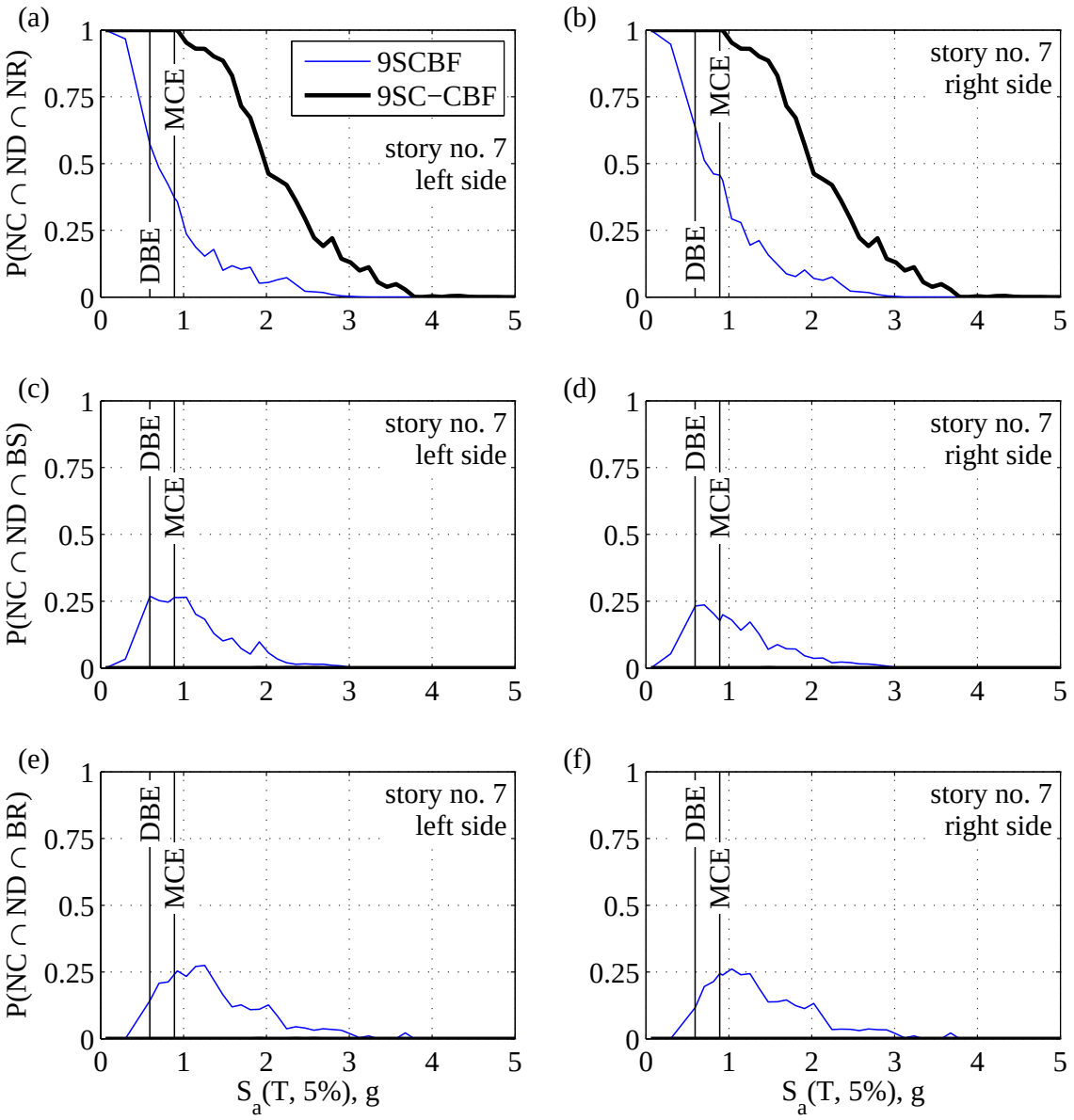

Figure 7.23: Comparison of brace damage scenario fragilities for 7th story of 9-story archetype buildings: (a) $NC \cap ND \cap NR$ for left side brace; (b) $NC \cap ND \cap NR$ for right side brace; (c) $NC \cap ND \cap BS$ for left side brace; (d) $NC \cap ND \cap BS$ for right side brace; (e) $NC \cap ND \cap BR$ for left side brace; and (f) $NC \cap ND \cap BR$ for right side brace;

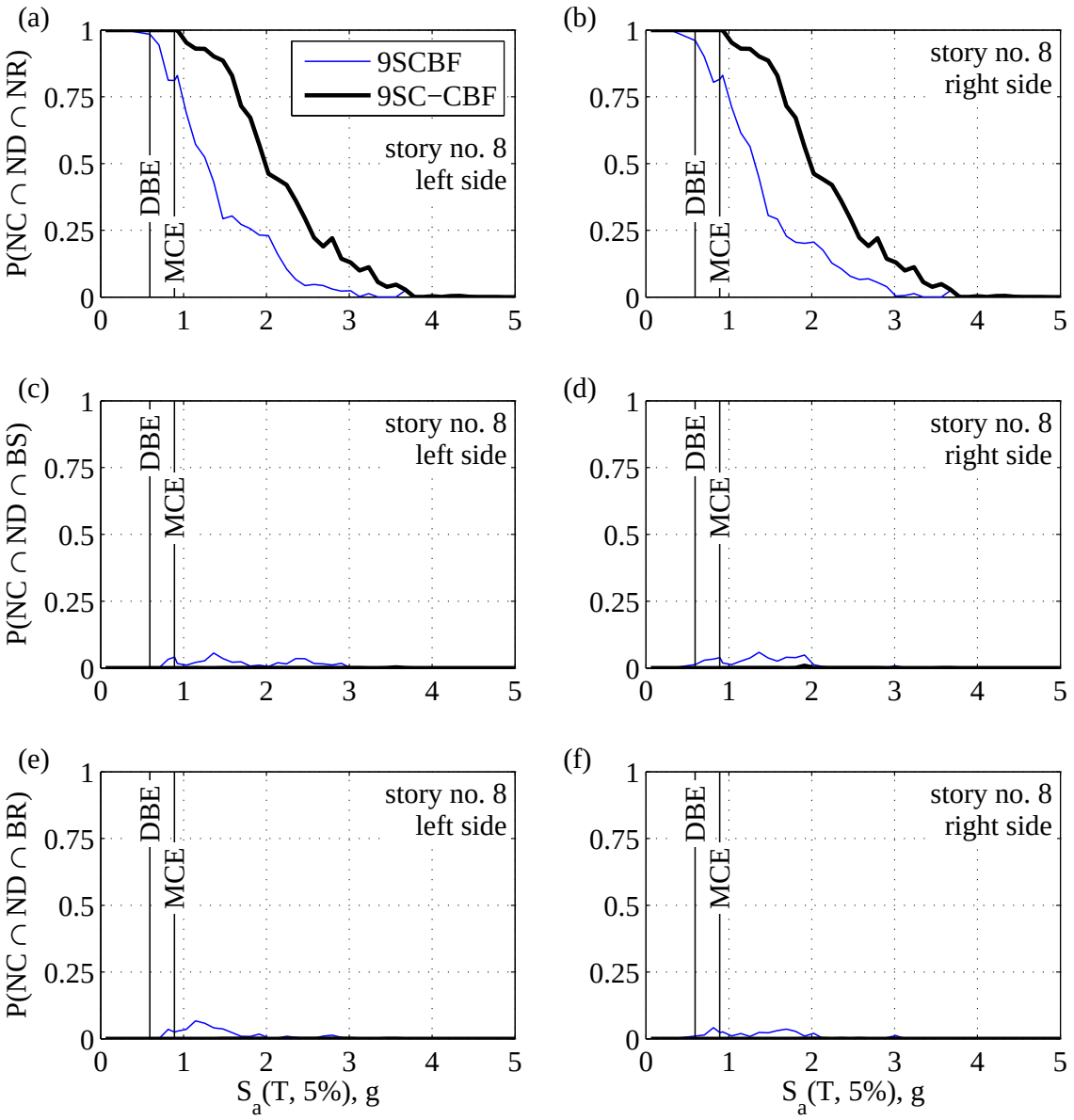

Figure 7.24: Comparison of brace damage scenario fragilities for 8th story of 9-story archetype buildings: (a) $NC \cap ND \cap NR$ for left side brace; (b) $NC \cap ND \cap NR$ for right side brace; (c) $NC \cap ND \cap BS$ for left side brace; (d) $NC \cap ND \cap BS$ for right side brace; (e) $NC \cap ND \cap BR$ for left side brace; and (f) $NC \cap ND \cap BR$ for right side brace;

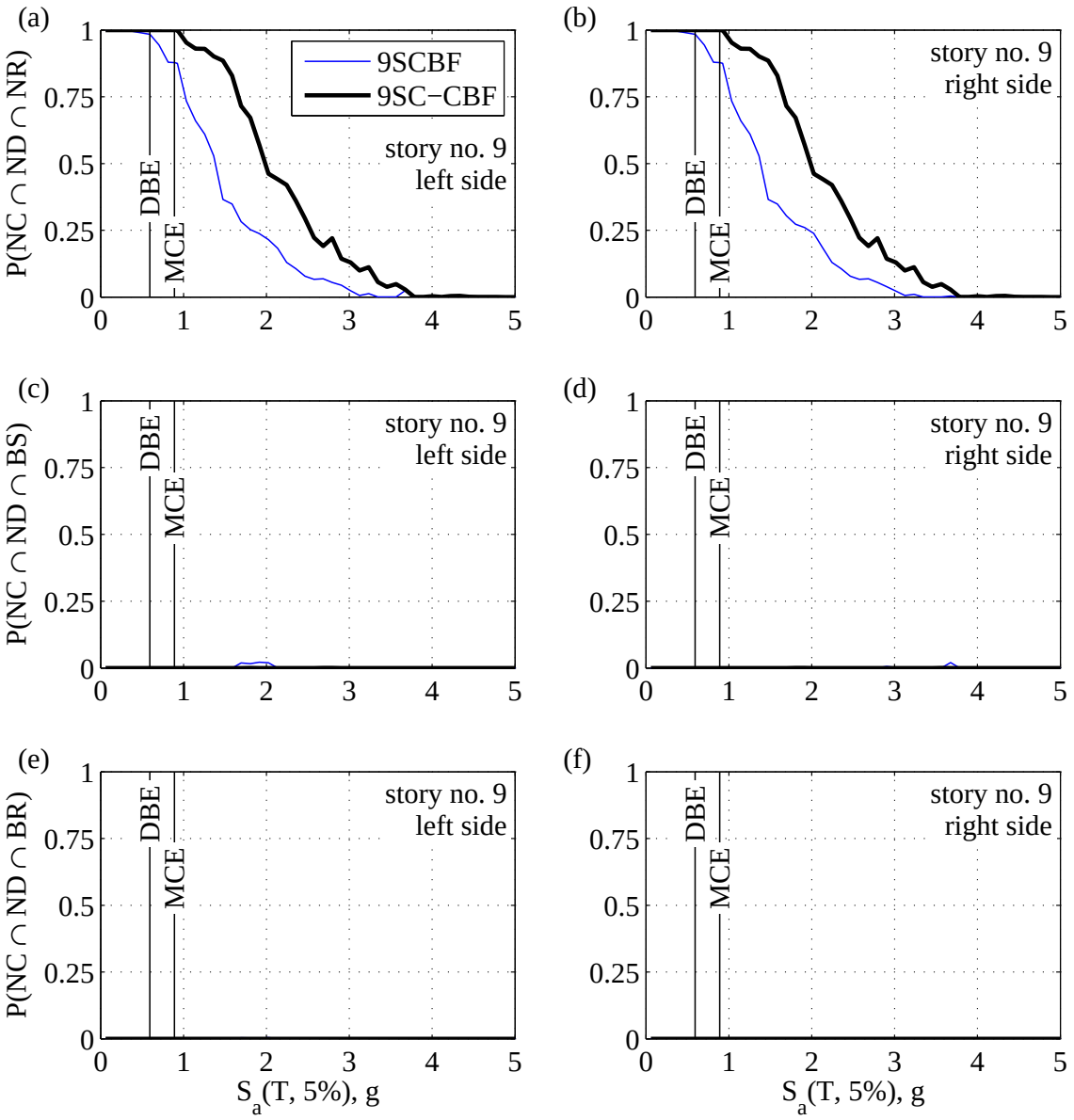

Figure 7.25: Comparison of brace damage scenario fragilities for 9th story of 9-story archetype buildings: (a) $NC \cap ND \cap NR$ for left side brace; (b) $NC \cap ND \cap NR$ for right side brace; (c) $NC \cap ND \cap BS$ for left side brace; (d) $NC \cap ND \cap BS$ for right side brace; (e) $NC \cap ND \cap BR$ for left side brace; and (f) $NC \cap ND \cap BR$ for right side brace;

7.5 Comparison of Damage Scenario Fragilities for 12-story Archetype Buildings

The damage scenario fragilities for the 12SCBF and 12SC-CBF archetype buildings are presented and discussed in this section. The C damage scenario fragility is shown in Figure 7.26. It can be seen from Figure 7.26 that $P(C)$ for the 12SC-CBF archetype building is smaller than $P(C)$ for the 12SCBF archetype building at all $S_a(T,5\%)$. It can also be seen that the $S_a(T,5\%)$ value at 50% probability of collapse is close to $\hat{S}_{CT} = 2.64g$ for the 12SC-CBF archetype building and $\hat{S}_{CT} = 1.83g$ for the 12SCBF archetype building, presented previously in Chapter 4, Table 4.2, based on the performance evaluation methodology of FEMA P695 document [23]. The $P(C)$ values are negligible at the DBE and MCE hazard levels for the 12SCBF and 12SC-CBF archetype buildings.

The $NC \cap D$ damage scenario fragility, calculated using Equation (7.2), is shown in Figure 7.27 for the 12SCBF and 12SC-CBF archetype buildings. It can be seen that $P(NC \cap D)$ for the 12SCBF archetype building starts from approximately 0 at $S_a(T,5\%) \approx 0.5g$, increases to approximately 50% at $S_a(T,5\%) \approx 1.5g$, and then decreases to less than 10% at $S_a(T,5\%) \approx 3.0g$. The $P(NC \cap D)$ value for the 12SC-CBF archetype building starts from approximately 0 at $S_a(T,5\%) \approx 1g$, increases to approximately 30% at $S_a(T,5\%) \approx 2.0g$, and then decreases to less than 10% at $S_a(T,5\%) \approx 4.0g$. It can clearly be seen from Figure 7.16 that the $NC \cap D$ damage scenario fragility for the 12SC-CBF archetype building is shifted towards larger values of $S_a(T,5\%)$, compared to the 12SCBF archetype building. This shift of the $NC \cap D$ damage scenario fragility shows that a larger $S_a(T,5\%)$ value (i.e., a more intense GM or greater hazard) is needed to produce the same $P(NC \cap D)$ (i.e., probability of damage leading to demolition when collapse has not occurred) for the 12SC-CBF archetype building. It can also be seen that the maximum $P(NC \cap D)$ value is smaller for the 12SC-CBF archetype building. The $P(NC \cap D)$ value is negligible at the

DBE and MCE hazard levels for the 12SC-CBF archetype building. The $P(NC \cap D)$ value is negligible at the DBE hazard level but is considerable at the MCE hazard level for the 12SCBF archetype building.

The brace damage scenario fragilities for the 12SCBF archetype building and the 12SC-CBF archetype building, calculated using Equations (7.3), (7.4), and (7.5), are shown in Figure 7.28 through Figure 7.39 for the 1st story through the 12th story, respectively. The $NC \cap ND \cap NR$ damage scenario fragilities for all braces are shown in parts (a) and (b) of Figure 7.28 through Figure 7.39. It can be seen that for all braces, the $P(NC \cap ND \cap NR)$ value (i.e., the probability of no damage to the braces) is greater for the 12SC-CBF archetype building than for the 12SCBF archetype building at all $S_a(T, 5\%)$ values. For the 12SC-CBF archetype building, the probability of no brace damage is approximately 100% for all braces at the DBE hazard level and close to 100% for all braces at the MCE hazard level. For the 12SCBF archetype building, the probability of no brace damage is much lower for the 1st through the 11th story braces at the DBE and MCE hazard levels.

The $NC \cap ND \cap BS$ damage scenario fragilities for all braces of the 12SCBF and 12SC-CBF archetype buildings are shown in parts (c) and (d) of Figure 7.28 through Figure 7.39. The $P(NC \cap ND \cap BS)$ value is negligible for the 1st story through 8th story, 11th story, and 12th story braces of the 12SC-CBF archetype building. For the 12SCBF archetype building, however, the $P(NC \cap ND \cap BS)$ value is considerable for the 1st story through 5th story, 7th story, and 9th through 11th story braces. The $P(NC \cap ND \cap BS)$ value is small or negligible for the 6th story, 8th story, and 12th story braces of the 12SCBF archetype building. It can be seen from Figure 7.36(c) and (d) and Figure 7.37(c) and (d) that non-negligible $P(NC \cap ND \cap BS)$ values (i.e., probability of brace straightening) start at much smaller $S_a(T, 5\%)$ values for the 9th story and 10th story braces of the 12SCBF archetype building compared to the 12SC-CBF archetype building. For the 10th story left side brace, the maximum $P(NC \cap ND \cap BS)$ value is greater for the 12SC-CBF archetype building

(approximately 15%) than for the 12SCBF archetype building (approximately 10%), as it can be seen in Figure 7.37(c). The maximum $P(NC \cap ND \cap BS)$ value of approximately 10% for the 10th story right side brace of the 12SC-CBF archetype building is not large, and the difference between this maximum value and that of the 12SCBF archetype building is small. The $P(NC \cap ND \cap BS)$ value is negligible at the DBE and MCE hazard levels for all braces of the 12SC-CBF archetype building. The $P(NC \cap ND \cap BS)$ value is non-negligible at the DBE and MCE hazard levels for the 1st story through 5th story, 7th story, 9th story, and 11th story braces of the 12SCBF archetype building.

The $NC \cap ND \cap BR$ damage scenario fragilities for all braces of the 12SCBF and 12SC-CBF archetype buildings are shown in parts (e) and (f) of Figure 7.28 through Figure 7.39. The $P(NC \cap ND \cap BR)$ value is negligible for the 1st story through the 8th story, 11th story, and 12th story braces of the 12SC-CBF archetype building. The $P(NC \cap ND \cap BR)$ value is considerable for the 1st story through 10th story braces and is negligible for the 11th and 12th story braces of the 12SCBF archetype building. The $P(NC \cap ND \cap BR)$ value for the 9th and 10th story braces are smaller for the 12SC-CBF archetype building than for the 12SCBF archetype building. It can be seen from Figure 7.36(e) and (f) and Figure 7.37(e) and (f) that non-negligible $P(NC \cap ND \cap BR)$ values (i.e., probability of brace replacement) is seen at much smaller $S_a(T, 5\%)$ values for the 9th and 10th story braces of the 12SCBF archetype building than for the 12SC-CBF archetype building. The $P(NC \cap ND \cap BR)$ value is negligible at the DBE and MCE hazard levels for all the braces of the 12SC-CBF archetype building. The $P(NC \cap ND \cap BS)$ value is considerable at the DBE and MCE hazard levels for the 1st story through 10th story braces of the 12SCBF archetype building.

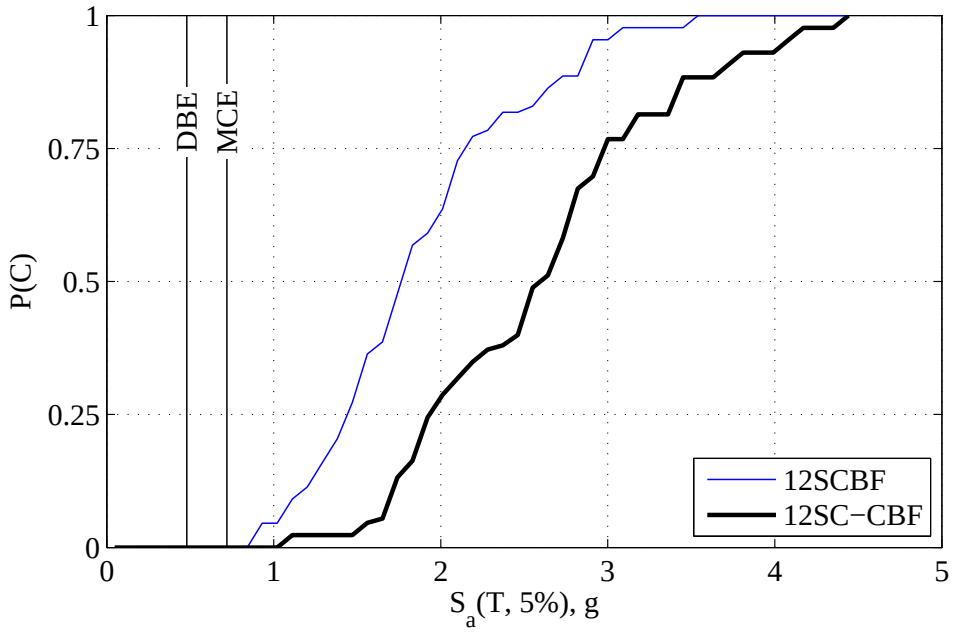

Figure 7.26: Comparison of *C* damage scenario fragility for 12-story archetype buildings

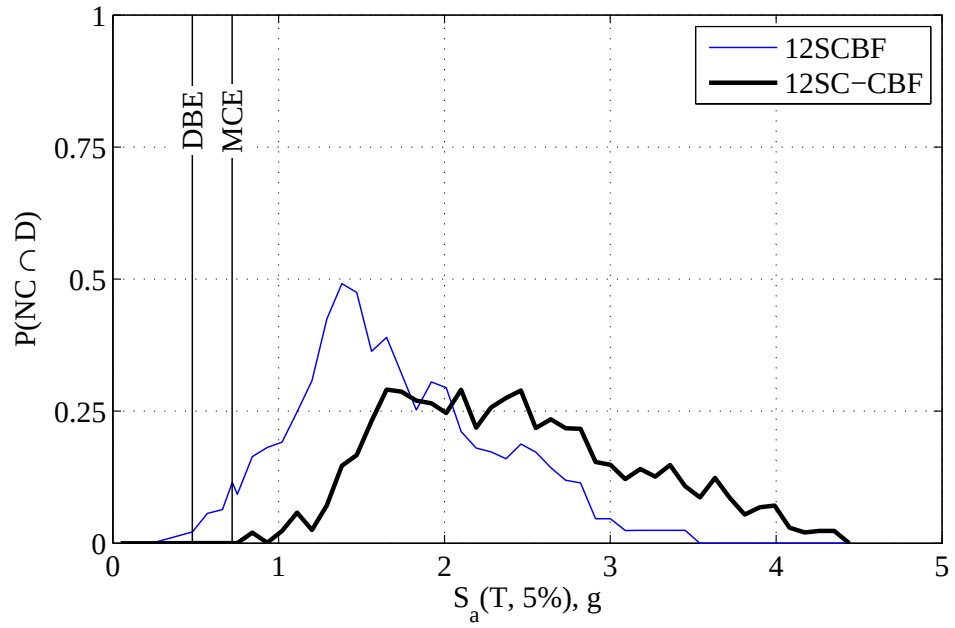

Figure 7.27: Comparison of $NC \cap D$ damage scenario fragility for 12-story archetype buildings

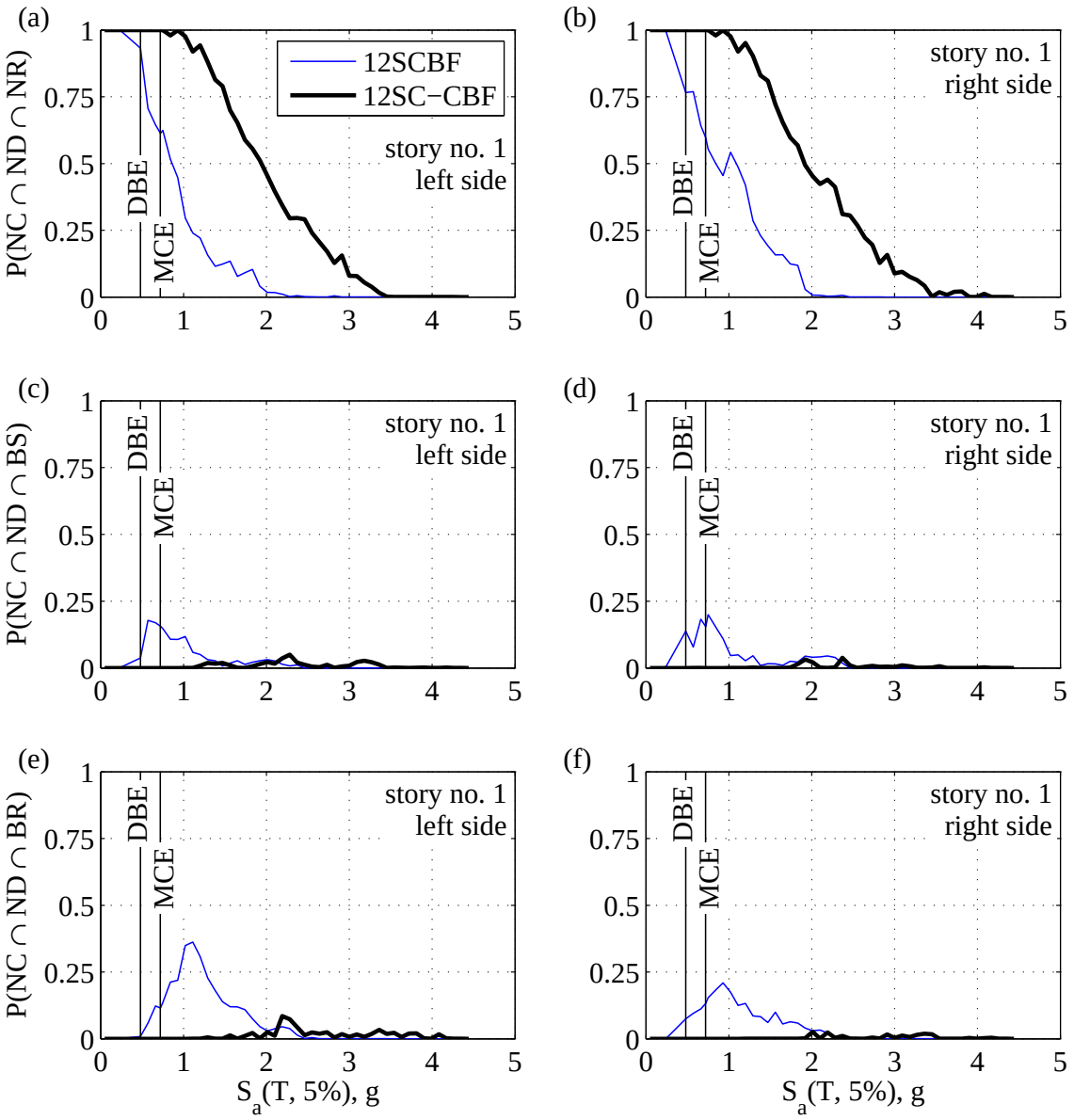

Figure 7.28: Comparison of brace damage scenario fragilities for 1st story of 12-story archetype buildings: (a) $NC \cap ND \cap NR$ for left side brace; (b) $NC \cap ND \cap NR$ for right side brace; (c) $NC \cap ND \cap BS$ for left side brace; (d) $NC \cap ND \cap BS$ for right side brace; (e) $NC \cap ND \cap BR$ for left side brace; and (f) $NC \cap ND \cap BR$ for right side brace;

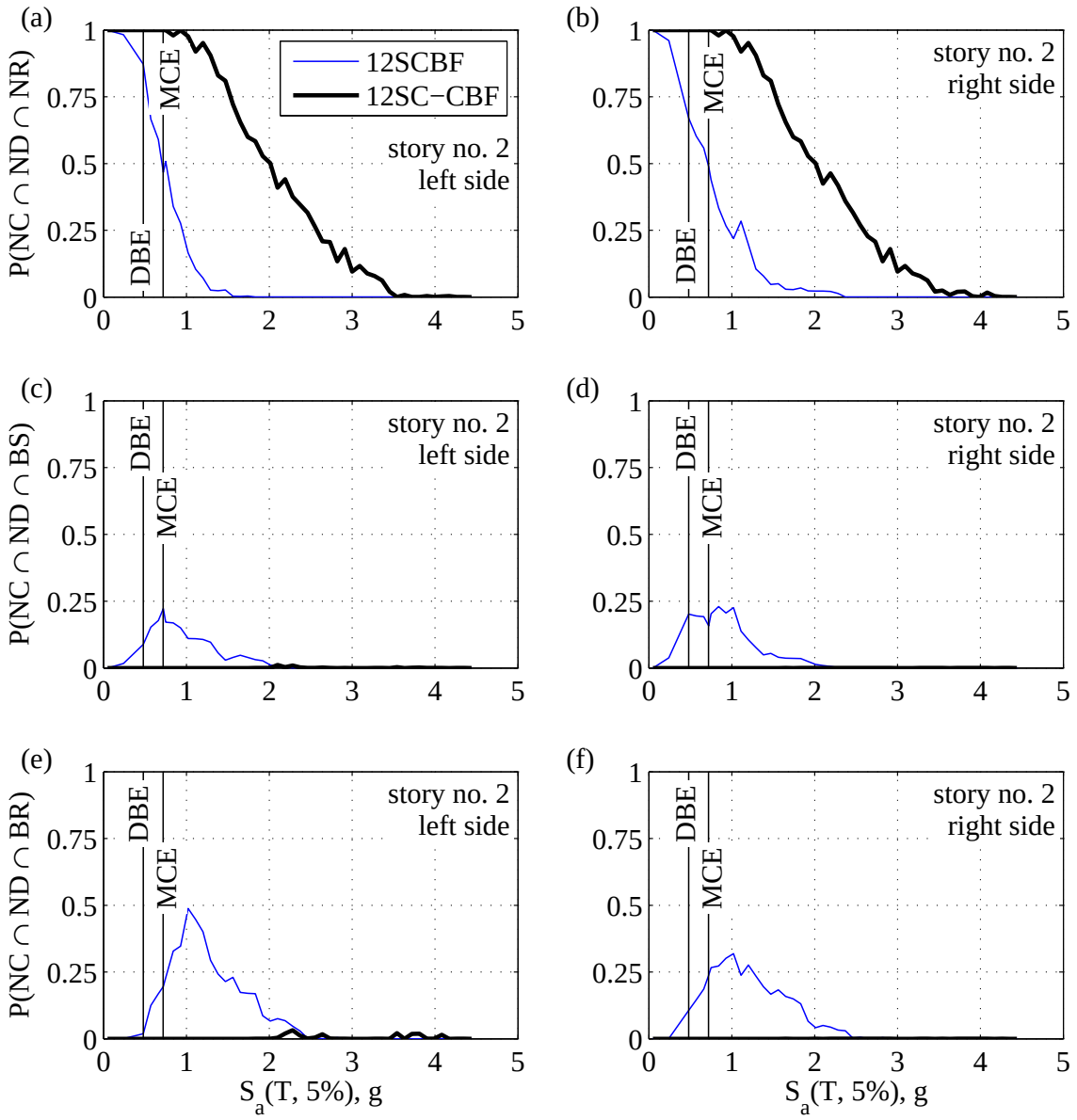

Figure 7.29: Comparison of brace damage scenario fragilities for 2nd story of 12-story archetype buildings: (a) $NC \cap ND \cap NR$ for left side brace; (b) $NC \cap ND \cap NR$ for right side brace; (c) $NC \cap ND \cap BS$ for left side brace; (d) $NC \cap ND \cap BS$ for right side brace; (e) $NC \cap ND \cap BR$ for left side brace; and (f) $NC \cap ND \cap BR$ for right side brace;

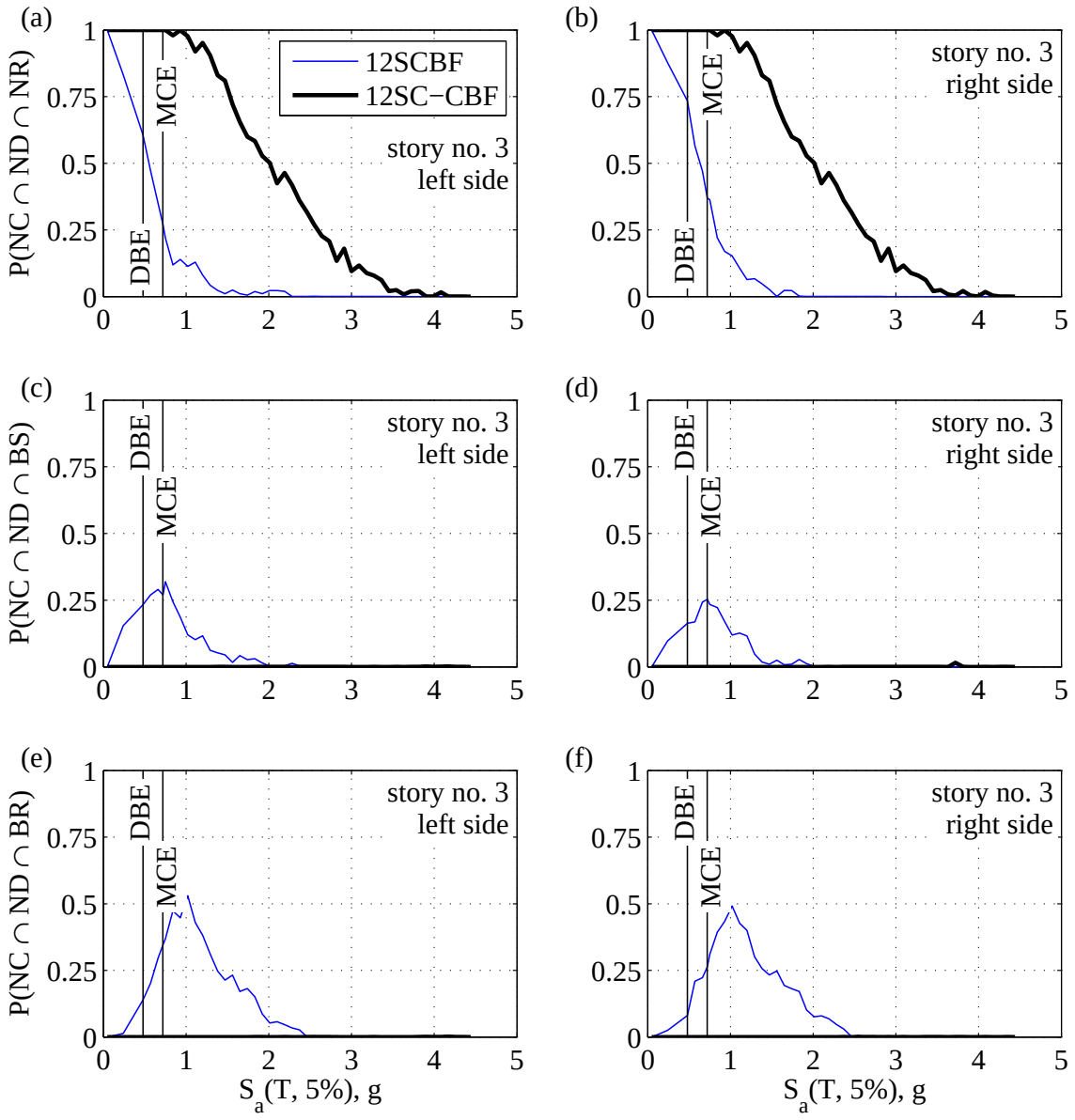

Figure 7.30: Comparison of brace damage scenario fragilities for 3rd story of 12-story archetype buildings: (a) $NC \cap ND \cap NR$ for left side brace; (b) $NC \cap ND \cap NR$ for right side brace; (c) $NC \cap ND \cap BS$ for left side brace; (d) $NC \cap ND \cap BS$ for right side brace; (e) $NC \cap ND \cap BR$ for left side brace; and (f) $NC \cap ND \cap BR$ for right side brace;

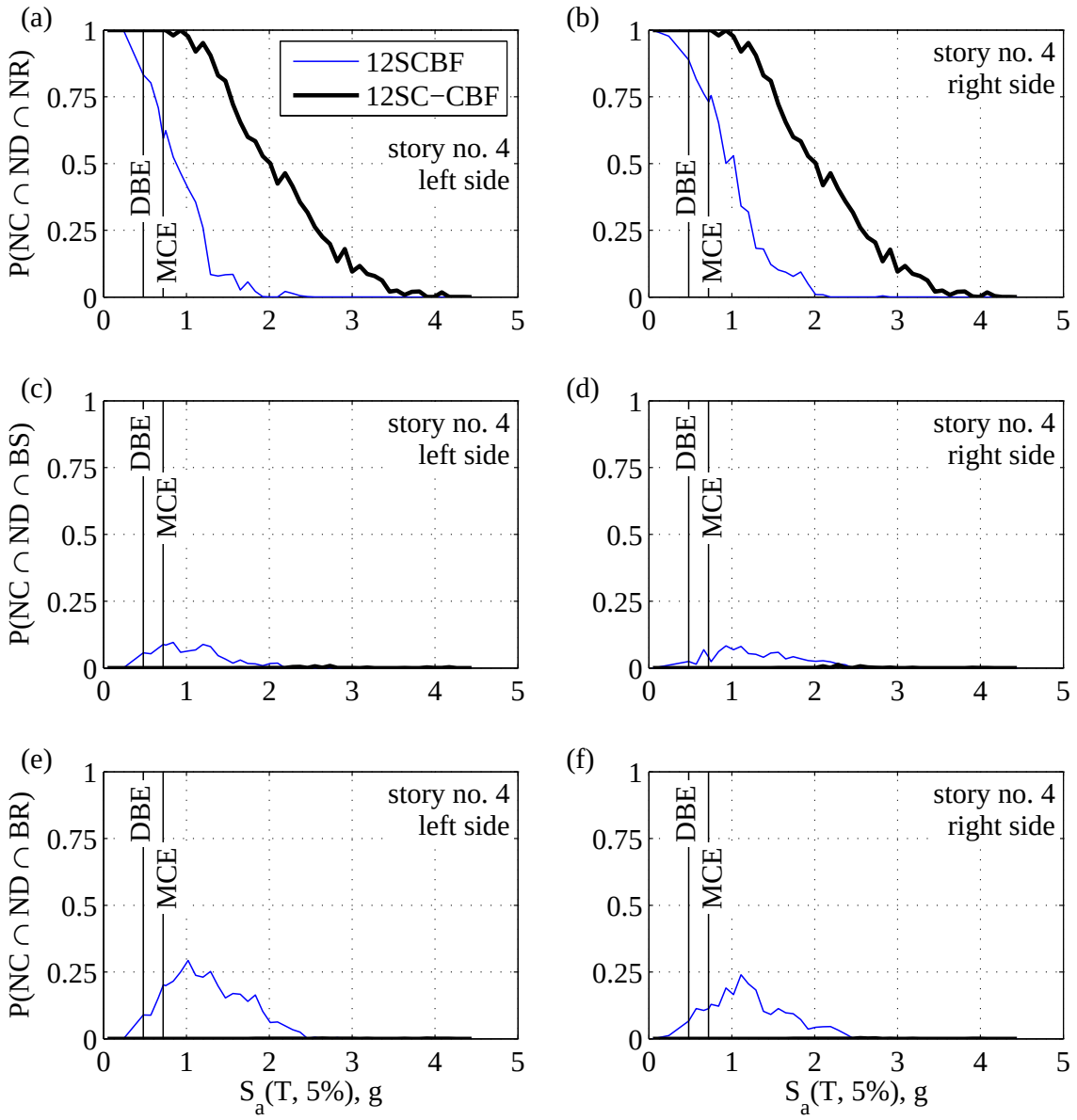

Figure 7.31: Comparison of brace damage scenario fragilities for 4th story of 12-story archetype buildings: (a) $NC \cap ND \cap NR$ for left side brace; (b) $NC \cap ND \cap NR$ for right side brace; (c) $NC \cap ND \cap BS$ for left side brace; (d) $NC \cap ND \cap BS$ for right side brace; (e) $NC \cap ND \cap BR$ for left side brace; and (f) $NC \cap ND \cap BR$ for right side brace;

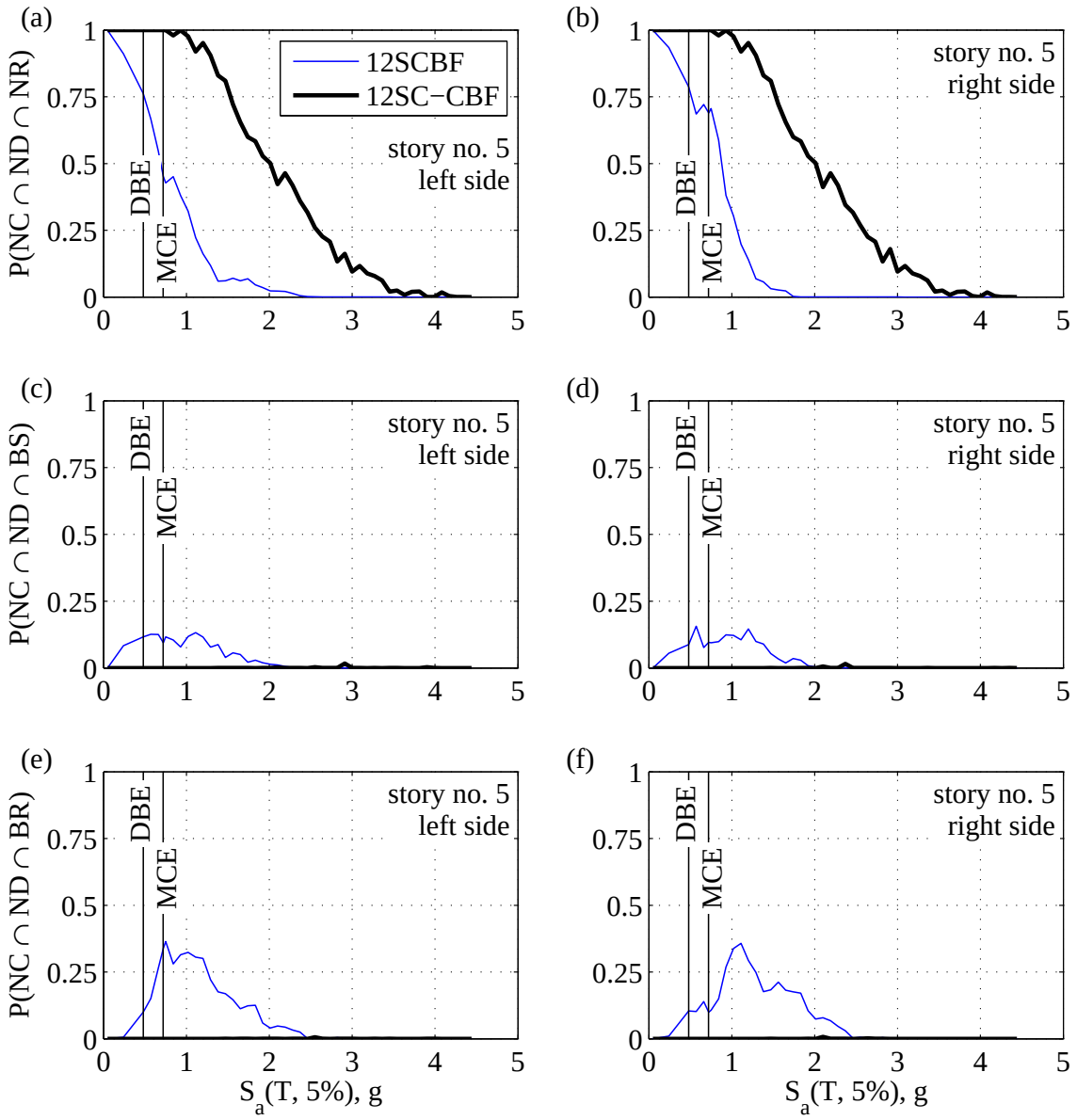

Figure 7.32: Comparison of brace damage scenario fragilities for 5th story of 12-story archetype buildings: (a) $NC \cap ND \cap NR$ for left side brace; (b) $NC \cap ND \cap NR$ for right side brace; (c) $NC \cap ND \cap BS$ for left side brace; (d) $NC \cap ND \cap BS$ for right side brace; (e) $NC \cap ND \cap BR$ for left side brace; and (f) $NC \cap ND \cap BR$ for right side brace;

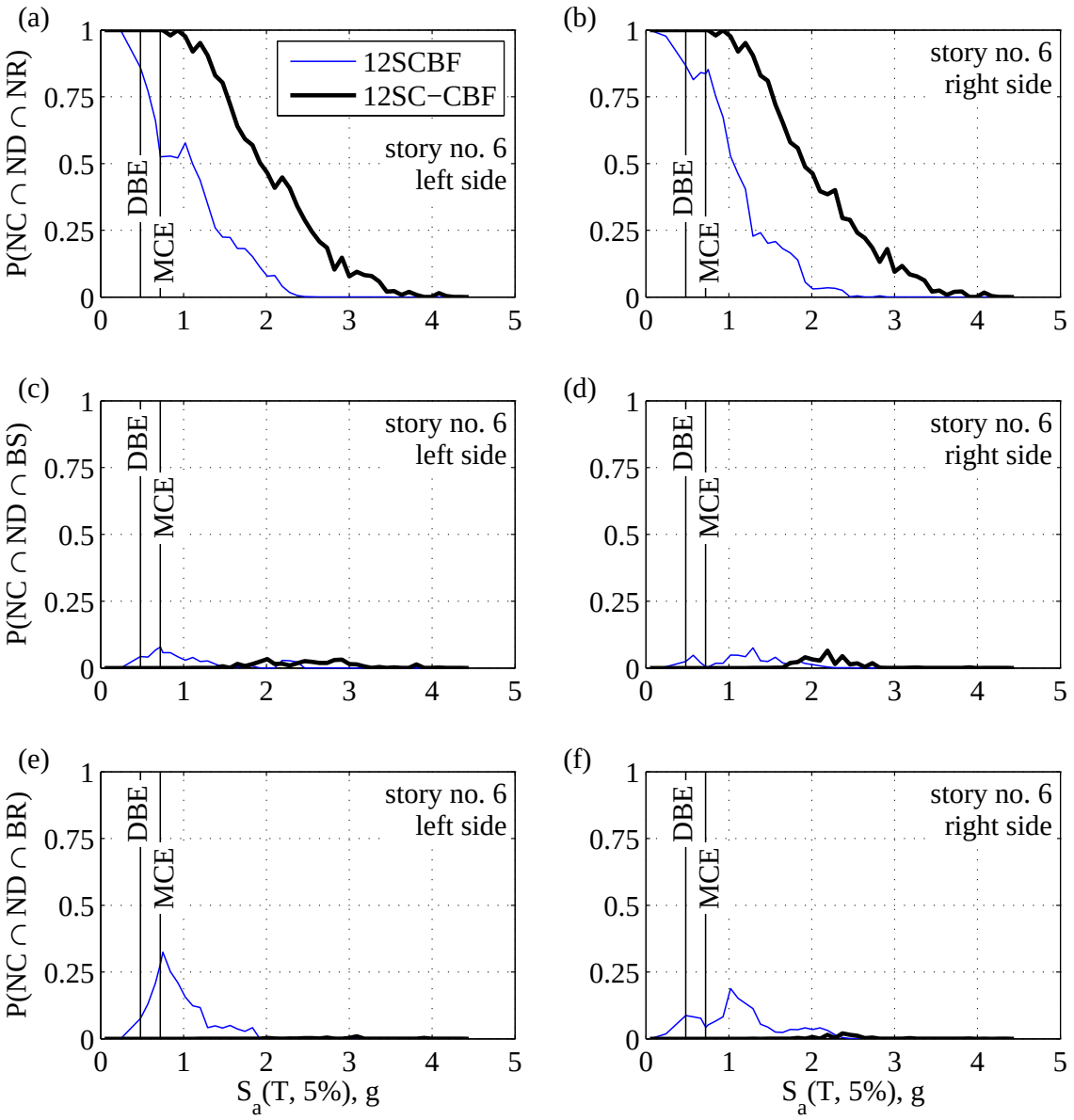

Figure 7.33: Comparison of brace damage scenario fragilities for 6th story of 12-story archetype buildings: (a) $NC \cap ND \cap NR$ for left side brace; (b) $NC \cap ND \cap NR$ for right side brace; (c) $NC \cap ND \cap BS$ for left side brace; (d) $NC \cap ND \cap BS$ for right side brace; (e) $NC \cap ND \cap BR$ for left side brace; and (f) $NC \cap ND \cap BR$ for right side brace;

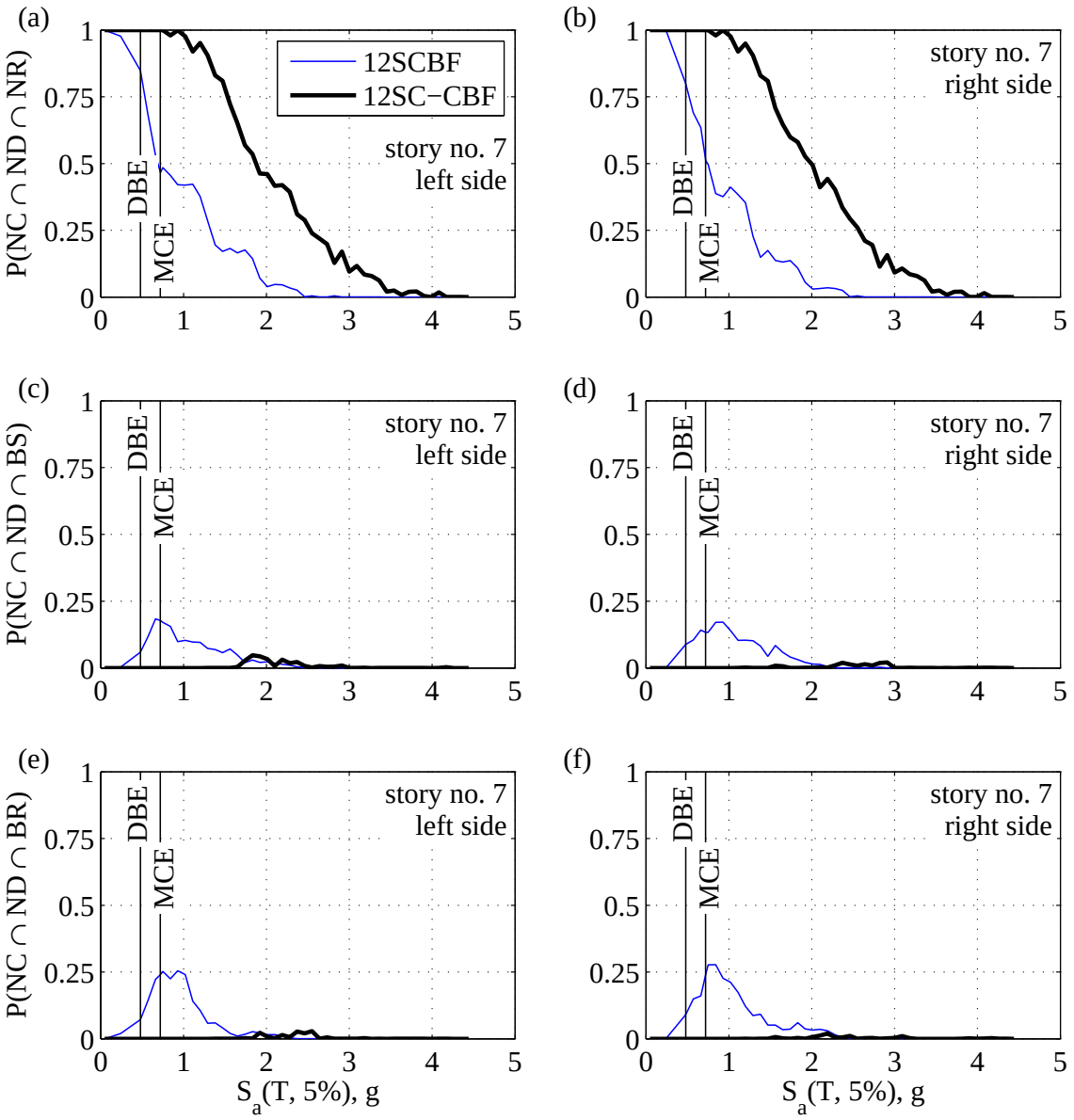

Figure 7.34: Comparison of brace damage scenario fragilities for 7th story of 12-story archetype buildings: (a) $NC \cap ND \cap NR$ for left side brace; (b) $NC \cap ND \cap NR$ for right side brace; (c) $NC \cap ND \cap BS$ for left side brace; (d) $NC \cap ND \cap BS$ for right side brace; (e) $NC \cap ND \cap BR$ for left side brace; and (f) $NC \cap ND \cap BR$ for right side brace;

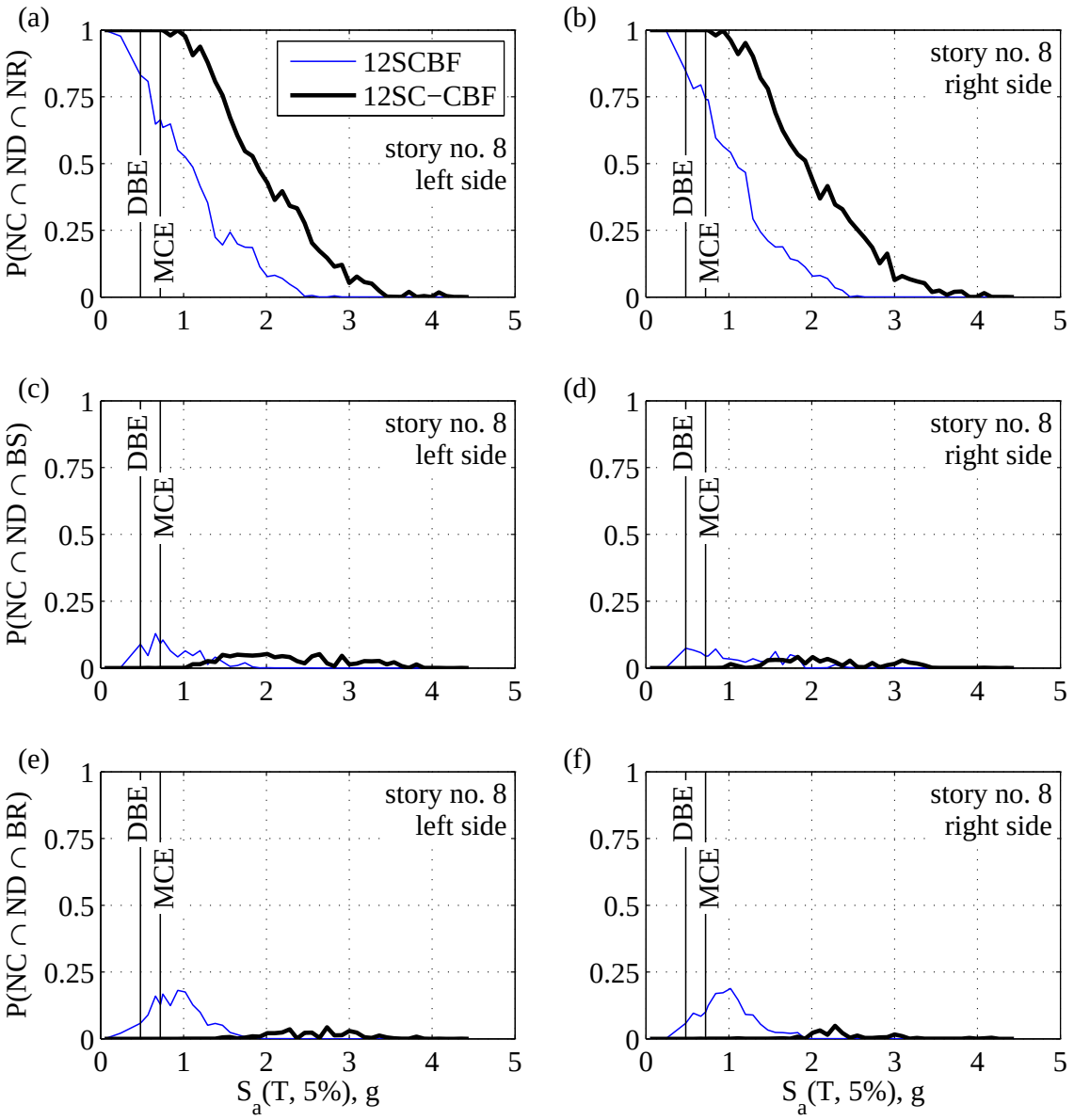

Figure 7.35: Comparison of brace damage scenario fragilities for 8th story of 12-story archetype buildings: (a) $NC \cap ND \cap NR$ for left side brace; (b) $NC \cap ND \cap NR$ for right side brace; (c) $NC \cap ND \cap BS$ for left side brace; (d) $NC \cap ND \cap BS$ for right side brace; (e) $NC \cap ND \cap BR$ for left side brace; and (f) $NC \cap ND \cap BR$ for right side brace;

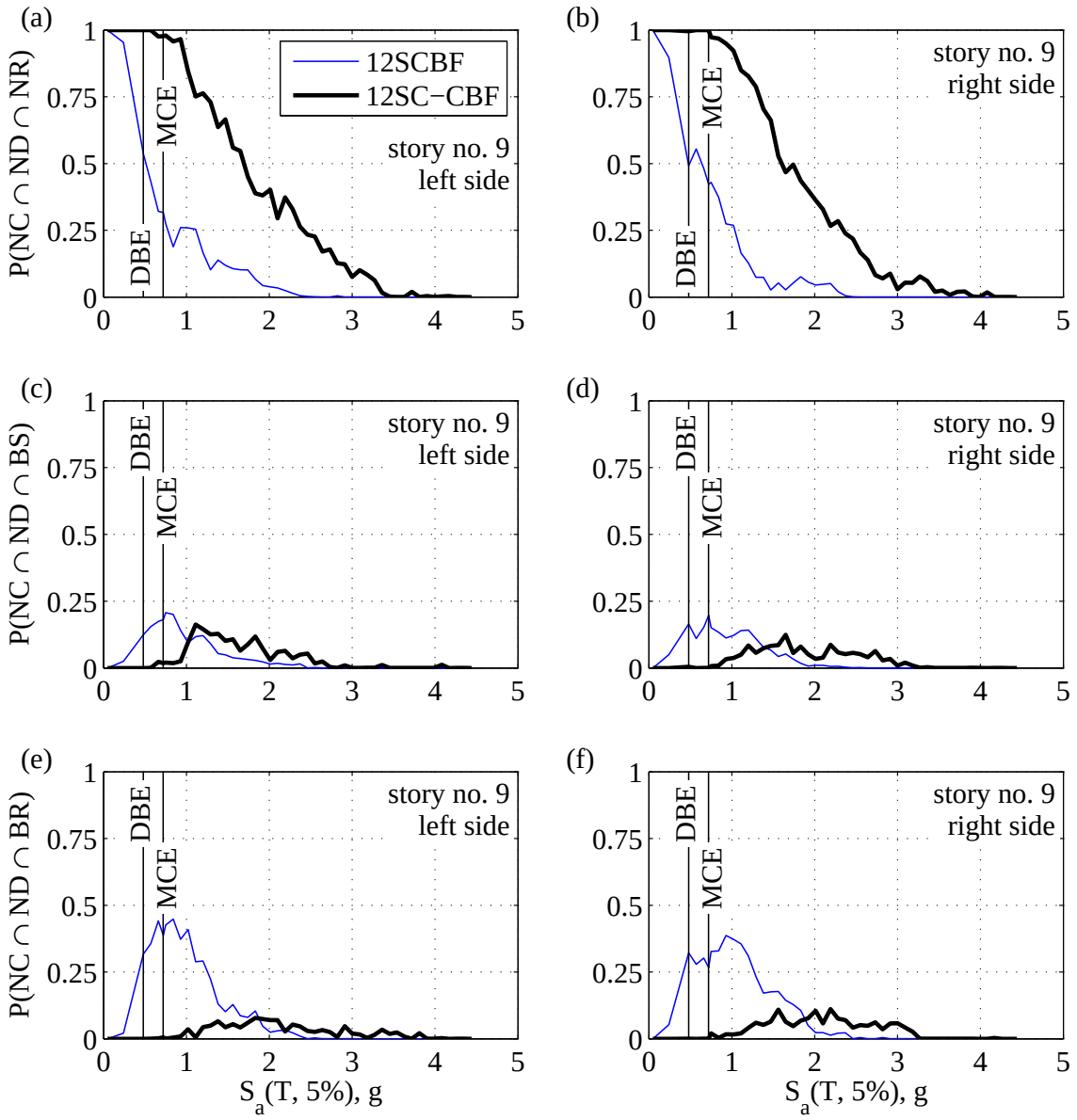

Figure 7.36: Comparison of brace damage scenario fragilities for 9th story of 12-story archetype buildings: (a) $NC \cap ND \cap NR$ for left side brace; (b) $NC \cap ND \cap NR$ for right side brace; (c) $NC \cap ND \cap BS$ for left side brace; (d) $NC \cap ND \cap BS$ for right side brace; (e) $NC \cap ND \cap BR$ for left side brace; and (f) $NC \cap ND \cap BR$ for right side brace;

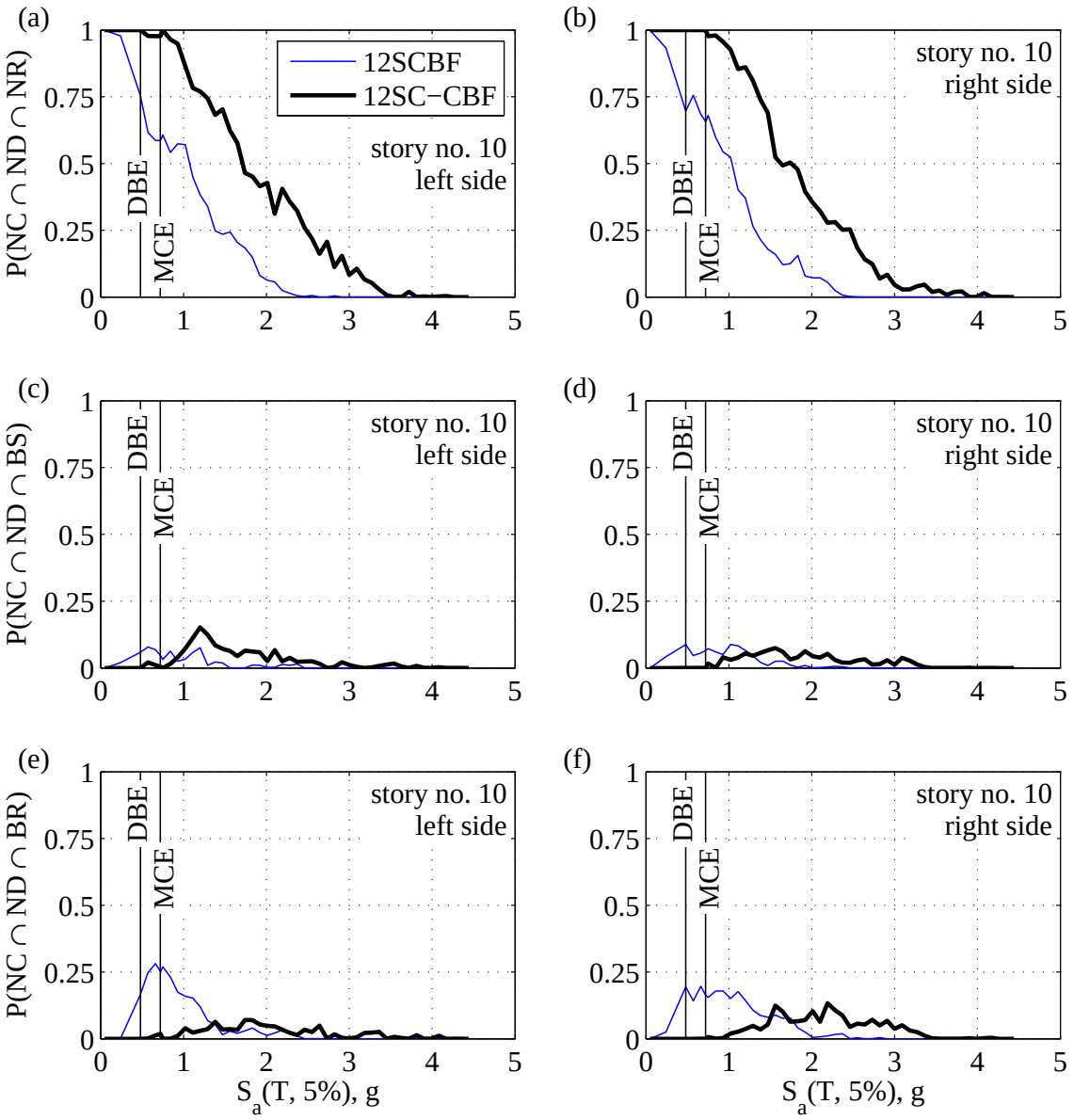

Figure 7.37: Comparison of brace damage scenario fragilities for 10th story of 12-story archetype buildings: (a) $NC \cap ND \cap NR$ for left side brace; (b) $NC \cap ND \cap NR$ for right side brace; (c) $NC \cap ND \cap BS$ for left side brace; (d) $NC \cap ND \cap BS$ for right side brace; (e) $NC \cap ND \cap BR$ for left side brace; and (f) $NC \cap ND \cap BR$ for right side brace;

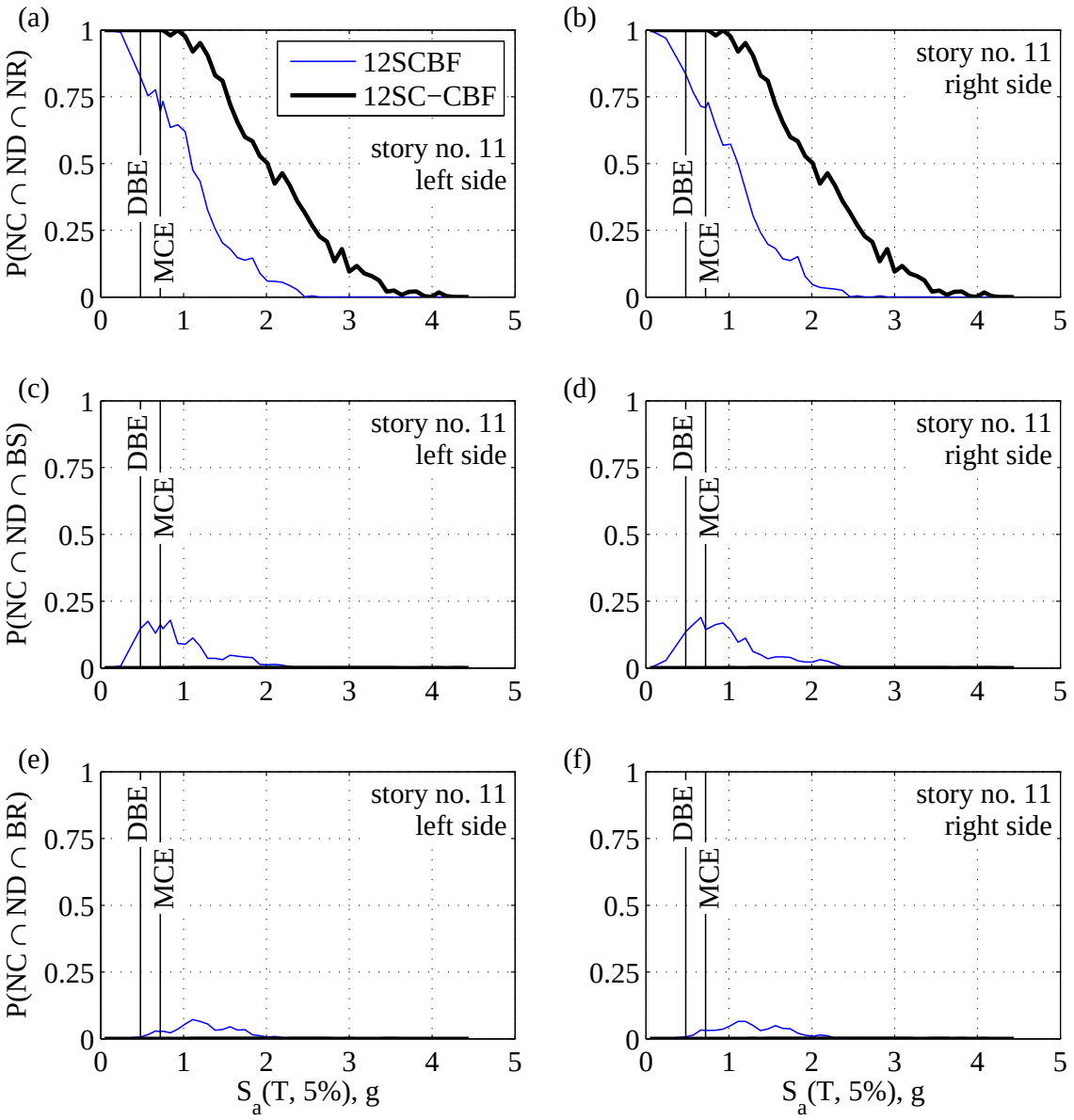

Figure 7.38: Comparison of brace damage scenario fragilities for 11th story of 12-story archetype buildings: (a) $NC \cap ND \cap NR$ for left side brace; (b) $NC \cap ND \cap NR$ for right side brace; (c) $NC \cap ND \cap BS$ for left side brace; (d) $NC \cap ND \cap BS$ for right side brace; (e) $NC \cap ND \cap BR$ for left side brace; and (f) $NC \cap ND \cap BR$ for right side brace;

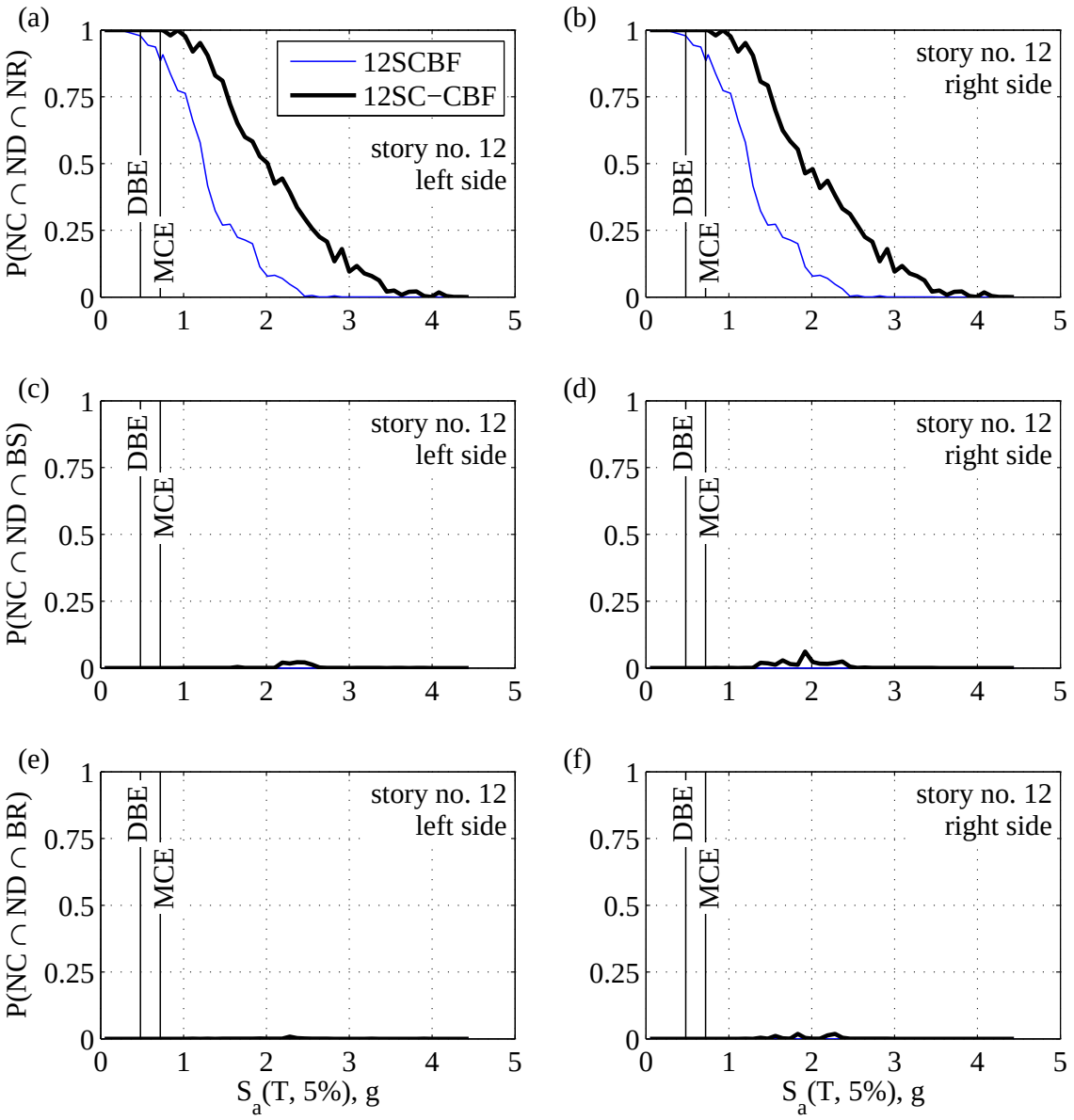

Figure 7.39: Comparison of brace damage scenario fragilities for 12th story of 12-story archetype buildings: (a) $NC \cap ND \cap NR$ for left side brace; (b) $NC \cap ND \cap NR$ for right side brace; (c) $NC \cap ND \cap BS$ for left side brace; (d) $NC \cap ND \cap BS$ for right side brace; (e) $NC \cap ND \cap BR$ for left side brace; and (f) $NC \cap ND \cap BR$ for right side brace;

7.6 Damage Scenario Fragilities Including Damage to PT bars

This section presents results for damage scenarios including damage of the PT bars of the SC-CBF archetype buildings. The PT bars of each SC-CBF archetype building are considered at the component level of the DSTA. The PT bars of each SC-CBF are treated as a single component. Loss of prestressing force (PT_0) in the PT bars and fracture of the PT bars during the seismic response of an SC-CBF archetype building are the types of damage considered. Four damage states (DS) with corresponding repair actions are considered: (i) less than 10% loss in PT_0 corresponding to no repair; (ii) more than 10% and less than 50% loss in PT_0 corresponding to the repair action of restressing of the PT bars; (iii) more than 50% loss in PT_0 without fracture of the PT bars corresponding to the repair action of replacement of the PT bars; and (iv) fracture of the PT bars which is considered to be an additional collapse condition (as discussed later). Note that PT_0 is the initial prestressing force in the PT bars which is determined in the design process for the SC-CBF system, as discussed in Chapter 3.

The maximum strain in the PT bars during a response history analysis, denoted by $\varepsilon_{PT,m}$, is used as the EDP to quantify the probability of being in a PT bar damage state (denoted by PT_{DS}). Three $\varepsilon_{PT,m}$ limit values are used to separate the four PT_{DS}. The $\varepsilon_{PT,m}$ limit value separating the PT_{DS} for no repair from the PT_{DS} for restressing the PT bars is denoted by $\varepsilon_{PT,m,res}$; the $\varepsilon_{PT,m}$ limit value separating the PT_{DS} for restressing the PT bars from the PT_{DS} for replacing the PT bars is denoted by $\varepsilon_{PT,m,rep}$; and the $\varepsilon_{PT,m}$ limit value identifying the PT_{DS} for fracture of the PT bars is denoted by $\varepsilon_{PT,m,frc}$.

Therefore, the probability of being in each PT_{DS} at a given IM value can be evaluated

using these $\varepsilon_{PT,m}$ limit values as follows:

$$P(PT_{NR}|IM) = P(\varepsilon_{PT,m} < \varepsilon_{PT,m,res}|IM) \tag{7.6}$$

$$P(PT_{res}|IM) = P(\varepsilon_{PT,m,res} \leq \varepsilon_{PT,m} < \varepsilon_{PT,m,rep}|IM) \tag{7.7}$$

$$P(PT_{rep}|IM) = P(\varepsilon_{PT,m,rep} \leq \varepsilon_{PT,m} < \varepsilon_{PT,m,frc}|IM) \tag{7.8}$$

$$P(PT_{frc}|IM) = P(\varepsilon_{PT,m,frc} \leq \varepsilon_{PT,m}|IM) \tag{7.9}$$

where PT_{NR} is the PT_{DS} corresponding to no repair, PT_{res} is the PT_{DS} corresponding to PT bar restressing, PT_{rep} is the PT_{DS} corresponding to PT bar replacement, and PT_{frc} is the PT bar fracture DS.

It is assumed that $\varepsilon_{PT,m,res}$, $\varepsilon_{PT,m,rep}$, and $\varepsilon_{PT,m,frc}$ follow a lognormal distribution, truncated for low values of $\varepsilon_{PT,m}$ at $\varepsilon_{PT,Y}$, where $\varepsilon_{PT,Y}$ is the strain at yield for the PT bars. The probability of each PT_{DS} is assumed to be zero for $\varepsilon_{PT,m} < \varepsilon_{PT,Y}$. The median value of $\varepsilon_{PT,m,res}$ and $\varepsilon_{PT,m,rep}$ is set at the value of the maximum PT bar strain $\varepsilon_{PT,m}$, corresponding to 10% and 50% loss in PT_0, respectively, and is different for each SC-CBF archetype building. The relationship between the maximum PT bar strain $\varepsilon_{PT,m}$ and the initial PT bar strain $\varepsilon_{PT,0}$ (i.e., strain in PT bars after applying the initial prestressing force PT_0) is based on an assumed uniaxial bilinear material with hardening, and can be stated as follows:

$$\varepsilon_{PT,m} = \frac{PT_0 - PT_r}{PT_0} \cdot \frac{1}{1-b_0}\varepsilon_{PT,0} + \varepsilon_{PT,Y} \tag{7.10}$$

where PT_r is the residual axial force in the PT bars at the end of a response history analysis, b_0 is the strain hardening ratio (i.e., ratio between post-yield tangent modulus and initial

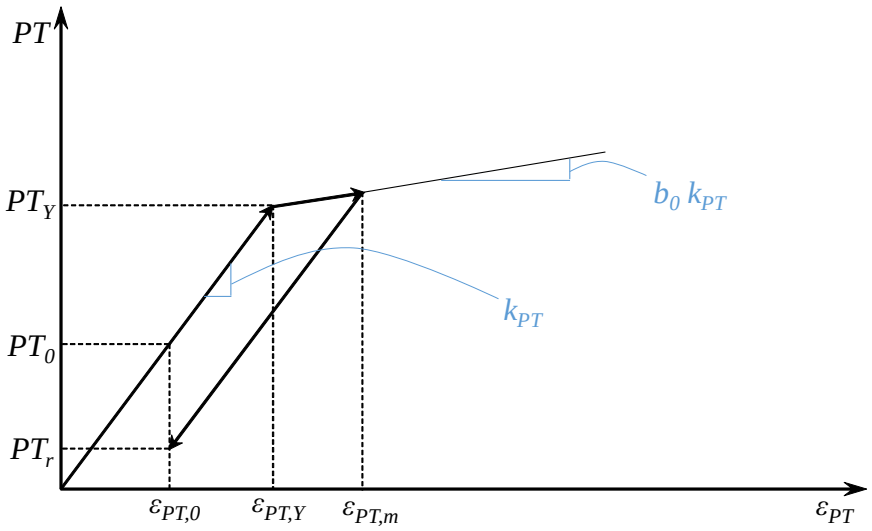

Figure 7.40: Schematic of the PT force-strain relationship

elastic modulus), $\varepsilon_{PT,0}$ is the initial strain in the PT bars (due to the prestressing force PT_0), and $\varepsilon_{PT,Y}$ is the PT bar strain at yield, as shown in Figure 7.40. The $\varepsilon_{PT,m,res}$ value and $\varepsilon_{PT,m,rep}$ value are determined, using Equation (7.10), for each SC-CBF archetype building as follows:

$$\varepsilon_{PT,m,res} = 0.1 \cdot \frac{1}{1-b_0}\varepsilon_{PT,0} + \varepsilon_{PT,Y} \tag{7.11}$$

$$\varepsilon_{PT,m,rep} = 0.5 \cdot \frac{1}{1-b_0}\varepsilon_{PT,0} + \varepsilon_{PT,Y} \tag{7.12}$$

A median value of 0.078 is assumed for $\varepsilon_{PT,m,frc}$ based on tension test results for PT bars [58]. A coefficient of variation of 0.2 is assumed for $\varepsilon_{PT,m,res}$ and $\varepsilon_{PT,m,rep}$ to represent epistemic uncertainty in the loss of prestressing force ($PT_0 - PT_r$) corresponding to the repair action of restressing and replacing the PT bars. A coefficient of variation of 0.15 is assumed for $\varepsilon_{PT,m,frc}$ to represent uncertainty in the fracture strain for the PT bars.

The $NC \cap ND \cap DS_{c,q,n}$ damage scenario fragilities are developed using Equation (5.24) for the SC-CBF archetype buildings with the PT bars as the component for which the

damage assessment is performed (i.e., $DS_{c,q,n} = PT_{DS}$). Equation (5.24) can be rewritten using $DS_{c,q,n} = PT_{DS}$ for the four PT_{DS} as follows:

$$P(NC \cap ND \cap PT_{NR}|IM) = \sum_{all\ GM_l} \bar{F}_{IM_{C,l}}(IM) \cdot \bar{F}_{\theta_{r,D}}(\theta_{r_l}) \cdot \left(1 - F_{\varepsilon_{PT,m,res}}(\varepsilon_{PT,m})\right) \cdot P(GM = GM_l|IM) \quad (7.13)$$

$$P(NC \cap ND \cap PT_{res}|IM) = \sum_{all\ GM_l} \bar{F}_{IM_{C,l}}(IM) \cdot \bar{F}_{\theta_{r,D}}(\theta_{r_l}) \cdot \left(F_{\varepsilon_{PT,m,res}}(\varepsilon_{PT,m}) - F_{\varepsilon_{PT,m,rep}}(\varepsilon_{PT,m})\right) \cdot P(GM = GM_l|IM) \quad (7.14)$$

$$P(NC \cap ND \cap PT_{rep}|IM) = \sum_{all\ GM_l} \bar{F}_{IM_{C,l}}(IM) \cdot \bar{F}_{\theta_{r,D}}(\theta_{r_l}) \cdot \left(F_{\varepsilon_{PT,m,rep}}(\varepsilon_{PT,m}) - F_{\varepsilon_{PT,m,fcr}}(\varepsilon_{PT,m})\right) \cdot P(GM = GM_l|IM) \quad (7.15)$$

$$P(NC \cap ND \cap PT_{frc}|IM) = \sum_{all\ GM_l} \bar{F}_{IM_{C,l}}(IM) \cdot \bar{F}_{\theta_{r,D}}(\theta_{r_l}) \cdot F_{\varepsilon_{PT,m,fcr}}(\varepsilon_{PT,m}) \cdot P(GM = GM_l|IM) \quad (7.16)$$

The $NC \cap ND \cap PT_{DS}$ damage scenario fragilities are shown in Figure 7.41 through Figure 7.44 for the SC-CBF archetype buildings. It can be seen that $P(NC \cap ND \cap PT_{rep})$ is considerably greater than $P(NC \cap ND \cap PT_{res})$ at most $S_a(T, 5\%)$ values for the 4SC-CBF archetype building. Similarly $P(NC \cap ND \cap PT_{rep})$ is greater than $P(NC \cap ND \cap PT_{res})$ for the 6SC-CBF archetype building as shown in Figure 7.42. The difference between $P(NC \cap ND \cap PT_{rep})$ and $P(NC \cap ND \cap PT_{res})$ for the 6SC-CBF archetype building is smaller than for the 4SC-CBF archetype building.

It can be seen from Figure 7.43 that $P(NC \cap ND \cap PT_{rep})$ is slightly greater than $P(NC \cap ND \cap PT_{res})$ at most $S_a(T, 5\%)$ values for the 9SC-CBF archetype building. The difference between $P(NC \cap ND \cap PT_{rep})$ and $P(NC \cap ND \cap PT_{res})$ is much smaller for the 9SC-CBF archetype building than for the 4SC-CBF and 6SC-CBF archetype building.

For the 12SC-CBF archetype building, $P(NC \cap ND \cap PT_{rep})$ and $P(NC \cap ND \cap PT_{res})$ are close to each other at most $S_a(T, 5\%)$ values. The $P(NC \cap ND \cap PT_{rep})$ value is slightly less than the $P(NC \cap ND \cap PT_{res})$ value at $S_a(T, 5\%)$ values approximately less than 0.8g, and the $P(NC \cap ND \cap PT_{rep})$ value is slightly greater than the $P(NC \cap ND \cap PT_{res})$ value at $S_a(T, 5\%)$ values approximately greater than 0.8g

The change in the difference between $P(NC \cap ND \cap PT_{res})$ and $P(NC \cap ND \cap PT_{rep})$ as the number of stories increases, shows that the $\varepsilon_{PT,m}$ value is generally decreasing as the number of stories of the SC-CBF archetype buildings increases. Since all of the SC-CBF archetype buildings have identical width, and taller archetype buildings have longer PT bars, the increasing numbers of stories (i.e., increase in height-to-width aspect ratio of the SC-CBF) increases the PT bar yield deformation capacity. Therefore, the amount of PT bar plastic deformation for a taller SC-CBF is less than the amount of PT bar plastic deformation for a shorter SC-CBF.

The $P(NC \cap ND \cap PT_{res})$ values and $P(NC \cap ND \cap PT_{rep})$ values are negligible at the DBE hazard level for all SC-CBF archetype buildings. The $P(NC \cap ND \cap PT_{res})$ values and $P(NC \cap ND \cap PT_{rep})$ values are considerable at the MCE hazard level for the 4SC-CBF and 6SC-CBF archetype buildings, but small for the 9SC-CBF and 12SC-CBF archetype buildings. The probability of PT bar damage at the DBE and MCE hazard level is greater than the probability of brace damage at the DBE and MCE hazard level (presented earlier in this chapter). In the design process of an SC-CBF system, the PT bars are designed for 50% probability of exceedance at the DBE while the braces are designed for 10% probability of

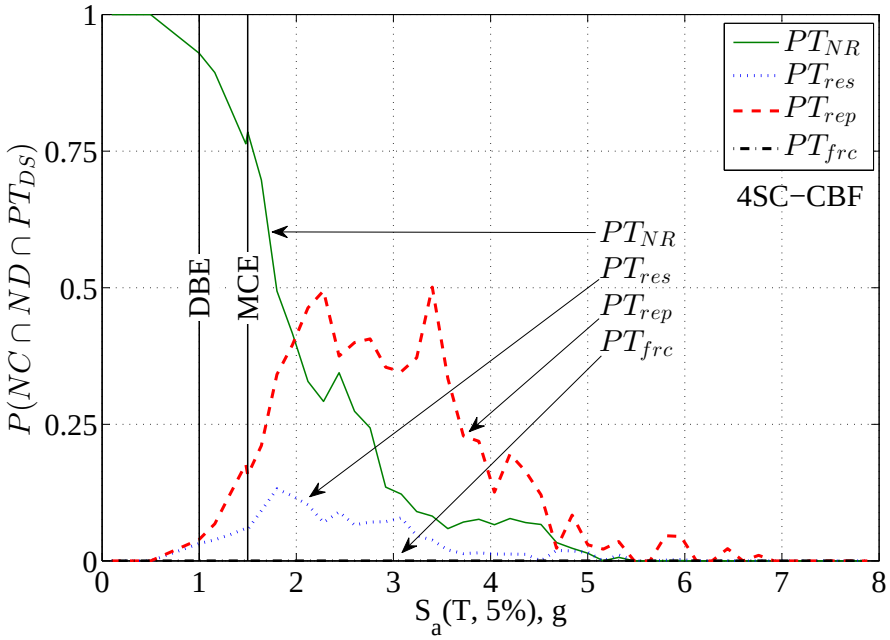

Figure 7.41: Damage scenario fragilities including PT bar damage for 4SC-CBF archetype building

exceedance at the DBE [11].

The $P(NC \cap ND \cap PT_{frc})$ values are negligible for all archetype buildings. This result is expected, since the observed $\varepsilon_{PT,m}$ at fracture of the PT bars is about 0.078 [58]; which is significantly larger than the observed $\varepsilon_{PT,m}$ values from the structural response history analyses. Note that PT bar fracture was not included in the numerical models used for structural response history analyses (see Chapter 3), during the analyses, however the $\varepsilon_{PT,m}$ values from the analyses have been checked. The 4SC-CBF archetype building has the largest $\varepsilon_{PT,m}$ values since it has the smallest height-to-width ratio among the SC-CBF archetype buildings. At the 10% maximum story drift ratio (i.e., $\theta_m = 0.1$), the value of $\varepsilon_{PT,m}$ is approximately 0.022, which is far smaller than the observed $\varepsilon_{PT,m}$ value at fracture of the PT bars (i.e., 0.078).

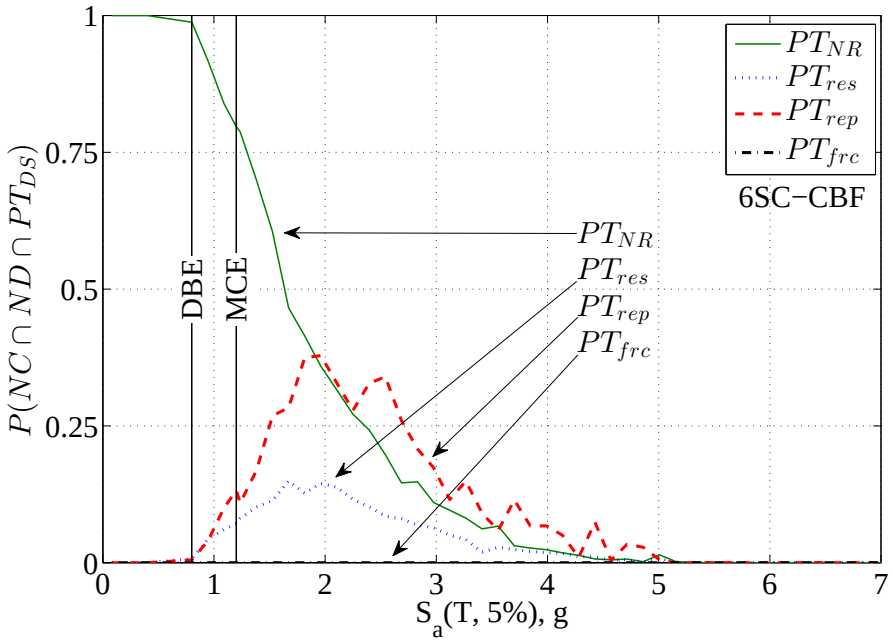

Figure 7.42: Damage scenario fragilities including PT bar damage for 6SC-CBF archetype building

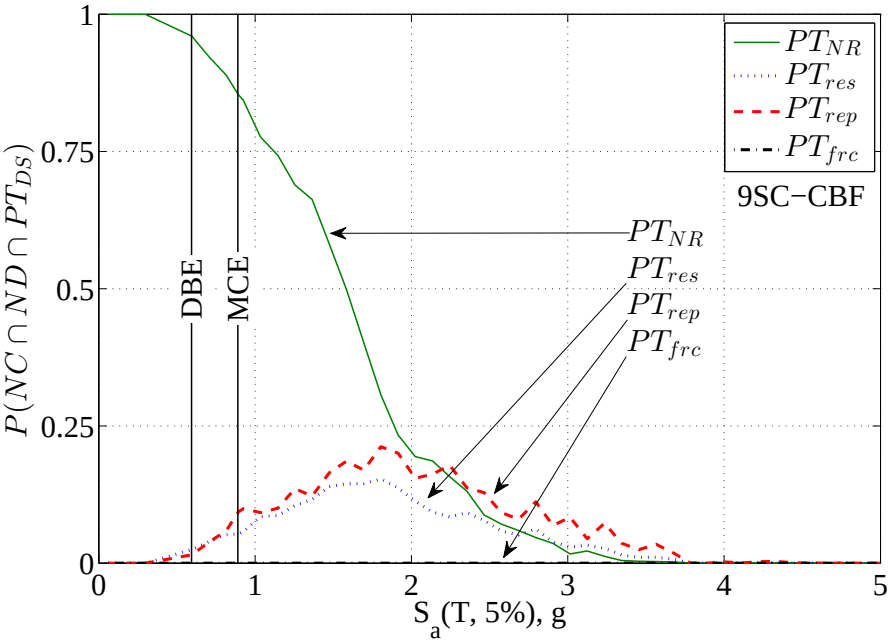

Figure 7.43: Damage scenario fragilities including PT bar damage for 9SC-CBF archetype building

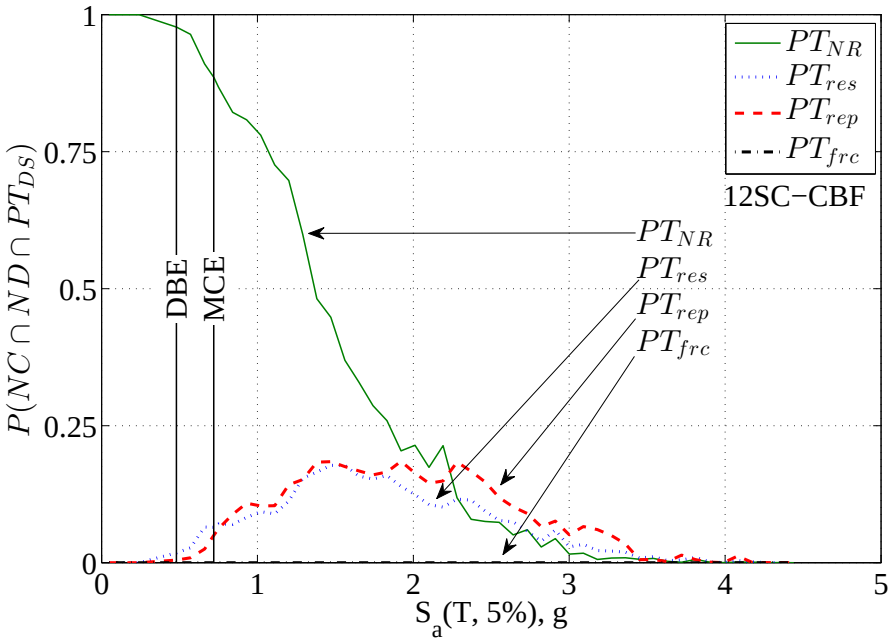

Figure 7.44: Damage scenario fragilities including PT bar damage for 12SC-CBF archetype building

7.7 Summary and Findings

The damage scenario tree analysis (DSTA) technique is applied to the SCBF and SC-CBF archetype buildings in this chapter. Damage scenarios of collapse, non-collapse with demolition, and non-collapse with non-demolition and component damage are studied. Damage to the braces of the SCBF and SC-CBF systems are considered at the component level damage assessment. Damage to the post tensioning (PT) bars are considered at the component level damage assessment for the SC-CBF archetype buildings.

It is observed that the probability of collapse for the SC-CBF archetype buildings is smaller than the probability of collapse for the SCBF archetype buildings with a similar number of stories at all $S_a(T,5\%)$ values. The probability of collapse is observed to be negligible at the DBE and MCE hazard level for the SCBF and the SC-CBF archetype buildings.

It is observed that fragilities for the non-collapse with demolition damage scenario for the SC-CBF archetype buildings are shifted towards the larger $S_a(T,5\%)$ values compared to the SCBF archetype buildings. This shift of the non-collapse with demolition damage scenario fragility to larger $S_a(T,5\%)$ values shows that a larger $S_a(T,5\%)$ value, corresponding to more intense GM or greater seismic hazard, is needed to produce the same damage scenario (non-collapse with demolition) probability for the SC-CBF archetype buildings compared to the SCBF archetype buildings. The probability of non-collapse with demolition is observed to be negligible at the DBE hazard level for the SCBF and the SC-CBF archetype buildings. At the MCE hazard level, the probability of non-collapse with demolition is observed to be negligible for the SC-CBF archetype buildings but non-negligible for the SCBF archetype buildings.

The probabilities for the damage scenarios including brace damage are observed to be considerably smaller for the SC-CBF archetype buildings in comparison with the SCBF archetype buildings. The number of stories with negligible probability of damage to the braces was considerably larger for the SC-CBF archetype buildings than for the SCBF archetype buildings. At the MCE and DBE hazard level, the probabilities of brace damage were observed to be considerable for the SCBF archetype buildings but negligible for the SC-CBF archetype buildings.

The damage scenarios including PT bar damage show that the probability of replacing the PT bars because of PT bar yielding is greater than the probability of restressing the PT bars for the shorter archetype buildings. As the number of stories of the SC-CBF archetype buildings increases (i.e., height-to-width aspect ratio increases), the probability of replacing the PT bars decreases and becomes smaller than the probability of restressing the PT bars. The probabilities of restressing or replacing the PT bars are observed to be negligible at the DBE hazard level for all SC-CBF archetype buildings. At the MCE hazard level, the probabilities of restressing or replacing the PT bars are observed to be considerable for the

4SC-CBF and 6SC-CBF archetype buildings, but small for the 9SC-CBF and 12SC-CBF archetype buildings.

The probability of PT bar damage is observed to be greater than the probability of brace damage for the SC-CBF archetype buildings. This difference is due to the different design criteria for PT bars and braces in the design process of the SC-CBF system [11], in which the PT bars yield limit state has about 50% probability of exceedance under the DBE and yielding or buckling limit state for the main structural members of the CBF has about 10% probability of exceedance under the DBE.

Chapter 8

Summary and Conclusions

8.1 Summary

8.1.1 Motivation

This research was conducted with the overall objective of understanding the potential for earthquake induced damage of the innovative steel self-centering concentrically braced frame (SC-CBF) system and comparing this damage potential with the damage potential for the conventional SCBF system. The SC-CBF system is a new seismic lateral force resisting system (SLFRS) that was developed and studied at ATLSS Engineering Research Center at Lehigh University. Extensive analytical simulations and experimental hybrid simulations were conducted on a 60% scale 4-story SC-CBF system using the Network for Earthquake Engineering Simulation (NEES) facility located at the ATLSS center [66]. This work showed that the SC-CBF remains damage free under the design basis earthquake (DBE), and demonstrated excellent self-centering response under the maximum considered earthquake (MCE) [73].

While the SC-CBF system was damage free under the ground motions at the DBE hazard level and self-centered under the ground motions at the MCE hazard level [73], the potential for damage of the SC-CBF system at hazard intensities beyond MCE had not been studied. To understand the potential for earthquake-induced damage to the SC-CBF system, comprehensive structural response history analyses under ground motions with var-

ious intensities were needed. Fragility curves for different damage states of the SC-CBF system, based on the results of comprehensive structural response history analyses across a range of hazard level were needed. Since the SC-CBF system is similar to, and benefits from the efficient lateral stiffness of the special concentrically braced frame (SCBF) system, the SCBF system provides a basis for assessing the damage potential of the SC-CBF. A comparison of this type, in terms of fragility curves, was needed.

8.1.2 Research objectives

To understand the potential for earthquake-induced damage of the SC-CBF system under ground motions at various hazard levels, and compare this damage potential with the damage potential of the conventional SCBF system, the following specific objectives were defined:

1. To conduct a collapse performance evaluation of the SC-CBF system and the SCBF system in accordance with the FEMA P695 document methodology [23], and compare the results

2. To develop a framework for conducting probabilistic seismic damage analysis of buildings

3. To include damage states other than building collapse in the probabilistic seismic damage analysis, using this framework

4. To include the effect of system parameter variability and modeling uncertainty in the probabilistic seismic damage analysis framework

5. To compare the probabilities of different damage scenarios for the SC-CBF system and the SCBF system

8.1.3 Research scope

To achieve the specific research objectives, several tasks were undertaken as follows:

1. **Archetype building development and design**

   Four buildings with different numbers of stories were considered in this research. The two seismic lateral force resisting systems, SCBF and SC-CBF were used for each building. So a total of eight archetype buildings were developed. The SCBF archetype buildings were designed in accordance with the ASCE 7-10 [4]. The SC-CBF archetype buildings were designed using the design process proposed by Roke [66] and modified by Chancellor [11].

2. **Numerical model development**

   Two dimensional nonlinear numerical models appropriate for each archetype building were developed in OpenSEES computational framework. Stiffness deterioration, strength deterioration, and fracture of the main structural members are included in the numerical models.

3. **Nonlinear static pushover analyses and dynamic response history analyses**

   Nonlinear static pushover analyses were conducted for the archetype buildings. Important lateral strength and deformation parameters were calculated from the static pushover analyses results for each archetype building. Nonlinear dynamic response history analyses were conducted in the form of incremental dynamic analyses for each archetype building.

4. **Collapse performance evaluation**

   The collapse capacity of each archetype buildings was estimated from the incremental dynamic analysis results. The collapse margin ratio and adjusted collapse margin ratio were determined for each archetype building in accordance with the FEMA

P695 document methodology [23]. Collapse fragility curves were developed for each archetype building using the incremental dynamic analysis results.

5. **Probabilistic seismic damage analysis framework**

   A probabilistic seismic damage analysis framework was developed for buildings using the event tree diagram concept. Damage states other than the collapse of the building were considered in developing the probabilistic seismic damage analysis framework. In the framework, damage assessments are performed at the system level, subsystem level, and component level. Damage scenarios are defined using the three levels of damage assessments. Mathematical formulas were developed for evaluating the damage scenario probabilities.

6. **Extension for system parameter variability and modeling uncertainty**

   Mathematical formulas were developed for including system parameter variability and modeling uncertainty in the probabilistic seismic damage analysis framework using results from Monte Carlo simulation. These mathematical formulas were demonstrated using a 9-story SCBF archetype building as an example. An approximate method for including the system parameter variability and modeling uncertainty in the damage scenario probabilities was developed and presented.

7. **Damage scenario probability comparison for SC-CBF and SCBF systems**

   Fragilities were developed for different damage scenarios for the SCBF and SC-CBF archetype buildings using the probabilistic seismic damage analysis framework. Damage scenario fragilities were compared for the SCBF and SC-CBF archetype buildings.

8.2 Findings

This section presents the findings of the research.

1. **Collapse performance evaluation**

   The adjusted collapse margin ratio value for each SCBF and SC-CBF archetype buildings is observed to be greater than the acceptable values set forth by FEMA P695 [23]. It is observed that the margin against collapse for each SC-CBF archetype building is greater than the margin against collapse for the corresponding SCBF archetype building with the same number of stories. The larger margins against collapse for the SC-CBF archetype buildings, show that the rocking and self-centering features of the SC-CBF system do not reduce the margin against collapse of the system, but actually increase the margin against collapse. By varying two collapse criteria of (i) a limit on the slope reduction of the IDA curve and (ii) a limit on the maximum story drift ratio, it is observed that varying the slope reduction limit in a range of 70% to 90%, has a small effect on the adjusted collapse margin ratio value for maximum story drift ratio limits of 0.02, 0.04, and 0.06, but has a more significant effect on the adjusted collapse margin ratio value for maximum story drift ratio limits of 0.08 and 0.10. By comparing the median residual story drift ratio for the SCBF and SC-CBF archetype buildings, it is observed that the median residual story drift ratio for the SC-CBF archetype buildings starts to increase from zero at a considerably larger hazard intensity level compared to the SCBF archetype buildings, indicating that larger intensity ground motions are required to produce residual drift of the SC-CBF system, relative to the SCBF system.

2. **Probabilistic seismic damage analysis framework**

   The damage scenario tree analysis (DSTA) technique provides a comprehensive framework for a probabilistic seismic damage analysis of buildings. By defining mutually exclusive and collectively exhaustive damage states at each level of damage assessment, the resulting damage scenarios are mutually exclusive and the collection of all possible damage scenarios are also collectively exhaustive, when evaluated for

a given component. The DSTA can be conducted using an intensity measure-based method, an engineering demand parameter-based method, or a combination of both methods. Two approaches were developed to use a set of ground motion records to include the record-to-record (RTR) variability in structural response: (i) the record-set approach, and (ii) the record-by-record approach. Application of the DSTA shows that the record-set approach for evaluating the damage scenario probabilities is ineffective and becomes more inaccurate as the hazard intensity level increases. The record-by-record approach avoids the expensive and inaccurate process of estimating the joint probability density functions and directly considers the correlation between the engineering demand parameters involved in damage assessments at different levels. The record-by-record approach also enables the use of ground motion record-specific damage state fragility functions when conducting a DSTA, which is shown to be useful for including the epistemic uncertainty in the collapse DS criteria.

3. **Extension for system parameter variability and modeling uncertainty**

   It is shown that the effect of system parameter variability and modeling uncertainty can be included in the DSTA using the results of Monte Carlo simulation. It is observed from the 9-story SCBF archetype building example that variation of the brace initial out-of-straightness and the live load present in the building when the earthquake strikes as random system parameters has a small effect on the collapse damage scenario and non-collapse with demolition damage scenario fragilities of the 9-story SCBF archetype building. It is also observed that variation of brace initial out-of-straightness has a significant effect on the damage scenario fragilities which include brace damage. It is observed that the damage state fragility functions can be modified using Monte Carlo simulation results to approximate the effect of system parameter variability and modeling uncertainty. The approximate method is found to be effective when the structural response for a numerical model with median values of the

random system parameters is close to the median structural response for numerical models with varying values of the random system parameters. This condition was observed to be valid for the maximum story drift ratio and the residual story drift ratio values but not for residual out-of-plane deformation of the brace members of the 9-story SCBF archetype building. It is observed that the effect of system parameter variability at smaller hazard intensity levels on the non-collapse with demolition damage scenario fragility is caused by the effect of random system parameters on the demolition fragility function. It is also observed that the effect of system parameter variability at larger hazard intensity levels on the non-collapse with demolition damage scenario fragility is caused by the effect of random system parameters on the collapse fragility function.

4. **Damage scenario probability comparison for SC-CBF and SCBF systems**

   It is observed that the probability of collapse for each SC-CBF archetype buildings is smaller than the probability of collapse for the corresponding SCBF archetype building with the same number of stories. It is also observed that the fragility for the non-collapse with demolition damage scenario for each SC-CBF archetype building is shifted towards the larger hazard levels compared to the corresponding SCBF archetype buildings. Non-negligible values for the non-collapse with demolition fragility is seen at much smaller hazard levels for each SCBF archetype building compared to the corresponding SC-CBF archetype building. A similar shift to larger hazard levels is observed for damage scenarios including brace damage for the SC-CBF archetype buildings compared to the corresponding SCBF archetype buildings. The fragilities for damage scenarios including damage to the post tensioning (PT) bars of the SC-CBF archetype buildings show that the probability of replacing the PT bars and the probability of restressing the PT bars decreases as the height of the SC-CBF archetype buildings increases. The probability of replacing the PT bars is

observed to be much greater than the probability of restressing the PT bars for shorter SC-CBF archetype buildings. The probability of replacing the PT bars decreases more than the probability of restressing the PT bars as the height of the SC-CBF archetype buildings increases. Therefore, the difference between the probability of replacing the PT bars and the probability of replacing the PT bars decreases as the height of the SC-CBF archetype building increases. The decreasing probabilities of replacing and restressing the PT bars with increasing building height shows that PT bar damage is less probable for taller SC-CBF archetype buildings.

8.3 Conclusions

The major conclusions of this research are as follows:

1. The SC-CBF system is shown to have an acceptable margin against collapse in accordance with FEMA P695 document methodology [22]. In comparison with the conventional SCBF system, the SC-CBF system has a greater margin against collapse.

2. Organizing a probabilistic seismic damage analysis of buildings into damage assessments at the system level, subsystem level, and component level within a damage scenario tree (i.e., using a damage scenario tree analysis or DSTA), enables various damage scenarios, including damage states other than the collapse damage state, to be understood and rigorously quantified.

3. Evaluating the probability of a damage scenario using a record-by-record approach enables the record-to-record variability of structural response to be rigorously included in quantifying the probability of the damage scenario. The correlation among engineering demand parameters used to quantify the damage states that contribute to a damage scenario is rigorously included by using the record-by-record approach.

4. System parameter variability and modeling uncertainty can be included in a DSTA using the results of Monte Carlo simulation.

5. The damage scenario fragilities, developed for the SCBF and SC-CBF systems using the DSTA technique show that the SC-CBF system has a smaller probability of collapse than the SCBF system, and has smaller probability of structural damage (when collapse has not occurred) than the SCBF system.

8.4 Original Contributions

The original contributions of this research can be stated as follows:

1. Seismic performance of the SC-CBF system is evaluated in accordance with FEMA P695 document methodology [22]. The seismic performance of the SC-CBF system is compared to the seismic performance of the conventional SCBF system.

2. A damage scenario tree analysis (DSTA) technique is provided as a general framework for conducting probabilistic seismic damage analysis of buildings. A method called the "record-by-record" approach is described for evaluating the probability of each damage scenario in the damage scenario tree.

3. Methods for including system parameter variability and modeling uncertainty in the DSTA are presented.

4. Damage scenario fragilities, including damage states other than the collapse damage state, are developed for four different SC-CBF archetype buildings using the DSTA technique. These damage scenario fragilities are compared to the damage scenario fragilities for four corresponding SCBF archetype buildings. The results show that the SC-CBF system has less potential for earthquake-induced damage.

8.5 Future Research

In future research, the damage scenario fragilities developed here, for SC-CBF and SCBF archetype buildings, can be used as input for seismic loss analysis of the SC-CBF system in comparison with the SCBF system. Including design and construction costs of SC-CBF buildings in the loss estimation and comparing with similarly estimated losses for conventional seismic lateral force resisting systems such as the SCBF system, can help stakeholders make informed decisions about the possible advantages of the SC-CBF system.

The effect of system parameter variability and modeling uncertainty can be considered more comprehensively for SC-CBF buildings in a future research. The variability of parameters specific to the SC-CBF system can be included in a damage scenario tree analysis. Additionally, the effect of changes in the SC-CBF parameters can be considered in a probabilistic seismic damage analysis.

The damage assessments conducted at the system level, subsystem level, and component level in DSTA, were evaluated using single variate damage state fragility functions. Future research can consider using multi-variate damage state fragility functions in a DSTA. Multi-variate damage state fragility functions may provide more accurate quantification of the damage state.

The seismic lateral force resisting system of the building was the only subsystem considered in the DSTA presented in this research. Other subsystems can be considered in future research when assessing the damage at the subsystem level, and damge to these subsystems can be included in estimating the probability of demolition of the building after an earthquake.

The braces and the post tensioning bars of the SC-CBF system were considered as structural members in the component level damage assessments. In future research, non-

structural components can be also included in various damage scenarios.

References

[1] Christoph Adam, Luis F Ibarra, and Helmut Krawinkler. Evaluation of P-delta effects in non-deteriorating MDOF structures from equivalent SDOF systems. In *Proceedings of 13th World Conference on Earthquake Engineering*, Vancouver, BC, Canada, 2004.

[2] AISC. Seismic provisions for structural steel buildings. ANSI/AISC 341-10, American Institute of Steel Construction, Chicago, IL, 2010.

[3] Gulce Akbas. Probabilistic earthquake structural damage assessment of steel special CBF and steel self-centering CBF buildings. MS thesis, Department of Civil and Environmental Engineering, Lehigh University, Bethlehem, PA, 2012.

[4] ASCE. Minimum design loads for buildings and other structures. ASCE/SEI 7-10, American Society of Civil Engineers, Reston, VA, 2010.

[5] Hesameddin Aslani. Probabilistic earthquake loss estimation and loss disaggregation in buildings. PhD dissertation, Department of Civil and Environmental Engineering, Stanford University, Stanford, CA, 2005.

[6] Jack W Baker and C Allin Cornell. A vector-valued ground motion intensity measure consisting of spectral acceleration and epsilon. *Earthquake Engineering & Structural Dynamics*, 34(10):1193–1217, 2005.

[7] Jack W Baker and C Allin Cornell. Spectral shape, epsilon and record selection. *Earthquake Engineering & Structural Dynamics*, 35(9):1077–1095, 2006.

[8] Jack W Baker and C Allin Cornell. Uncertainty specification and propagation for loss estimation using FOSM method. PEER Report 2003/07, Pacific Earthquake Engineering Research Center, University of California, Berkeley, CA, 2003.

[9] Jack W Baker and C Allin Cornell. Uncertainty propagation in probabilistic seismic loss estimation. *Structural Safety*, 30(3):236–252, 2008.

[10] R Gary Black, W A B Wenger, and E P Popov. Inelastic buckling of steel struts under cyclic load reversals. Report no. UCB/EERC-80/40, Earthquake Engineering Research Center, University of California, Berkeley, CA, 1980.

[11] Nathan Brent Chancellor. Seismic Design and Performance of Self-Centering Concentrically-Braced Frames. PhD dissertation, Department of Civil and Environmental Engineering, Lehigh University, Bethlehem, PA, 2014.

[12] Constantin Christopoulos, Andre Filiatrault, Chia-Ming Uang, and Bryan Folz. Post-tensioned energy dissipating connections for moment-resisting steel frames. *Journal of Structural Engineering*, 128(9):1111–1120, 2002.

[13] Constantin Christopoulos, Stefano Pampanin, and MJ Nigel Priestley. Performance-based seismic response of frame structures including residual deformations part I: single-degree of freedom systems. *Journal of Earthquake Engineering*, 7(01):97–118, 2003.

[14] Ray W Clough and Arthur A Huckelbridge. Preliminary experimental study of seismic uplift of a steel frame. , Earthquake Engineering Research Center, College of Engineering, University of California, Berkeley, CA, 1977.

[15] ASCE/SEI Seismic Rehabilitation Standards Committee. Seismic rehabilitation of existing buildings. ASCE/SEI 41-06, American Society of Civil Engineers, Reston, VA, 2007.

[16] SEAOC Vision 2000 Committee. Performance-based seismic engineering. , Structural Engineers Association of California, Sacramento, CA, 1995.

[17] C. Allin Cornell, Fatemeh Jalayer, Ronald O. Hamburger, and Douglas A. Foutch. Probabilistic basis for 2000 SAC federal emergency management agency steel moment frame guidelines. *Journal of Structural Engineering*, 128(4):526–533, 2002.

[18] Matthew Eatherton, Jerome Hajjar, Gregory Deierlein, Xiang Ma, and Helmut Krawinkler. Hybrid simulation testing of a controlled rocking steel braced frame system. In *9 th US National and 10 th Canadian Conference on Earthquake Engineering*, Toronto, 2010.

[19] Matthew Eatherton, Jerome Hajjar, Xiang Ma, Helmut Krawinkler, and Greg Deierlein. Seismic design and behavior of steel frames with controlled rocking–part I: concepts and quasi-static subassembly testing. In *Proc., ASCE/SEI Structures Congress*, Orlando, Florida, 2010.

[20] Bruce Ellingwood and Theodore V Galambos. Probability-based criteria for structural design. *Structural Safety*, 1(1):15–26, 1983.

[21] Clifton A Ericson. *Hazard analysis techniques for system safety*. John Wiley & Sons, 2005.

[22] FEMA. State of art report on performance prediction and evaluation of steel moment-frame buildings. FEMA-F355, Federal Emergency Management Agency, Washington, DC, 2000.

[23] FEMA. Quantification of building seismic performance factors. FEMA P695, Federal Emergency Management Agency, Washington, DC, 2009.

[24] Douglas A Foutch and Shan Shi. Effects of hysteresis type on the seismic response of buildings. In *Proceedings of the 6th US National Conference on Earthquake Engineering*, pages 1–12, 1998.

[25] Maria M Garlock, James M Ricles, and Richard Sause. Experimental studies of full-scale posttensioned steel connections. *Journal of Structural Engineering*, 131(3):438–448, 2005.

[26] Maria M Garlock, Richard Sause, and James M Ricles. Behavior and design of post-tensioned steel frame systems. *Journal of Structural Engineering*, 133(3):389–399, 2007.

[27] Christine A Goulet, Curt B Haselton, Judith Mitrani-Reiser, James L Beck, Gregory G Deierlein, Keith A Porter, and Jonathan P Stewart. Evaluation of the seismic performance of a code-conforming reinforced-concrete frame buildingfrom seismic hazard to collapse safety and economic losses. *Earthquake Engineering & Structural Dynamics*, 36(13):1973–1997, 2007.

[28] Ronald O Hamburger, Douglas A Foutch, and C Allin Cornell. Translating research to practice: FEMA/SAC performance-based design procedures. *Earthquake Spectra*, 19(2):255–267, 2003.

[29] CB Haselton and JW Baker. Ground motion intensity measures for collapse capacity prediction: Choice of optimal spectral period and effect of spectral shape. In *8th National Conference on Earthquake Engineering*, pages 18–22, 2006.

[30] Curt B Haselton. Assessing seismic collapse safety of modern reinforced concrete moment frame buildings. PhD dissertation, Department of Civil and Environmental Engineering, Stanford University, Palo Alto, CA, 2006.

[31] Curt B Haselton, Abbie B Liel, Gregory G Deierlein, Brian S Dean, and Jason H Chou. Seismic collapse safety of reinforced concrete buildings. I: assessment of ductile moment frames. *Journal of Structural Engineering*, 137(4):481–491, 2010.

[32] Curtis B. Haselton and Gregory G. Deierlein. Assessing seismic collapse safety of modern reinforced concrete moment frame buildings. Report No. 156, The John A. Blume Earthquake Engineering Center, Stanford University, Stanford, CA, 2007.

[33] L Ibarra, R Medina, and H Krawinkler. Collapse assessment of deteriorating SDOF systems. In *Proceedings of the 12th European Conference on Earthquake Engineering*, page Paper 665, London, 2002. Elsevier Science Ltd.

[34] Luis Ibarra and Helmut Krawinkler. Variance of collapse capacity of SDOF systems under earthquake excitations. *Earthquake engineering & structural dynamics*, 40(12):1299–1314, 2011.

[35] Luis F Ibarra and Helmut Krawinkler. Global collapse of frame structures under seismic excitations. , John A. Blume Earthquake Engineering Center, Stanford University, Stanford, CA, 2005.

[36] Luis F Ibarra, Ricardo A Medina, and Helmut Krawinkler. Hysteretic models that incorporate strength and stiffness deterioration. *Earthquake engineering and structural dynamics*, 34(12):1489–1512, 2005.

[37] J Iyama, CY Seo, JM Ricles, and R Sause. Self-centering MRFs with bottom flange friction devices under earthquake loading. *Journal of Constructional Steel Research*, 65(2):314–325, 2009.

[38] Kazuhiko Kawashima. Seismic design and retrofit of bridges. In *Proceedings of the Twelfth World Conference on Earthquake Engineering*, (Paper 2828), pages 265–285, Auckland, New Zealand, 2000.

[39] Kazuhiko Kawashima, Gregory A MacRae, Jyun-ichi Hoshikuma, and Kazuhiro Nagaya. Residual displacement response spectrum. *Journal of Structural Engineering*, 124(5):523–530, 1998.

[40] Hyung-Joon Kim and Constantin Christopoulos. Friction damped posttensioned self-centering steel moment-resisting frames. *Journal of Structural Engineering*, 134(11):1768–1779, 2008.

[41] Hyung-Joon Kim and Constantin Christopoulos. Seismic design procedure and seismic response of post-tensioned self-centering steel frames. *Earthquake Engineering & Structural Dynamics*, 38(3):355–376, 2009.

[42] Charles A Kircher, Robert K Reitherman, Robert V Whitman, and Christopher Arnold. Estimation of earthquake losses to buildings. *Earthquake spectra*, 13(4):703–720, 1997.

[43] Yahya Kurama, Richard Sause, Stephen Pessiki, and Le-Wu Lu. Lateral load behavior and seismic design of unbonded post-tensioned precast concrete walls. *ACI Structural Journal*, 96(4), 1999.

[44] Abbie B Liel, Curt B Haselton, and Gregory G Deierlein. Seismic collapse safety of reinforced concrete buildings. II: comparative assessment of nonductile and ductile moment frames. *Journal of Structural Engineering*, 137(4):492–502, 2010.

[45] Abbie B Liel, Curt B Haselton, Gregory G Deierlein, and Jack W Baker. Incorporating modeling uncertainties in the assessment of seismic collapse risk of buildings. *Structural Safety*, 31(2):197–211, 2009.

[46] Ying-Cheng Lin, JM Ricles, Richard Sause, and Choung-Yeol Seo. Earthquake simulations on a self-centering steel moment resisting frame with web friction devices. In *14th world conference on earthquake engineering*, 2008.

[47] Nicolas Luco and C Allin Cornell. Effects of random connection fractures on the demands and reliability for a 3-story pre-northridge smrf structure. In *Proceedings of the 6th US national conference on earthquake engineering*, volume 244, pages 1–12, 1998.

[48] Nicolas Luco and C Allin Cornell. Effects of connection fractures on SMRF seismic drift demands. *Journal of Structural Engineering*, 2000.

[49] Xiang Ma, Matthew Eatherton, Jerome Hajjar, Helmut Krawinkler, and Greg Deierlein. Seismic design and behavior of steel frames with controlled rocking - part II: large scale shake table testing and system collapse analysis. In *Proc., ASCE/SEI Structures Congress*, Orlando, Florida, 2010.

[50] Gregory A MacRae and Kazuhiko Kawashima. Post-earthquake residual displacements of bilinear oscillators. *Earthquake engineering & structural dynamics*, 26(7):701–716, 1997.

[51] Stephen A Mahin and Vitelmo V Bertero. An evaluation of inelastic seismic design spectra. *Journal of the Structural Division*, 107(9):1777–1795, 1981.

[52] Michael D McKay, Richard J Beckman, and William J Conover. Comparison of three methods for selecting values of input variables in the analysis of output from a computer code. *Technometrics*, 21(2):239–245, 1979.

[53] Francis Thomas Mckenna. Object-oriented finite element programming: frameworks for analysis, algorithms and parallel computing. PhD dissertation, University of California, Berkeley, CA, 1997.

[54] VZ Meimand and BW Schafer. Impact of load combinations on structural reliability determined from testing cold-formed steel components. *Structural Safety*, 48:25–32, 2014.

[55] Jack Moehle and Gregory G Deierlein. A framework methodology for performance-based earthquake engineering. In *Proceedings of the 13th World conference on earthquake engineering*, pages 3812–3814, 2004.

[56] OpenSEES. Open system for earthquake engineering simulation. http://opensees.berkeley.edu/. Retrieved August 2015.

[57] Stefano Pampanin, Constantin Christopoulos, and MJ Nigel Priestley. Performance-based seismic response of frame structures including residual deformations part II: multi-degree of freedom systems. *Journal of Earthquake Engineering*, 7(01):119–147, 2003.

[58] Felipe J Perez, Stephen Pessiki, and Richard Sause. Experimental and analytical lateral load response of unbonded post-tensioned precast concrete walls. ATLSS Report 04-11, ATLSS Engineering Research Center, Lehigh University, Bethlehem, PA, 2004.

[59] Jacob A Powell. Evaluation of special concentrically braced frames for improved seismic performance and constructability. MS thesis, University of Washington, Seattle, WA, 2010.

[60] C Marcelo Ramirez and Eduardo Miranda. Significance of residual drifts in building earthquake loss estimation. *Earthquake Engineering & Structural Dynamics*, 41(11):1477–1493, 2012.

[61] James M Ricles, Richard Sause, Maria M Garlock, and Chen Zhao. Posttensioned seismic-resistant connections for steel frames. *Journal of Structural Engineering*, 127(2):113–121, 2001.

[62] JM Ricles, R Sause, SW Peng, and LW Lu. Experimental evaluation of earthquake resistant posttensioned steel connections. *Journal of Structural Engineering*, 128(7):850–859, 2002.

[63] P Rojas, JM Ricles, and R Sause. Seismic performance of post-tensioned steel moment resisting frames with friction devices. *Journal of Structural Engineering*, 131(4):529–540, 2005.

[64] David Roke, Richard Sause, James M Ricles, and Nathaniel Gonner. Design concepts for damage-free seismicresistant self-centering steel concentrically-braced frames. In *Proceedings of the 14th World Conference on Earthquake Engineering*, pages 12–17, Beijing, China, 2008.

[65] David Roke, Richard Sause, James M Ricles, Choung-Yeol Seo, and Kyung-Sik Lee. Self-centering seismic-resistant steel concentrically-braced frames. In *Proceedings of the 8th US National Conference on Earthquake Engineering, EERI, San Francisco, April*, pages 18–22, 2006.

[66] David Alan Roke. Damage-free seismic-resistant self-centering concentrically-braced frames. PhD dissertation, Department of Civil and Environmental Engineering, Lehigh University, Bethlehem, PA, 2010.

[67] David Alan Roke, Richard Sause, J.M. Ricles, and Chancellor N.B. Damage-free seismic-resistant self-centering concentrically-braced frames. ATLSS Report 10-09, ATLSS Engineering Research Center, Lehigh University, Bethlehem, PA, 2010.

[68] Emilio Rosenblueth. The 1985 earthquake: causes and effects in Mexico City. *Concrete Journal, American Concrete Institute*, 8(5):23–24, 1986.

[69] Emilio Rosenblueth and R. Meli. The 1985 earthquake: causes and effects in Mexico City. *Concrete International*, 8(5):23–24, 1986.

[70] Jorge Ruiz-García and Eduardo Miranda. Evaluation of residual drift demands in regular multi-storey frames for performance-based seismic assessment. *Earthquake engineering & structural dynamics*, 35(13):1609–1629, 2006.

[71] Jorge Ruiz-García and Eduardo Miranda. Residual displacement ratios for assessment of existing structures. *Earthquake engineering & structural dynamics*, 35(3):315–336, 2006.

[72] Mehrdad Sasani and Jesse Kropelnicki. Progressive collapse analysis of an RC structure. *The Structural Design of Tall and Special Buildings*, 17(4):757–771, 2008.

[73] R Sause, J Ricles, D Roke, N Chancellor, and N Gonner. Large-scale experimental studies of damage-free self-centering concentrically-braced frame under seismic loading. In *Structures Congress, ASCE*, 2010.

[74] R Sause, JM Ricles, DA Roke, NB Chancellor, and NP Gonner. Seismic performance of a self-centering rocking concentrically-braced frame. In *Proceeding of the 9th US National and 10th Canadian Conference on Earthquake Engineering*, pages 25–29, 2010.

[75] Richard Sause, James M Ricles, David Roke, Choung-Yeol Seo, and Kyung-Sik Lee. Design of self-centering steel concentrically-braced frames. In *Proc. Of Sessions of the 4th International Conference on Earthquake Engineering, Taipei Taiwan*, 2006.

[76] Choung-Yeol Seo. Influence of ground motion characteristics and structural parameters on seismic responses of SDOF systems. PhD dissertation, Department of Civil and Environmental Engineering, Lehigh University, Bethlehem, PA, 2005.

[77] Choung-Yeol Seo and Richard Sause. Ductility demands on self-centering systems under earthquake loading. *ACI Structural Journal*, 102(2), 2005.

[78] Mohamed Talaat and Khalid M Mosalam. Modeling progressive collapse in reinforced concrete buildings using direct element removal. *Earthquake Engineering & Structural Dynamics*, 38(5):609–634, 2009.

[79] R Tremblay, LP Poirier, N Bouaanani, M Leclerc, V Rene, L Fronteddu, and S Rivest. Innovative viscously damped rocking braced steel frames. In *Proceedings of the 14th World Conference on Earthquake Engineering, Beijing, China*, pages 12–17, 2008.

[80] Robert Tremblay, M Lacerte, and C Christopoulos. Seismic response of multistory buildings with self-centering energy dissipative steel braces. *Journal of structural engineering*, 134(1):108–120, 2008.

[81] SR Uma, Stefano Pampanin, and Constantin Christopoulos. Development of probabilistic framework for performance-based seismic assessment of structures considering residual deformations. *Journal of Earthquake Engineering*, 14(7):1092–1111, 2010.

[82] P Uriz and SA Mahin. Toward earthquake-resistant design of concentrically braced steel-frame structures. PEER report no. 2008/08, Pacific Earthquake Engineering Research Center, University of California, Berkeley, CA, 2008.

[83] Patxi Uriz. Towards earthquake resistant design of concentrically braced steel structures. PhD dissertation, University of California, Berkeley, CA, 2005.

[84] Patxi Uriz, Filip C Filippou, and Stephen A Mahin. Model for cyclic inelastic buckling of steel braces. *Journal of structural engineering*, 134(4):619–628, 2008.

[85] Dimitrios Vamvatsikos. Seismic performance uncertainty estimation via ida with progressive accelerogram-wise latin hypercube sampling. *Journal of Structural Engineering*, 140(8), 2014.

[86] Dimitrios Vamvatsikos and C Allin Cornell. Incremental dynamic analysis. *Earthquake Engineering & Structural Dynamics*, 31(3):491–514, 2002.

[87] Dimitrios Vamvatsikos and Michalis Fragiadakis. Incremental dynamic analysis for estimating seismic performance sensitivity and uncertainty. *Earthquake engineering & structural dynamics*, 39(2):141–163, 2010.

[88] Lydell Wiebe, Constantin Christopoulos, Robert Tremblay, and Martin Leclerc. Mechanisms to limit higher mode effects in a controlled rocking steel frame. 1: Concept, modelling, and low-amplitude shake table testing. *Earthquake Engineering & Structural Dynamics*, 42(7):1053–1068, 2013.

[89] Lydell Wiebe, Constantin Christopoulos, Robert Tremblay, and Martin Leclerc. Mechanisms to limit higher mode effects in a controlled rocking steel frame. 2: Large-amplitude shake table testing. *Earthquake Engineering & Structural Dynamics*, 42(7):1069–1086, 2013.

[90] Michael Wolski, James M Ricles, and Richard Sause. Experimental study of a self-centering beam–column connection with bottom flange friction device. *Journal of structural engineering*, 135(5):479–488, 2009.

[91] Michael E Wolski. Experimental evaluation of a bottom flange friction device for a self centering seismic moment resistant frame with post-tensioned steel moment connections. MS thesis, Department of Civil and Environmental Engineering, Lehigh University, Bethlehem, PA, 2006.

[92] Farzin Zareian. Simplified performance-based earthquake engineering. PhD dissertation, Stanford University, Stanford, CA, 2006.

[93] Farzin Zareian and Helmut Krawinkler. Assessment of probability of collapse and design for collapse safety. *Earthquake Engineering & Structural Dynamics*, 36(13):1901–1914, 2007.

[94] Farzin Zareian, Helmut Krawinkler, Luis Ibarra, and Dimitrios Lignos. Basic concepts and performance measures in prediction of collapse of buildings under earthquake ground motions. *The Structural Design of Tall and Special Buildings*, 19(1):167–181, 2010.

Vita

Ebrahim Tahmasebi was born in Shiraz, Iran to Abbasali Tahmasebi and his wife Tahereh Bostanian. He attended Shiraz University, Shiraz, Iran where he earned his Bachelor of Science degree in Civil Engineering in 2007. He was admitted to the Master's program of Sharif University of Technology, Tehran, Iran in the fall of 2007. He completed his thesis on application of friction dampers in buildings under the supervision of Professor Fayaz Rahimzadeh Rofooei. He graduated from Sharif University of Technology in 2009 with a Master of Science degree in Earthquake Engineering. Ebrahim was awarded the Gibson Fellowship from Lehigh University to pursue his doctoral studies in the fall of 2009. During his doctoral studies at Lehigh University, he was awarded the Lehigh University P.C. Rossin Fellowship in 2012. He was appointed as an adjunct instructor at Lehigh University in the summer and fall of 2013. He was also appointed as research assistant and teaching assistant for several research projects and courses during his doctoral studies at Lehigh University. He will receive his Doctor of Philosophy degree in Structural Engineering in January 2016.